Dynamics of rotating machinery: analysis, identification and control

A thesis submitted to the University of Pisa
for the degree of Doctor of Philosophy

By

EMILIANO RUSTIGHI

Supervisors

Prof. C. Carmignani Prof.ssa. P. Forte

Corso di dottorato di ricerca in Ingegneria Meccanica, II° Ciclo
Department of Mechanical, Nuclear and Production Engineering
University of Pisa, Italy

February 2004

Title: "Dynamics of rotating machinery: analysis, identification and control"

Abstract: The performance requirements that modern rotating machines must satisfy have introduced a trend toward higher speeds and more stringent vibration levels. The basic tools to fulfil the reduction of vibrations are the analysis and the identification of rotor systems to design proper rotating elements, and the use of control devices.

Supports, which are important rotor elements, are characterized with difficulty. The modulating functions identification method was applied to identify the parameters of hydrodynamic bearings. They were identified, both numerically and experimentally, with encouraging results.

Moreover, the design of a magneto-rheological squeeze film damper is presented and discussed. A numerical simulation and an experimental campaign were carried out. Since the damping characteristics can be varied continuously by controlling the magnetic field, it is possible to set the optimum conditions for each operating condition. An automatic semi-active control algorithm was devised by means of fuzzy logic and genetic algorithm.

Finally, the vibrations of flexible rotating disks in the presence of dry friction were studied. This is a crucial problem, common to many industrial fields. The results of an experimental investigation, carried out on a commercial paper cutting machine and on a test rig, are presented and discussed. The investigation has shown the influence of some operating and design parameters on the system dynamic behaviour.

Titolo: "Dinamica degli organi rotanti: analisi, identificazione e controllo"

Sommario: Gli organi rotanti di macchinari moderni sono soggetti a velocità sempre più elevate e limiti vibratori sempre più ristretti. Gli strumenti per ridurre tali vibrazioni sono l'analisi e l'identificazione dei sistemi per un opportuno dimensionamento delle parti rotanti, e l'utilizzo di appropriati smorzatori.

Elementi importanti nella dinamica dei rotori ma di difficile caratterizzazione sono i supporti. Il metodo identificativo delle funzioni modulanti è stato applicato all'identificazione dei coefficienti dinamici di cuscinetti idrodinamici. Sono stati ottenuti risultati incoraggianti sia dalle analisi numeriche che sperimentali.

Inoltre è presentato il progetto di uno smorzatore magnetoreologico a "squeeze-film". Sono stati condotti sia una analisi numerica che una campagna sperimentale. Poichè il coefficiente smorzante del cuscinetto può essere variato con continuità è stato possibile impostare le condizioni di funzionamento ottimo per ogni condizione operativa. Un controllore automatico è stato progettato con l'uso di logica Fuzzy e algoritmi genetici.

Infine sono state studiate le vibrazioni di dischi sottili rotanti in presenza di attrito secco, problema molto complesso e molto sentito in vari ambiti industriali. Sono quindi presentati e discussi i risultati di un'indagine sperimentale condotta sia su un macchinario commerciale di una cartiera che su una attrezzatura sperimentale. È stata mostrata l'influeza di alcuni parametri sull'insorgere delle vibrazioni.

Acknowledgements

I would like to express my gratitude to my supervisors, Prof. C. Carmignani and Prof.ssa P. Forte. I gratefully acknowledge their technical and strategic expertise, as well as their immense patience.

Special thanks are extended to my colleagues and friends for the useful discussions, ideas and help. In particular I would like to thank Riccardo Ciolini for his encouraging support and friendship.

Furthermore, I am indebted to the students Cristiano Arfanotti, Alessandro Bechi, Gabriele Bicci, Andrea Borzoni, Marco Paternò and Marcello Venturi for their valuable contribution to my work.

Finally, I would like to thank my family and my girlfriend Ilaria for their love, patience and support. Without their help this thesis would not have been completed.

Contents

1 Introduction **1**

2 Identification of rotor supports **6**
2.1 Introduction 6
2.2 Parametric identification techniques 9
2.2.1 The modulating function identification algorithm . . . 9
2.2.2 The recursive identification algorithm 12
2.3 Simulated identification of mechanical systems 13
2.3.1 One and two degree of freedom systems 13
2.3.2 The rotor-bearing system 23
2.4 Experimental tests on a single degree of freedom system . . . 27
2.4.1 Design of the test rig 27
2.4.2 Experimental results 28
2.5 Experimental tests on a hydrodynamic bearing 34
2.5.1 Design of the test rig 34
2.5.2 Experimental results 35
2.6 Conclusions 38

3 Semi-active control of a rotating shaft: the magnetorheological squeeze-film damper **39**
3.1 Introduction 39
3.2 Passive, active and semi-active control of rotors 40
3.3 Squeeze film bearings 43
3.4 The magnetorheological fluids 44
3.5 Adjustable squeeze film dampers 50
3.6 Modelling of a squeeze film damper with magnetorheological fluid 55
3.7 Modelling of the rotor-damper system 59
3.8 Design of the MR squeeze-film damper 68
3.8.1 Description of the device 68
3.8.2 Design of the magnetic circuit 69

3.8.3 The test-rig . . . 71
3.9 Experimental results . . . 75
3.10 Design of the controller . . . 79
3.10.1 A dynamic empirical model of the rotor-damper system 79
3.10.2 An empirical fuzzy controller . . . 83
3.10.3 A fuzzy controller designed by means of genetic algorithm 91
3.11 Conclusions . . . 102

4 Investigation on the dynamic behaviour of disc blades during sharpening 104
4.1 Introduction . . . 104
4.2 Dynamics of rotating disks . . . 106
4.2.1 General considerations . . . 106
4.2.2 Free vibration of a stationary disk . . . 108
4.2.3 Forced vibration of a stationary disk . . . 115
4.2.4 Free vibration of a rotating disk . . . 115
4.2.5 Forced vibration of a rotating disk . . . 116
4.2.6 Lock-in instability . . . 117
4.3 Starting practical problem . . . 124
4.3.1 Impact tests . . . 126
4.3.2 Modal analysis . . . 127
4.3.3 Sharpening tests . . . 129
4.3.4 Comments on the results . . . 130
4.4 Design of the test rig . . . 131
4.4.1 Description of the test rig . . . 131
4.4.2 Fem modal analysis . . . 138
4.5 Fem transient dynamic simulations . . . 141
4.5.1 Model definition . . . 141
4.5.2 Impact and sharpening simulations . . . 145
4.6 Experimental investigation . . . 154
4.6.1 Signal analysis . . . 156
4.6.2 Impact modal testing . . . 160
4.6.3 Modal investigation during sharpening . . . 163
4.6.4 Analysis of the sharpening process . . . 170
4.7 Conclusions . . . 174

5 Conclusions and suggestions for further work 176

A Publications 179

B Education and training 181

Bibliography **183**

To my parents

Chapter 1

Introduction

The performance requirements that modern rotating machines and equipments must satisfy have introduced a trend toward higher speeds and more stringent vibration levels. At lower speeds, the design of most rotors presents few problems which can be solved by relatively simple means. At higher speeds, which are sometimes in the range of 10000 rpm, the design of rotors can be an engineering challenge which requires sophisticated solutions of interrelated problems in mechanical design, balancing procedures, bearing design, and the stability of the complete assembly. Reduction and control of the vibratory level of machinery aims at improving their comfort and efficiency. Designers are required to have a deep knowledge of the dynamics of rotating machinery. Their tools to fulfil the reduction of vibrations are the analysis and the identification of the rotor systems in order to suitably revise the design and eventually include control devices.

It is important to build a reliable model of the rotating machinery system in order to single out the more significant parameters in the process under examination. Thus, a proper design of the system can be done allowing machines to be designed with rotor resonances outside the operating speed range and reducing mechanical losses.

In order to plan the right strategy to cope with vibrations the parameters of the model must be known with a great degree of accuracy. The dynamic characteristics of modern turbomachines, generally operating beyond few critical speeds, have to be predicted precisely to avoid the possibility of operating near the critical speeds or in the unstable speed range and further to identify the sources of vibration. If the machine is supported by fluid-film bearings, the dynamic behaviour is significantly influenced by the stiffness and damping characteristics of the oil film of the bearing, but the exact values of stiffness and damping coefficients are not known. The stiffness and damping characteristics are greatly dependent on many physical and me-

chanical parameters, such as temperature, load, speed and misalignment of the system and they are quite difficult to account. Hence, to simulate the dynamic characteristics of the rotor bearing system, the stiffness and damping characteristics of the fluid film bearings have to be identified. Moreover the application of modal identification for diagnostics of machine operational malfunctions presents an important task.

Several time-domain and frequency-domain techniques have been developed for determining the oil-film coefficients. Many works have dealt with the identification of bearing coefficients and rotor-bearing system parameters using impulse, step change in force, and synchronous and non-synchronous excitation techniques. For example, Muszynska et al. [1] have applied a sweep frequency rotating force perturbation method to rotating systems for dynamic stiffness identification and showed that excellent signal-to-noise ratio data can be obtained for identification of the rotor-bearing system parameters.

Once the model is known exactly, the designer can choose the action to undertake. Apart from a smart design, the designer can use control devices in order to respect the vibratory requirements, and among them he can choose passive, active and semi-active control devices.

Passive devices are well-known components that are added to the main structure in order to absorb vibratory energy, such as springs, dampers and tuned vibration absorber. Such devices are called passive since they do not need any energy supply and their characteristics cannot be modified while they are on duty. In rotating machinery passive components are usually linear dampers placed between the bearings and the foundation or "squeeze-film" dampers. Moreover, auxiliary masses can be attached to vibrating systems by springs and damping devices to assist in controlling the amplitude of vibration of the system. An important industrial use of auxiliary mass systems is to neutralize the unbalance of centrifugal machinery. A common application is the balance ring in the spin dryer of a home washing machine [2]. The operation of such a balancer is dependent upon the basket of the washer rotating at a speed greater than the natural frequency of its support. If the displacement of the weights or fluids in the balance ring occurs above the natural frequency, the center of gravity tends to move closer to the dynamic location of the axis. Thus the eccentricity is brought toward zero and the rotor is automatically balanced. The balancing elements can take several forms, such as spheres or cylinders free to move in a race concentric with the axis of the rotor.

Active control devices are devised to reduce vibrations of rotating machinery by the generation of new excitation forces that act on the system. The new forces can lower the vibratory level if properly varied in time. For

example magnetic bearings can be used to reduce the vibration of rotors. Active magnetic bearing are becoming increasingly significant for various types of rotating machinery. Examples are turbo-compressors, centrifuges, high speed milling and grinding spindles, vacuum pumps and space applications. Thanks to the rapid progress and drastic cost reduction in power- and micro-electronics, the number of active magnetic bearing applications is growing very fast. One of the most outstanding advantages of magnetic rotor bearings is their ability to actively control the vibrations occurring in a rotor system: damping can be introduced in order to improve the transient rotor behaviour or to facilitate the passing of bending critical speeds [3].

Also active hydrostatic bearings have been designed and commercialized. The Bently ServoFluid^{TM} Control Bearing uses fluid forces to compensate for rotor-related forces. It consists of a hydrostatic (externally pressurized) bearing which supports the rotor loads, position-sensing eddy current transducers, high-speed electrohydraulic valves, and a control system acting as a closed-loop system. The radial hydrostatic bearing is a four-pocket design, and the thrust is a two-pocket design. Both have been designed with adequate pocket areas to perform active and static load support, and enough bearing surface to allow for fault conditions. The control system uses linear-type PID (proportional-integral-derivative) controllers. The designed controller concentrates on both active anti-swirl control and active radial pressurized control. The design of the active radial bearings incorporates the positive features from previous bearing designs, while eliminating some of their problems.

Active control also makes perturbation testing practical. It allows designers to simulate certain operating conditions at the test stage to evaluate stresses, so that designs can be iterated, and confirms stability predictions. Real-time active control allows the user to measure the forces that the control system compensates for, thus creating another useful tool to diagnose machine malfunctions, and to determine the actual health of the machine

Anyways, active controls are usually energetically expensive and they can cause some new instabilities on the main system while passive systems are not versatile. Semi-active controls are then the compromise between the two techniques. Practically, semi-active devices are passive-devices whose physical characteristics can be changed in order to tune them to the hosting system and keep the vibratory level as small as possible. Such strategy is quite recent and few applications have been used in controlling rotor vibrations. For example the damping behaviour of tilting pad journal bearings can be adjusted by piezoelectric [4] or hydraulic [5] actuators connected to the bearing pads. In the same way the dynamic characteristics of a hydrodynamic bearing can be controlled changing the thickness and geometry of the

oil film [6]. However a lot of examples can be found in civil buildings and car suspensions. As the mechanical structure which hosts the semi-active device has to be equipped with sensors, the diagnostic and health monitoring of the machine can be done as well as for active system. Moreover, such devices are intrinsically stable and they do not cause the arising of new instability in the global system.

There are many interesting aspects to investigate involving rotating machinery but one of the most complex and intriguing phenomena is the vibratory motion of flexible rotating disk in presence of dry friction. Similar problems such as those related to grinding [7, 8], saw blades, turbine rotors, computer magnetic recording disks [9, 10, 11, 12] and brake disks [13, 14] were dealt with. The problems mainly concern the response of a rotating disk to an external transverse force. For example, Lisini and Bartalucci [7, 8] studied the grinding process and showed that the regenerative effect of grinding wheels is the predominant effect of the process instability: rotation oscillations of grinding wheel and work-piece feed successive vibrations, that are strictly connected with cutting forces. The problem was studied with a linear model in spite of non-linearity caused by backlash, friction, deformation, wear etc. studying only the onset of instability.

To suppress the out-of-plane vibration, the industry of hard disk drives is developing alternative substrate materials for the disks [12]. Some propose ceramic substrate with extremely high stiffness to reduce the vibration amplitude and to shift the resonances to higher frequencies. Others propose laminated disks consisting of a viscoelastic polymer core sandwiched between two aluminum disks. The vibration energy is dissipated through cyclic shear deformation of the viscoelastic polymer.

Beside passive techniques to control disk lateral vibrations, active techniques have been developed. As transverse vibrations of circular saw are detrimental to their cutting performance, Ellis and Mote [15] presented a method for reducing saw vibration using electromagnetically induced guiding forces in a feedback controller system. A linear proportionally-derivative feedback controller was designed. The controller increased the transverse stiffness and damping of a circular saw without increasing the thickness of the blade decreasing the material kerf loss during cutting. This system controlled low frequency vibration, but excited higher frequency instability above the bandwidth of their control system.

In order to limit controller instability, Radcliffe and Mote [16] designed a controller that applied electromagnetically an active control force to the disk to suppress the amplitude of only the dominant mode. The control force was equivalent to the generalized force distribution of the mode under control and other modes could not be excited.

Recently modern control techniques have been applied for the control of the transverse vibration of a rotating saw disk, such as state feedback [17] and sliding mode control system [18].

However, the knowledge of the vibrational behaviour and of the instability phenomenon is essential to plan the methodology to control the vibration by means of passive or active controller.

The aim of the study presented in this thesis was to learn the basic and advanced tools to cope with vibratory problems in rotating machinery focusing on the identification of rotor-bearing systems and the design of controllable devices to limit the vibratory levels of rotors. Moreover the vibratory motion of flexible rotating disks in the presence of dry friction has been investigated.

Following the introduction, chapter two discusses the application of the modulating functions method to the identification of the characteristics of rotor-bearing systems. In particular, the parameters of hydrodynamic bearings are numerically and experimentally identified. Chapter three presents the design of a magneto-rheological squeeze film damper. Numerical and experimental results are shown and discussed. Moreover, the design and optimization of a Fuzzy logic controller are presented. Chapter four deals with the flexural vibration arising in the sharpening process of disc blades. Numerical and experimental investigations show the influence of some operating and design parameters on the system dynamic behaviour. Finally, chapter five resumes the whole work.

Chapter 2

Identification of rotor supports

2.1 Introduction

The numerical simulation of a physical phenomenon requires a good theoretical model and experimentally identified coefficients in order to predict and control the dynamic behaviour of the real system. Moreover the real coefficients vary in time and for an effective system control a repeated identification may be necessary.

The system identification problem consists in the estimation of a model of a system on the basis of observed input-output data. There are several ways to describe a system and to estimate its performance. In the construction of a model from data three basic entities are involved:

- The data record: *estimation data* are the data set that is used to fit a model to data while *validation data* are the data set that is used for model validation purpose;
- A model structure;
- A rule by which candidate models can be assessed using the data, like the least squares selection rule.

The identification process consists of repeatedly selecting a model structure, computing the best model, and evaluating the model properties to see if they are satisfactory. The cycle can be itemized as follows [19]:

1. Design an experiment and collect input-output data from the process to be identified;
2. Clean it so as to remove trends and outliers, and select useful portions of the original data;

3. Possibly apply filtering to enhance important frequency ranges;
4. Select and define a model structure within which a model is to be found;
5. Compute the best model in the model structure according to the input-output data and a given criterion of fit;
6. Examine the obtained model's behaviour in order to validate the model. Model validation can be carried out taking in account the mean squared error, the difference of the spectra or the coherence function between estimation and validation data.

The choice of the model structure to be adopted is the most important and difficult phase of the system identification procedure. The knowledge of the system behaviour can lead to a model set, based on basic physical laws and other well established relationships with some unknown physical parameters. In other cases standard linear models may be employed, without reference to the physical background. Such a model set, whose parameters are basically viewed as vehicles for adjusting the fit to the data and do not reflect physical considerations, is called a *black box*. Model sets with adjustable parameters with physical interpretation may, accordingly, be called *gray boxes* [20].

The techniques that estimate the parameters in given model structures are called *parametric identification methods*. Basically it is a matter of finding those value of the parameters that give the best agreement between the model's output and the measured one. *Nonparametric identification methods* are techniques to estimate model behaviour without using a given parametrized model set [19].

The physics of the problem, the reasons why the system is studied and the system complexity lead the choice between black and gray boxes. In fact if the system is very complex the use of a physical model can lead to a model that cannot be handled easily. Moreover, sometimes the description of a system can be impossible. In these situations the use of black box models is straightforward.

The identification methods, in spite of the adopted model of the system, can be developed either in the time or in the frequency domains. While identification in the frequency domain generally aims at identifying the system harmonic transfer function, in the time domain it aims at reproducing the signal from the experimental time response. Although there is a completely equivalence between time and frequency domain, there can exist significant differences in the practical application of such techniques. Frequency domain techniques perform better where there is essentially no limit on the amount of data that can be collected and when the transfer function is required over

a limited frequency range only and is not easily modelled by a low-order rational model [21]. Unluckily frequency domain techniques show some fundamental limitations in accuracy when there is a finite quantity of noisy data and time domain technique should be preferred. Moreover time domain are more suitable to depict non linearities. Both techniques cannot deal with non-stationary system parameters.

The fundamental principle of the identification techniques is the minimization of the difference between the analytical response, evaluated in the time or frequency domain, and the measured response of the real system subjected to the same excitation. The different methods employed to minimize such difference are mainly based on the least squares approach.

The modulating function identification algorithm is a parametric identification method that works on a physical description of the model. The idea of adopting the modulating functions for system identification goes back to the 60's, when Shinbrot [22] suggested the application of an integral transform to reduce the negative effects of noise. Afterwards many researchers have focused their attention on this technique and in particular on its application to non-linear systems and on the choice of the most effective function type. Balestrino et al. [23] proposed a technique for the identification of continuous systems with multiple input subjected to delay, based on the use of spline modulating functions. Such technique has shown the following advantages:

- the system of differential equations describing the dynamic equilibrium is replaced by a system of algebraic equations;
- there is no need to derive the signal;
- the identification is carried out directly in the continuous time domain;
- the technique is robust as regards noise.

Up to now this method has been used only for the identification of the characteristics of electric and electronic systems yielding very good results.

The objective of the work outlined in this chapter is the application of the modulating function identification algorithm to the identification of dynamic coefficients of rotor supports. Because of the complexity of such problem, the work started from a simple 1dof mass-spring system and then it extended to a more complex system made of a flexible rotor supported by a plain hydrodynamic bearing, of great practical significance. As far as the latter application is concerned, it is well known that in rotor dynamics the hydrodynamic bearing is commonly modelled by 8 linearized coefficients, but such model is quite useless if it is not identified experimentally. In the literature many

papers deal with the experimental determination of the dynamic coefficients of bearings by various techniques in the time and frequency domains and with various excitation means applied to the rotor or to the bearing case: forced orbits [24, 25], non-synchronous harmonic forces [25, 26, 1], impulse forces [27, 28, 29], and white noise [30]. A problem common to these different methods is their sensitivity to noise and their in-situ applicability.

2.2 Parametric identification techniques

2.2.1 The modulating function identification algorithm

The identification procedure is briefly described. The modulating functions $\varphi(t)$ have the following properties:

$$\varphi(t) = \begin{cases} \varphi(t) & 0 \leq t \leq T \\ 0 & \text{otherwise} \end{cases} \tag{2.1}$$

$$\frac{\mathrm{d}^i\varphi(t)}{\mathrm{d}t^i} \exists \quad ; \quad \frac{\mathrm{d}^i\varphi(0)}{\mathrm{d}t^i} = \frac{\mathrm{d}^i\varphi(T)}{\mathrm{d}t^i} = 0, \; i \leq n \tag{2.2}$$

where T is the modulating time interval.

The choice of the modulating functions is empirical. A group of modulating functions made by a modulating function and its n derivatives can be considered:

$$\mathbf{\Phi}_n = \{\varphi_{n,j}\} \quad j = 0, 1, \ldots, n \tag{2.3}$$

where n indicates the group order and j the derivative order. A group of spline modulating functions (Malentinsky spline functions) can be obtained considering the following n^{th} order derivative of the modulating function, made of a series of impulses and shown in Figure 2.1:

$$\varphi_{m,n} = \sum_{i=n}^{N} (-1)^n \begin{pmatrix} n \\ i \end{pmatrix} \delta(iT - t) \tag{2.4}$$

where T is the period of the modulating function, $\delta(t)$ is the Dirac function and t is the time inside the period $[0, nT]$. The group is obtained by a series of integrations of such function, which is, for that reason, called the "root" function. Figure 2.2 shows the group of spline modulating function given by:

$$\begin{gathered} \varphi_{n,j}(t) = \int_0^{nT} \overbrace{\cdots\cdots\cdots}^{k=n-j} \int_0^{nT} \varphi_{n,m}(t)\mathrm{d}t^k \\ k = 0, 1, \ldots, n \qquad t \in [0, nT] \end{gathered} \tag{2.5}$$

The algorithm can be suitably applied if the dynamic behaviour of a system is described by the linear stationary physical model

$$\sum_{i=0}^{n} a_i \frac{\mathrm{d}^i y}{\mathrm{d}t^i} = \sum_{i=0}^{m} b_i \frac{\mathrm{d}^i u}{\mathrm{d}t^i} \qquad m \leq n \qquad a_0 = 1 \tag{2.6}$$

where y and u are the output and input variables respectively whereas a_i and b_i are the parameters to be identified. Both members of equation 2.1 can be multiplied by $\varphi(t)$ and integrated from t to $T + t$. The spline function order is generally chosen so as to be greater than the order of the system. The resultant model is then given by

$$\sum_{i=0}^{n} a_i \int_t^{t+T} \varphi(t) \frac{\mathrm{d}^i y}{\mathrm{d}t^i} \mathrm{d}t = \sum_{i=0}^{m} b_i \int_t^{t+T} \varphi(t) \frac{\mathrm{d}^i u}{\mathrm{d}t^i} \mathrm{d}t \tag{2.7}$$

Integration by parts and the property of modulating functions of being equal to zero at the two limits of the period yield:

$$\sum_{i=0}^{n} a_i (-1)^i \int_t^{t+T} \frac{\mathrm{d}^i \varphi}{\mathrm{d}t^i} y \mathrm{d}t = \sum_{i=0}^{m} b_i (-1)^i \int_t^{t+T} \frac{\mathrm{d}^i \varphi}{\mathrm{d}t^i} u \mathrm{d}t \tag{2.8}$$

which is an algebraic equation of the unknown parameters a_i and b_i in which only the signals (usually noisy) and not their derivatives are present.

In order to identify the unknown parameters, an excitation signal is set as input to the system (generally white noise because it has a wide frequency content) and the output is measured. An algebraic equation is obtained for each differential equation by Simpson's numerical integration. Exciting the system long enough and dividing the acquired data in time intervals of the size of the so called identification window, many linearly independent equations can be obtained. An alternative is to use the same time interval and different modulating functions. If the number of equations is greater than the number of unknown parameters, the system is solved using the pseudo-inverse matrix and the least squares approach.

A crucial step in the identifying process is the choice of the identification window T. As a matter of fact the integration operation is a low-pass filter whose cut frequency is proportional to $1/T$ and moreover it is closely related to the type of modulating function. A small window implies a wide band so that even the signal components due to noise are considered. On the contrary a large window implies a narrow band with the risk of cancelling some components of the signal. Some researchers [23] suggest to choose a window of the same size of the main time constant of the mechanical system.

The identification technique has been implemented in a software code developed in a MATLAB® environment, suitably modifying a source code provided by its authors [23].

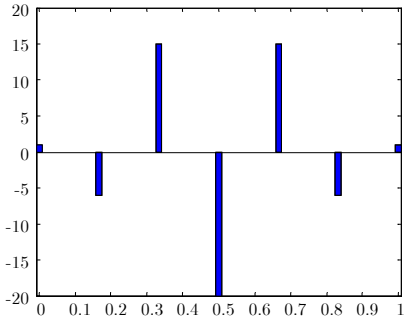

Figure 2.1: The root function of the group of spline modulating functions

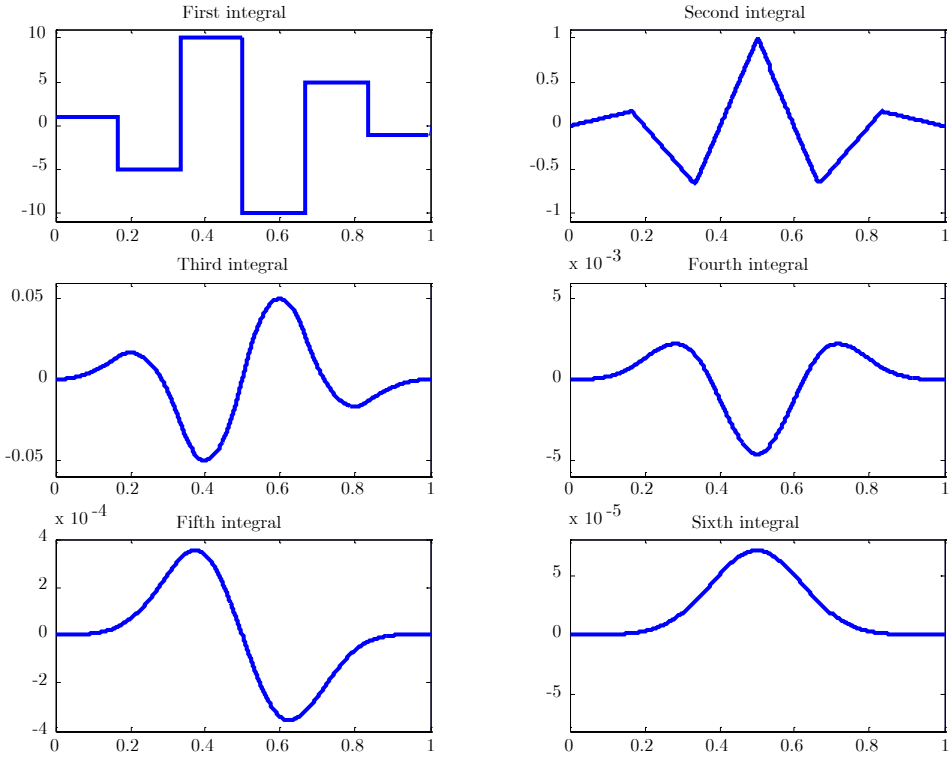

Figure 2.2: Spline modulating functions obtained by subsequent integrations

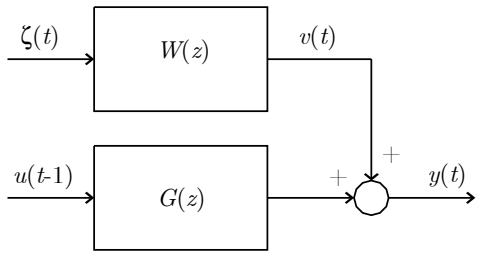

Figure 2.3: System model of recursive identification

2.2.2 The recursive identification algorithm

Recursive identification is a parametric technique that deals with simple linear time-invariant models which, despite their simplicity, are useful in a lot of practical situations. Moreover, these models take into account also the disturbance. In fact the model is obtained by adding the outputs of two systems (see figure 2.3). One system, $G(z)$, describes the direct influence of the input, $u(t)$, on the output, $y(t)$, when there is no disturbance. The other, $W(z)$, deals with the error in the estimation, whether it comes from model inaccuracies or from measurement errors. The input of this block, $\zeta(t)$, is white noise. The resulting system is described by the following equation

$$y(t) = G(z)u(t-1) + W(z)\zeta(t) \tag{2.9}$$

in which it is assumed that the output at time t, $y(t)$, depends only on the input till time $t-1$, $u(t-1)$. Actually this is a common situation in practical applications.

During this work ARX and ARMAX have been used. The ARX model is the most used model structure and the simple linear difference equation which relates the current output $y(t)$ to a finite number of past outputs and inputs, is given by:

$$\begin{aligned} y(t) = {} & a_1 y(t-1) + a_2 y(t-2) + \ldots + a_{na} y(t-na) + \\ & + b_1 u(t-1) + b_2 u(t-2) + \ldots + b_{nb} u(t-nb) + \zeta(t) \end{aligned} \tag{2.10}$$

where na is equal to the number of poles and nb is the number of zeros.

There are several modified versions of the basic ARX model, where different disturbance models are introduced. These include well known model types, such as ARMAX, Output-Error, and Box-Jenkins. For instance the

ARMAX model is described by the following equation:

$$y(t) = a_1 y(t-1) + a_2 y(t-2) + \ldots + a_{na} y(t-na) + \\ + b_1 u(t-1) + b_2 u(t-2) + \ldots + b_{nb} u(t-nb) + w(t) \tag{2.11}$$

where

$$w(t) = \zeta(t) + c_1 \zeta(t-1) + \ldots + c_{nc} \zeta(t-nc) \tag{2.12}$$

is a colored noise obtained by the addition of white noise signals gathered at different instants.

In order to compute the best model the averaged squared error, I, is considered:

$$I = \frac{1}{N} \sum_{0}^{N} \varepsilon(t)^2 \tag{2.13}$$

where the error ε is computed as the difference between the output signals of the system to be validated and that to be identified. The system with the lower averaged squared error is the optimal one. Nonetheless the knowledge of other characteristics of the system is important. For instance the dynamic characteristics of the model should be considered.

2.3 Simulated identification of mechanical systems

The identification process has been firstly simulated using the SIMULINK® toolbox. The purpose was to test the effectiveness of the modulating function identification algorithm and to optimize the identification parameters (i.e. the sampling period of input and output signals and the width of the integration window T) before experimental tests were carried out.

2.3.1 One and two degree of freedom systems

First the effectiveness of the method was tested on the simplest mechanical system made of a mass, a spring and a damper. The modulating function method requires the definition of the mathematical model representing the physical system. Therefore, referring to the schematic of figure 2.4, that represents the experimental configuration shown onward, the following assumptions are made:

- the springs have concentrated masses at their ends, which can be evaluated by means of an energy equivalence; in this way only the first natural frequency is taken into account in the model while the real

system has more resonant frequencies because of the spring real mass distribution; therefore the validity of the model is related to the actual negligibility of the vibration amplitudes associated with the higher natural frequencies;

- an equivalent constant viscous damping coefficient is considered, the real damping being partly hysteretic and partly due to Coulomb friction.

Consequently the equilibrium equation is

$$m_{eq}\ddot{x}_o(t) + c_1[\dot{x}_o(t) - \dot{x}_i(t)] + k_1[x_o(t) - x_i(t)] + c_2 x_o(t) + k_2 x_o(t) = 0 \quad (2.14)$$

where the equivalent mass is given by

$$m_{eq} = m + \frac{1}{3}m_1 + \frac{1}{3}m_2 \quad (2.15)$$

m is the mass of the block between the two spring, x_o is its displacement and x_i is the displacement imposed to the upper base. m_1, k_1 and c_1 are the mass, stiffness and viscous damping of the upper spring and m_2, k_2 and c_2 the same quantities of the lower spring.

Applying the modulating function method the equation becomes

$$\begin{aligned} m_{eq}\int_0^T \ddot{\varphi}(t)x_o(t)\mathrm{d}t + c_1\int_0^T \dot{\varphi}(t)[x_o(t) - x_i(t)]\mathrm{d}t + \\ + k_1\int_0^T \varphi(t)[x_o(t) - x_i(t)]\mathrm{d}t + c_2\int_0^T \dot{\varphi}(t)x_o(t)\mathrm{d}t + \\ + k_2\int_0^T \varphi(t)x_o(t) \;=\; 0 \end{aligned} \quad (2.16)$$

As a white noise is imposed as x_i, the displacement x_o is measured, and a linear equation in the unknown dynamic parameters (c_1, k_1, c_2 and k_2) is obtained by integration, while several equations can be obtained by dividing the excitation period in sub-intervals. In order to use this technique, at least one of the dynamic parameters must be known so that the other identified parameters will be normalized with respect to it. In this specific case the only parameter which could be known with sufficient accuracy was the equivalent mass.

The simulated identification process, as shown in figure 2.5, is made of the following steps:

1. Simulation of the system to be validated with *assigned parameters*. The response data obtained from such a simulation are called *response data with assigned parameters*.

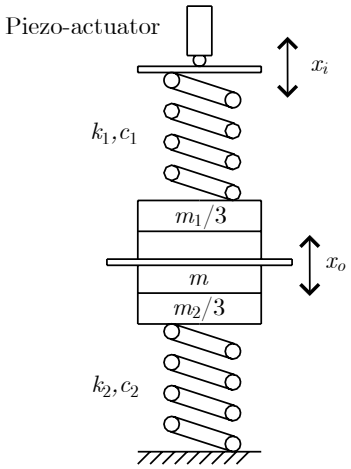

Figure 2.4: Sketch of the 1dof system

2. Use the response data with assigned parameters to identify the parameters assigned at the first step.

3. Simulate the same system but using the *identified parameters*. In the same way, the data obtained are called *response data with identified parameters*.

4. Validate the identification process comparing response data with assigned and identified parameters.

The simulations were carried out on a system with the properties depicted in table 2.1. Such a system has a natural frequency of about 100 Hz. So a sampling frequency of 1000 Hz was considered proper to conduct the simulations. The critical parameters in the modulating function identification process are the width of the integration window (T in equation 2.8) and the order of the group of the modulating function n. A Gaussian white noise, with null mean value, was used as input displacement x_i. The duration of a single run was 6 sec. No noise was added to the signals.

Firstly an optimal value of the width of the integration window was sought. The optimal number of window N_f, that minimized the averaged squared value of the error I (see figure 2.6(a)), is 299, i.e. $T = 0.02$ sec. The same result (see figure 2.6(b)) was obtained minimizing the function $G(N_f)$ given by

$$G = \varepsilon^2 (G_{x_o} - G_{\hat{x}_o}) \tag{2.17}$$

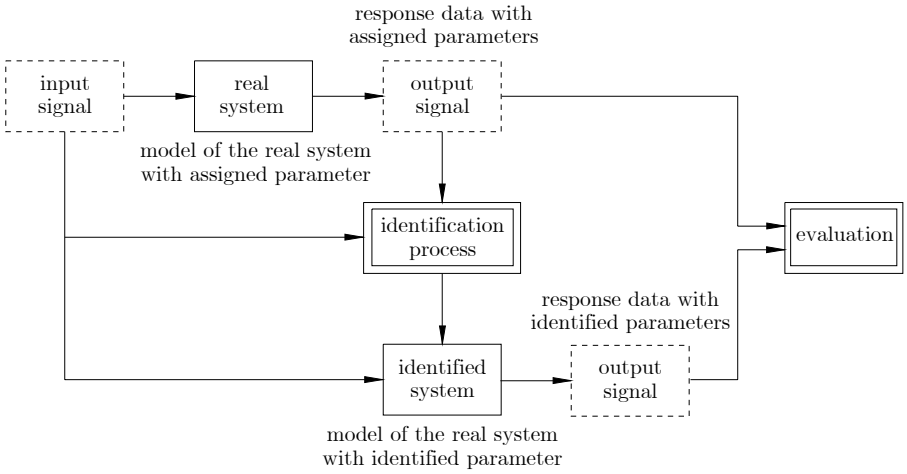

Figure 2.5: Flow chart of identification and evaluation processes

where the G operator is the spectrum of the signal, x_o is the response data with assigned parameters and $\hat{x}_o$ is the response data with identified parameters. The results of the identification using such period of integration are reported in table 2.1 in which, for convenience, the quantity k_t and c_t are shown, given by:

$$k_t = k_1 + k_2 \tag{2.18}$$

$$c_t = c_1 + c_2 \tag{2.19}$$

The stiffness has been identified with an almost null error. The value obtained for the damping is completely different and with an opposite sign. This peculiar result has been obtained always using the modulating function algorithm and up to now no reasonable explanation has been found. Anyways the good agreement between response data with assigned and identified parameters is shown in figure 2.7 where the error between estimation and validation data is less then 10%. The nature of the signal difference is that of a white noise. This means that the identification is good because the identified system contains all the information of the system and the error is due to uncertainties.

The good results can be shown also in the frequency domain. Figure 2.8 shows the coherence and the power spectral density (PSD) of the signals. The spectra are identical up to 350 Hz. Sometimes a phase error can be present. This observation suggests that the averaged squared error, and all the validation parameters estimated in the time domain, are not always proper.

Parameters	Imposed	Identified	Error [%]
m [kg]	0.15384	0.15384	known
c_t [N sec/m]	0.4	0.425	5.88
k_t [N/m]	69600	69605	0.00718
c_1 [N sec/m]	0.2	-16.786	–
k_1 [N/m]	34800	30902	11.20

Table 2.1: Parameters of the 1dof system identified by the modulating function algorithm carrying out simulations with white noise input

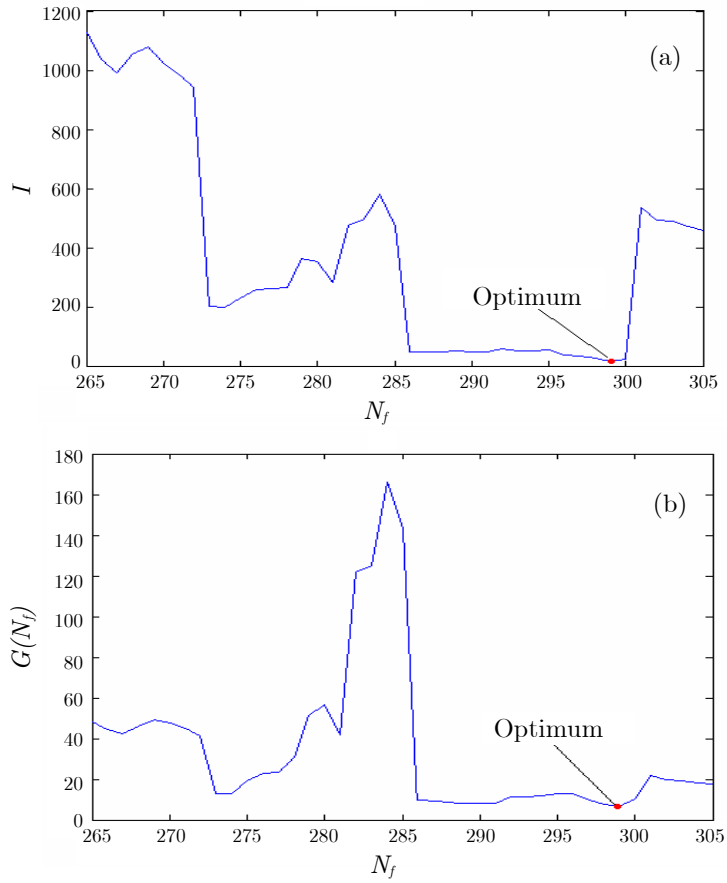

Figure 2.6: Research of the optimal number of integration windows N_f: (a) averaged squared error I; (b) function of the spectrum of the signals G

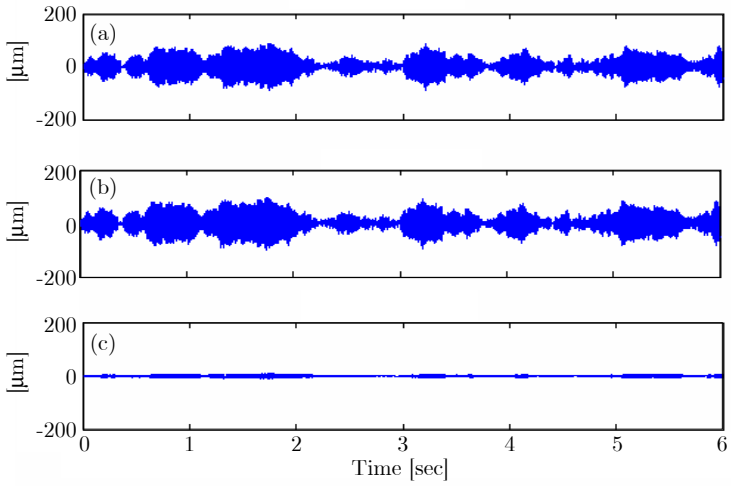

Figure 2.7: Temporal validation of simulated identification: mass displacement of assigned model (a), identified model (b) and difference (c)

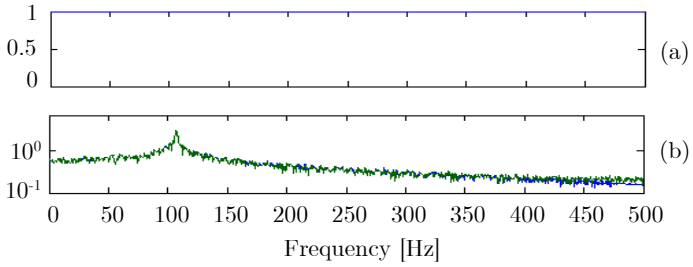

Figure 2.8: Frequency validation of simulated modulating function identification: coherence (a) and PSD of response data with assigned and identified parameters (b)

Parameters	**Imposed**	**Identified**	**Error [%]**
m [kg]	0.15384	0.15384	known
c_t [N sec/m]	0.4	0.4042	1
k_t [N/m]	69600	69605	0.0072
c_1 [N sec/m]	0.2	0.202	0.99
k_1 [N/m]	34800	34803	0.0086

Table 2.2: Parameters of the 1dof system identified by the modulating function algorithm carrying out simulations with sine wave input

The identified model has been then validated using different signals for the input x_i, and obtaining x_o and $\hat{x}_o$. The identified model has shown very good performances. An analysis on the sampling period of data acquisition showed that its decrease can improve the identification of the damping coefficient.

Moreover, the identification with the modulating function algorithm has been carried out using a sinusoidal signal as input displacement. The results are shown in table 2.2. Using a sinusoidal excitation the identification has improved and the algorithm has become more robust. In fact the algorithm is less sensitive to the change of the integration period. The reason is that the integration process is not very effective when the signal presents discontinuities as those generated using a noise excitation. Nevertheless the white noise excitation is necessary with more complex systems in order to depict all the system dynamical characteristics.

Also the simulation time was investigated. Simulation times larger than 6 seconds have shown no improvement in the identification process while decreasing the simulation time worsened the identification, and below 1 second the identification of the damping coefficient was impossible.

The effect of the higher order of the modulating function, n, has been analyzed. The lower value of this parameter is given by the order of the real system. The identification has shown good performance for values of n between 4 and 12. The optimum is for $n \cong 7$. Over 12 the identification has a poor quality because of the difficulty of integrating functions of high order.

In order to test the robustness of the algorithm some noise was added to the estimation data. Thus, a disturbance white noise between 0 and 100% of the power of the excitation white noise was added to input and output signals used for the identification process. The robustness of the system is shown in figure 2.9. The use of a sinusoidal excitation signal showed an absolute weakness. In fact only adding 0.001% of noise makes identification impossible.

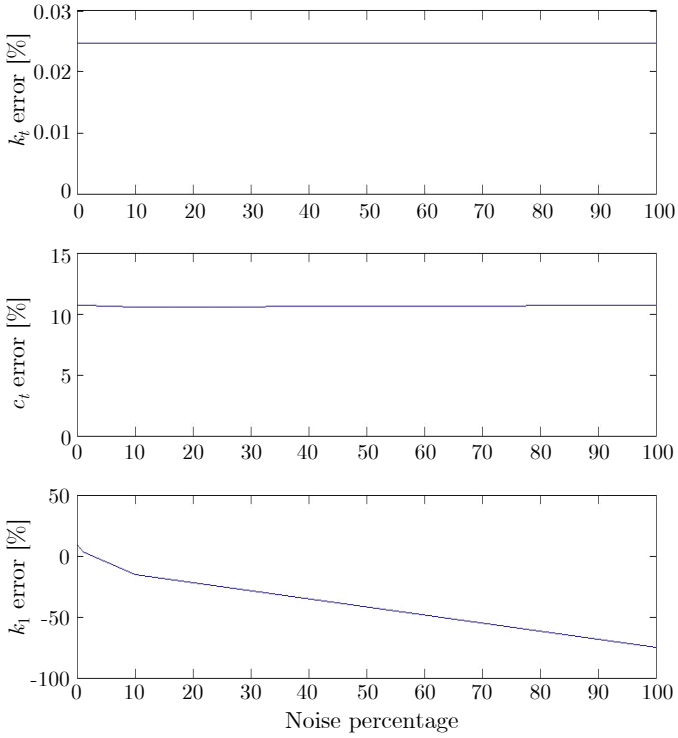

Figure 2.9: Robustness of the modulating function identification algorithm: percentage error on the identified parameters versus added noise percentage

Parameters	**Imposed**	**Identified**	**Error [%]**
m [kg]	0.15384	0.15384	known
c_t [N sec/m]	0.4	0.427	5.88
k_t [N/m]	69600	69631	0.044
c_1 [N sec/m]	0.2	0.0359	82
k_1 [N/m]	34800	31848	8.48

Table 2.3: Simulated identification with the recursive algorithm

The same identification was carried out also by the use of recursive algorithms. The SIMULINK® identification toolbox was used and an ARX 221 model has been considered. The input and output signals with assigned parameters were the same used with the modulating function algorithm. The results are shown in table 2.3 and figure 2.10. The estimation of the damping coefficient has improved but the error on the signals has increased. Also a higher order system was used but no improvement has been recorded. Moreover in higher order models the identified parameter have no direct link with the physical properties of the system.

The simulation time does not affect this method. Even with a simulation time of 5 seconds a good identification is still possible. A robustness analysis has shown that also this algorithm handles noise well, because of the white noise source included in the model.

The same analysis were then carried on a 2dof system with the properties of table 2.4. In the table the results of the simulation using the modulating function methods are shown. The simulation was carried out with a sampling time of 10 kHz that is greater enough than the higher resonance frequency. Such a system has two resonance frequencies, the first at about 110 Hz and the second at about 200 Hz. The amplitude of the integration window was sought trying to minimize the function G, so 335 windows (N_f) have been used. A modulating function order of 14 was chosen. In this case, the identification algorithm managed to identify all the parameters of the system with high accuracy.

The following conclusion can be drawn. The model coefficients were identified with negligible errors as far as stiffness is concerned while larger errors were obtained for damping and the output signals were reproduced with errors of about 10%. To take into account disturbances affecting real systems, a random noise was introduced in the mass-spring system but the sensitivity of the identified parameter error was negligible, showing the robustness of the method. However often the disturbances are of different kind, such as for

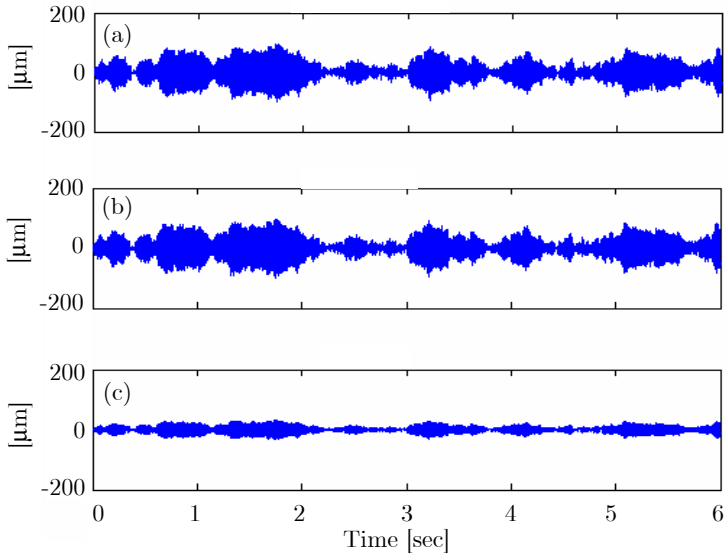

Figure 2.10: Temporal validation of simulated recursive identification: mass displacement of estimation model (a), validation model (b) and difference (c)

Parameters	**Imposed**	**Identified**	**Error [%]**
m_1 [kg]	0.05521	0.05521	known
m_2 [kg]	0.0769	0.0769	known
c_1 [N sec/m]	0.2	0.261	23
k_1 [N/m]	34800	34803	0.008
c_2 [N sec/m]	0.2	0.2	0
k_2 [N/m]	34800	34799	0.003
c_3 [N sec/m]	0.2	0.199	0.5
k_3 [N/m]	34800	34802	0.006

Table 2.4: Parameters of the 2dof system identified by the modulating function algorithm carrying out simulations with white noise input

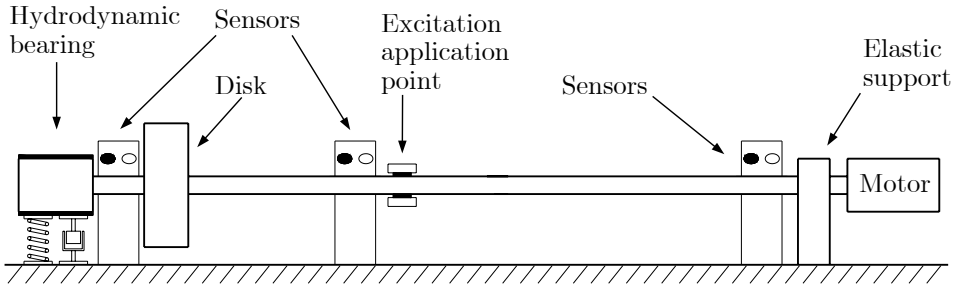

Figure 2.11: Sketch of the rotor-bearing system

example unexpected periodic inputs, not considered in the model. Therefore for the method to work, it is essential that all significant dynamic phenomena involved are taken into account and modelled.

2.3.2 The rotor-bearing system

In order to identify the dynamic characteristics of a hydrodynamic bearing the approach described above was first tried according to the schematic of figure 2.11, which shows a flexible shaft supported by two bearings, one of which is a hydrodynamic one. A disk of mass m is mounted on the shaft nearby such bearing.

Referring to the schematic of figure 2.11, assuming small journal displacements and a plain hydrodynamic bearing linear model, the following equilibrium equation can be written:

$$\begin{bmatrix} m & 0 \\ 0 & m \end{bmatrix} \begin{Bmatrix} \ddot{x}_1 \\ \ddot{y}_1 \end{Bmatrix} + \begin{bmatrix} c_{xx} & c_{xy} \\ c_{yx} & c_{yy} \end{bmatrix} \begin{Bmatrix} \dot{x}_1 \\ \dot{y}_1 \end{Bmatrix} + \begin{bmatrix} k_{xx} & k_{xy} \\ k_{yx} & k_{yy} \end{bmatrix} \begin{Bmatrix} x_1 \\ y_1 \end{Bmatrix} = \\ = \begin{bmatrix} k_a & 0 \\ 0 & k_a \end{bmatrix} \begin{Bmatrix} x_2 - x_3(\alpha+1) - x_1\alpha \\ y_2 - y_3(\alpha+1) - y_1\alpha \end{Bmatrix} \quad (2.20)$$

where the hydrodynamic bearing is modelled with 8 linearized coefficients: four linearized stiffness coefficients (k_{xx}, k_{xy}, k_{yx} and k_{yy}) and four linearized damping coefficients (c_{xx}, c_{xy}, c_{yx} and c_{yy}). x_1 and y_1 are the displacements measured near the disk in two orthogonal directions, x_2 and y_2 are the displacements gathered near the excitation point, x_3 and y_3 are those near the elastic support. k_a is the stiffness of the flexible shaft. α is the rigid rotation of the shaft around the journal bearing. The terms on the right-hand side represent the excitation force transmitted by the elastic shaft acting on

the bearing and the disk unbalance force respectively. The shaft internal damping and mass are neglected.

Using the modulating functions a system of two linear equations is obtained or a system of several equations if time sub-intervals are considered, in the unknown parameters, that is in the bearing dynamic coefficients and in the rotor static unbalance:

$$\begin{cases} m\displaystyle\int_0^T \ddot{\varphi}x_1 \mathrm{d}t + c_{xx}\int_0^T \dot{\varphi}x_1 \mathrm{d}t + c_{xy}\int_0^T \dot{\varphi}y_1 \mathrm{d}t + \\ \qquad + k_{xx}\displaystyle\int_0^T \varphi x_1 \mathrm{d}t + k_{xy}\int_0^T \varphi y_0 \mathrm{d}t = \\ \qquad = k_a \displaystyle\int_0^T \varphi[x_2 - (\alpha+1)x_3 - \alpha x_1]\mathrm{d}t \\ m\displaystyle\int_0^T \ddot{\varphi}y_1 \mathrm{d}t + c_{yy}\int_0^T \dot{\varphi}y_1 \mathrm{d}t + c_{yx}\int_0^T \dot{\varphi}x_1 \mathrm{d}t + \\ \qquad + k_{yy}\displaystyle\int_0^T \varphi y_1 \mathrm{d}t + k_{yx}\int_0^T \varphi x_0 \mathrm{d}t = \\ \qquad = k_a \displaystyle\int_0^T \varphi[x_2 - (\alpha+1)x_3 - \alpha x_1]\mathrm{d}t \end{cases} \tag{2.21}$$

As far as the known parameters are concerned, one can assign the equivalent mass and/or the shaft stiffness. Measuring the displacements x_1, y_1, x_2, y_2, x_3 e y_3 thus the shaft deflection, the elastic force exerted on the bearing to be identified is practically known. Then the procedure is the same as that described above. A noise excitation and an impulse excitation were both considered.

In order to verify the applicability of the modulating function method to the real case, and to tune the parameters that control the identification technique (the input and output signal sampling period and the integration window) before experimental testing, the identification process was simulated by means of software programs developed in the SIMULINK® environment.

Laplace transforms were applied to equations 2.20, and the corresponding transfer functions implemented in the simulation program. Both white noise and impulse input simulations were carried out. Table 2.5 shows the coefficients used to set up the numerical model. The dynamical coefficients of the hydrodynamic bearing were calculated using the linearized analytical expression of the Ocvirk short bearing for a rotation speed (Ω) of 1500 rpm,

given by [31]:

$$k_{xx} = \frac{W_0}{c}\frac{4[\pi^2(1-\varepsilon^2)(1+2\varepsilon^2)+32\varepsilon^2(1+\varepsilon^2)]}{1-\varepsilon^2}f^3(\varepsilon) \quad (2.22)$$

$$k_{yy} = \frac{W_0}{c}4[\pi^2(2-\varepsilon^2)+16\varepsilon^2]f^3(\varepsilon) \quad (2.23)$$

$$k_{xy} = \frac{W_0}{c}\frac{\pi[\pi^2(1-\varepsilon^2)(1+2\varepsilon^2)+32\varepsilon^2(1+\varepsilon^2)]}{\varepsilon\sqrt{1-\varepsilon^2}}f^3(\varepsilon) \quad (2.24)$$

$$k_{yx} = -\frac{W_0}{c}\frac{\pi[\pi^2(1-\varepsilon^2)^2-16\varepsilon^4]}{\varepsilon\sqrt{1-\varepsilon^2}}f^3(\varepsilon) \quad (2.25)$$

$$c_{xx} = \frac{W_0}{c\Omega}\frac{2\pi[\pi^2(1-\varepsilon^2)^2+48\varepsilon^2]}{\varepsilon\sqrt{1-\varepsilon^2}}f^3(\varepsilon) \quad (2.26)$$

$$c_{yy} = 2\pi\frac{W_0}{c\Omega}\sqrt{\frac{1-\varepsilon^2}{\varepsilon}}[\pi^2(1+2\varepsilon^2)-16\varepsilon^2]f^3(\varepsilon) \quad (2.27)$$

$$c_{xy} = c_{yx} = 8\frac{W_0}{c\Omega}[\pi^2(1+2\varepsilon^2)-16\varepsilon^2]f^3(\varepsilon) \quad (2.28)$$

where ε, c and W_0 are the eccentricity ratio, the bearing clearance and the static load respectively, and

$$f(\varepsilon) = \frac{1}{\sqrt{16\varepsilon^2+\pi^2(1-\varepsilon^2)}} \quad (2.29)$$

Usually for a damped system it is advisable to use a sampling frequency that is at least eight times the inverse of the constant time of the system to be identified. Therefore the step response of the model was evaluated with a sampling frequency of 100 kHz. The simulation time was set to 3 seconds, the number of integration time windows, N_f, to 550 and the order of the modulating function, n, to 12. In order to apply the identification algorithm the value of the shaft stiffness, k_a, was considered known.

The model coefficients were identified with negligible errors and the output signals (see figure 2.12) were reproduced with errors of about 5%.

Due to the impossibility to use a noise excitation in the experimental tests, because of the lack of proper equipment, an impulsive excitation was used. Using a repeated impulsive excitation (an impulse every second for a simulation time of 6 sec) the modulating function algorithm has shown an excellent performance in the identification of the coefficient and in the dynamical reconstruction of the signals (see figure 2.13). The absolute error is only within the order of 0.1%. A reason of such a good result can be sought in the integration step of the identification algorithm. In fact the smoother a signal is the closer the numerical integration is to the theoretical value.

Parameters		Imposed	Identified	Error [%]
m	[kg]	1	1.055	5
k_{xx}	[N/m]	600000	752820	20
k_{xy}	[N/m]	1400000	1340200	4
k_{yx}	[N/m]	-750000	-753620	0.48
k_{yy}	[N/m]	800000	801730	0.21
c_{xx}	[N sec/m]	8000	7943	0.75
c_{xy}	[N sec/m]	2600	2169	16
c_{yx}	[N sec/m]	2600	2586	0.53
c_{yy}	[N sec/m]	3200	3194	0.175
k_a	[N/m]	30190	30190	known

Table 2.5: Parameters of the hydrodynamic bearing system identified by the modulating function algorithm carrying out simulations with white noise input

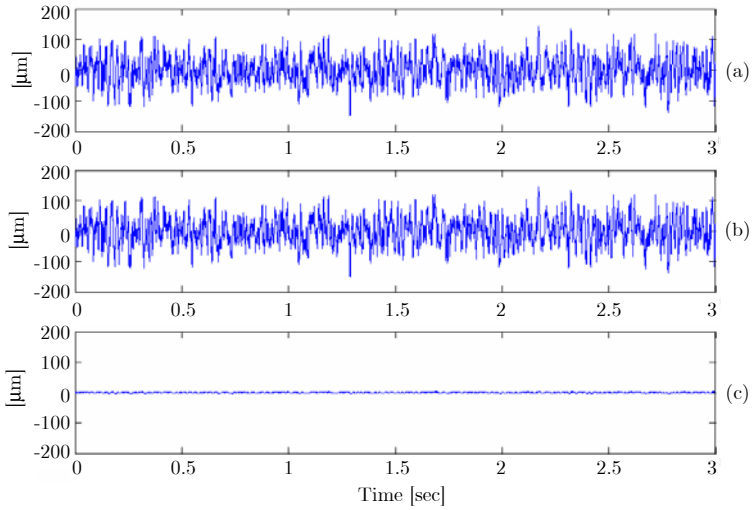

Figure 2.12: Simulated identification of the hydrodynamic bearing coefficients by means of a white noise excitation input: displacement x_0 of assigned model (a), identified model (b) and difference (c)

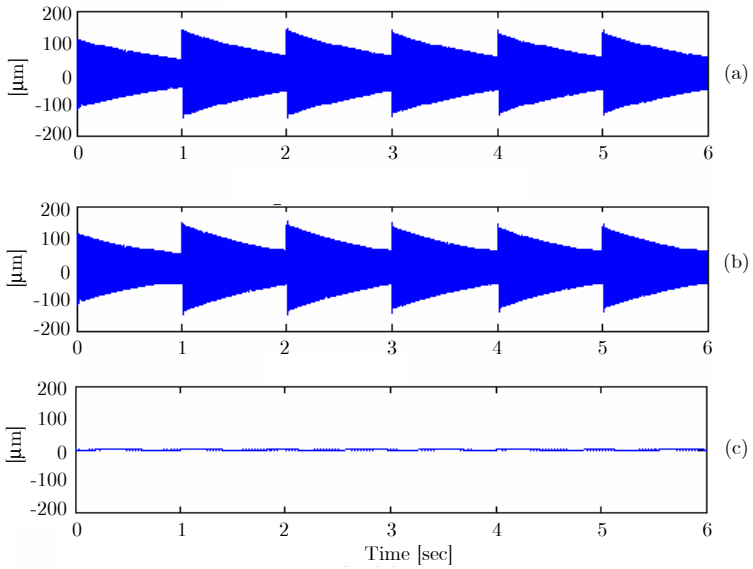

Figure 2.13: Simulated identification of the hydrodynamic bearing coefficients by means of a impulsive excitation input: displacement x_0 of estimation model (a), validation model (b) and difference (c)

As data caused from a train of impulses are smoother than those generated from noise excitation, such data are more suitable to the application of the modulating function identification algorithm.

2.4 Experimental tests on a single degree of freedom system

2.4.1 Design of the test rig

As far as the mass-spring system is concerned, a proper test rig has been set up, made of a bell-shaped rigid structure (figure 2.14) housing a cylindrical mass (149 g), the springs (nominal stiffness 35 N/mm), a piezoelectric actuator, a displacement sensors, a spring set restraining the transversal displacements. The mass and the spring have been set horizontally as shown in figure 2.4. The piezoelectric actuator has been posed above the spring mass system in order to generate the excitation input displacement x_i. Such actuator is a Physik Instrumente P-840.40 (maximum displacement 60 μm,

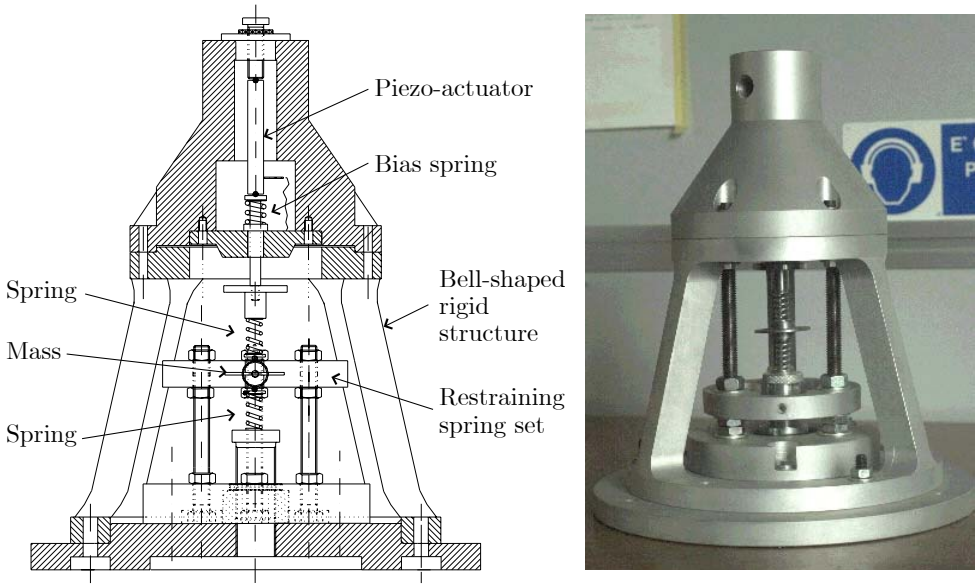

Figure 2.14: Test rig for the identification uniaxial mechanical system: (a) a drawing; (b) a photo

force -1000 N/+100 N, stiffness 25 N/μm). The axial displacements of the mass and of the end of the upper spring where the load is applied are measured by two Bently Nevada eddy current probes (3300 NSV^{TM} Probe) with a sensitivity of 7.87 mV/mm.

The actuator and the sensors were connected to a PC by means of a National Instrument DAQ board (PCI-MIO-16E-4). The DAQ programs were developed in a LabVIEW environment. A sampling frequency of 10 kHz and an actuation frequency of 1 kHz were used. In accordance with the simulations the experiment time was 6 sec.

The mechanical characteristics of the device are the same used in the numerical simulations and are reported in table 2.1. In order to the test the algorithm in a different condition a system with a reduced mass (m_{eq}=0.0819 kg) was also considered.

2.4.2 Experimental results

In this section the results of applying the modulating function identification algorithm to a mechanical discrete uniaxial system are reported. This tech-

nique is compared to some recursive algorithms of the Control toolbox in MATLAB® . The effects of a sinusoidal excitation and of filtering the signal are also illustrated.

Before starting with the experimental identification a qualitative analysis of the signals was carried out. The signal output, x_o, obtained for white noise excitation is shown in figure 2.15(a). The input displacement, x_i, was also recorded and, since the input displacement should be like the signals of excitation sent to the actuator, the noisiness of this signal was evaluated. Figure 2.15(b) shows that the signal is almost a noise with a uniformly distributed frequency content.

On a narrower frequency range, the output signal shows that there are two peaks at about 116 Hz and 190 Hz (see figure 2.16(b)). The first one is the resonance frequency of the first mode of the structure while the second one is due to the non-linearities in the system (Coulomb friction, non linear stiffness of the springs, etc.). Such an explanation is proved by the coherence function between input and output (see figure 2.16). In fact the coherence is very poor near the second frequency.

Since the aim was to identify the simplest model, i.e. a 1dof mechanical model, the second frequency is undesirable. Luckily the influence of this non-linear mode is quite negligible if the amplitude of the excitation is reduced. The coherence is also low for frequencies greater than 350 Hz, but this is out of the investigation range. In fact a mechanical system acts like a low-pass filter and the noise becomes more important as the signals become smaller. The coherence appears decreased also near the first resonance because of an inadequate resolution. From this qualitative analysis it appears that the system acts mainly like a 1dof system below 180 Hz and it is suitable for the identification process.

Figure 2.17 shows the real signal of the displacement of the mass of the 1dof system together with that reproduced by means of the modulating function identification process. The corresponding error is also reported. The optimum number of windows (317) was determined on the basis of the maximum coherence between the real and the identified signals, i.e. minimizing the function G of equation 2.17. In order to show the accuracy of the measurement system the plot of the coherence between the output and input signals is presented (figure 2.18). Figure 2.19 shows that the PSD of the identified system is a good 1dof approximation of the real system. The identified stiffness constants of the two springs are 40.3 e 40.7 N/mm respectively. The identified damping coefficients are -1.63 and 1.61 Nsec/m respectively. The reason of a negative value of the damping coefficient has been not yet fully understood. Maybe the use of a viscous constant damping to model the system damping is not appropriate. In fact the system damping is due

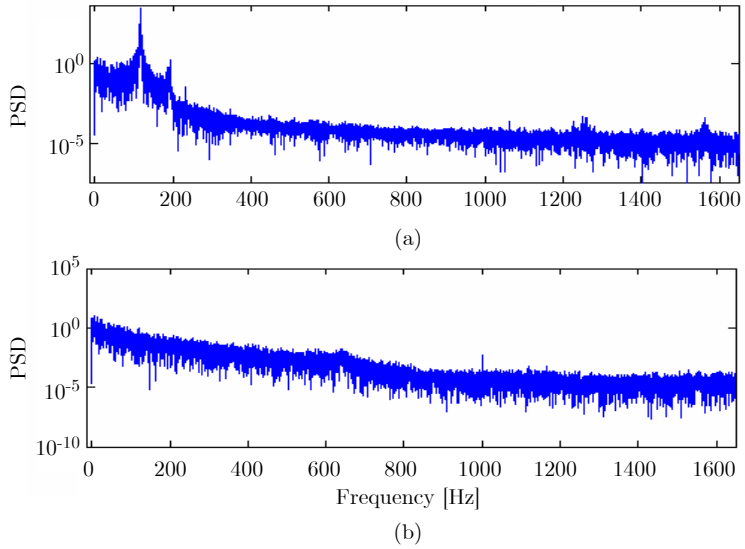

Figure 2.15: Qualitative analysis of experimental signals in the identification of uniaxial mechanical system: PSD of input x_i (a) and output x_o (b) signals

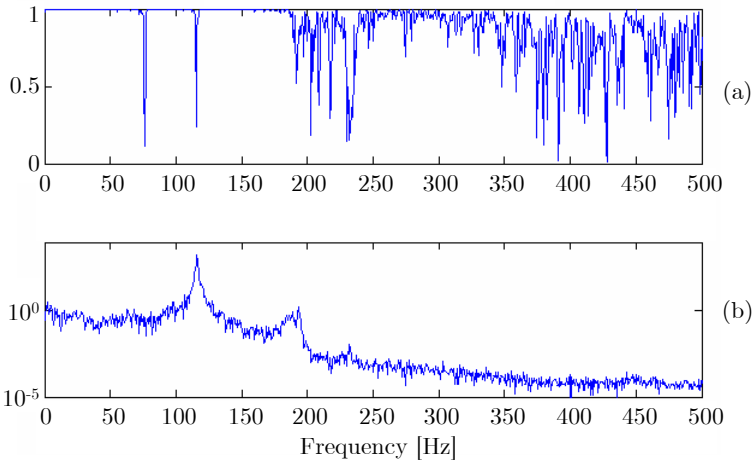

Figure 2.16: Coherence of experimental signals (a) and PSD of the output signal x_o (b) in the identification of uniaxial mechanical system

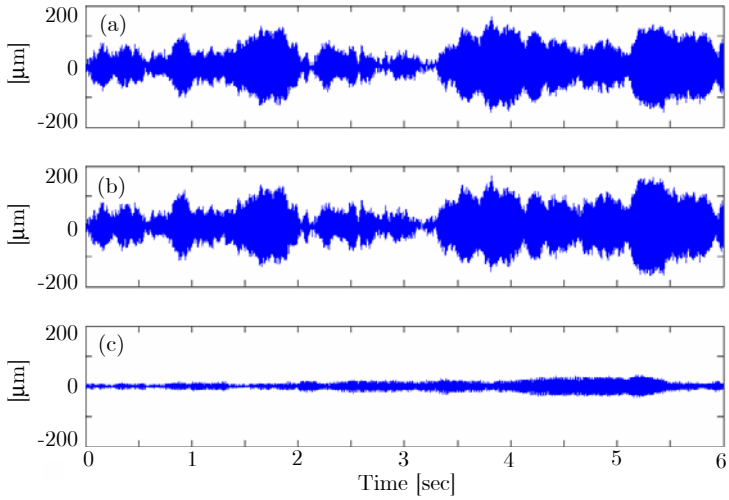

Figure 2.17: Experimental identification of the 1dof system by means of a white noise excitation input: displacement x_0 of assigned model (a), identified model (b) and difference (c)

to both viscous and Coulomb frictions which have different effects on the behaviour of the system. For instance, the Coulomb friction do not change the natural frequency of the system while the viscous damping does. Moreover, the experiment time (6 sec) may be too small to fully characterize the system. In fact, even if there is a good reproduction of the signal, the error is in the order of 10% because of a time lag due to the poor identification of the damping coefficient. Anyway a validation of the identified system has shown good performances of such model. In fact imposing different excitation to the real and identified system the output signals of the two systems are still very similar (the error is always less than 10%).

The identification of the system with a reduced mass has given worse results. In fact the reduction of the mass makes the system more sensitive to noise and non-linearities.

During the simulation tests a sinusoidal excitation signal was also used. It showed a very good performance but also a very low robustness with respect to noise. So the experimental tests, in which noise is an intrinsic characteristic, had worse identification results than using a white noise excitation. So such results are not shown because scarcely significant.

Usually data are filtered in order to attenuate noise effects and to identify the behaviour of the system in a given frequency range. So in order to limit

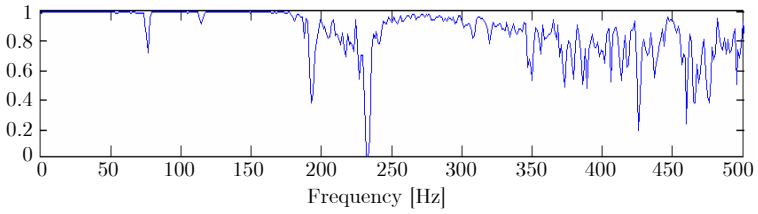

Figure 2.18: Coherence between signals in the experimental test of uniaxial mechanical system

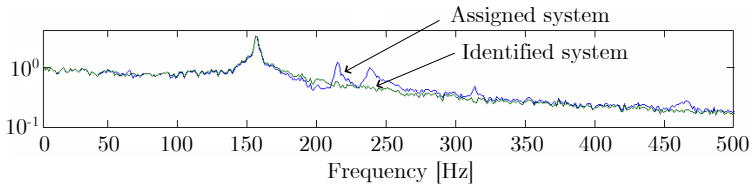

Figure 2.19: Experimental PSD of assigned (blue line) and identified (green line) system

the identification only around the first natural frequency a Butterworth 6th order low pass filter at 800 rad/s (127 Hz) was used. If the signal was pre-filtered the error reduction was noticeable (see figure 2.20). The identified stiffness constants of the two springs are 39.5 e 41.5 N/mm respectively. The identified values are comparable with the previous ones. The identified damping coefficients are 1.13 and -1.06 Ns/m respectively. Even if a damping coefficient is still negative the total damping coefficient (c_t given by equation 2.19) of the system is now positive.

The errors found in the signal reproduced by the proposed method and those reproduced using MATLAB® Control toolbox routines, based on ARX techniques are compared in figure 2.21. As the errors are about 20%, these results show a worse identification than that obtained with the modulating function algorithm.

It is noteworthy that while for unfiltered data the minimum order of the ARX model that makes identification possible is higher than that of the analytical model (ARX 441), with pre-filtered data a lower order model can be used (ARX 221). Since the corresponding transfer function is a lower order one, in the latter case it is possible to determine easily the physical parameters of the system. The identified stiffness constants of the two springs are

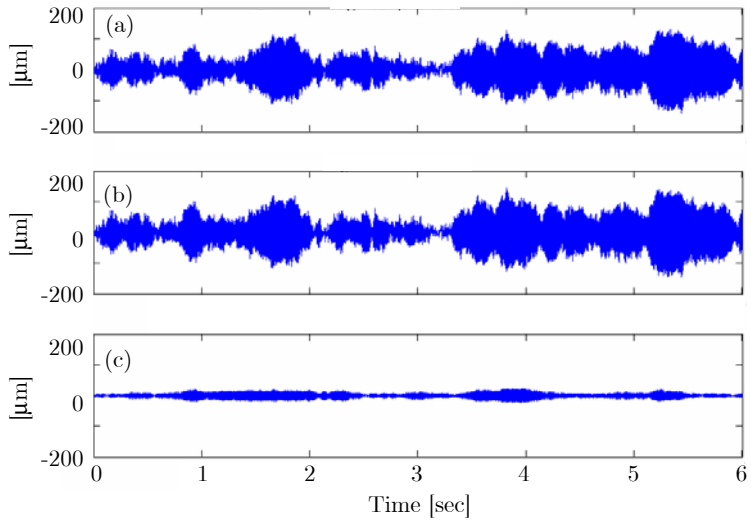

Figure 2.20: Experimental identification of the 1dof system on filtered data by means of a white noise excitation input: displacement x_0 of assigned model (a), identified model (b) and difference (c)

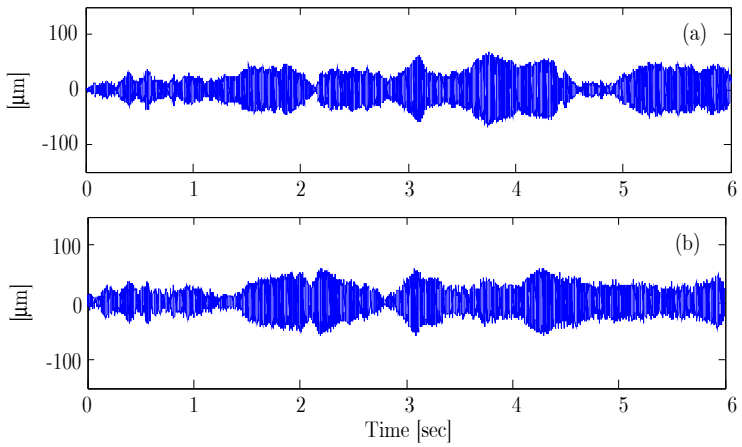

Figure 2.21: Difference between response signals with assigned and identified parameters with ARX 221 (a) and ARX441 models (b)

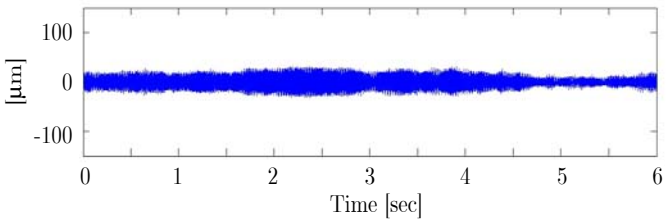

Figure 2.22: Difference between signals with experimental and identified parameters in the validation test

39.6 e 41.4 N/mm. Such results are comparable with the previously calculated ones. The total identified damping coefficient, c_t, is 0.11 Nsec/m, that is a realistic value, but the coefficients of each spring weren't well identified. The modulating function technique however shows its superiority because it makes the evaluation of the model coefficients possible with a lower response error. Moreover the recursive method showed a poor performance concerning the non modelled noise. ARX models take in account the noise but only in the way described previously in this section. As soon as a little noise is introduced, like in all real systems, this algorithm shows its weaknesses.

The identified model was validated using the signals of another experimental test (validation test). Figure 2.22 shows that the difference between the experimental and output signals by identified parameters of the validation test is always very small.

2.5 Experimental tests on a hydrodynamic bearing

2.5.1 Design of the test rig

As far as the rotor-bearing system is concerned, Bently Nevada Rotor-kit with the oil-whirl option was used. It is made of a 10 mm diameter steel shaft, 450 mm long, supported by an adjustable oilite journal bearing and by a hydrodynamic bearing made of a plastic transparent case and operating with colored oil in order to emphasize the film characteristics. A 0.8 kg disk was mounted on the shaft nearby the hydrodynamic bearing. Two displacement sensors (3300 NSV^{TM}), arranged at 90°, were placed in each of the three measurement planes as shown in the diagram (figure 2.11) and in the photo (figure 2.23).

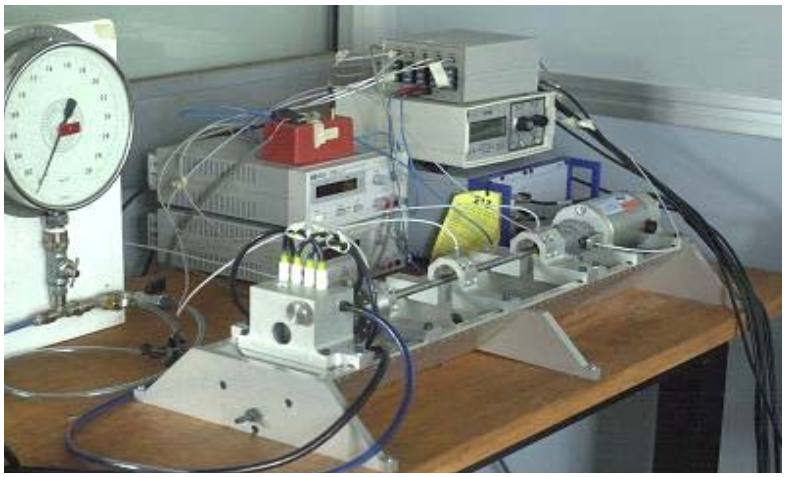

Figure 2.23: Photo of the Rotor Kit with Whirl option

The actuators and the sensors were connected to the same PC described previously. A sampling frequency ranging from 1 to 10 kHz and an actuation frequency of 1 kHz were used.

Initially a white noise displacement was supposed to be applied to the shaft by means of two piezoelectric actuators (Physik Instrumente P-840.40) arranged at 90°. However, due to the practical difficulty of getting a proper interface between the actuators and the rotating shaft an impulse signal, to be applied with an impulse hammer, was preferred. A PCB impact hammer was used. However the use of a modal hammer did not cope with all the problems. In fact it is very difficult to hit the rotating shaft always in the same point and in the same direction.

2.5.2 Experimental results

As far as the rotor/bearing system is concerned, the test was carried out at 1500 rpm, with a sampling frequency of 360 samples/rev for 2 s. The data were filtered with a low pass filter at 2150 rad/s (342.2 Hz) and the identification was carried out with 1100 time windows.

The model used to apply the identification has been lightly modified in order to take in account the unbalance always present in the real systems. A centrifugal force applied at the mass m has been considered and added to

m [kg]	k_{xx} [N/m]	k_{xx} [N/m]	c_{xx} [N sec/m]	c_{xy} [N sec/m]	F_{c1} [N]	F_{c2} [N]
0.04531	4859	4412	25.91	57.01	55076	-48171

Table 2.6: Parameters of the hydrodynamic bearing system identified by the modulating function algorithm carrying out experimental tests with impulsive noise input

the parameters to be identified:

$$\begin{bmatrix} m & 0 \\ 0 & m \end{bmatrix} \begin{Bmatrix} \ddot{x}_1 \\ \ddot{y}_1 \end{Bmatrix} + \begin{bmatrix} c_{xx} & c_{xy} \\ c_{yx} & c_{yy} \end{bmatrix} \begin{Bmatrix} \dot{x}_1 \\ \dot{y}_1 \end{Bmatrix} + \begin{bmatrix} k_{xx} & k_{xy} \\ k_{yx} & k_{yy} \end{bmatrix} \begin{Bmatrix} x_1 \\ y_1 \end{Bmatrix} = \\ = \begin{bmatrix} k_a & 0 \\ 0 & k_a \end{bmatrix} \begin{Bmatrix} x_2 - x_3(\alpha+1) - x_1\alpha \\ y_2 - y_3(\alpha+1) - y_1\alpha \end{Bmatrix} + \begin{Bmatrix} F_{cx} \\ F_{cy} \end{Bmatrix} \quad (2.30)$$

where F_{cx} and F_{cy} are the centrifugal forces.

Figure 2.24 shows the results of the modulating function identification. The journal displacement x_1 at the bearing location is reported. The errors in the signal reconstruction are about 10%. Comparing the signal produced by the identified system (a) and the real one (b) and the corresponding error (c), they appear quite satisfactory. The value of the error seems big but it is due only to a phase lag between the response data with assigned and identified parameters. The reconstruction performance is less dependent on the number of integral windows than the uniaxial problem.

In figure 2.25 the coherence between such displacement, x_1, and that at the point of application of the impulse load, x_2, is plotted. The coherence is reasonably good up to 350 Hz, that is the cut-off frequency of the filter.

Table 2.6 shows the identified parameters. The identified value of the mass resulted much less than the real value. Some further investigation showed that the value of the mass didn't influence the validation data. A reason of this behaviour can be the presence of a node just where the disk is placed. Moreover some tests varying the parameter N_f have been carried out. The identified parameter wobbled in a wide range but less than the order of magnitude of each parameter. Moreover, the dependency of the identified coefficients on the choice of the time windows resulted excessive requiring a long tuning job.

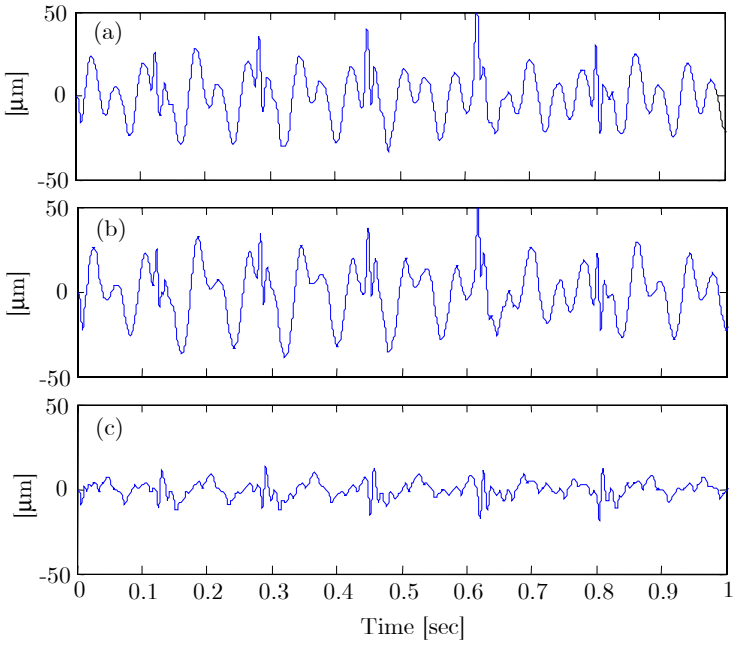

Figure 2.24: Journal displacement x_1 of the hydrodynamic bearing system identified by the modulating function algorithm carrying out experimental tests with impulsive noise input: signal with identified parameters (a), signal with assigned parameters (b) and difference (c)

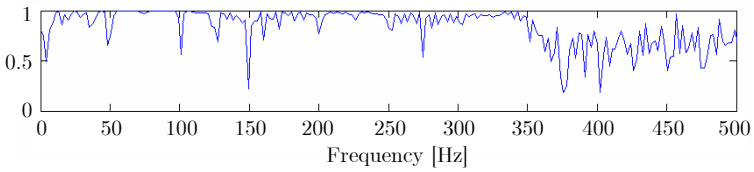

Figure 2.25: Coherence between shaft displacements at the bearing x_0 and at the impact load application point x_1

2.6 Conclusions

The investigation on the application of the modulating function technique for the identification of the characteristic dynamic parameters of a mechanical system has pointed out on one hand its effectiveness and accuracy compared to other methods, on the other the necessity of a deep knowledge of the system to be identified and of a full and detailed model. Therefore, also for the dependency of results on the time windows, the method appears to be suitable only for a particularly expert user.

It was shown that the modulating function technique can be applied also to the identification of hydrodynamic bearing characteristics. However, the industrial application of such a method to the rotor-bearing on-line characterization is possible in spite of the small errors recorded in the identified damping coefficients.

Chapter 3

Semi-active control of a rotating shaft: the magnetorheological squeeze-film damper

3.1 Introduction

As the present trend is to drive rotors at increasingly higher speeds, the rotor dynamic stability problems grow in proportion. The problem of vibrations in rotordynamics is commonly faced with passive squeeze fluid film or elastomeric dampers. Unfortunately their effect varies with the rotor speed; experimental evidence shows that in order to dissipate energy at the critical speeds the rotor displacement in the damper has to be significant, meaning that viscosity must be low. On the contrary in non critical conditions higher values are required [32].

In the last decade there has been an increasing attention toward the employment of electro-rheological (ER) and magneto-rheological (MR) fluids, suspensions of micron-sized dielectric or ferromagnetic particles respectively which, when subjected to electric or magnetic fields, undergo changes in their mechanical characteristics, viscosity and stiffness in particular. Their macroscopic behaviour is represented by the Bingham plastic model. These "smart" materials have been successfully used in valves, dampers and clutches and adaptive structures [33, 34, 35, 36] but we are still far from industrial applications in rotordynamics.

In recent years, manufacturers have shown an increased interest in MR devices. For instance, the Lord Corporation has been developing MR fluid

and manufacturing MR truck seat dampers for a number of years. These seat dampers are retrofits that replace hydraulic seat dampers that are original equipment on many large commercial trucks. Lord Corporation's truck seat dampers are arguably the most successful commercial MR dampers to date. In addition to truck seat dampers, other commercial MR dampers are available. General Motors, for instance, uses an MR damper suspension system on some 2003 Cadillac models. MR dampers are not restricted, however, to vehicle applications. Recently, the military has shown interest in using MR dampers to control gun recoil on Naval gun turrets and field artillery. Another area of study that has incorporated MR dampers is the stabilization of buildings during earthquakes. This increase in commercial interest is largely due to the success of research projects and through the efforts of Lord Corporation, which is a leader in the field of MR devices.

In the literature theoretical and experimental studies on the employment of ER fluids in active journal bearings and squeeze dampers [37, 38, 39, 40, 41, 42] are reported. More limited information is available to date regarding MR fluids in similar applications. In fact while general aspects and applications of MR fluids have been dealt with to some extent [43, 44, 45, 46] showing their promising characteristics, only quite recently some paper has appeared on rotor dampers [47].

Using special characteristics of magneto-rheological (MR) a novel controllable magneto-rheological fluid squeeze film damper was devised. In this chapter the theoretical modelling, the design and the experimental characterization of such an MR squeeze film damper are presented and discussed. The mechanical characteristics of the MR squeeze film damper, the damping in particular, change with the magnetic field at which the fluid is subjected. Thus it is possible to design an adaptable passive device or a so called semi-active device. In order to make this smart device useful in practical applications a controller has to be coupled to the device. So a fuzzy controller has been designed, optimized and numerically tested.

3.2 Passive, active and semi-active control of rotors

Control of structures has become a word-wide need, especially for important or strategic buildings. Damage mitigation and vibration reduction were tailored by improving the structural behaviour in two main directions: reducing the excitation influencing the structure (isolation) or adding supplemental damping devices (dissipators). As a first step, passive techniques were stud-

ied and applied. Then the field of active control was greatly developed since it has a higher performance compared to the passive one. Researchers are therefore now focusing on semi-active control, i.e. devices that are more reliable and require a lower power supply than active ones and in the meantime are much more efficient than purely passive dampers [48]. Semi-active control systems maintain the reliability of passive control systems while taking advantage of the adjustable parameter characteristics of an active control system. The three major classes of control systems may be defined as follows [49]:

Passive control systems A passive control system may be defined as a system which does not require an external power source for operation and utilizes the motion of the structure to develop the control forces. Control forces are developed as a function of the response of the structure at the location of the passive control system.

A passive control system may be used to increase the energy dissipation capacity of a structure through localized, discrete energy dissipation devices located over the structure. Such systems may be referred to as supplemental energy dissipation systems. The objective of these systems is to absorb a significant amount of the excitation input energy, thus reducing the demand on the structural system. Depending on their construction, these systems may also increase the stiffness and strength of the structure to which they are attached. A passive control system does not require an external power source for operation. Rather, the motion of the structure is utilized to produce relative motion within the passive control devices which, in turn, dissipate energy. Supplemental energy dissipation devices may take many forms and dissipate energy through a variety of mechanisms including the yielding of mild steel, viscoelastic action in rubber-like materials, shearing of viscous fluid, orificing of fluid, and sliding friction.

Active control systems An active control system may be defined as a system which typically requires a large power source for operation of actuators which supply control forces to the structure. Control forces are developed based on feedback from sensors that measure the excitation and/or the response of the structure. The feedback from the structural response may be measured at locations remote from the location of the active control system.

The primary effect of some experimentally tested active control systems has been to modify the level of damping with a minor modification of stiffness.

Active control techniques were taken from mechanical and electric engineering and were applied to civil structures. The effect can be considered strongly positive and effectiveness of active control is world-wide accepted. One heavy problem of active systems is, however, that they require a lot of energy to function. This should be avoided from the point of view of economical convenience and reliability [50].

Semi-active control systems A semi-active control system may be defined as a system which typically requires a small external power source for operation and utilizes the motion of the structure to develop the control forces, the magnitude of which can be adjusted by the external power source. Control forces are developed based on feedback from sensors that measure the excitation and/or the response of the structure. The feedback from the structural response may be measured at locations remote from the location of the semiactive control system.

A semi-active control system generally originates from a passive control system which has been subsequently modified to allow for the adjustment of mechanical properties. For example, supplemental energy dissipation devices which dissipate energy through shearing of viscous fluid, orificing of fluid, and sliding friction have been modified to behave in a semi-active manner. The mechanical properties of these systems may be adjusted based on feedback from the excitation and/or from the measured response. As in an active control system, a controller monitors the feedback measurements and generates an appropriate command signal for the semi-active devices. As in a passive control system, however, the control forces are developed as a result of the motion of the structure itself. The control forces are developed through appropriate (based on a pre-determined control algorithm) adjustment of the mechanical properties of the semi-active control system. Furthermore, the control forces in many semi-active control systems primarily act to oppose the motion of the structural system and therefore promote the global stability of the structure. Semiactive control systems generally require a small amount of external power for operation.

Note that the three major classes of control systems described above are sometimes combined to form so-called hybrid control systems. Hybrid control systems can consist of combined passive and active devices or combined passive and semi-active devices.

The choice of the most proper manner to obtain a reduction in vibration amplitude depends on the objective the designer has in his mind: nevertheless practical, economical and implementation aspects are very important.

Control strategies can be used to reduce the vibration of rotors. In most cases the desired behaviour of rotor can not be achieved by merely using passive damping elements, or by optimal adjustmen of the design parameters. Major improvements are possible by using active components. The control forces can be applied directly by means of a magnetic bearing or, in case of limited access to the rotor due to space limitations, the control forces are applied via the bearing housing. Different kinds of actuator can be used in the design of active bearing: magnetic actuators [51], hydraulic actuators [51] and piezoelectric actuators [52].

For a flexible rotor system, squeeze film damper are generally used to decrease vibration amplitude. There have been numerous researches on the characteristics of squeeze film dampers, however, the characteristics are always restricted by lubricant viscosity. If the viscosity can be controlled, the efficiency of the squeeze film dampers may be extended to a higher degree.

3.3 Squeeze film bearings

Many rotating systems have very little inherent damping and so artificial damping is often introduced by pumping oil via holes or grooves into annuli typically of about 0.2 mm clearance between the outer race of some of the rolling-element bearings supporting a rotor and the casing of the machine. The films of oil so formed are called squeeze films since they provide damping by squeeze action during vibration.

Squeeze film bearings have been used for many years in rotating machines to control the rotor vibration. Many rotor systems have little inherent damping if run above their critical speed, as this increases the stability of the rotor. However introducing damping into the stationary parts of the bearings also increases the stability of the machine, and reduce the shaft vibration. In a squeeze film damper a journal, which is restrained from rotating by a pin, is connected to the rotor through a rolling element bearing. The journal is located in a bearing and the oil between them is prevented to move axially by seals at the ends. Radial displacements of the journal cause the oil to move circumferentially, and this movement provides the required damping. Squeeze film dampers can be accompanied by a parallel spring in the form of a squirrel cage. This spring will usually be included if there is the need to tune a system resonance away from the operating speed range or to centralize the rotor bearing in the damper annulus to minimize the effect of squeeze film damper non-linearities.

The conventional squeeze film damper uses low viscosity lubricating oil between the bearing outer race and the bearing housing to provide a flexible

support. The stiffness of the oil film is vanishingly small and no unstabilizing effect, linked to the circumferential motion of the oil, is present [53]. If the damping is fairly light the squeeze film damper has little effect on the speed at which resonance occurs but, if the damping becomes excessive, its contribution will approximate that of a rigid link and it will therefore lock out the centring spring and negate its contribution [54].

The properties of the damper are set by the physical constraints of the oil path, and by the oil viscosity, which varies with temperature. For a given machine and operating temperature, the squeeze film damper will provide a significant level of damping. However, such device is highly non-linear in character since this damping depends on the amplitude of motion. This can lead to problems in analysis and performance such as undesirable sub-harmonics and jump phenomena in vibration responses.

There have been many publications on squeeze film dampers. A paper by Holmes [54] gives a good overview of the background operation, several application examples, and a review of the typical responses obtained from such devices.

The squeeze film damper is one of the most effective supports for adding external damping to a rotor system, as for example of high-speed aero-engines. This is because of its relative simplicity to be manufactured and effectiveness in attenuating the vibration of rotor systems and transmitted force in a properly designed case. However, some undesired operation states characterised by higher rotor vibration and transmitted force may occur in the rotor-damper system due to high non-linearity of oil film forces produced by the squeeze film damper. Besides, the behaviour of the squeeze film damper cannot easily be controlled on-line to meet the different requirements of the rotor system in different conditions, especially when the rotor passes through several critical speeds. Therefore, the effectiveness of the squeeze film damper is limited. Because of the high reliability of the properly designed squeeze film damper, it seems natural to develop controllable dampers based on the conventional one.

3.4 The magnetorheological fluids

Magnetorheological (MR) fluids are materials that respond to an applied magnetic field with a change in rheological behaviour. Typically, this change is manifested by the development of a yield stress that monotonically increases with the applied field. Interest in magnetorheological fluids derives from their ability to provide simple, quiet, rapid-response interfaces between electronic controls and mechanical systems [45].

MR fluids are non-colloidal suspensions of polarizable particles having a size of a few microns. The magnetorheological response of MR fluids results from the polarization induced in the suspended particles by the application of an external field. The interaction between the resulting induced dipoles causes the particles to form columnar structures, parallel to the applied field. These chain-like structures restrict the motion of the fluid, thereby increasing the viscous characteristics of the suspension. The mechanical energy needed to yield these chain-like structures increases as the applied field increases resulting in a field dependent yield stress [45].

MR fluids are considerably less well known than their electrorheological (ER) fluid analogs. However, while the commercial success of ER fluids has remained elusive, MR fluids have enjoyed recent commercial success because they have more attractive characteristics as shown in the following comparison [55, 56]:

- MR fluids have a yield stress, τ_0, an order of magnitude greater than their ER counterpart (ER fluids τ_0=2-5 kPa, MR fluids τ_0=50-100 kPa).

- The design equations indicate that for comparable mechanical performance the amount of active fluid needed in an ER fluid device will be about two orders of magnitude greater than that of an MR device. Naturally, the size of a device also includes such factors as the electrodes and high voltage insulation for ER fluids and the electromagnetic coil and steel pole pieces for the MR fluids. The large size of the volume ratio does point out, however, that because of their very large yield strengths, MR fluid device may be substantially smaller than ER fluid devices capable of similar performance.

- ER and MR fluid devices have similar power requirements of about 50 Watts (ER fluids 2000-5000 V, 1-10 mA, MR fluids 12-24 V, 1-2 A). The primary difference will be that the ER supply must provide high voltage at low current while the MR power supply provides higher current at only a low voltage so MR devices can be run directly on common low-voltage power sources.

- Apart from the relatively low yield strength exhibited by most ER fluids, factors which have limited their use in many practical applications include temperature sensitivity and sensitivity to the presence of contaminants or impurities. The importance of both of these factors stems from the fact that all ER fluids ultimately depend on the movement of ions or electric charge to function. Contaminants have little effect on MR fluids.

Therefore MR fluid have been chosen since they have a greater yield stress, they need a low-voltage supply and they are not sensitive to contaminants and impurities. Moreover, MR devices are usually small.

In the absence of an applied magnetic field, MR fluids exhibit Newtonian-like behaviour. Thus the behaviour of these controllable fluids is often represented as a Bingham plastic having a variable yield strength. In this model, the flow is governed by Bingham's equations [45]:

$$\tau = \tau_0(H) + \mu\dot{\gamma} \quad \tau \geq \tau_0 \tag{3.1}$$

at fluid stresses τ above the yield stress τ_0, that is magnetic field dependent. In equation 3.1, H is the magnetic field, $\dot{\gamma}$ is the fluid shear rate, and μ is the plastic viscosity (i.e., viscosity at $H = 0$).

Below the yield stress (at strains of order 10^{-3}), the material behaves viscoelastically:

$$\tau = G\gamma \quad \tau < \tau_0 \tag{3.2}$$

where G is the complex material modulus. It has been observed in the literature that the complex modulus is also field dependent. Nevertheless, the model can be simplified, in order to obtain the analytical solution of lubrication equations, considering the complex material modulus G as infinite. Such a model has been used in lubrication for many years to describe the behaviour of greases. The fluid is characterized by only two parameters, the yield shear stress τ_0 and the viscosity μ. When the magnitude of the deviatoric stress tensor is less then the yield stress, the material is rigid; when the yield stress is exceeded, the material flows in a quasi-Newtonian manner [38].

True MR fluid behaviour exhibits some significant departures from the Bingham plastic model. Perhaps the most significant of these departures involves the non-Newtonian behaviour of MR fluids in the absence of a magnetic field. Still, if used properly, equation 3.1 provides a useful basis for the design of many MR fluid-based devices [57].

In this model the dependence of the viscosity on magnetic field and temperature is neglected. The so called "shear tinning" effect is also neglected, that is the lowering of the viscosity when the shear rate increases, but these effects are too complex to be dealt with analytically.

Most devices that use MR fluids can be classified as having either fixed poles (pressure driven flow mode) or relatively moveable poles (direct-shear mode). Examples of pressure driven flow mode devices include servo-valves, dampers and shock absorbers. Examples of direct-shear mode devices include clutches, brakes, chucking and locking devices. A third mode of operation

known as squeeze-film mode has also been used in low motion, high force applications [57].

The magnetic, rheological, tribological and settling properties of controllable fluids depend on concentration and density of particles, particle size and shape distribution, properties of the carrier fluid, additional additives, applied field, temperature, and other factors [45]. So the choice of the fluid more suitable for the specific application is a great challenge.

During the design of the device the MR fluids of two different companies were considered. The first was a product of the Lord Corporation and the second of the Liquids Research Limited. Oil based fluids were considered because they exhibit many beneficial characteristics like fast response time, high dynamic yield stress, low plastic viscosity, broad operational temperature range, high resistance to hard settling and easiness to remix. Those characteristics, and above of all the low viscosity, make such MR fluids suitable for the squeeze film damper designed during this work.

The fluid with the lowest viscosity was chosen in order to limit the damping effect on the device when no magnetic field is applied. The aim was to evaluate the effect of the presence of the MR fluid. Because of the small size of the test rig only small forces can be applied to the rotor and hence to the MR fluid film. Such forces are just sufficient to justify a very small increase of the damping effect of the device when the fluid is added.

The fluid of the Lord Corporation was the Rheonetic fluid MRF-132LD. It has a viscosity of 0.07 Pas at a temperature of 40°C, interpolating at the values of the shear rate of 500 s^{-1} and 800 s^{-1}. Table 3.1 summarizes the properties of this fluid and figure 3.1 shows the trend of the viscosity of the fluid as a function of the shear rate. Other information about compatibility, separation, settling and toxicity is also available: such a fluid is not compatible with natural rubber or some hydrocarbon based synthetic rubber formulations; it develops a clear layer of approximately 30% (by volume) in a 1 liter container after 6 months storage at 25°C; the fluid is developed to settle softly and it will remix with a 2-3 cycles of the device. The response time of the MR fluid is of the order of magnitude of milliseconds.

Then the MR fluid MRHBS4 by Liquids Research Limited was taken into account. It has a viscosity of 0.013 Pas at a temperature of 40°C and at a shear rate of 680 s^{-1}. It has a density of 2.49 g/ml. Such company started producing MR fluid only recently and not much technical information is available. Anyways figure 3.2 shows the trend of the fluid viscosity as a function of the shear rate.

From the experimental data of figure 3.1 different values of the shear stress were computed for some values of the shear rate from 0 to 1000 s^{-1}. The evaluated value of the viscosity is the slope of the interpolation straight

Properties	**Value/Limits**
Base Fluid	Synthetic Oil
Operating Temperature	-40°C to 150°C
Density	3.0055 g/cc
Color	Dark gray
Weight Percent Solids	80.74%
Coefficient of Thermal Expansion	Unit Volume per °C
from 0 to 50°C	0.55×10^{-3}
from 50 to 100°C	0.66×10^{-3}
from 100 to 150°C	0.67×10^{-3}
Specific Heat at 25°C	0.80 J/g°C
Thermal Conductivity at 25°C	0.25-1.06 w/m°C
Viscosity (Pas)	
at 10 s^{-1} Shear Rate	0.94
at 80 s^{-1} Shear Rate	0.33

Table 3.1: Properties of the MR fluid MRF-132LD by Lord Corporation

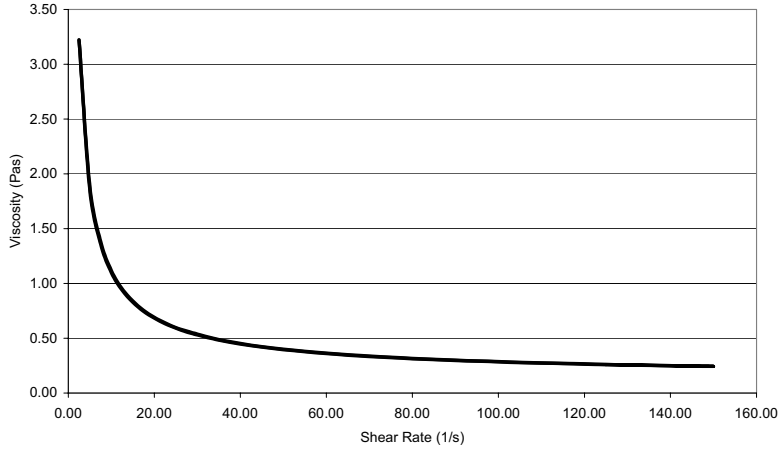

Figure 3.1: Plastic viscosity of MR Lord fluid MRF-132LD as a function of shear rate with no magnetic field applied at ambient temperature (25°C)

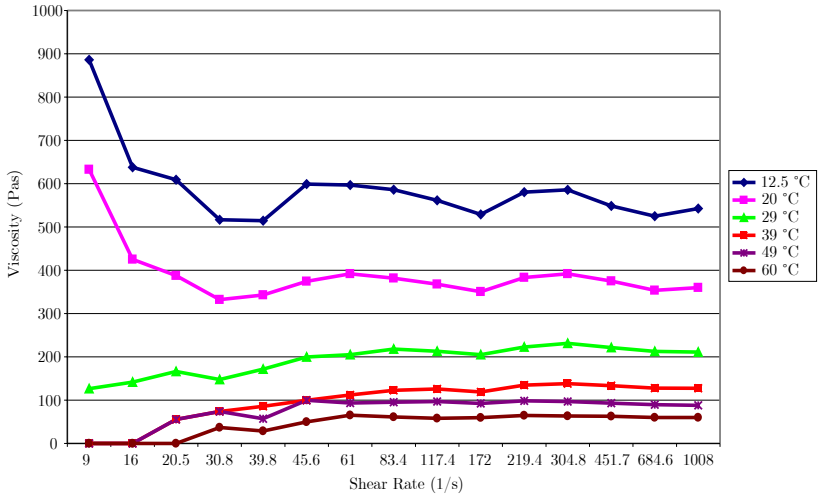

Figure 3.2: Plastic viscosity of the MR Liquids Research fluid MRHBS4 as a function of shear rate with no magnetic field applied at different temperatures

line and it was 0.18 Pas. Such a value was derived with no magnetic field applied and because of lack of data it was extended also to the situations when the magnetic field is applied.

Understanding the magnetic properties of MR fluids is important for designing MR fluid-based devices. In many devices, the MR fluid represents the largest magnetic reluctance within the magnetic circuit. These magnetic properties may also prove useful in providing insight into the characteristic and formation of particle structures within the fluid.

Magnetic induction curves, or B-H curves, of the MR fluids are shown in figure 3.4. The relationship between the magnetic induction B and the magnetic field H is given by

$$B = \mu_r \mu_0 H \tag{3.3}$$

where μ_r is the differential permeability and $\mu_0 = 4\pi \times 10^{-7}$ N/A^2 is the permeability of a vacuum. As it can be seen, the MR fluids exhibit approximately linear magnetic properties up to an applied field of about 16 A/m. In this region, the differential permeability (μ_r is the slope of $B(H)$) of the MR fluids is relatively constant. These permeabilities vary from 5 to 9 times that of a vacuum. The magnetic properties of MR fluids vary significantly from the properties of most bulk ferromagnetic properties in that ferromagnetic induction can typically be linearized over a much broader range of applied field and the corresponding permeabilities are several orders of magnitude

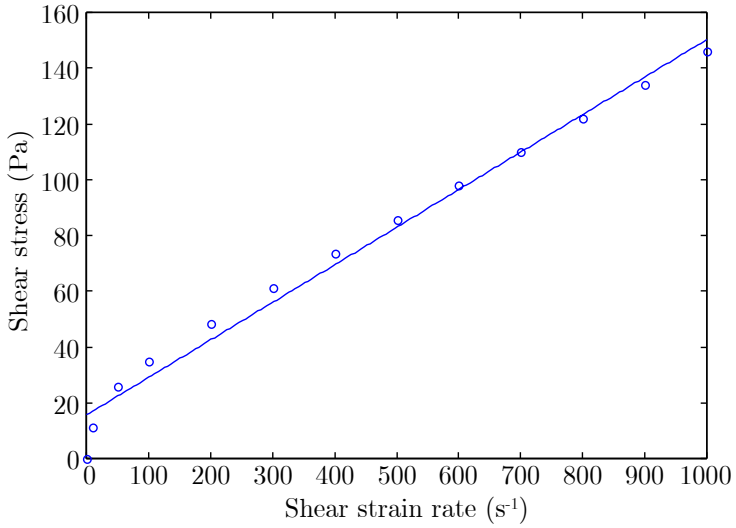

Figure 3.3: Viscosity evaluation from interpolation of experimental data: — interpolation line; ∘ experimental data

greater. MR fluids begin to exhibit gradual magnetic saturation beyond the linear regime. Complete saturation typically occurs at fields beyond 318 A/m [45].

As the magnetic induction needed by the designed device is quite small the linearity of the induction curve is assured and a differential permeability of μ_r=5 was assumed. This information was obtained from the Lord fluid data due to the lack in the specification of the Liquids Research fluid.

3.5 Adjustable squeeze film dampers

Several researchers have tried to produce mechanical operating adjustment dampers which will allow the parameters to be changed during machine operation. The characteristics of ER and MR fluids provide a possibility to control the dynamic characteristics of conventional fluid dampers [47].

Nikolajsen and Hoque [58] first presented a multidisk ER fluid damper operating in shear mode and used it to control the vibration of rotor systems when passing through the critical speeds. Vance and Yang [59] systematically studied the dynamics of a rotor supported on the multi-disk ER fluid damper. Moreover, Morishita and Mitsui [60] presented an ER fluid damper operating in squeeze film mode and studied the dynamics of a rotor supported on the

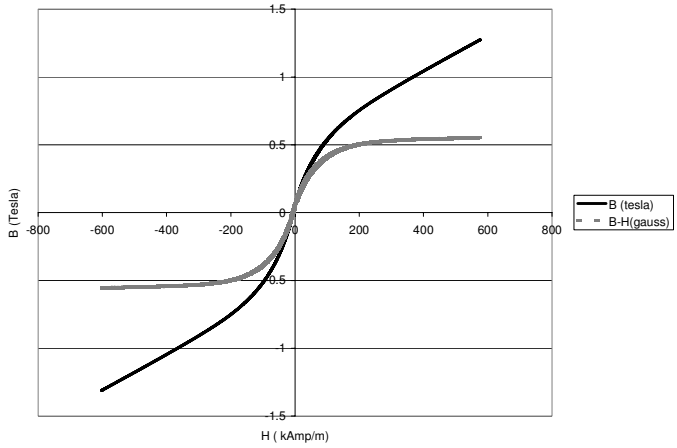

Figure 3.4: Typical magnetic properties of the oil based fluid MRF132LD

ER fluid squeeze film damper.

These researches have been shown that the ER fluid dampers can effectively control the vibration of a rotor system for a wide range of rotating speeds. However, for the ER fluid dampers, a more than 2000 V voltage should be applied to the surfaces of fixed and moving components; if these components with high voltage touch or the electrical insulation is not perfect, the reliability of the dampers is compromised. In comparison with the properties of the ER fluid, the MR fluid inherently has higher yield strength, and therefore is capable of generating a greater damping force. Further, the MR fluid is activated by an external magnetic field, produced by a simple, low-voltage electromagnetic coil, which avoids the arcing of the ER fluid squeeze film damper. However, only few papers by Zhu et al [47, 61, 62, 63] have dealt with the application of MR fluid in the squeeze film and disk type damper [47, 64, 65].

Zhu et al [47] showed that the dynamic characteristics of the MR fluid dampers can be easily controlled with a low voltage (less than 50 V) and that the MR damper are very effective for attenuating the vibration of rotor systems. It is possible to give the optimum support damping and stiffness for every vibration mode in rotor systems by controlling the applied current in the MR dampers, if they are not located at the main nodes of the rotor systems.

Zhu [47, 62] after analyzing the effects of the MR fluid, the externally applied magnetic flux density and the radial clearance of the damper on the behavior of a flexible rotor supported on the MR fluid squeeze film damper

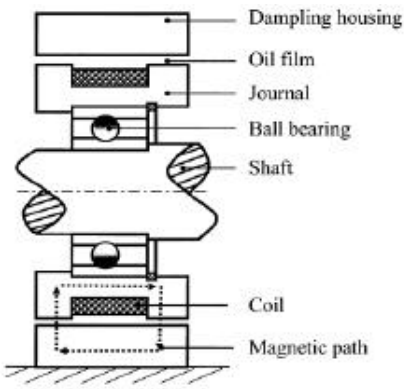

Figure 3.5: Cross section of MR squeeze-film damper [62]

in the non-rotating state, carried out an experimental study on the controllability and effectiveness of the MR fluid squeeze film damper on the rotor vibration in the rotating state. The results from the non-rotating tests and the rotating imbalance response tests showed that the dynamic characteristics of the MR fluid squeeze film damper can be easily controlled and that the MR fluid damper is very effective to control the rotor vibration. The applied voltage in the coil, required to change the dynamic characteristics of the rotor system, was much lower than that in the ER fluid device and the MR fluid squeeze film damper would easily be used in real rotating machinery. The MR fluid squeeze film damper appears a very effective way to control the vibration of a rotor system.

The basic structure of the studied MR fluid squeeze film damper was similar to that of the conventional one, but with an additional coil winded circumferentially in the journal (see figure 3.5). The radial clearances between the journal and damper housing were filled with the MR fluid. Two annular flexible rubber seals were located in the sides of the damper. When a DC voltage was applied to the coil, the magnetic flux densities in the radial clearances changed and caused the viscosity of the MR fluid in the radial clearances to change. The number of coil turns was 1000, the diameter of wire was 0.5 mm, the resistance was 23.1 Ω, the width of half load length was 15 mm, the diameter of the journal was 130 mm and the radial clearance was 1.35 mm.

He also discussed the existing problems, such as unbalanced magnetic pull force, and MR fluid sediment, which may result in the failure of the MR fluid squeeze film damper application. He recorded that, upon the application of an external magnetic field to the MR fluid SFD, there were an unbalanced

magnetic pull force between the journal and damper housing due to the eccentricity of the journal with respect to the damper housing, and a damping force produced by eddy current, in addition to the oil film force and the spring restoring force. A large unbalance magnetic pull force could lock up the journal and it could make impossible to apply the external magnetic field to change the dynamic characteristics of the MR fluid SFD system.

Sediment was one of the existing problems in MR fluid to be solved. The lower the initial viscosity of the MR fluid in the absence of a magnetic field is, the easier the sediment appears. In order to reduce the MR fluid sediment, the MR fluid should be mixed before each experiment or supplied by a pump with high flow rate. In designing the MR fluid SFD, it is also necessary to pay attention to choosing the magnetic material. The residual magnetic field of the magnetic material used in the MR fluid SFD should be as small as possible since this residual magnetic field will quicken the MR fluid sediment.

Zhu et al [47, 65] developed a disc-type MR fluid damper based on shear mode operation and verified its ability to modify the dynamic behaviour of a carefully designed rotor system and hence its effectiveness for attenuating and controlling the vibration of a rotor system. In their paper, the dynamic characteristics of the disc-type MR fluid damper were investigated experimentally and theoretically in a flexible rotor with an over-hung disc designed to exploit changes in both stiffness and damping at the bearing supports. The effects of the applied magnetising current, rotor unbalance and different mixtures of MR fluid on the rotor dynamic characteristics were systemically examined. The disc-type MR fluid damper, shown in figure 3.6, was composed of a moving disc mounted on the outer race of the journal, two magnetic poles, a coil wound circumferentially, and a damper housing, which form the magnetic path with two identical axial gaps. The moving disc, the damper housing and the magnetic poles were made of mild steel, the journal and the seal rings were made of aluminium. The axial gaps between the magnetic poles and the moving disc, and the radial clearance between the inner diameter of the magnetic poles and the outer diameter of the journal were filled with the MR fluid. Two annular flexible rubber membranes sealed the damper. The radial clearance chosen was more than 3.5 mm in order to avoid a significant squeeze film force being generated by the varying radial clearance. When the journal was whirling, the moving disc sheared the MR fluid in the axial gaps and produced a resistive fluid force to dissipate the vibration energy from the rotor system. A change of magnetising current altered the fluid characteristics and hence the shear force. Thus, the dynamic characteristics of the damper could be adjusted in a very simple manner to provide optimum system damping at each critical speed and also to improve rotor stability. The coil had 1000 turns; the diameter of wire

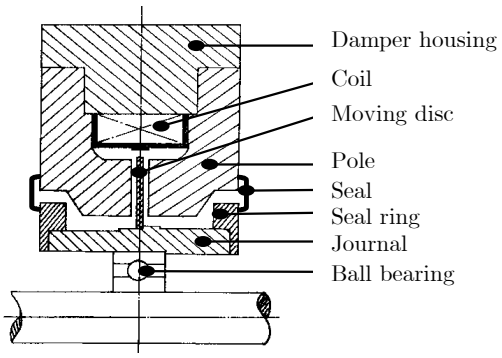

Figure 3.6: A disk-type MR fluid damper [65]

was 0.50 mm; and the resistance of the coil was 43.6 Ω. Each axial gap was 2.5 mm; the inner and outer diameters of magnetic poles were 80 mm and 124 mm, respectively.

For the disk type MR fluid damper as the magnetic field in the two axial gap was uniform, there was no unbalanced magnetic force. Since the outer and inner radii of the moving disk were almost the same as those of the magnetic pole, the eddy current was very small. It was observed that the eddy current had visually no effect on the dynamic characteristics of the disk-type MR fluid damper.

In order to investigate the effectiveness of a MR fluid damper for active control rotor vibration, a simple on-off control algorithm based on rotational speed feedback was used in the primary stage [61, 64]. The applied current of the MR fluid damper was switched at special speeds, in order to minimize the required objective, in this case it was the unbalance response of the main mass of the rotor. The transient took a short period, general less than 1 second. It was shown that the disk vibration amplitude was effectively controlled and the on-off control was effective to reach the required objective.

The MR squeeze film damper subject of this work is a novel device designed with an innovative configuration. In fact, the damper works with only one gap of MR fluid by means of a special magnetic circuit and two coils properly connected. Such a device does not show problems of magnetic pull force or fluid sediment.

3.6 Modelling of a squeeze film damper with magnetorheological fluid

In this section the analysis performed by Tichy [37, 38] for the one dimensional squeeze film damper bearing is followed. He made a steady state model of the squeeze film damper filled with a Bingham fluid and, he obtained a modified Reynolds equation, from which the bearing behaviour can be predicted. He predicted the damper forces as function of the eccentricity ratio, and a dimensionless parameter which depends on the yield shear stress. He also performed calculations for a simple rotor-dynamic system, illustrating the optimization of eccentricity and transmissibility by varying the yield stress. When a Bingham fluid is used a rigid core forms midway across the film, the core thickness being proportional to the yield shear stress.

In the Bingham plastic model the components of the cartesian deformation rate tensor $\dot{\gamma}_{ij}$, are defined in terms of the velocity field u_i by

$$\dot{\gamma}_{ij} = \frac{\partial u_i}{\partial x_j} + \frac{\partial u_j}{\partial x_i} \tag{3.4}$$

and related to the shear stress components τ_{ij} through

$$\begin{aligned} \dot{\gamma}_{ij} &= \frac{\tau_{ij}}{\left(\mu + \dfrac{\tau_0}{|\dot{\gamma}|}\right)} & |\tau| > \tau_0 \\ \dot{\gamma}_{ij} &= 0 & |\tau| < \tau_0 \end{aligned} \tag{3.5}$$

where τ_0 is the yield shear stress. For shear stress magnitude $|\tau|$ greater than a yield shear parameter τ_0, the material flows as a Newtonian fluid with viscosity μ; otherwise, the material remains rigid. The shear stress magnitude and the deformation rate magnitude are defined by:

$$|\tau| = \sqrt{|\frac{1}{2}\tau_{ij}\tau_{ij}|} \text{ and } |\dot{\gamma}| = \sqrt{|\frac{1}{2}\dot{\gamma}_{ij}\dot{\gamma}_{ij}|} \tag{3.6}$$

where the convention of repeated indices is adopted.

For the lubrication geometry of the one-dimensional bearing illustrated in figure 3.7 is $u = u_1 \gg v = u_2$, $\partial/\partial x = \partial/\partial x_1 \gg \partial/\partial y = \partial/\partial x_2$, and $w = u_3 = \partial/\partial z = \partial/\partial x_3 = 0$. u and v are the velocities of the fluid in the circumferential and radial directions respectively. x, y and z are the spatial co-ordinates in the circumferential, radial and axial directions respectively. In this case, for the so called Bingham model:

$$\begin{aligned} \frac{\partial u}{\partial y} &= 0 & \text{for} \quad |\tau| \leq \tau_0 \\ \tau = \tau_{xy} &= \mu\frac{\partial u}{\partial y} \pm \tau_0 & \text{for} \quad |\tau| > \tau_0 \end{aligned} \tag{3.7}$$

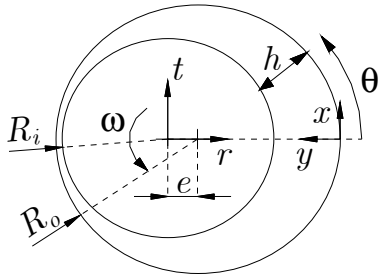

Figure 3.7: Schematic of damper geometry

the continuity equation can be obtained:

$$\frac{\partial u}{\partial x} + \frac{\partial v}{\partial y} = 0 \tag{3.8}$$

and the inertialess x- and y-momentum equations:

$$0 = -\frac{\partial p}{\partial x} + \frac{\partial \tau}{\partial y} \text{ and } 0 = \frac{\partial p}{\partial y} \tag{3.9}$$

For the squeeze film damper, the film thickness is defined as:

$$h = c(1 + \varepsilon \cos\theta) \tag{3.10}$$

where c is the bearing radial clearance, $c = R_0 - R_i \ll R_0 \approx R$ (see figure 3.7), ε is the eccentricity ratio, $\varepsilon = e/c$, θ is the angular coordinate measured from the maximum film thickness location and $x = R\theta$.

Therefore, the selected coordinate system rotates with the journal at a constant speed, ω. With respect to the rotating system, the problem is steady and the velocity boundary conditions are:

$$\begin{array}{lll} u = -\omega R,\ v = 0 & \text{for} & y = 0 \\ u = -\omega R,\ v = \omega c \varepsilon \sin\theta & \text{for} & y = h \end{array} \tag{3.11}$$

Substitution of the constitutive equation into the x- momentum equation, and integration for $p = p(\theta)$, shows that the velocity, u, is either constant or quadratic with respect to y. In either case, u is symmetric and τ is antisymmetric about the mid-plane $y = h/2$, based on the previous boundary conditions. Thus $\tau(\theta, h/2) = 0$, and a rigid core must exist in the vicinity for any non-zero τ_0. Furthermore, for parabolic u this is the only possible core, and only the domain $0 \le y \le h/2$ needs to be considered.

Solving equations using $\tau(\theta, h/2) = 0$ as second boundary condition the velocity field is found:

$$\begin{aligned} u &= -\omega R + \frac{1}{2\mu R}\frac{\mathrm{d}p}{\mathrm{d}\theta}(y^2 - hy) - \frac{\pm\tau_0}{\mu}y \qquad \text{for} \quad 0 \le y \le h_a \\ u &= -\omega R + \frac{h^2}{8\mu R}\frac{\mathrm{d}p}{\mathrm{d}\theta} - \frac{\pm\tau_0}{2\mu}h - \frac{R\tau_0^2}{2\mu\,\mathrm{d}p/\mathrm{d}\theta} \quad \text{for} \quad h_a \le y \le \frac{h}{2} \end{aligned} \tag{3.12}$$

where

$$h_a = \frac{h}{2} \pm R\frac{\tau_0}{\mathrm{d}p/\mathrm{d}\theta} = \left(\frac{\pm\tau_0 - \tau_1}{\mathrm{d}p/\mathrm{d}x}\right) \tag{3.13}$$

and

$$\tau_1 = \frac{\mathrm{d}p/\mathrm{d}x}{2h\,\mathrm{d}p/\mathrm{d}x \pm \tau_0}\left(h^2\frac{\mathrm{d}p}{\mathrm{d}x} \pm 2h\tau_0\right) \tag{3.14}$$

The core extends from h_a to $(h - h_a)$ and τ_1 is the shear stress at $y = 0$. The shear rate $\partial u/\partial y$ equals zero at the core interface $y = h_a$. The $+\tau_0$ condition is used when $\mathrm{d}p/\mathrm{d}\theta$ is negative and viceversa. The interface between the flow region and the floating centered rigid core is denoted $h_a(\theta)$ where $\tau = \pm\tau_0$.

By integrating the continuity equation, the volume flow rate per bearing axial length is determined:

$$q = 2\int_0^{h/2} u\;\mathrm{d}y = constant \tag{3.15}$$

substituting and performing the indicated integrations, the following implicit form of the Reynolds equation is obtained:

$$\left(h\frac{\mathrm{d}p}{\mathrm{d}x}\right)^3 + 3\left(\frac{\mathrm{d}p}{\mathrm{d}x}\right)^2[4\mu(\omega Rh + q) \pm h^2\tau_0] - (\pm 4\tau_0)^3 = 0 \tag{3.16}$$

Equation 3.16, being a cubic equation, has a standard analytical solution for $\mathrm{d}p/\mathrm{d}x$. However, any of the three roots may be the physically meaningful one and τ_0 can be positive or negative, depending on the value of the parameters. For instance complex solutions are discarded as well as positive solutions when $+\tau_0$ is used or negative solution when $-\tau_0$ is considered. Moreover the film thickness of the core must not exceed the film thickness.

Equation 3.16 can be solved if the fluid parameters μ and τ_0 are known together with the damper parameters ω, c and R. A guess of the constant flow rate parameter q is made, beginning with the value, from Newtonian lubrication theory,

$$q = 12\omega Rc\frac{1 - \varepsilon^2}{2 + \varepsilon^2} \tag{3.17}$$

Pressure is determined by integrating the pressure gradient expression and adjusting the constant flow rate q so as to satisfy the periodicity condition $p(0,q) = p(2\pi,q)$:

$$p(\theta,q) = \int_0^\theta \frac{\mathrm{d}p}{\mathrm{d}\theta'}\mathrm{d}\theta' + p(0,q) \tag{3.18}$$

The radial, F_r, and tangential, F_t, forces on the rotor due to the film pressure are found by performing the following integrations:

$$F_r = RL\int_\pi^{2\pi} p\cos\theta \mathrm{d}\theta \tag{3.19}$$

$$F_t = RL\int_\pi^{2\pi} p\sin\theta \mathrm{d}\theta \tag{3.20}$$

in which simple cavitation Gümbel conditions are assumed (π film), i.e., cavitation occurs when $p(\theta) < p(0)$.

Figure 3.8 shows typical dimensionless velocity profiles u^* for different values of the dimensionless yield shear stress parameter τ_0^*. The results are adimensionalized according to:

$$\begin{aligned} u^* &= \frac{u}{U}, \qquad y^* = \frac{y}{h}, \\ \tau_0^* &= \frac{\tau_0 c}{\mu U} \quad p^* = \frac{[p-p(0)]c^2}{\mu\omega R^2} \end{aligned} \tag{3.21}$$

The surfaces are both sliding in the reverse direction with $U_1 = U_2 = -U$. The flow is symmetric about the midplane $y = h/2$, where the shear stress is zero. In the Newtonian case, a Poiseuille flow takes place with a uniform negative velocity superimposed. It is observed that as the yield stress τ_0 increases, a floating core thickens about the midplane.

Behaviour of the dimensionless pressure p^* as a function of the angular coordinate θ is shown for a high eccentricity ratio $\varepsilon = 0.5$, in figure 3.9. The low eccentricity case is more affected by the yield shear stress. This difference is due to the fact that at high eccentricity the pressurized region has a small angular extent with high shear rate, where the yield shear stress has less influence.

In figure 3.10 the thickness of the floating central core is presented, for high eccentricity $\varepsilon = 0.5$ and different values of the dimensionless yield shear stress. The upper and lower lines are the boundaries between the core and the fluid film. The core is in the middle. The core thickens with increasing τ_0^* and fills the gap at two locations θ_m where $h/c = q^*$. Beginning at $\theta = 0$, the pressure gradient is negative, the shear rate is positive, and $+\tau_0$ is used

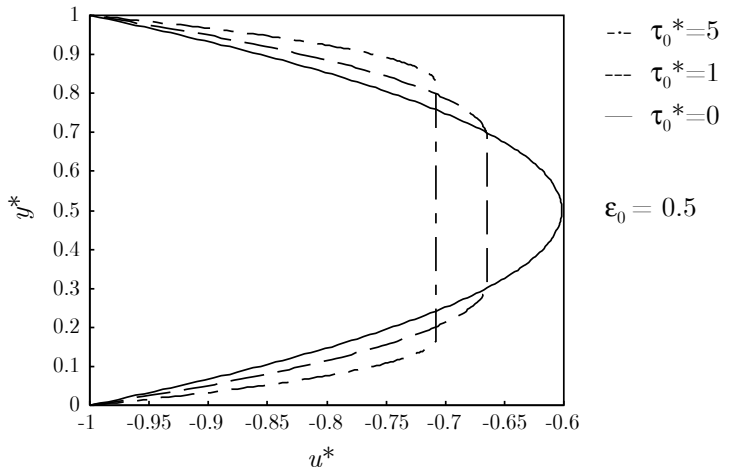

Figure 3.8: Typical dimensionless velocity profiles

in equation 3.16. These conditions reverse every time $\theta = \theta_m$. Intuitively the pressure in the gap increases with the shear rate stress because the increase in the core thickness decreases the useful gap.

3.7 Modelling of the rotor-damper system

In the previous section the lubrication theory with Bingham fluid has been explained and used to solve the squeeze film damper problem. The results obtained are here used in order to see the effect of the squeeze film damper filled with Bingham fluid on the dynamics of a statically unbalanced rotor. Firstly the forces generated by the pressure field of the damper on the inner journal are determined. Then the equilibrium equations of the rotor supported by the squeeze film damper can be written. Studying the behaviour of the rotor at different values of the yield stress of the Bingham fluid the performance of the squeeze film damper can be obtained.

Simultaneously the characteristic dimensions of the fluid film were chosen. The axial length, L, the radial clearance, c, and the radius, R, of the bearing were taken respectively as 20 mm, 2.5 mm and 32 mm. The inner radius was kept as small as possible considering the small size of the test rig and taking into account the space for a sleeve, a rolling bearing and the material needed to realize the magnetic circuit. On the contrary the axial length of the film was kept as long as possible in order to minimize boundary effects.

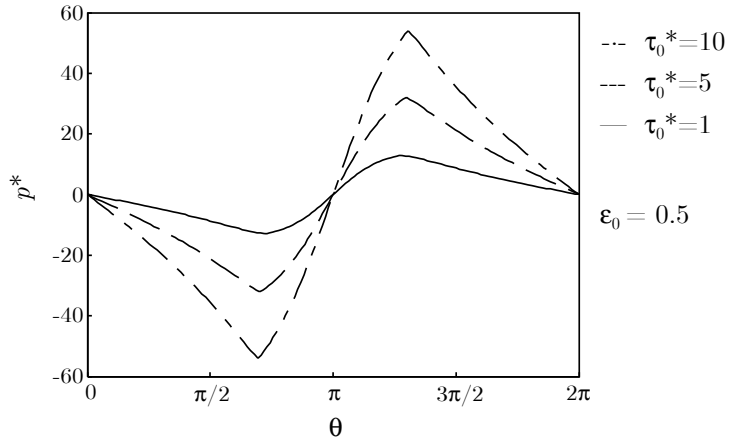

Figure 3.9: Squeeze film damper dimensionless pressure distribution

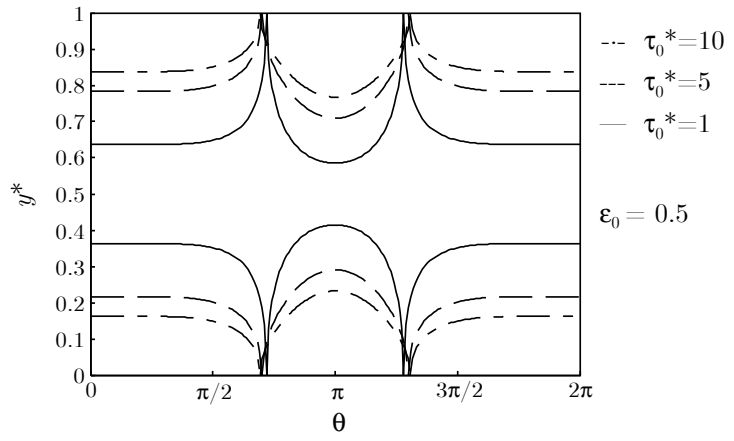

Figure 3.10: Squeeze film damper profile of the core boundaries

The radial clearance was a geometrical parameter more hard to set. A small value of the radial clearance is suitable in order to design an efficient magnetic generation. In fact the MR fluid has a low magnetic permeability, $\mu_r \cong 5$, compared to that of the steel C40, $\mu_r \cong 2000$, used to build the magnetic flux path. As the current that generates the magnetic field inside the fluid gap is inversely proportional to the fluid thickness, a small value of the radial clearance entails a lower current in the coils, that is a lower power and higher compactness of such coils. On the other hand, if a small radial clearance is chosen, a great static unbalance or a big central mass are necessary in order to exhibit the MR squeeze film damper performances. As the MR squeeze film damper was designed to fit the Rotor-Kit by Bently Nevada that uses a 10 mm diameter shaft, great unbalance might be unsafe and damage the equipment. Different values of the radial clearance were considered but a value c =2.5 mm was chosen. In fact even if this value is outside the limits of the Reynolds theory it permits to exploit all the potentialities of the MR fluid. Then the Reynolds theory was adopted anyway just as an indication for the design of the squeeze film damper, keeping in mind its limitation and planning to check its validity by experimental testing. Even if the experimental setup needed a big clearance, industrial realizations usually need a small clearance in order to cope with the large forces generated. So industrial applications will need less current to generate the same magnetic flux, that is industrial devices should be more compact.

The viscosity, μ was assumed 0.18 Pas in accordance with the oil based MR fluid MRF 132-LD produced by the Lord Corporation. An average value for the viscosity was considered neglecting the so called *shear thinning effect*, i.e, the relationship between viscosity and shear rate. Radial and tangential forces were calculated considering different values for the yield stress (τ_0=500, 10000 and 20000 Pa) and for the whirling velocity (ω= 50, 500 and 1000 rad/sec). Figures 3.11, 3.12 and 3.13 show these radial and tangential forces as function of the eccentricity ratio ε.

Both the radial and tangential forces increase with the yield shear stress. Thus the tangential force has a finite value when $\varepsilon \to 0$. Such behaviour can be explained considering Bingham's fluid constitutive equation.

Figures 3.11, 3.12 and 3.13 suggest the following analytical expressions for F_t and F_r:

$$F_r = a_r(\omega, \tau_0) \left(\frac{e}{c}\right)^2 \tag{3.22}$$

$$F_t = a_t(\omega, \tau_0) + b_t(\omega, \tau_0)\frac{e}{c} \tag{3.23}$$

A further analysis carried out with a film thickness $c = 1$ mm showed the influence of such variable on the damper characteristics. The forces produced

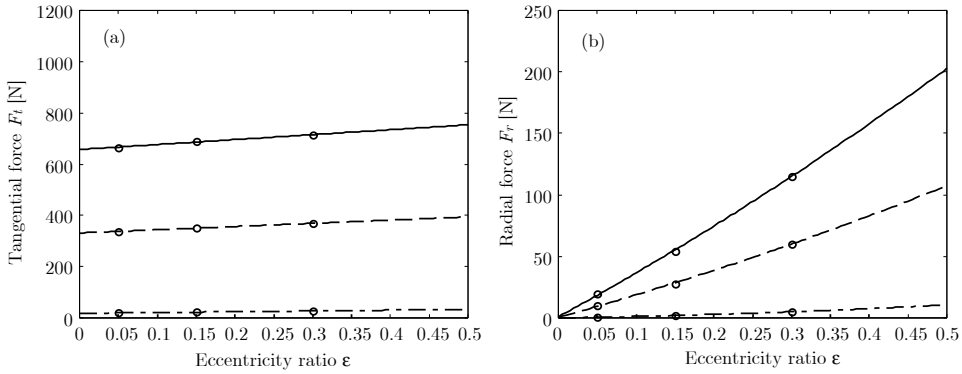

Figure 3.11: Tangential (a) and radial (b) forces due to the pressure field in the gap for a rotating speed ω of 50 rad/s: — $\tau_0 = 20000$ Pa; - - - $\tau_0 = 10000$ Pa; $-\cdot-$ $\tau_0 = 50$ Pa

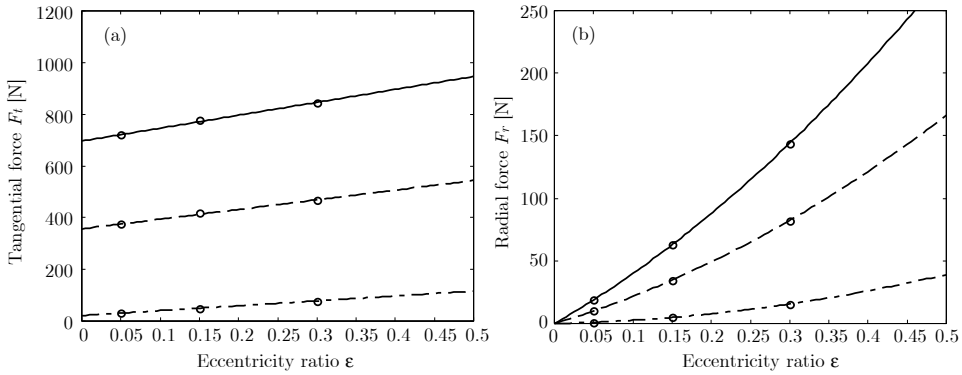

Figure 3.12: Tangential (a) and radial (b) forces due to the pressure field in the gap for a rotating speed ω of 500 rad/s: — $\tau_0 = 20000$ Pa; - - - $\tau_0 = 10000$ Pa; $-\cdot-$ $\tau_0 = 50$ Pa

by the squeeze effect are inversely proportional to the film thickness and their value grossly increases five time from $c = 1$ mm to $c = 2.5$ mm. Such result is in accordance with the results obtained in the adimensional analysis depicted in the previous section. In fact the pressure in the fluid film is proportional to the squared value of its thickness. Even if during the design phase of the work both values of film thickness were considered, only the results referring to the chosen value (2.5 mm film thickness) are presented onward.

The results of the analysis can now be adopted to solve the global problem of a flexible rotor supported by adjustable bearings and a MR squeeze film damper. The same hypotheses used to solve the film pressure field in the squeeze film damper have to be adopted. So a quasi-static analysis was carried out, studying the system at different steady state conditions of synchronous precessional speed, neglecting the transient effects. Therefore the film pressure is only function of the radial displacement of the inner journal and of the angular speed of the rotor.

In figure 3.14 the schematic model of the rotor-damper system is presented. It is made of an elastic shaft, with a disk with mass m_D connected in the middle, hinged at both ends. The shaft is also supported by the squeeze-film damper. Two coordinate systems rotating with the shaft at its whirling velocity ω are defined. The center of mass of the disk is offset by a distance δ from the geometric center of the shaft due to the unbalance, m_g. Thus, the unbalance vector makes a constant arbitrary angle β with respect to the X_1 direction. The coordinates (x_1, y_1) describe the displacement of the geometric center of the disk while x_2 describes the radial displacement of the inner cylinder of the damper (see section 3.8 for the description of the device). The inertia of the damper journal is accounted for by adding a second mass, M_2, to the shaft.

The tangential force due to the pressure generated in the damper acts in the Y_2 direction while the radial force acts in the X_2 direction. The inner cylinder of the damper can be constrained by a squirrel cage (see section 3.8) which is accounted for in the analytical model by adding a radial stiffness, k_{sc}. The four unknown values x_1, y_1, x_2 and β can be found by writing and solving the four equilibrium equations written in the X_1, X_2, Y_1 and Y_2 directions. In these equations we consider the centrifugal forces due to the masses M_1 and M_2, the elastic reactions of the shaft (using the linear stiffness coefficient k_{11}, k_{12}, k_{22}), and the possible damper reaction:

$$\begin{cases} k_{11}x_1 + k_{12}x_2 = M_1\omega^2(x_1 + \delta\cos\beta) \\ k_{11}y_1 = M_1\omega^2(y_1 + \delta\sin\beta) \\ k_{12}x_1 + k_{22}x_2 + k_{sc}x_2 + F_r(\omega, \tau_0) = M_2\omega^2 x_2 \\ k_{12}y_1 + F_t(\omega, \tau_0) = 0 \end{cases} \tag{3.24}$$

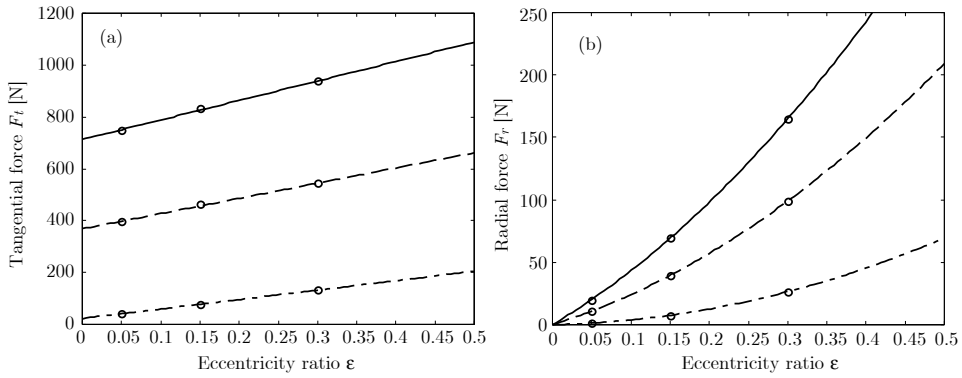

Figure 3.13: Tangential (a) and radial (b) forces due to the pressure field in the gap for a rotating speed ω of 1000 rad/s: — $\tau_0 = 20000$ Pa; - - - $\tau_0 = 10000$ Pa; $-\cdot-$ $\tau_0 = 50$ Pa

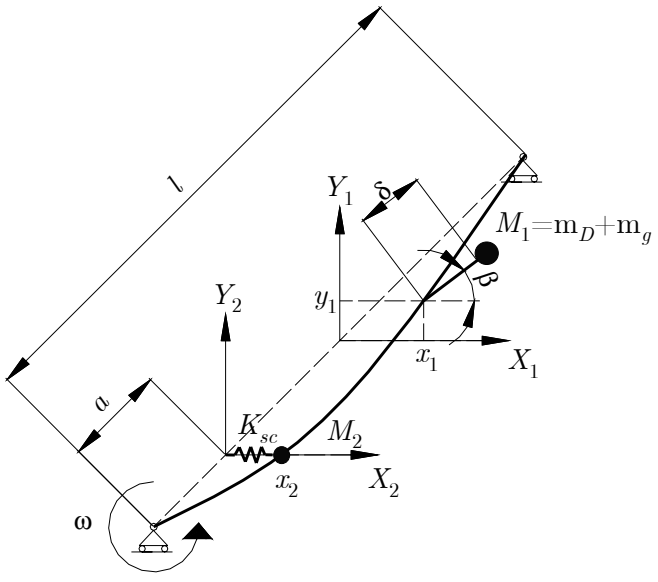

Figure 3.14: Schematic model of the rotor-damper system

Length of the shaft	l	0.42 m
Damper position	a	0.11 m
Shaft stiffness	k_{11}	452140 N/m
	k_{12}	-539820 N/m
	k_{22}	756200 N/m
Squirrel cage stiffness	k_{sc}	174000 N/m
Disc mass	m_d	0.800 kg
Unbalance mass	m_g	0.007 kg
Main mass	M_1	0.807 kg
Damper mass	M_2	0.400 kg
Unbalance radius	δ	2.625×10^{-4} m

Table 3.2: Numerical values for the simulation of the damped operation

Equations 3.24 are solved for several values of the yield stress and for angular velocities varying from 0 up to 10000 rpm. That is actually the range of velocities which can be explored using the Bently Nevada Rotor Kit (see section 3.8.1).

For every ω and τ_0 four solutions are found among which the physically meaningful one is chosen. When no meaningful solution arises it means that the forces due to unbalance are not high enough to break the columnar structures created in the MR fluid and the damper acts on the shaft as a rigid constraint.

The numerical values used in the simulation are reported in table 3.2. Using such values the first critical speed is about 2700 rpm when the rotor is supported only by two bearings. When the squeeze film damper is added, the critical speed increases up to 3800 rpm because of the addition of the squirrel cage stiffness to the shaft stiffness and moreover a second critical speed at about 16000 rpm arises due to the mass of the squeeze film damper journal added to the rotor. Test rig speed are allowed up to 10000 rpm so the second resonance of the system cannot be investigated.

In figure 3.15 the radial displacement of the geometric center of the disk placed in the middle of the shaft versus the angular velocity of the shaft is shown. When the yield shear stress is zero the influence of the squeeze film damper on the rotor dynamics is quite small. In order to fully exploit the MR fluid characteristics and increase the damper performances it is important to limit the squeeze film damper effectiveness when no magnetic field is generated. As the yield shear stress is increased, the speed range in which the journal is constrained (i.e. the solid core fills all the damper gap) increases

as well. When the yield stress shear is $\tau_0 = 2500$ Pa the original critical speed (2700 rpm) is crossed keeping the rotor orbit very small. In fact the squeeze film damper acts like a new rigid constraint and the rotor stiffness is increased. Anyways at greater rotating velocities the inertial forces generated by the shaft manage to break the ties of the MR fluid core and a beneficial reduction in the global stiffness is recorded. Further increases in the yield shear stress enlarge the range in which the MR damper acts like a rigid bearing and increase the natural frequency of the system. At a yield shear stress $\tau_0 = 20000$ Pa the new critical speed is about 6800 rpm.

The numerical results shown above suggest two different simple ways to control the shaft dynamic instability:

- the first is a simple on-off procedure consisting in turning the device on while the shaft is passing through the critical speed and turning it off when the displacements start to increase again; when the device is active, the magnetic field applied on the fluid has to be high enough to maintain the fluid solid in every zone of the gap
- the second procedure consists in setting the magnetic field at a constant value to obtain the shaft behaviour shown in figure 5 (Yield stress = 5000 Pa).

Even if such strategies are very simple and can be employed with no effort, they have the drawback to have a small versatility. In fact they cannot cope with a change in the operating conditions or in the system dynamics because of deposition, damage or wear. Thus the employment of a high level controller with the damper is necessary to design a device with optimal performance.

Whatever strategy will be adopted the potentialities of the fluid will not be fully exploited. In fact, even if the yield shear stress of MR fluid can easily reach 50000 Pa, the maximum unbalance and the rotor stiffness of the test rig restrict the exploitation of the MR fluid. A solution can be a further increase in the film gap, but then the realization of the magnetic field becomes very hard. In fact too bulky and heavy magnetic circuit and coils are necessary.

A limit of this calculation is that it doesn't consider the effects of the magnetic field on the mobile parts of the damper but the solution of this complex problem is beyond the scope of this work.

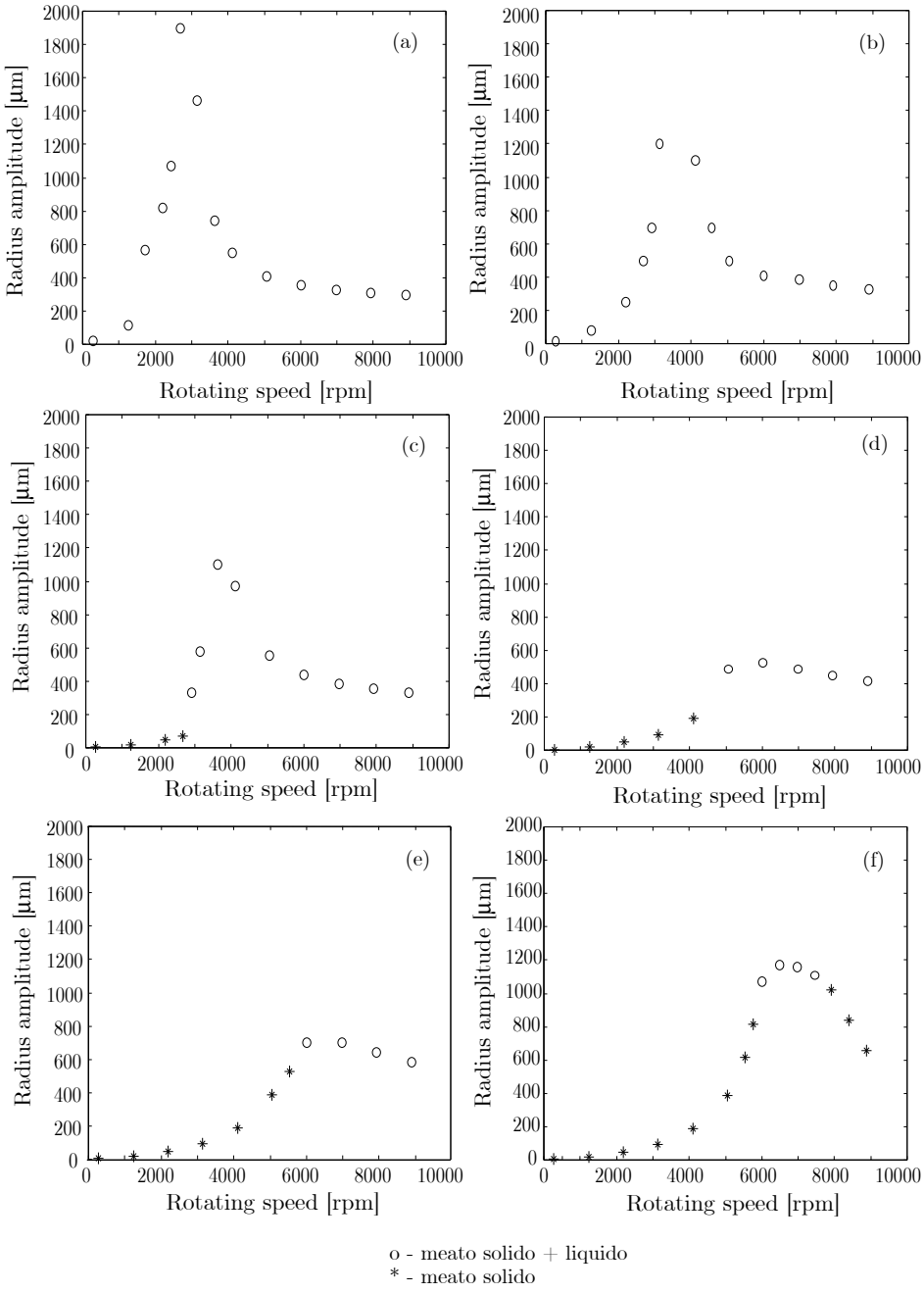

Figure 3.15: Effects of the fluid yield stress increase on the rotor behaviour: Free shaft (a), Newtonian behaviour (b), Bingham behaviour with yield stress τ_0=2500 Pa (c), τ_0=5000 Pa (d), τ_0= 10000 Pa (e) and τ_0= 2000 Pa (f)

3.8 Design of the MR squeeze-film damper

3.8.1 Description of the device

The traditional configuration of squeeze film dampers has been modified in order to use an MR fluid instead of the usual lubricants. The design of the device aims at creating the magnetic field, necessary to change the rheologic characteristic of the fluid, within the gap of the squeeze film damper. Thus such a device is just a magnetic circuit that must lead the magnetic flux generated by an electric coil to the MR fluid film.

Figure 3.16 shows a photo of the device set up on the test rig. Figure 3.17 presents the longitudinal section of the device. It is characterized by one gap, filled up with MR fluid, and two electrical coils. Other authors [47] used a different configuration that involves two gaps and one coil. Such latter configuration is electrically simpler and energetically more efficient but mechanically more complex.

The device is entirely made of C40 steel except for the the shaft bush made of an aluminium alloy. Each coil has 240 windings of a 0.63 mm diameter wire, capable of bearing a constant current of 1 A, value that can rise up to 2 A for a limited time. The electrical resistance of each coil is 4.3 Ω. The wires coming out of the coils are connected to each other so that the two coils are run by the current in opposite directions.

The basic parameters of the MR film are the same already used for the evaluation of the radial and tangential forces of the squeeze film damper. So the length, L, the radial clearance, c, and the radius of the bearing were set respectively 20 mm, 2.5 mm and 32 mm.

In order to satisfy the one-dimensional bearing hypothesis and neglect the flow in the axial direction and, because a non sealed configuration can expose the user to the toxicity of MR vapours, the gap was sealed by two planar flexible annular rubber membranes.

The rubber gaskets are planar annular membranes with a 0.4 mm thickness. A study of the optimal shape was done in order to find the configuration with the smallest stiffness. In fact the stiffness of such elements can increase the stiffness of the damper and worsen the performance of the test rig. Even if some non-planar configuration is theoretically better, the planar configuration was chosen because it permits to make thinner and therefore more compliant.

Between the shaft and the journal of the damper a single row radial rolling bearing has been used. The rotation of the transversal section of the shaft was allowed by the elasticity of the flexible gaskets placed at the fluid film ends. The rubber gaskets have also to prevent the damper journal rotation

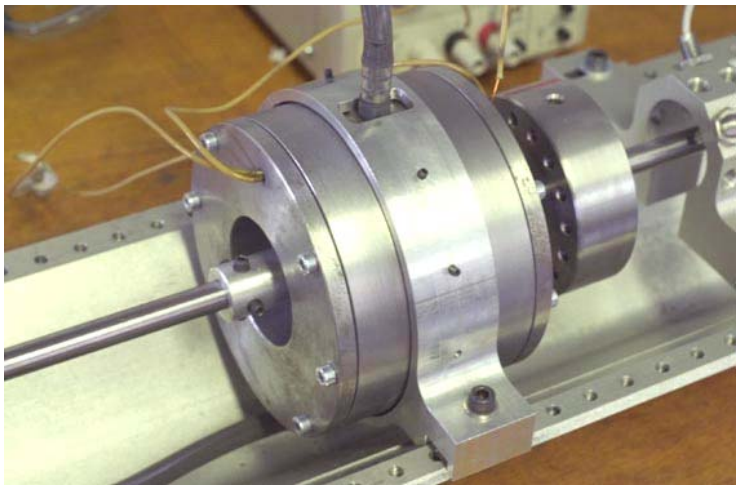

Figure 3.16: A photo of the MR squeeze film damper

and thus to bear the rotational stress, in fact no squirrel cage has been used in order to avoid any stiffening source. Anyways an interface was devised to have the possibility to connect a squirrel cage later on if necessary.

The MR fluid can be introduced into the gap by means of a syringe through two inlets with a G1/8" thread. The filling is made off-line before each experiment in order to avoid deposition problems. A continuous flow was discarded because the high density (3.055 g/cc) and the strong deposition of the MR fluid can damage the pumping system.

3.8.2 Design of the magnetic circuit

From the electromagnetic point of view the damper structure can be considered as a circuit concentrating the magnetic field generated by the coils and guiding it through the MR fluid. The magnetic circuit was designed so that the magnetic field crosses the MR fluid film perpendicularly as much as possible in order to exploit at best the performance of the fluid. In fact in such a situation the columnar structures that form inside the fluid are working perpendicular to the displacement of the moving parts of the damper.

The MR damper magnetic circuit uses low carbon steel, which has a high magnetic permeability and saturation, to build the magnetic circuit, concentrate and guide the magnetic flux lines into the fluid gap. The current density through the coils necessary to generate the magnetic field was determined. The optimal design of the magnetic circuit requires to maximize the mag-

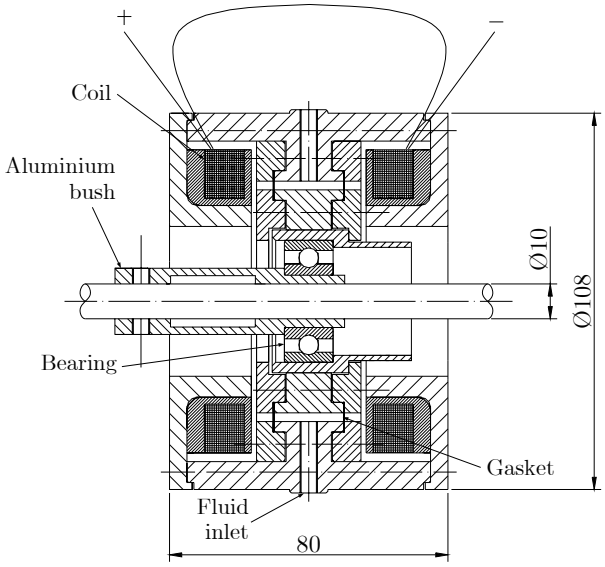

Figure 3.17: The MR fluid damper

netic field energy in the fluid gap and to minimize the energy losses in the magnetic conduit and in the non-working areas. The total amount of steel in the magnetic circuit was minimized in order to reduce the weight of the device. However, sufficient cross-section of steel must be maintained to keep the magnetic field in the steel components of the device at an appropriate level.

An analysis of the magnetic behaviour of the device was carried out by using a finite elements code (ANSYS®) relating the value of the electric current running in the coils and the value of the magnetic field in the fluid. An axial-symmetric model was employed since the objective of the analysis was only to optimize the geometry of the magnetic circuit. All materials magnetic properties were assumed linear, i.e, constant relative magnetic permeability, $\mu_r = 2000$ for steel and $\mu_r = 5$ for the MR fluid, were used. All aluminium parts were treated as air, that is with $\mu_r = 1$. The bearing magnetic permeability was neglected because of the discontinuous structure (i.e. balls and plastic cage). Figure 3.18 shows the different parts that form the axial-symmetric model. Figures 3.19 and 3.20 show the values of the magnetic field and the flux lines in the device for a current density J_s=7 A/mm^2, that corresponds to a current of 2 A.

Inside the gap the magnetic field is almost constant with a value of B_{MR}=0.55 T. The linear relationship between the current density in the

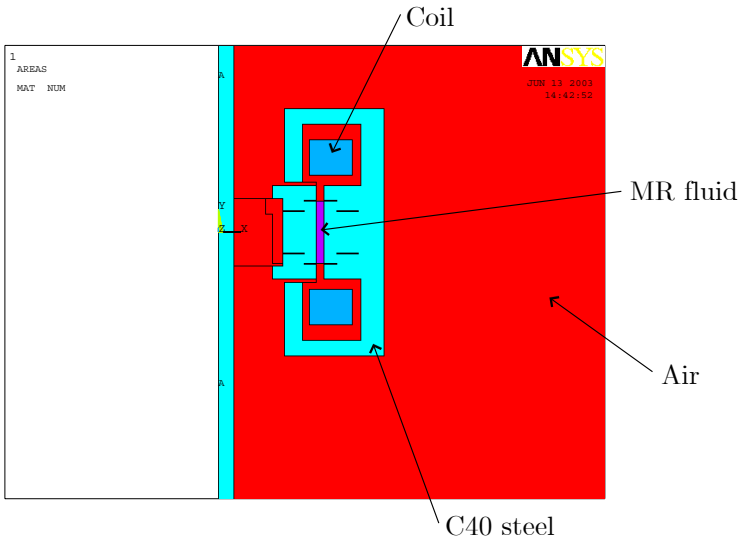

Figure 3.18: The magnetic fem model of the device

coils (measured in A/mm^2) and the magnetic induction in the MR fluid B_{MR} (measured in T) is expressed by the following equation:

$$B_{MR} = 7.86 \times 10^{-2} J_s \tag{3.25}$$

Thus it is possible to correlate the value of the current density in the coils to the magnetic induction, and then the magnetic induction to the yield shear stress of the MR fluid using the experimental graph shown in figure 3.21. Assuming that the yield shear stress is τ_0=30 kPa for an induction of 0.55 tesla and that the relationship between them is linear, the relationship between the yield shear stress, τ_0 (measured in Pa), and the current through the coils, I (measured in A), can be expressed by the following equation:

$$\tau_0 \simeq 15I \tag{3.26}$$

Since the induction in the film gap is no more than 0.55 tesla the linearization is acceptable and the shear thinning phenomenon, occurring at high induction, is not a problem.

3.8.3 The test-rig

The MR squeeze film damper was designed to be assembled on the Bently Nevada Rotor Kit, a demo bench already described in section 2.5.1. Figure

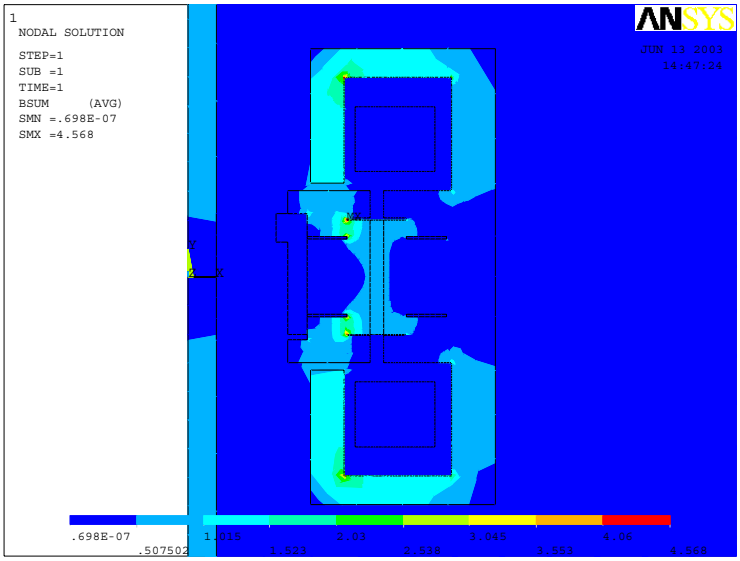

Figure 3.19: The magnetic field in the device

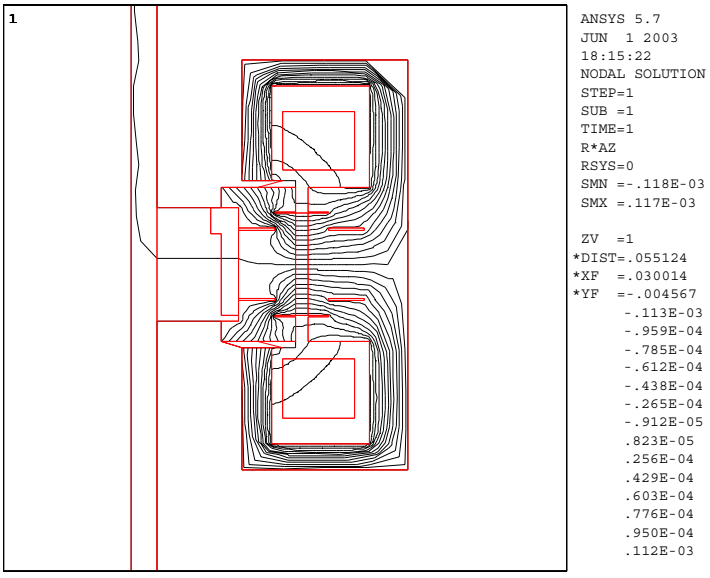

Figure 3.20: 2-D flux lines of the magnetic field in the device

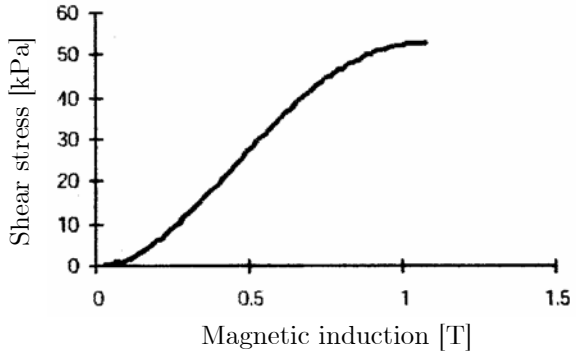

Figure 3.21: Shear stress vs magnetic induction in the fluid

3.22 shows the MR squeeze film damper fitted on the Bently Nevada Rotor Kit in the experimental configuration.

The damper was supported by an aluminium ring connected to the pedestal of the Rotor-Kit, and was mounted on the shaft by means of an aluminium bush. It was connected to a current generator (Thurlby Thandar Instruments EL302P power supply) in order to supply the coils with a maximum constant current of 2 A at a maximum voltage of 30 V. The power supply had a resolution of 10 mA in constant current generation and 10 mV in constant voltage generation. Such a power supply had also a remote control to drive it through an RS-232 serial interface.

Both the Rotor Kit and the current generator were connected to a PC supplied with an acquisition device: the PCI-MIO-16E-4 board by National Instruments. The acquisition device had 16 analogue input ports and 2 analogue output ports and a maximum scan frequency of 250 kHz. The communication between the PC and the test rig was driven by LabVIEW^{TM} programs, written on purpose by the author.

The Rotor Kit journal bearing was characterized by a large clearance and a small stiffness. So a new support had to be designed employing a rolling bearing. The maximum radial clearance was reduced from 0.052 mm to 0.0015 mm and the stiffness was increased using self-aligning ball bearings. Figure 3.23 shows the design of the new support.

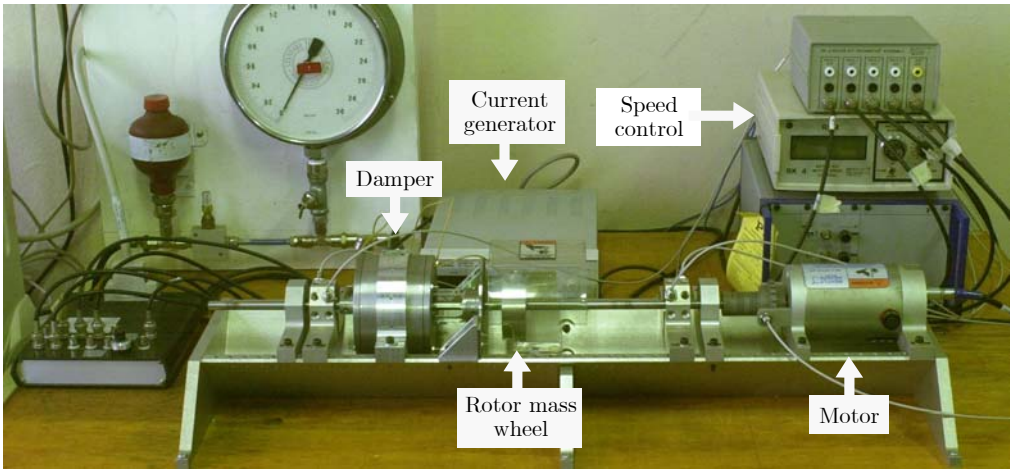

Figure 3.22: The test-rig

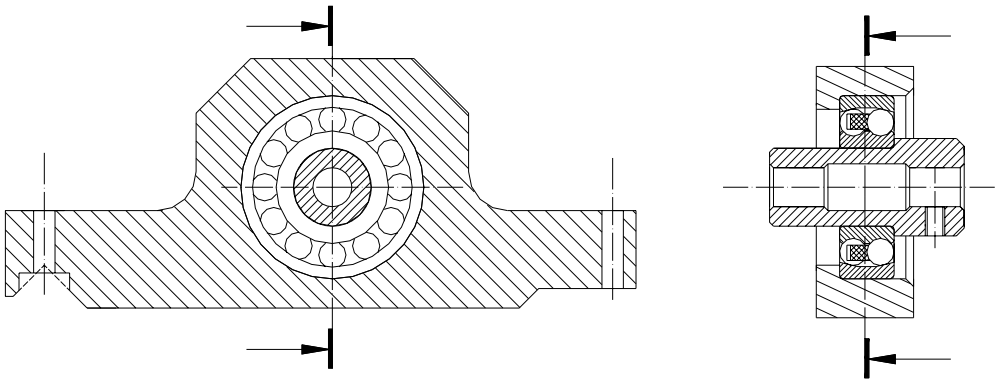

Figure 3.23: The new support with reduced clearance

3.9 Experimental results

Preliminary tests have been performed. In the tested configuration the rolling bearing supports were 500 mm apart and the damper was placed at a distance of 180 mm from one of them. The disk of 0.8 kg mass, was placed in the middle of the shaft and unbalanced with a 1.5 g grain. This value appears quite high in relation to the shaft and disk dimensions, in fact it is the highest value of unbalance that can be used without spoiling the device. Anyway during the numerical simulations it was observed that such an unbalance is necessary to test the characteristics of the MR fluid used since a lighter grain wouldn't generate a sufficient high force to break the columnar structure created in the fluid and activate the damper unless the yield stress was extremely small.

The sensors were placed at a distance of 75 mm from the disk mass farther from the damper. They were placed not too close to the whirling disk in order to avoid off-scale problems since the tests are characterized by great deformations of the shaft. The test configuration is shown in figure 3.22.

The first tests were carried out on the empty squeeze film damper i.e. with no fluid inside the gap. The purpose was to investigate how much the rotor dynamics is influenced by the damper and, in particular, by the rubber membranes because their characteristics could not be estimated a priori. Moreover, a current was supplied to the coils in order to generate a magnetic field inside the damper gap and to see the effect of the magnetic field on the rotor dynamics.

Rotational speed varying from 500 up to 7000 rpm were investigated with an interval of 50 rpm from each test. The displacements of two sections of the shaft were gathered for 30 revolutions at a frequency of 30 point per revolution. The behaviour of the damper with no field applied and with different values of the current through the coils (0.20 A, 0.40 A, 0.60 A and 1.00 A) were investigated. The calculated corresponding fields generated in the fluid were 0.055 T, 0.11 T, 0.165 T and 0.275 T respectively. The corresponding yield stress can be found from the relationship shown in figure 3.21. Figure 3.24 shows the amplitude of the revolution orbit when the empty damper is supplied with different current amplitudes.

The critical speed with no field applied is about 2000 rpm and it is in perfect accordance with the theoretical value, computed neglecting the stiffness of the rubber gaskets. That means the the stiffness of the membranes is small enough to be neglected.

Figure 3.24 shows also that the magnetic field does not modify the behaviour of the rotor-damper system. That is the magnetic force generated

Fluid	**Viscosity @ 40°C**
Hydraulic lubricant HF95Y Enerpac	0.025 Pa s
MR fluid MRF-132-LD Rheonetic	0.070 Pa s
MR fluid MRHCCS4 Liquids Research Limited	0.013 Pa s

Table 3.3: Viscosity of the fluid experimentally tested

by the coils on the journal of the squeeze film damper cannot reduce the amplitude of the orbits described by the rotor.

The squeeze film damper was then filled up with different fluids in order to choose the most suitable for the application. Two MR fluids were examined, that is the MRF-132-LD produced by Rheonetic and the MRHCCS4 produced by Liquids Research Limited. An extended description of their properties has been given in section 3.4. Besides those fluids, a hydraulic oil, the HF95Y produced by Enerpac, was tested in order to see the influence of the viscosity on the damper performance. Table 3.3 summarizes the viscosities of such fluids at a temperature of 40°C, i.e. a temperature close to the operating conditions. The comparison test was made with no magnetic field applied to the device. In fact the purpose of the test was to see the passive effect of the damper with the lowest viscosity that the fluid can provide. Higher viscosity can be obtained applying a magnetic field. Every fluid has been tested from 500 to 9000 rpm as shown in figure 3.25.

The MR fluid MRF-132-LD produced by Rheonetic increased the critical speed from 2000 rpm to 6500 rpm even with no applied magnetic field. This new critical speed is the critical speed of the system when the section of the damper is fully constrained. That means that the viscosity of the fluid is too high and the squeeze damper acts almost like a rigid bearing. The application of the magnetic field is useless because even if it can increase the viscosity of the damper it cannot shift the value of the critical speed any more. Thus the performance of such a smart MR squeeze film damper was very poor. The hydraulic oil Enerpac HF95Y showed a better behaviour but unfortunately it has no magneto-rheological properties.

If the damper gap is filled up with the Liquids Research Limited fluid MRHCCS4 the critical speed of the system with the empty damper is not shifted, even if the effect of the squeeze action is shown by the attenuation of the maximum radius of the orbit. The application of the magnetic field first decreases the peak and shift the resonance speed from 2000 rpm to 5500 rpm, and then it increases again the peak of the orbit amplitude while the fluid viscosity becomes greater and greater. Figure 3.26 shows the value of the

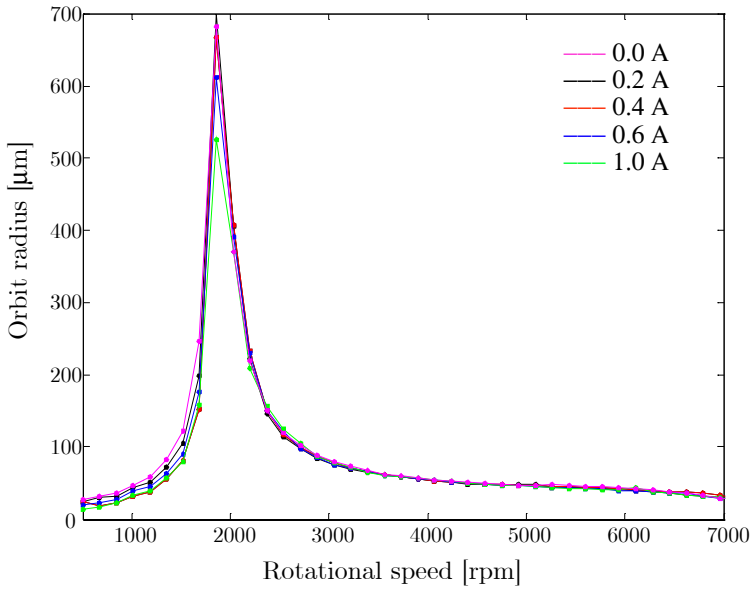

Figure 3.24: Experimental result of application of the magnetic field to the empty damper

radial displacement of the shaft versus the rotational speed when the Liquids Research Limited fluid is used and a current of 0.10 A, 0.15 A, 0.20 A, 0.30 A, 0.50 A, 1.00 A and 1.50 A is applied to the coil leads. The magnetic field inside the film gap increases the yield shear stress of the MR fluid and the stiffness of the damper grows up. With the increase of the magnetic field, the action of the damper is more and more comparable to a rigid constraint. The effect is a shift in the critical speed of about 3500 rpm.

The behaviour recorded during the test is almost the same predicted by the rotor-damper model based on the modified Reynolds equation and the Bingham model to describe the magneto-rheological effect. Compared to the numerical simulation the behaviour is similar to the expected one but there's a difference in the value of the effective damping and hence of the effective critical speed. That can have different explanations. The first is related to the problem encountered in filling completely the gap. Then there might be some vacuum zones that increase the value of the current needed to generate the field and the corresponding yield stress. Moreover, since during the motion the magnetic field in the device is not axial-symmetric, the magnetic field in the fluid and, consequently the yield stress, might vary significantly along the angular coordinate. Finally there might be some non linearities not taken into account in the analytical model.

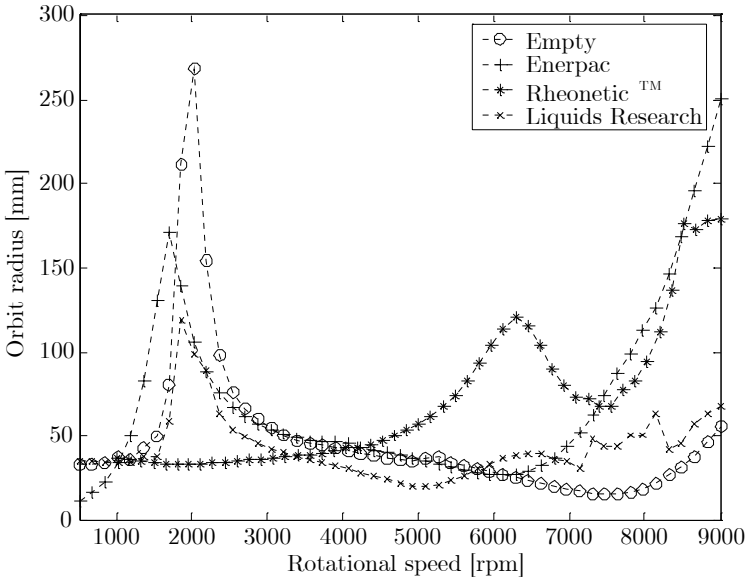

Figure 3.25: Comparison of different fluid performance used to fill the damper

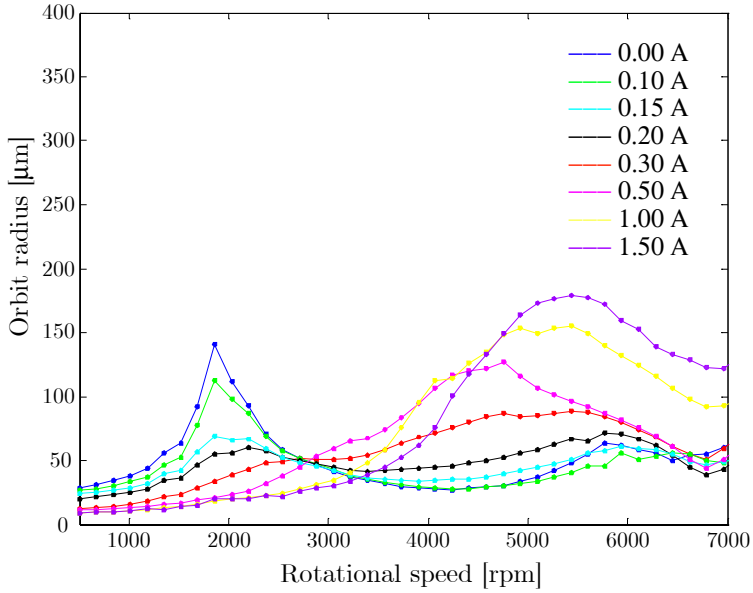

Figure 3.26: Performance of the squeeze film damper filled with the MR fluid by Liquids Research MRHCCS4

3.10 Design of the controller

3.10.1 A dynamic empirical model of the rotor-damper system

The aim of the study was then focused on the demonstration of the feasibility of a controller to automatically adapt the viscosity of the damper to the working condition of the rotor system. A simplified dynamic model was set up in order to perform a numerical analysis of the system and design a proper controller.

The squeeze film damper was modelled using 2-by-2 four coefficients stiffness and damping coefficient matrices. The relationship between the electric current running through the coils and the coefficients of the damping and stiffness matrices was supposed linear. Posing that the stiffness and damping matrices had the value K_{SFD} and C_{SFD} when the maximum current is supplied to the coils a pseudo-current parameter $\tilde{I}$ can be used to describe the fraction of current applied. When the pseudo-current is $\tilde{I} = 1$ then the current supplied to the coils is the maximum and the value of the stiffness and damping matrices of the damper are K_{SFD} and C_{SFD}. When the pseudo-current is $0 < \tilde{I} < 1$ then the value of the stiffness and damping matrices of the damper are $\tilde{I}K_{SFD}$ and $\tilde{I}C_{SFD}$. When the pseudo-current is $\tilde{I} = 0$ no current is supplied to the coils and the stiffness and damping matrices are zero matrices, but this is a non-real situation because the damper has a viscosity different from zero even if no magnetic field is applied to it. Then the value that the pseudo-current can take was limited to $0.2 < \tilde{I} < 1$.

The rotor was modelled as a flexible shaft supported at the ends and with a big mass in the middle and with the mass of the journal of the damper close to one support. The four degrees of freedom system is shown in figure 3.27. x_1 and y_1 are the central mass coordinates and x_2 and y_2 are the coordinates of the journal referred to a fixed system. The equilibrium equation system can be written as:

$$\begin{cases} m_1\ddot{x}_1 + k_{11}x_1 + k_{12}x_2 = F_{cx1} \\ m_1\ddot{y}_1 + k_{11}y_1 + k_{12}y_2 = F_{cy1} \\ m_2\ddot{x}_2 + k_{12}x_1 + k_{22}x_2 + k_{xx}x_2 + k_{xy}y_2 + c_{xx}\dot{x}_2 + c_{xy}\dot{y}_2 = F_{cx2} \\ m_2\ddot{y}_2 + k_{12}y_1 + k_{22}y_2 + k_{yx}x_2 + k_{yy}y_2 + c_{yx}\dot{x}_2 + c_{yy}\dot{y}_2 = F_{cy2} \end{cases} \tag{3.27}$$

where F_{cx1}, F_{cy1}, F_{cx2} and F_{cy2} are the components of the centrifugal forces applied to the central mass and to journal of the damper; c_{xx}, c_{xy}, c_{yx} and c_{yy} are the four damping coefficients of the damper and k_{xx}, k_{xy}, k_{yx} and k_{yy} are its four stiffness coefficients; m_1 is the mass of the central mass and m_2 is the mass of the damper journal. k_{11}, $k_{12} = k_{21}$ and k_{22} are the stiffness

Central mass	m_1	0.8 kg
Journal mass	m_2	0.2 kg
Unbalance mass	m_3	0.0015 kg
Unbalance distance from axis	δ	0.01 m
Shaft stiffness coefficients	k_{11}	656320 N/m
	k_{12}	-690340 N/m
	k_{22}	772740 N/m
Damper damping coefficients	c_{xx}^{max}	10000 Ns/m
	c_{xy}^{max}	500 Ns/m
	c_{yx}^{max}	500 Ns/m
	c_{yy}^{max}	10000 Ns/m
Damper stiffness coefficients	k_{xx}^{max}	1×10^6 N/m
	k_{xy}^{max}	-1000 N/m
	k_{yx}^{max}	1000 N/m
	k_{yy}^{max}	1×10^6 N/m

Table 3.4: Simulation parameters for dynamic model

coefficients of the shaft. The numerical values adopted in the simulations are shown in table 3.4.

Assuming that the journal of the damper is balanced and the mass m_1 has an unbalance m_3 placed at a distance $\delta = 0.01$ m from the rotor axis the centrifugal forces have the following values:

$$\begin{aligned} F_{cx1} &= m_3\delta\Omega^2\sin(\Omega t) \\ F_{cy1} &= m_3\delta\Omega^2\cos(\Omega t) \\ F_{cx2} &= 0 \\ F_{cy2} &= 0 \end{aligned} \tag{3.28}$$

where Ω is the rotational speed of the rotor.

The equation system 3.27 can be written in a matrix form:

$$\begin{bmatrix} m_1 & 0 & 0 & 0 \\ 0 & m_1 & 0 & 0 \\ 0 & 0 & m_2 & 0 \\ 0 & 0 & 0 & m_2 \end{bmatrix} \begin{Bmatrix} \ddot{x_1} \\ \ddot{y_1} \\ \ddot{x_2} \\ \ddot{y_2} \end{Bmatrix} + \begin{bmatrix} k_{11} & 0 & k_{12} & 0 \\ 0 & k_{11} & 0 & k_{12} \\ k_{12} & 0 & k_{22} & 0 \\ 0 & k_{12} & 0 & k_{22} \end{bmatrix} \begin{Bmatrix} x_1 \\ y_1 \\ x_2 \\ y_2 \end{Bmatrix} = \begin{Bmatrix} F_{cx1} \\ F_{cy1} \\ F_{SFDx2} \\ F_{SFDy2} \end{Bmatrix} \tag{3.29}$$

where the viscous and stiffness forces, F_{SFDx2} and F_{SFDy2}, are considered excitation forces that act on the journal damper mass:

$$\left\{ \begin{array}{c} F_{SFDx2} \\ F_{SFDy2} \end{array} \right\} = - \left[\begin{array}{cc} k_{xx} & k_{xy} \\ k_{yx} & k_{yy} \end{array} \right] \left\{ \begin{array}{c} x_2 \\ y_2 \end{array} \right\} - \left[\begin{array}{cc} c_{xx} & c_{xy} \\ c_{yx} & c_{yy} \end{array} \right] \left\{ \begin{array}{c} \dot{x}_2 \\ \dot{y}_2 \end{array} \right\} \tag{3.30}$$

From equation 3.29 it is possible to obtain the mass matrix, $[M]$, the damping matrix, $[C]$ and the stiffness matrix $[K]$ of the system. Posing the input vector $\underline{u} = \{F_{cx1}, F_{cy1}, F_{SFDx2}, F_{SFDy2}\}^{\mathrm{T}}$, the state vector $\underline{z} = \{x_1, y_1, x_2, y_2, \dot{x}_1, \dot{y}_1, \dot{x}_2, \dot{y}_2\}^{\mathrm{T}}$ and the output vector $\underline{y} = \underline{z}$ it is possible to write the same system in the state space as:

$$\begin{array}{rcl} \dot{\underline{z}} & = & \left(\begin{array}{cc} Z(4,4) & I(4,4) \\ -M^{-1}K & -M^{-1}C \end{array} \right) \underline{z} + \left[\begin{array}{c} Z(4,4) \\ M^{-1} \end{array} \right] \underline{u} \\ \underline{y} & = & \underline{z} \end{array} \tag{3.31}$$

where $Z(4,4)$ is a 4-by-4 matrix of zeros and $I(4,4)$ is a 4-by-4 identity matrix. The system was simply implemented in SIMULINK® and tested.

As a change in the pseudo-current causes a modification of the stiffness and damping coefficients of the damper and hence of the forces generated by the MR film (F_{SFDx2} and F_{SFDy2} in equation 3.30), it is possible to control the dynamic of the system using the smart squeeze film damper, in fact the forces F_{SFDx2} and F_{SFDy2} are components of the input vector of the system $\underline{u}$.

Figure 3.28 shows the amplitude of the radial displacement of the central mass of the system at different rotational speeds and values of the pseudo-current. The shift in the critical speed is evident, from about 2000 rpm to about 8500 rpm, where the latter value is the theoretical critical speed when the damper becomes a rigid support.

The comparison between figure 3.28 and figure 3.26 shows that the non-linearities, which exist in the real system, cause a smaller shift of the critical speed, from about 2000 rpm to about 5500 rpm. However the linear system model shows a good agreement with the real system for small values of the pseudo-current. In fact, it is clear that the behaviour of the real system is linear for currents below 0.3 A. When currents higher than 0.3 A are applied the curves are flatter than expected. The linear behaviour of the real system is well emulated by the numerical model for values of the pseudo-current up to 0.015. Thus in the range of pseudo-current from 0.002 to 0.015 the simulations have a good validity, whereas for larger values the validity should be checked with experimental tests. During the design of the controller the existence of two fields of validity was taken into account.

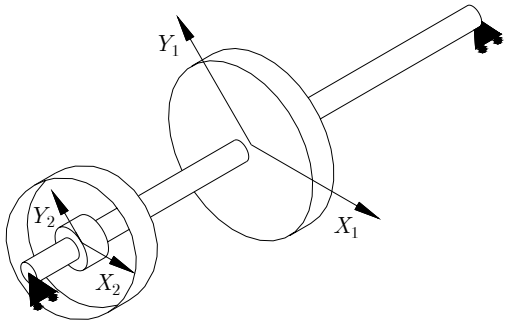

Figure 3.27: Rotor-damper model

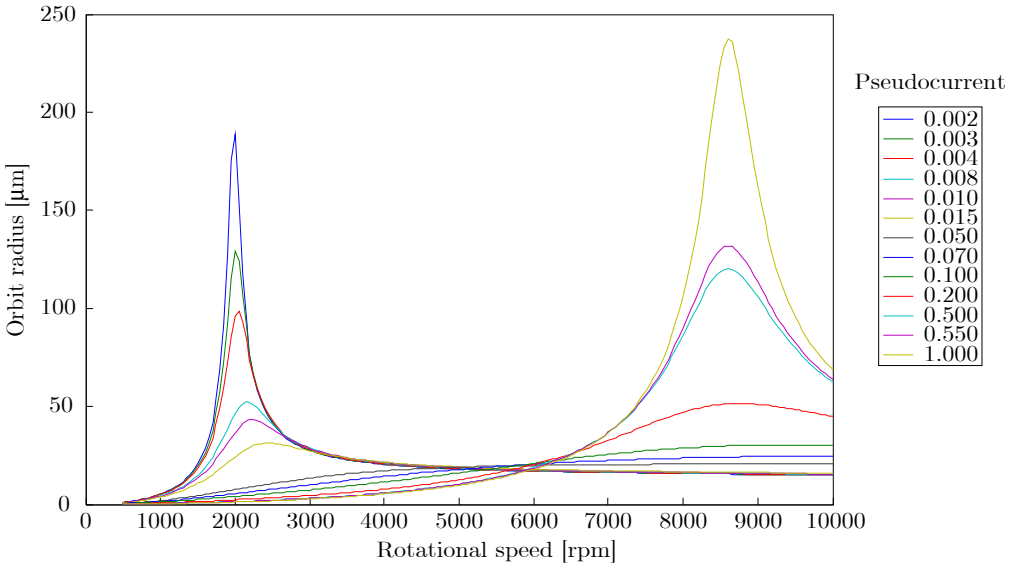

Figure 3.28: Performance of the rotor-damper dynamic model

3.10.2 An empirical fuzzy controller

The problem of designing an automatic controller for the MR squeeze film damper is a semi-active control problem. Semi-active control is a recently developed approach. Classical theory of active control cannot be applied to such problem. However, even if a global theory to face this problem is not yet available a lot of semi active control techniques have been proposed. For example sky-hook control, ground-hook control, continuous sky-hook control, continuous ground-hook control, clipping control, direct Lyapunov control and fuzzy logic control can be used to reduce the vibration of mechanical structure [48, 50, 66, 67] using semi-active control. Such techniques are based either on heuristic algorithms or properly modified classical ones. Moreover such techniques have been always applied to the control of non-rotating mechanical structures while no example of their application to the rotors can be found in the literature.

The control of rotors is very complicated because the equations of motion can be coupled making it difficult to predict the rotor-damper system dynamics and hence to design a control strategy. Fuzzy control is a practical alternative for a variety of challenging control applications since it provides a convenient method for constructing nonlinear controllers via the use of heuristic information [68]. Therefore it seemed the most suitable technique to design a controller and it was used to design the semi-active control of the MR squeeze-film damper subject of this work.

Heuristic information may come from an operator who has acted as a "human-in-the-loop" controller for a process. In the fuzzy control design methodology, this operator is asked to write down a set of rules on how to control the process, then these are incorporated into a fuzzy controller that emulates the decision-making process of the human. In other cases, the heuristic information may come from a control engineer who has performed extensive mathematical modeling, analysis, and development of control algorithms for a particular process [68]. Again, such expertise is loaded into the fuzzy controller to automate the reasoning processes and actions of the expert. Regardless of where the heuristic control knowledge comes from, fuzzy control provides a user-friendly formalism for representing and implementing the ideas we have about how to achieve high-performance control.

Some examples of the use of Fuzzy logic in the semi-active control of non-rotating mechanical structures can be found.

AL-Holou et al [69] used the fuzzy logic to develop a semi-active suspension system. The body-suspensions-wheels system was modeled as a two degree of freedom system. The fuzzy logic based model was developed for two inputs: the suspension velocity and the body velocity. The results showed

major improvement over passive suspension and minor improvement over the Sky-hook method.

Schurter and Roschke [70] described a new approach for reduction of environmentally induced vibration in constructed facilities by way of a neuro-fuzzy technique. The control technique has been tested on two types of building models. The energy of each building is dissipated through MR dampers whose damping properties are continously updated by a fuzzy controller. The semi-active control relied on development of a correlation between acceleration of the building and voltage applied to the MR damper. The fuzzy control was very effective on multiple degree of freedom structures.

Ting et al [71] designed a sliding mode fuzzy control strategy for the semi-active control of a quarter-car model of the active suspension system. Satisfactory performance were obtained under perturbed conditions.

The fuzzy controller has four main components [68]:

1. The "rule-base" holds the knowledge, in the form of a set of rules, of how best to control the system.

2. The inference mechanism evaluates which control rules are relevant at the current time and then decides what the input to the plant should be.

3. The fuzzification interface simply modifies the inputs so that they can be interpreted and compared to the rules in the rule-base.

4. The defuzzification interface converts the conclusions reached by the inference mechanism into the inputs to the plant.

Basically, the fuzzy logic controller (FLC) can be seen as an artificial decision maker that operates in a closed-loop system in real time. It gathers plant output data, compares it to the reference input, and then decides what the plant input should be to ensure that the performance objectives will be met.

Fuzzy control system design essentially amounts to choosing the fuzzy controller inputs and outputs, choosing the preprocessing that is needed for the controller inputs and possibly postprocessing that is needed for the outputs, and designing each of the four components of the fuzzy controller [68].

A fuzzy system is a static nonlinear mapping between its inputs and outputs. The inputs and outputs are "crisp", that is, they are real numbers, not fuzzy sets. The fuzzication block converts the crisp inputs to fuzzy sets, the inference mechanism uses the fuzzy rules in the rule-base to produce fuzzy conclusions, and the defuzzication block converts these fuzzy conclusions into the crisp outputs.

First, preprocessing the input means to quantify linguistic values using membership functions. A membership function is a curve that defines how each point in the input space is mapped to a membership value (or degree of membership) between 0 and 1 [72]. The input space is sometimes referred to as the universe of discourse.

Each fuzzy rule of the rule-base is made up by an *if* statement (antecedent) and a *then* statement (consequent). The interpretation of the if-then rules of the rule-base is considered by a three-part process [72]:

1. Fuzzify inputs: Resolve all fuzzy statements in the antecedent to a degree of membership between 0 and 1. If there is only one part to the antecedent, this is the degree of support for the rule.

2. Apply fuzzy operator to multiple part antecedents: If there are multiple parts to the antecedent, apply fuzzy logic operators and resolve the antecedent to a single number between 0 and 1. This is the degree of support for the rule.

3. Apply implication method: Use the degree of support for the entire rule to shape the output fuzzy set. The consequent of a fuzzy rule assigns an entire fuzzy set to the output. This fuzzy set is represented by a membership function that is chosen to indicate the qualities of the consequent. If the antecedent is only partially true, (i.e., is assigned a value less than 1), then the output fuzzy set is truncated according to the implication method.

Thus the output of each rule is a fuzzy set. The output fuzzy sets for each rule are then aggregated into a single output fuzzy set. Finally the resulting set is defuzzified, or resolved to a single number.

Fuzzy inference is the global process of formulating the mapping from a given input to an output using fuzzy logic. The mapping then provides a basis from which decisions can be made, or patterns discerned. There are two types of fuzzy inference systems that can be implemented in MATLAB® Fuzzy Logic Toolbox: Mamdani-type and Sugeno-type. These two types of inference systems vary somewhat in the way outputs are determined. Descriptions of these two types of fuzzy inference systems together with a more detailed explanation of the fuzzy logic procedures can be found in many bibliography references [68, 72].

People working in fuzzy control often say that a model is not needed to develop a fuzzy controller, and this is the main advantage of the approach, but for a safety-critical application, if you do not use a formal model, then it is not possible to perform mathematical analysis or simulation-based evaluations [68]. Basically, the role of modeling in fuzzy control design is quite

similar to its role in conventional control system design. In fuzzy control there is a more significant emphasis on the use of heuristics, but in many control approaches (e.g., PID control for process control) there is a similar emphasis. Basically, in fuzzy control there is a focus on the use of rules to represent how to control the plant rather than ordinary differential equations. This approach can offer some advantages in that the representation of knowledge in rules seems more lucid and natural.

Usually the fuzzy system is used to control non-linear systems difficult to be modelled. The rotor-damper system that has to be controlled is non-linear and classical control techniques cannot be applied. The non linear behaviour is accounted for by subordinating the change in the input vector to a change in the model itself. However, it can be linearized for small variations of the operating conditions. In fact a semi active system was designed, and, the capability of fuzzy logic to deal with heuristic rules makes it very suitable to design such a kind of controllers.

Moreover fuzzy logic has been chosen because it is tolerant of imprecise data and it can model nonlinear functions of arbitrary complexity. In fact fuzzy logic is a convenient way to map an input space to an output space and it is a very powerful tool for dealing quickly and efficiently with imprecision and nonlinearity.

As the Sugeno fuzzy inference process is computationally efficient and well-suited to mathematical analysis, it works well with optimization and adaptive techniques and it has guaranteed continuity of the output surface, it was chosen in order to build the damper FLC. Moreover this fuzzy inference model showed optimal performance in a lot of other different applications. The following options were chosen: the minimum option `min` for the "and method" (which truncates the output fuzzy set) and the weighted average option `wtaver` for the defuzzification process.

Three controller inputs were chosen: the radius of the orbit of the central mass, R_{k-1}, its rate of change, ΔR_{k-1}, and the variation of the pseudo-current, $\Delta\tilde{I}_{k-1}$. The only output of the controller is the rate of change of the pseudo-current, $\Delta\tilde{I}_k$, which is linearly correlated to the values of stiffness and damping coefficients of the squeeze film damper. The input are evaluated at the time step $k-1$ and sent to the controller that generates the output at the time step k. Figure 3.29 shows inputs and output of the FLC.

For the inputs R_{k-1} and $\Delta\tilde{I}_{k-1}$ the membership functions are characterized by four fuzzy set, that is negative (N), semi-negative (SN), semi-positive (SP) and positive (P). For the input R_{k-1} only two fuzzy set were used: small (S) and big (B). Figure 3.30 shows the input membership functions chosen for the inputs of one of the designed controllers. The output is characterized by four fuzzy set: negative (N), semi-negative (SN), semi-positive (SP) and

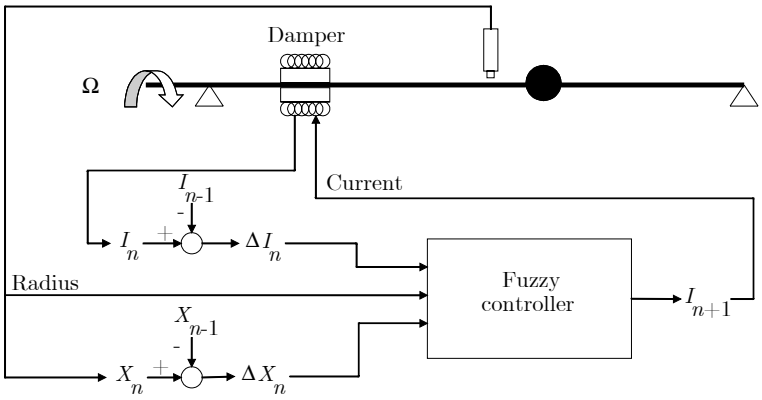

Figure 3.29: Scheme of the fuzzy control

R_k is S					
$\Delta\tilde{I}_k$		$\Delta\tilde{I}_{k-1}$			
		N	SN	SP	P
ΔR_{k-1}	N	N	P	P	P
	SN	SP	SP	SP	SN
	SP	SP	SP	SP	SN
	P	P	N	N	N

R_k is B					
$\Delta\tilde{I}_k$		$\Delta\tilde{I}_{k-1}$			
		N	SN	SP	P
ΔR_{k-1}	N	N	N	N	P
	SN	SN	N	N	SN
	SP	SP	N	N	SN
	P	P	N	N	N

Table 3.5: Heuristic rules of the fuzzy logic controller

positive (P). Constant membership functions were used at the values -0.005, -0.0025, +0.0025 and +0.005.

The rule-base was defined by the heuristic rules learnt during the experimental tests and the several numerical simulations. The rules are summarized in table 3.5. For instance a rule is *If* $\Delta\tilde{I}_{k-1}$ =*N and* ΔR_{k-1} =*N and* R_{k-1} =*S then* $\Delta\tilde{I}_k$ =*N* that means that if the current $\Delta\tilde{I}_{k-1}$ =N were increased and the radius were reduced ΔR_{k-1} =N then the current should be decreased again ($\Delta\tilde{I}_k$ =N) because the action of the controller was in the right direction. A discrimination between small and big radius was done in order to find when we are close to a resonance situation. It is also possibile to discriminate when the rotor is acting in the range of validity of the linear model.

The simulations of the designed FLC were carried out in SIMULINK® using the linearized state space model of the system already discussed. The evaluation of the rate of change of the pseudo-current and the radius were

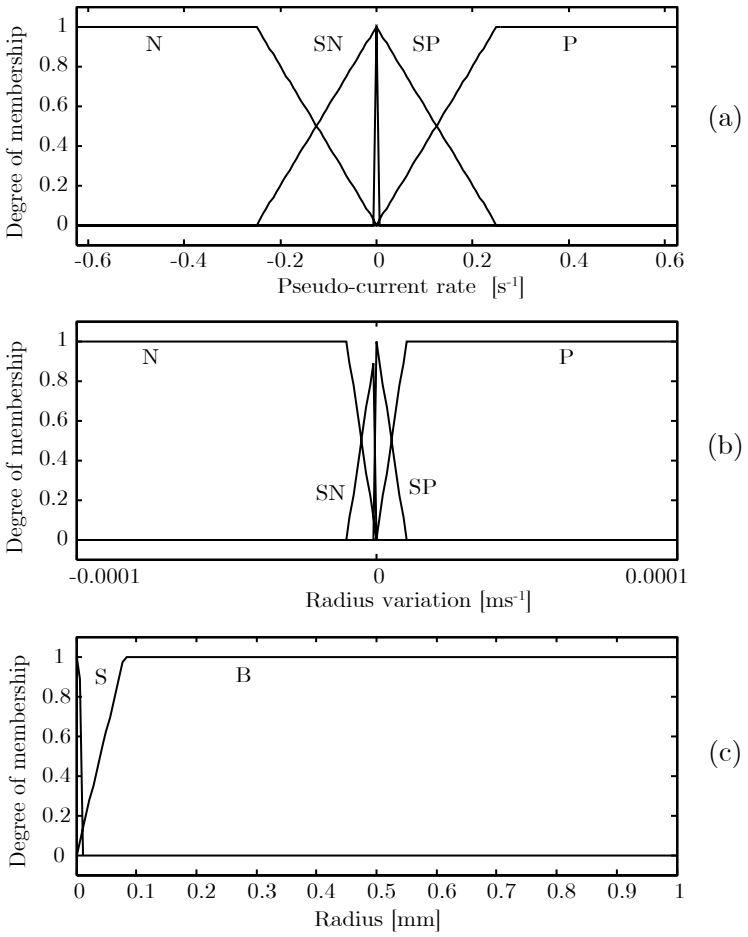

Figure 3.30: Input membership functions of the control 1: $\Delta\tilde{I}_{k-1}$ (a), ΔR_{k-1} (b) and R_{k-1} (c)

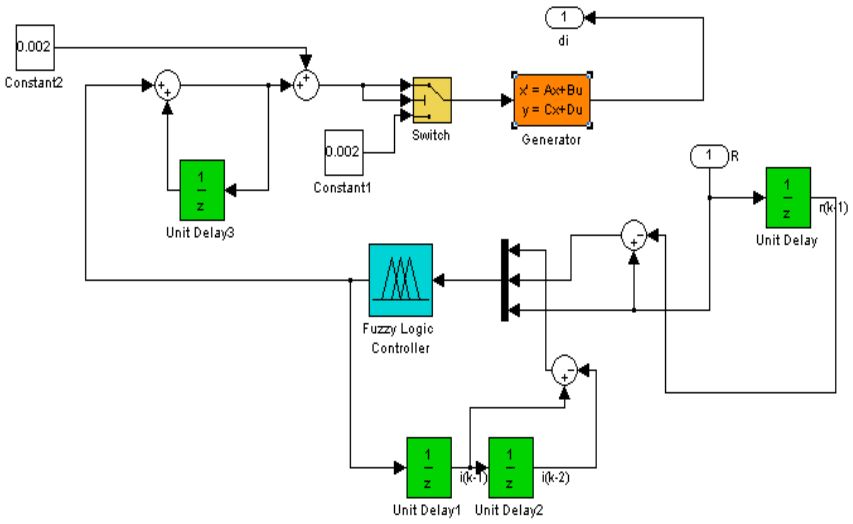

Figure 3.31: Sub-model of the fuzzy logic controller

made by means of the "unit delay" block (see equation 3.31). In the same figure the "switch" block was used to avoid the pseudo-current to decrease below 0.002, and the damper to take stiffness and damping unreal values. The "generator" block was build up in order to reconstruct the power supply dynamics. It takes into account the overshoot and the delay in the current supply.

The FLC is characterized by a huge number of parameters. For this reason the optimization of the FLC was reduced to the shape of the membership functions. In order to evaluate the performance of each tested controller a performance index E was designed as:

$$E = \int_0^{T_s} R \mathrm{d}t \tag{3.32}$$

where R is the radius of the central mass m_1, t is the time of the simulation and T_s is the final time of the simulation.

Each controller was tested during a run-up of the rotor of ten seconds, from 500 to 10000 rpm. During all the tests the same initial condition was used, $\underline{z} = \underline{0}$, because of the big computational time. Such controllers are not globally optimized but further tests can confirm their effectiveness in other situations.

The optimization process was performed manually. It was hard because of the huge number of parameters to take into account. Figure 3.32 shows

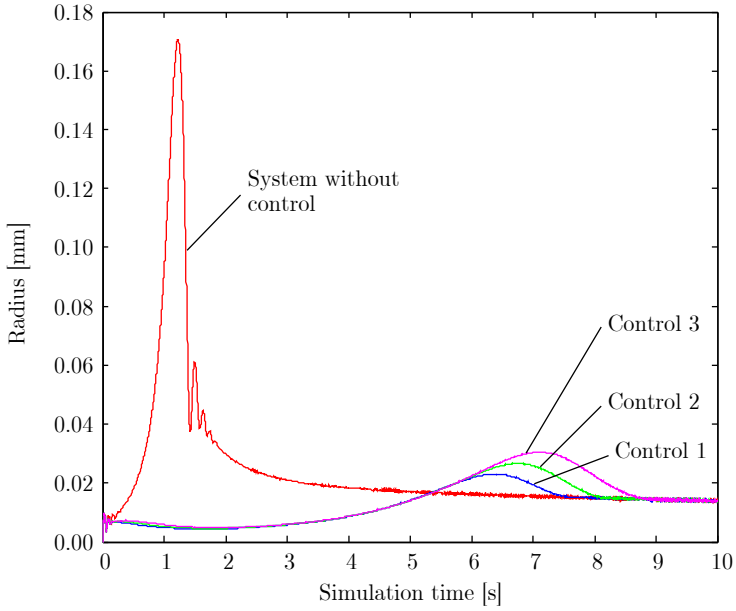

Figure 3.32: Performance of the fuzzy controller

the results of the simulation of three different controllers called for simplicity controller 1, 2 and 3, which resulted the best ones. In the same figure the response to the run-up of the rotor-damper system is shown. A peak reduction of about 82% was recorded.

The performance index (E) was 2.42×10^{-4} m s for the uncontrolled system, 1.1804×10^{-4} m s for controller 1, 1.2673×10^{-4} m s for controller 2 and 1.3841×10^{-4} m s for controller 3. Thus the use of such controller permitted to increase the performance of the system of about 50%.

Figure 3.33 shows the output (the pseudo-current) of the three controllers under examination. As the pseudo-current reaches values higher than 0.015, the controller works also outside the range of linear relationship between the real and the numerical model. Performing a manual optimization of the parameters it was not possible to keep the value of the pseudo-current under the threshold value of 0.015, so this goal was committed to an automatic automatization process described in the next section.

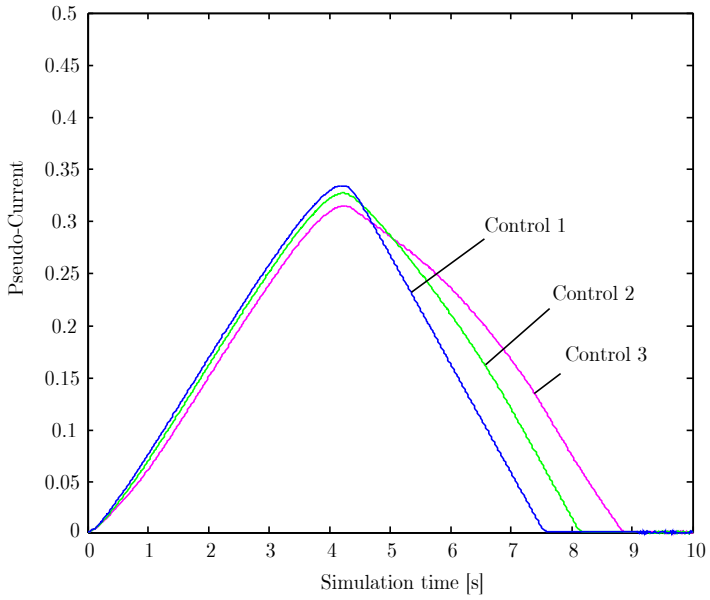

Figure 3.33: Pseudo-current led by the controller

3.10.3 A fuzzy controller designed by means of genetic algorithm

As a lot of difficulties were met trying to tune the parameters of the membership functions of he FLC inputs and outputs, an automatic algorithm for problem optimization and minimum search was used. Even if a lot of general purpose techniques are available, genetic algorithms (GAs) were chosen because of their good performances, flexibility and robustness.

GAs are adaptive methods which may be used to solve search and optimization problems. They are based on the genetic processes of biological organisms. Over many generations, natural populations evolve according to the principles of natural selection and survival of the fittest. By mimicking this process, genetic algorithms are able to "evolve" solutions to real world problems, if they have been suitably encoded [73].

GAs work with a population of "individuals", each representing a possible solution to a given problem. Each individual is assigned a "fitness score" according to how good a solution to the problem it is. The highly-fit individuals are given opportunities to "reproduce", by "cross breeding" with other individuals in the population. This produces new individuals as "offspring", which share some features taken from each "parent". The least fit members

of the population are less likely to get selected for reproduction, and so "die out". A whole new population of possible solutions is thus produced by selecting the best individuals from the current "generation", and mating them to produce a new set of individuals. This new generation contains a higher proportion of the characteristics possessed by the good members of the previous generation. In this way, over many generations, good characteristics are spread throughout the population. By favouring the mating of the more fit individuals, the most promising areas of the search space are explored and the population will converge to an optimal solution to the problem [73].

The power of GAs comes from the fact that the technique is robust, and can deal successfully with a wide range of problem areas, including those which are difficult for other methods to solve. GAs are not guaranteed to find the global optimum solution to a problem, but they are generally good at finding acceptably good solutions to problems acceptably quickly. Where specialised techniques exist for solving particular problems, they are likely to out-perform GAs in both speed and accuracy of the final result. The main ground for GAs, then, is in difficult areas where no such techniques exist. Even where existing techniques work well, improvements have been made by hybridising them with a GA [74].

Some example GA applications are numerical function optimisation, image processing, combinatorial optimisation, design optimisation and machine learning [74]. Moreover a major use of machine learning techniques has been in the field of control. In a large, complex system, such as a chemical plant, there may be many control parameters to be adjusted to keep the system running in an optimal way. The fitness of a set of rules may be assessed by judging their performance either on the real system itself, or on a computer model of it. GAs have been shown to be an effective strategy in the off-line design of control systems by a number of practitioners. They can be used both to establish the structure of the controller and to set the numerical values of the controller [75, 76].

Hashiyama et al [76] presented two new methods to generate fuzzy controllers through the GA. The first one focuses on finding appropriate fuzzy control rules without using expert knowledge. The other focuses on selecting adequate combinations of inputs variables, which are usually determined a priori by the designer of the controller in the conventional methods. They verified the effectiveness of the new approach in respect to fuzzy controllers for a semi-active suspension system.

Whilst there exist many good public-domain genetic algorithm packages none of these provide an environment that is immediately compatible with existing tools in the control domain. The MATLAB® Genetic Algorithm Toolbox [77] aims to make GAs accessible to the control engineer. This

allows the retention of existing modelling and simulation tools for building objective functions and allows the user to make direct comparisons between genetic methods and traditional procedures [78].

The Genetic Algorithm Toolbox for MATLAB® , developed at the Department of Automatic Control and Systems Engineering of the University of Sheffield, is freely available to download and has been utilized to carry out the automatic optimization of the controller.

Before a GA can be run, a suitable coding (or representation) of the problem must be devised. We also require a fitness function, which assigns a figure of merit to each coded solution. During the run, parents must be selected for reproduction, and recombined to generate offspring. It is assumed that a potential solution to a problem may be represented as a set of parameters (for example, the constants of a controller). These parameters (known as genes) are joined together to form a string of values (often referred to as a chromosome). For example, if our problem is to maximise a function of three variables we might represent each variable by a 10-bit binary number. Our chromosome would therefore contain three genes, and consist of 30 binary digits.

In genetics terms, the set of parameters represented by a particular chromosome is referred to as a genotype. The genotype contains the information required to construct an organism which is referred to as the phenotype. The same terms are used in GAs. The fitness of an individual depends on the performance of the phenotype. This can be inferred from the genotype, i.e. it can be computed from the chromosome, using the fitness function. A fitness function must be devised for each problem to be solved. Given a particular chromosome, the fitness function returns a single numerical "fitness," or "figure of merit," which is supposed to be proportional to the "utility" or "ability" of the individual which that chromosome represents.

During the reproductive phase of the GA, individuals are selected from the population and recombined, producing offspring which will comprise the next generation. Parents are selected randomly from the population using a scheme which favours the more fit individuals. Good individuals will probably be selected several times in a generation, poor ones may not be at all. Having selected two parents, their chromosomes are recombined, typically using the mechanisms of crossover and mutation. Crossover, in the most basic form, takes two individuals, and cuts their chromosome strings at some randomly chosen position, to produce two head segments, and two tail segments. The tail segments are then swapped over to produce two new full length chromosomes. This is known as single point crossover. Crossover is not usually applied to all pairs of individuals selected for mating. A random choice is made, where the likelihood of crossover being applied is typically

between 0.6 and 1.0 [74]. Mutation is applied to each child individually after crossover. It randomly alters each gene with a small probability (typically 0.001). Of course, crossover can also produce offspring of low fitness, but these will not be likely to get selected for reproduction in the next generation.

The population will evolve over successive generations so that the fitness of the best and the average individual in each generation increases towards the global optimum. Convergence is the progression towards increasing uniformity. A gene is said to have converged when 95% of the population share the same value [74]. The population is said to have converged when all of the genes have converged. As the population converges, the average fitness will approach that of the best individual.

The GAs were then applied to the FLC designed in the previous section in order to optimize the parameters of the membership functions of inputs and outputs. As the trapezoidal shape of the membership functions was not allowed to change, the parameters were just the positions of the corners of the trapezium. In order to exploit all the potentials GAs also the rule-base of the FLC has been optimized (see [76]). Thus each individual of the population was a FLC, whose genes were the corners of the membership functions and the rules of the FLC. Each controller had the same number of inputs and the same number of fuzzy sets. A binary codification was used in order to write the chromosome the individuals.

The first step in a genetic algorithm is to create an initial population consisting of random chromosomes (see function `crtbp` of the Genetic Algorithm Toolbox that produces a matrix containing random values in its elements in [78]). Each row of the chromosome matrix is an individual while each column is a gene of the chromosome. The value of each gene was randomly chosen inside a range of admissibility set by the user. The choice of such ranges it is very useful if the working conditions of the real system are known. The knowledge of the real system makes it possible to reject a priori unfit individuals, with unrealistic or disadvantageous chromosomes. The search of the minimum becomes faster, because the individuals that are unfit are not considered in the process. However if the user has not a deep knowledge of the system such ranges should be broader in order to avoid to exclude the fittest individuals from the search.

When the genotype of the first population is created, the function `bs2rv` can be used to decode the binary representation of the population into vectors of reals. The chromosomes are seen as concatenated binary strings of given length, and decoded into real numbers over a specified interval using standard binary coding. The resulting matrix contains the corresponding population phenotypes.

An objective function is used to provide a measure of how individuals have performed in the problem domain. In the case of a minimization problem, the fittest individuals will have the lowest numerical value of the associated objective function. This raw measure of fitness is usually only used as an intermediate stage in determining the relative performance of individuals in a GA. The fitness function is then normally used to transform the objective function value into a measure of the relative fitness. As the individuals of the population are controllers, the objective function should be a performance index [79]. Thus each individual (controller) was applied in SIMULINK® to the rotor-damper system to be controlled, and its performance evaluated.

The rotor-damper system is the same described in the previous section except that in the SIMULINK® model a "stop simulation" block was added in order to stop the simulation when the pseudo-current, driven by the controller, reaches the threshold value of linear correlation between the real system and its numerical model, i.e. $\tilde{I} = 0.015$. A run-up from 500 rpm to 10000 rpm in 10 s was applied to the rotor-damper system and the displacements of the central mass recorded in order to evaluate the performance of the controller. In order to extend the validity of the fitness function, each individuals was submitted to two tests. The first one with the system starting from the initial condition $\underline{z}(t=0) = \underline{z}_1 = \{0,0,0,0,0,0,0,0\}^{\mathrm{T}}$ while the second was started from the initial condition $\underline{z}(t=0) = \underline{z}_2 = \{0,0,0,0,0,0,0,0\}^{\mathrm{T}}$. For each test a performance index E^* was evaluated as:

$$E^* = \int_0^{t_{sim}} R(t)\mathrm{d}t + \rho \int_0^{t_{sim}} \tilde{I}\mathrm{d}t \tag{3.33}$$

where R is the radius of the central mass. Thanks to the weight coefficient, ρ, the performance index takes into account the activity of the controller, that is the energy used by the controller, besides the attenuation of the vibration. The use of such performance index permits to reduce both the amplitude of vibration and the energy of the controller, or at least to find a compromise between this two quantities.

From the performance index it is very simple to calculate the objective value of each individuals defining the fitness function as:

$$\mathcal{F} = \mathrm{e}^{\frac{1}{2}\left(\frac{E_1^*}{\hat{E}_1^*} + \frac{E_2^*}{\hat{E}_2^*}\right)} \tag{3.34}$$

where E_1^* and E_2^* are the performance indices when the initial conditions $\underline{z}_1$ and $\underline{z}_2$ are respectively considered and the controller is switched on; $\hat{E}_1^*$ and $\hat{E}_2^*$ are the performance indices of the rotor-damper system with the same initial condition but when the controller is switched off. Such a function

gives to each controller an objective value that is positive and larger than one. After evaluating the objective values of each individual the `ranking` function permits to rank individuals according to their objective values and returns a column vector containing the corresponding individual fitness values. This function ranks individuals for minimisation and gives the fitness value of two to the best individuals and zero to the worst.

After the ranking of the individuals the selection has to be performed. Selection is the process of determining the number of times a particular individual is chosen for reproduction and, thus, the number of offspring that an individual will produce. Firstly, the fitness values are transformed into a real-valued expectation of an individual's probability to reproduce and then the individuals are selected for reproduction based on the fitness of individuals relative to one another.

The stochastic universal sampling is the selection method that has been used. The probability of an individual being selected is then given by

$$\mathcal{F}(x_i) = \frac{f(x_i)}{\sum_{i=1}^{n} f(x_i)} \tag{3.35}$$

where $f(x_i)$ is the fitness of individual x_i, n is the population size and $\mathcal{F}(x_i)$ is the probability of that individual being selected. Whilst this fitness assignment ensures that each individual has a probability of reproducing according to its relative fitness, it fails to account for negative objective function values.

Finally a new population was produced by selection and recombination of individuals from the old population. Then to maintain the size of the original population, the new individuals have to be reinserted into the old population. The offspring is inserted into the current population by the function `reins` which replaces parents with offspring and returns the resulting population.

Because the GA is a stochastic search method, it is difficult to formally specify convergence criteria. As the fitness of a population may remain static for a number of generations before a superior individual is found, the application of conventional termination criteria becomes problematic. A common practice is to terminate the GA after a pre-specified number of generations and then test the quality of the best members of the population against the problem definition [78]. If no acceptable solutions are found, the GA may be restarted or a fresh search initiated. In this work, the GA is terminated after fifty generations and it is not repeated if there were no improvements in the last generations. Figure 3.34 shows the objective value of the best individual of each generation: the GA was terminated after fifty generations and the objective values do not show any significant improvement in the last fifteen generations.

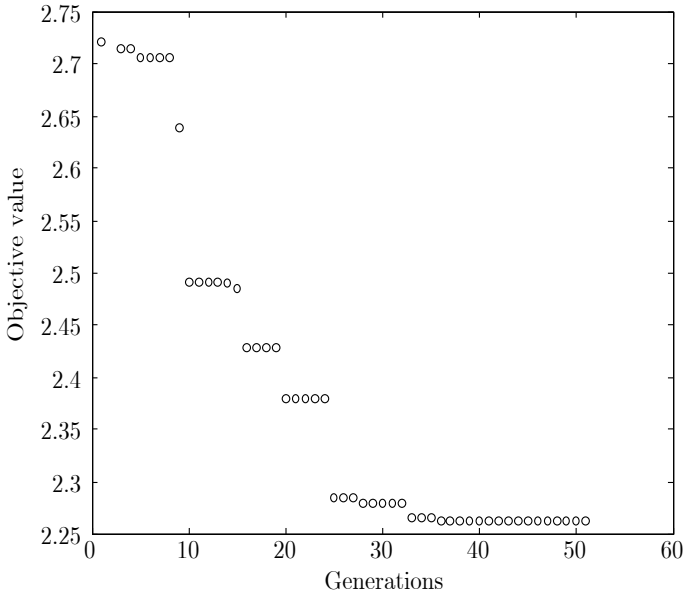

Figure 3.34: Objective value of the best individual of each generation

Several optimizations were performed but only the most significant results are shown. Such results are referred to three optimizations done with different performance indices. The first one uses the controller coefficient $\rho = 0$, that is the same used in the previous section, hence the results of such problem are comparable with the results of the heuristic optimization. The second and third optimization used a value of the controller coefficient of $\rho = 1$ and $\rho = 2$. The results of the three simulation are called "Genetic1", "Genetic2" and "Genetic3". Table 3.6 shows the rules of the controller Genetic1. In order to reduce the computational time the number of rules was reduced from 32 to 16. Figure 3.35 shows the membership function of such controller.

Figure 3.36 and figure 3.37 show the performance of the controller resulted from the GAs optimization when the rotor-damper system is subjected to a run-up excitation and it is starting from the initial state $\underline{z} = \underline{z}_1$. Figure 3.38 and figure 3.39 show the performance of the same controllers when the initial state is $\underline{z} = \underline{z}_2$.

The performance values of the first controller "Genetic1" are the following: $E_1^* = 1.9439 \times 10^{-4}$ m s and $E_2^* = 1.8375 \times 10^{-4}$ m s. It is evident that the performance index of the manually optimized controller was better, $E_1^* = 1.1804 \times 10^{-4}$ m s. Moreover the peak reduction was better (compare figure 3.32 to figure 3.36). In fact the manually optimized controller showed a

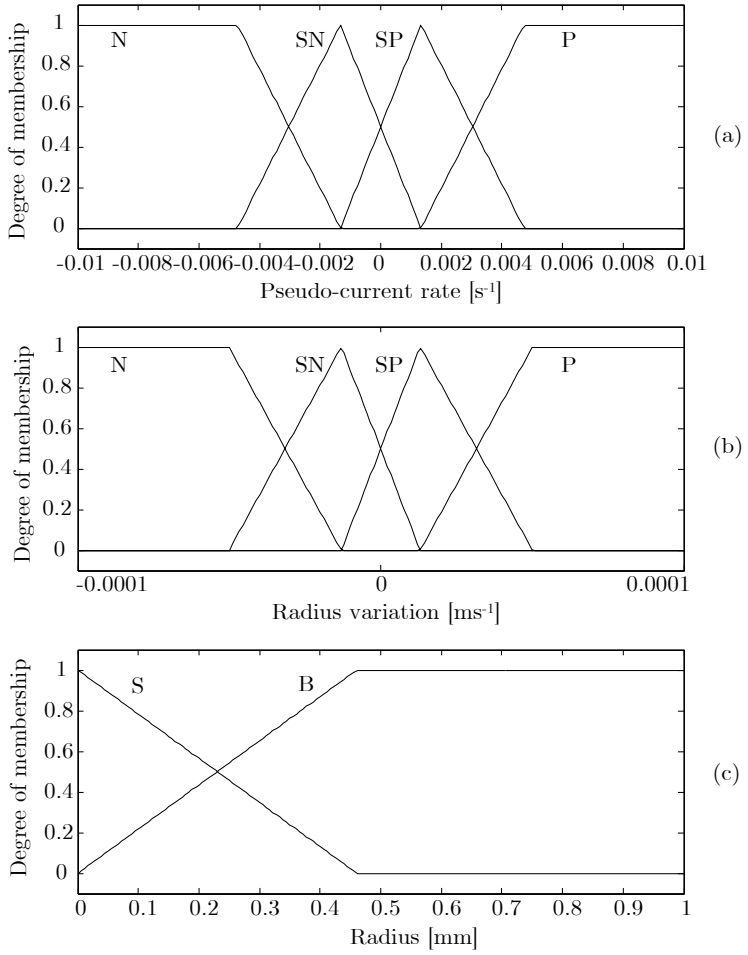

Figure 3.35: Input membership functions of the control genetic1: $\Delta\tilde{I}_{k-1}$ (a), ΔR_{k-1} (b) and R_{k-1} (c)

R_k is S					
$\Delta\tilde{I}_k$		$\Delta\tilde{I}_{k-1}$			
		N	SN	SP	P
ΔR_{k-1}	N				SN
	SN	N SP		N	
	SP	SP SN		P	
	P				

R_k is B					
$\Delta\tilde{I}_k$		$\Delta\tilde{I}_{k-1}$			
		N	SN	SP	P
ΔR_{k-1}	N		P		N SP
	SN		SN	SP	SN SP
	SP				SN
	P	SN			

Table 3.6: Rules of the fuzzy logic controller Genetic1

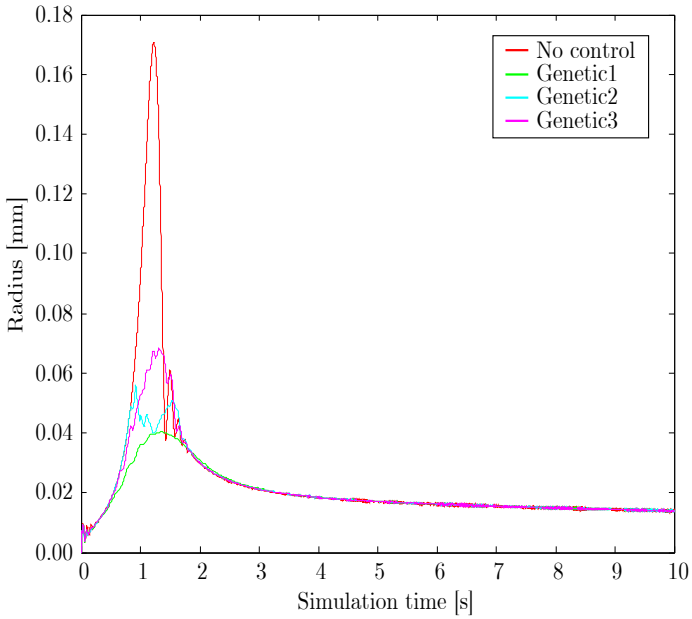

Figure 3.36: Performance of the controller during a run-up with zero initial conditions

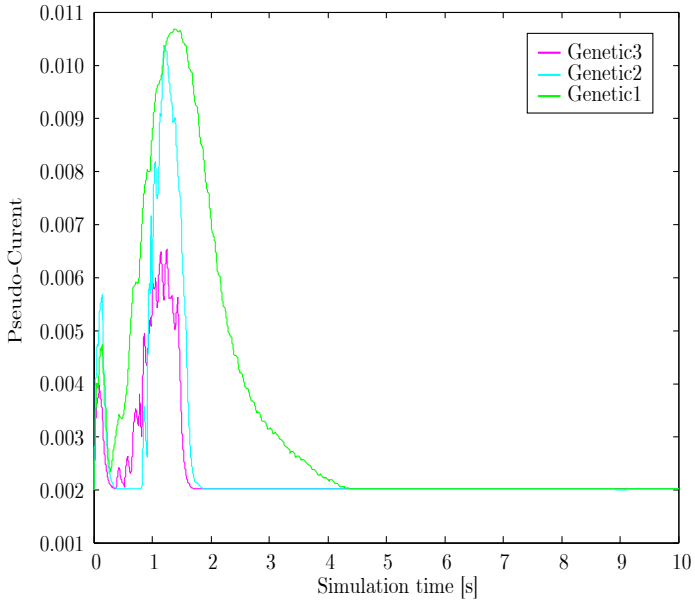

Figure 3.37: Pseudo-current led by the controller during a run-up with zero initial conditions

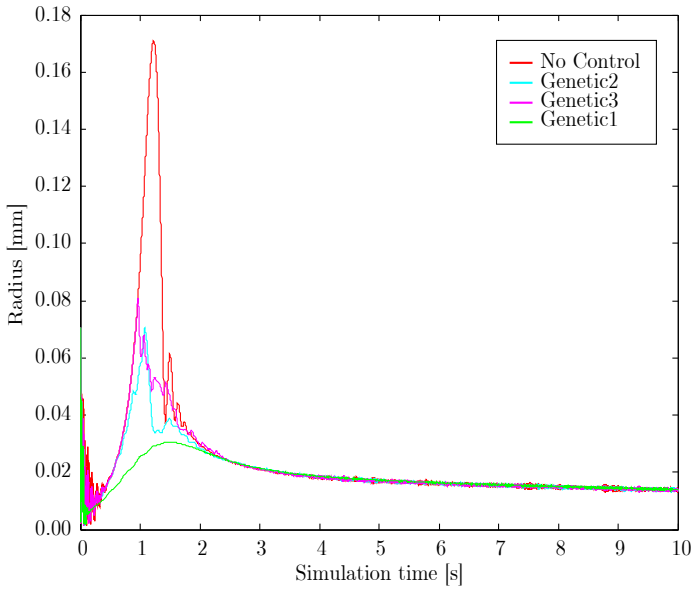

Figure 3.38: Performance of the controller during a run-up with non-zero initial conditions

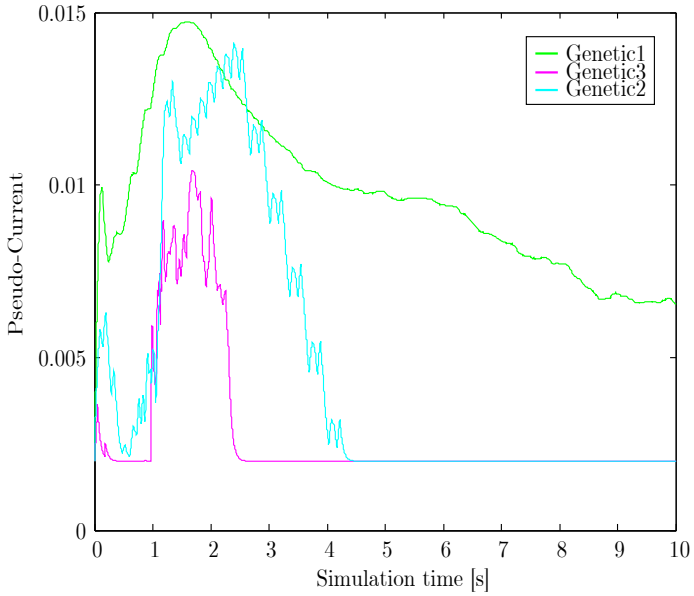

Figure 3.39: Pseudo-current led by the controller during a run-up with non-zero initial conditions

peak reduction of about 82% while the controller "Genetic1" showed a peak reduction of about 52%. Nonetheless the activity of the controller is very different. Even if the pseudo-current of the manually optimized controller has a more continuous shape it reached a peak value of 0.34. The pseudo-current generated by the "Genetic1" controller reached only 0.015, i.e. such a control consumes much more energy. Moreover, as such controller remained in the range of linear correlation between the numerical model and the real system, the results of its simulation are more reliable.

The controller "Genetic2" showed the performance indices $E_1^* = 2.0387 \times 10^{-4}$ m s and $E_2^* = 2.0064 \times 10^{-4}$ m s while the controller "Genetic3" showed $E_1^* = 2.1107 \times 10^{-4}$ m s and $E_2^* = 2.0112 \times 10^{-4}$ m s. Even if the performance indices of such controller seemed to worsen, the energy required by the damper decreased a bit more. The performance indices were also evaluated for the rotor-damper system with the controller switched off and the they were $\hat{E}_1^* = 2.4200 \times 10^{-4}$ m s and $\hat{E}_2^* = 2.4554 \times 10^{-4}$ m s.

All the controllers obtained by the GAs can reduce drastically the vibrations and use just a small amount of energy. During a run-up of the rotor from 500 rpm to 10000 rpm a peak reduction of at least 52% was recorded.

3.11 Conclusions

In this chapter a magneto-rheological fluid squeeze film damper has been presented. Firstly a numerical model of the damper has been set up. The magneto-rheological fluid has been modelled using the Bingham model, already used to describe the behaviour of greases. A modified Reynolds equation, for steady whirl motion of the journal of the bearing and Bingham fluid, has been utilized. The numerical simulations of the operating conditions on a quasi-static model of the rotor-damper system has given indication for the damper design.

The device has been built and utilized with the Rotor Kit of Bently Nevada. An extensive experimental investigation has been carried out in order to fully characterize the described device. The experimental results obtained with the developed device showed its effectiveness in dampening the rotor vibrations and controlling its dynamic characteristics by simply varying the current in the magnetic coils.

After the evaluation of the effectiveness of the magnetorheological squeeze film damper, a controller which can automatically tune the device has been designed. In order to have a numerical model useful for the design of the controller a new model of the rotor-damper system has been set-up. Thus a dynamic model that consider the linearized coefficients of the squeeze film damper has been used. The stiffness and damping coefficients of the damper were linearly related to the current that passes through the coils. A fuzzy logic controller has then designed using heuristic rules obtained from the numerical and experimental tests of the rotor-damper system carried out. The input of the controller were the amplitude of the orbit of the main rotating mass the rate of change of such quantity and the rate of change of the current applied to the coils of the damper. The output was the current supplied to the coils. Excellent results were obtained. During a run-up of the rotor there was a peak reduction of about 82%.

Very good results have been obtained by a manual optimization but the controller acted also beyond the linear boundaries of the model. Moreover, the optimization was very problematic and only expert users can design such controllers. Thus a search of the optimal membership function and rules of the controller has been automatically carried out using genetic algorithms. The new controllers showed a smaller performance (the peak reduction was about 52%) but they operated inside the linear model boundaries. Moreover these controllers consumed less energy than the previous one. They are also robust to change in the initial state.

The squeeze film damper appears to be a promising application of MR fluids to cope with changes of operation or transients since its more com-

plicated design is fully justified by the increase in performance and safety. As the magnetic field can be generated with relatively low voltages, such a device seems to have more potential for use in aero engines and other safety conscious industries. There do not appear to be fundamental theoretical difficulties, although many problems are unresolved such as cavitation, two-dimensional effects, etc.

Chapter 4

Investigation on the dynamic behaviour of disc blades during sharpening

4.1 Introduction

Vibrations arising during the sharpening process of disk blades are a crucial problem in paper manufacturing. In particular, since paper rolls are cut using disk blades, defects in the blade edge caused by vibrations, though small, can cause remarkable quality and productivity losses. Common practice has shown that in some cases the disk edge exhibits a thickness periodic irregularity caused by such vibrations. In the technical literature no specific work is reported but similar problems such as those related to grinding [7, 8], saw blades, turbine rotors, computer magnetic recording disks [9, 10, 11, 12] and brake disks [13, 14] are dealt with. The problems mainly concern the response of a rotating disk to an external transverse force.

Early work on the vibration of spinning elastic disks dealt with the determination of the natural frequencies and the effect of centrifugal stresses. In general, disk/spindle vibrations have both in-plane and out-of-plane components. The out-of-plane ones primarily result from the deflection of the spinning disks and can be predicted accurately by the classical vibration analysis of rotating disks.

Tobias and Arnold [80] made a significant contribution to the study of the response of a rotating disk to a stationary force. They presented a formulation of the modal response with damping, and put emphasis on the resonance to a static stationary force.

Mote [81] formulated the Green function for the transverse response of

a uniform, stationary, centrally clamped annular plate and determined the specific response for a harmonic load moving at constant velocity about the plate periphery and for a peripheral load circumnavigating the plate at a speed which is the sum of a constant and a harmonic component. Circular plates containing radially symmetric membrane stresses and thickness were also considered. He introduced a modern formulation of the undamped response of a disk to a moving force as an eigenfunction series on the basis of classical plate theory.

Iwan and Moeller [82] used the Galerkin method to study the stability of a spinning disk subjected to a spring-mass-dashpot load. Their analysis revealed that the disk system was unstable in a range speed above the critical speeds. When a load system is included, instabilities can occur at speeds other than the classical critical speeds of the disk. It has been shown that a combination of a mass, stiffness and damping in the load system gives rise to several regions of instability not directly related to the classical critical vibration speed of the disk.

Honda et al [83] presented a theoretical analysis of the steady state response of a stationary disk subjected to a concentrated harmonic force moving in a concentric circular path at a constant velocity. They neglected the effects that rotation has on the elastic properties of the disk and derived a formulation of the response with structural damping as an eigenfunction series. They discussed the modal response in detail, with emphasis on the vibratory modes. They also discussed the effect of imperfection in the axial symmetry. They found that the imperfection produces a much greater effect on the response near the resonance, but little effect on it off the resonance, and that standing wave and both moving with the force and fixed on the disk can be formed.

More recently, the dynamic behaviour of spinning disks in the storage system of modern computers has been studied. The most difficult problem encountered in the flexible disk drive is the interaction between the spinning disk and the recording head. Many researchers have formulated this problem according to different approaches. Huang and Chiou [11] considered also the radial motion of the head and determined the spinning disk response with a radially moving, harmonic excitation.

Two instability mechanism have been identified in a rotating disk problem [84]. It is well established that a rotating disk, when viewed with respect to an inertial frame, displays a response that admits a separation into a forward travelling wave motion and a backward travelling wave motion. With increasing disk rotational speed the frequency associated with the backward travelling wave approaches zero. The disk rotational speed at which this happens is identified as a critical speed, associated with a divergence instability

lead by a transverse load applied to the rotating disk. The other type of instability is a flutter instability which occurs on account of the coalescence of two vibratory modes.

Moreover, interface friction couples longitudinal and transversal degrees of freedom and makes the system potentially unstable [14]. The motion may not be continuous, but intermittent and proceed by a process of stick-slip. Stick-slip concerns low velocities and is due to the transition from static to dynamic friction in a range where the friction coefficient decreases with velocity. When damping is insufficient, unstable vibrations occur at the natural frequency of the damped system. Ouyang and others [85] studied the in-plane stick-slip vibration of a flexible disk rotating between elastic sliders, by means of a complex mathematical model. In any case there isn't yet a unique general theory for the occurrence of friction vibrations which are still unpredictable because the dependency of friction on velocity varies randomly with contamination, surface finish, misalignment of sliding surfaces and other factors.

Another cause of instability, when the disk is interfaced to a mechanical system by means of friction, is ascribed to self-excitation due to the coupling of two eigenvalues related to the natural modes of the contacting parts [86]. Such instability phenomenon is usually called lock-in instability.

In the work presented in this chapter the disk blade sharpening process is examined numerically and experimentally. After a short review of rotating disk dynamics, an experimental investigation carried out on a commercial paper roll cutting machine is presented, highlighting the problems concerning the sharpening of a disk blade. However, the on-situ investigation was not sufficient to single out the parameters which cause the onset of self-excited vibration during the sharpening process. Thus, a test rig to study the vibrations arising in the sharpening process of disc blades was designed and set up. Preliminary analytical work was carried out to support the analysis of the experimental results including modal analyses on the finite element method (fem) models of the test rig components, an analysis of lock-in instability on a simplified model and an analytical investigation by means of the explicit finite element code LS-DYNA® .

4.2 Dynamics of rotating disks

4.2.1 General considerations

The contact between the abrasive wheel and the rotating disk cannot be easily referred to a standard excitation problem. In fact the force that acts

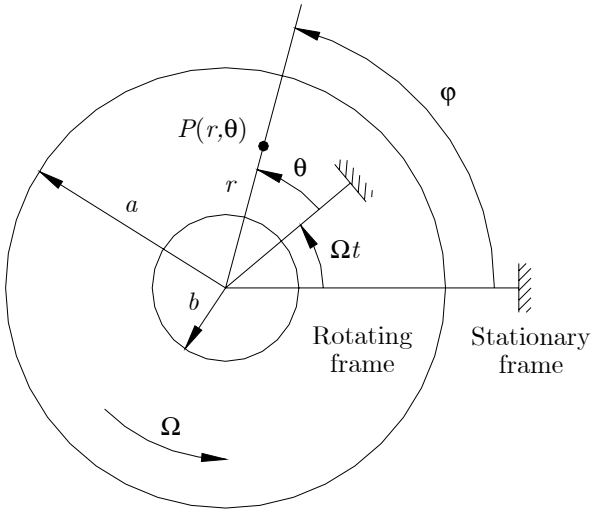

Figure 4.1: The configuration of the rotating disk

on the disk, or on the grinding wheel, is neither constant nor harmonic. This is the reason why a detailed research was carried out. However, a clear understanding of the response of rotating disks to harmonic excitation is essential in the investigation of the vibrations that arise from the sharpening process of disk blades, and in the evaluation of the obtained results. Although many researchers have explored the response of rotating disks [80, 81, 83, 87], a comprehensive theory of the forced response of rotating disks has not been presented. This section tries to draw a short review of the dynamics of stationary and rotating disks.

A disk which is truly axisymmetric and has a uniform constant thickness radial cross section (h) is considered. It is a relatively simple matter to extrapolate from the characteristics of these simple disk vibrations those of more complex engineering disk-like structures. Consequently, it is worthwhile to describe the vibration properties of such a disk in some detail.

Figure 4.1 shows the schematic diagram of the disk with inner radius $r = b$ and outer radius $r = a$, rotating at velocity Ω. Figure 4.1 shows also the co-ordinate systems: a co-ordinate system fixed to the disk, (r, θ), and a stationary co-ordinate system, (r, φ). In the future investigations small transverse deflections are assumed and, the rotary inertia and shear deformation effects are neglected. In addition, the centrifugal effects due to rotation are dropped out for simplicity .

4.2.2 Free vibration of a stationary disk

The study of the natural frequencies of a transversely vibrating plate is a classical problem. Moreover, the computation of the resonant frequencies of an annular disc clamped at its inner edge and free at its outer edge was tackled by several authors. The computation process shown in this section was derived from the work of few of them [88, 89].

For circular plates the exact solution is available, even if in a series solution form. The theory underlying this analysis neglects the effects of rotary inertia and of the additional deflection caused by shear forces. The equation of motion for free vibration in the out-of-plane direction is

$$D\nabla^4 w + \rho h \frac{\partial^2 w}{\partial t^2} = 0 \tag{4.1}$$

where ρ is the density of the disc material, h the thickness and w the out of plane displacement. D is the bending stiffness given by

$$D = \frac{Eh^3}{12(1-\nu^2)} \tag{4.2}$$

where E and ν are respectively the Young's modulus and Poisson's ratio of the disk material. In a cylindrical coordinate system the differential operator ∇ is given by

$$\nabla^2(\cdot) = \frac{\partial^2(\cdot)}{\partial r^2} + \frac{1}{r}\frac{\partial(\cdot)}{\partial r} + \frac{1}{r^2}\frac{\partial^2(\cdot)}{\partial \theta^2} \tag{4.3}$$

where r is the radial coordinate and θ the circumferential coordinate.

Recognizing that at a natural frequency every point in the elastic system moves harmonically, it can be assumed that

$$w(r,\theta,t) = Z(r,\theta)\mathrm{e}^{\mathrm{i}\omega t} \tag{4.4}$$

where ω is the natural frequency of the natural mode Z. Substituting equation 4.4 in equation 4.1 gives

$$D\nabla^4 Z - \rho h\omega^2 Z = 0 \tag{4.5}$$

that is the mode shape equation, in fact it is not time dependent.

Let

$$\lambda^4 = \frac{\rho h\omega^2}{D} \tag{4.6}$$

Equation 4.5 can then be written

$$\nabla^4 Z - \lambda^4 Z = 0 \tag{4.7}$$

The next step is to try the separation of variables

$$Z(r,\theta) = R(r)\Theta(\theta) \tag{4.8}$$

If this is possible, a set of ordinary differential equations results. Solutions of these equations have unknown coefficients. Substitution of these solutions into the separated boundary conditions will give a homogeneous set of equations. The determinant of these equations will furnish the so-called characteristic equation. The roots of this equation will give the natural frequencies.

Substituting equation 4.8 in equation 4.7 gives

$$r^2\left[\left(\frac{\mathrm{d}^2R}{\mathrm{d}r^2}+\frac{1}{r}\frac{\mathrm{d}R}{\mathrm{d}r}\right)\frac{1}{R}\pm\lambda^2\right] = -\frac{1}{\Theta}\frac{\mathrm{d}^2\Theta}{\mathrm{d}\theta^2} \tag{4.9}$$

This equation can only be satisfied if each expression is equal to the same constant n^2. This allows one to write

$$\frac{\mathrm{d}^2\Theta}{\mathrm{d}\theta^2}+n^2\Theta = 0 \tag{4.10}$$

and

$$\frac{\mathrm{d}^2R}{\mathrm{d}r^2}+\frac{1}{r}\frac{\mathrm{d}R}{\mathrm{d}r}+\left(\pm\lambda^2-\frac{n^2}{r^2}\right)R = 0 \tag{4.11}$$

The solution of equation 4.10 is

$$\Theta(\theta) = A_n\cos(n\theta)+B_n\sin(n\theta) \tag{4.12}$$

where A_n and B_n are the coefficients of the solution that must be defined from boundary conditions. In general n can be a fractional number. But for circular plates Θ must be a function of the period, 2π. In this case n becomes an integer:

$$n = 0, 1, 2, \ldots \tag{4.13}$$

Θ is the circumferential solution of mode shapes and the constant n is then the number of nodal diameters.

The radial solution can now be considered. Let introduce a new variable

$$\xi = \begin{cases} \lambda r & \text{for} + \lambda^2 \\ \mathrm{i}\lambda r & \text{for} - \lambda^2 \end{cases} \tag{4.14}$$

Equation 4.11 becomes

$$\frac{\mathrm{d}^2R}{\mathrm{d}\xi^2}+\frac{1}{\xi}\frac{\mathrm{d}R}{\mathrm{d}\xi}+\left(1-\frac{n^2}{\xi^2}\right)R = 0 \tag{4.15}$$

This is Bessel's equation of fractional order. The solution are in the form of series. They are classified in terms of Bessel functions [90, 91]. For $\xi = \lambda r$, the solution is in terms of the Bessel function of the first and second kind, $J_n(\lambda r)$ and $Y_n(\lambda r)$. For $\xi = \mathrm{i}\lambda r$, the solution is in terms of the modified Bessel function of the first and second kind, $I_n(\lambda r)$ and $K_n(\lambda r)$.

For the special category of circular plates n is an integer and the solution $R(r)$ is therefore

$$R(r) = C_n J_n(\lambda r) + D_n I_n(\lambda r) + E_n Y_n(\lambda r) + F_n K_n(\lambda r) \tag{4.16}$$

In order to find the characteristic equation and hence the natural frequencies, boundary conditions must be written. Boundary conditions are not time dependent but they depend only on the mode shapes.

For the clamped edge, $r = b$, the displacement and the rotations are zero

$$R(b) = 0 \tag{4.17}$$

$$\left.\frac{\mathrm{d}R}{\mathrm{d}r}\right|_{r=b} = 0 \tag{4.18}$$

For the free edge, $r = a$, the momentum and the shear are zero

$$\nabla^2 Z - (1-\nu)\left(\frac{1}{r}\frac{\partial Z}{\partial r} + \frac{1}{r^2}\frac{\partial^2 Z}{\partial \theta^2}\right) = 0 \tag{4.19}$$

$$\frac{\partial}{\partial r}\nabla^2 Z + \frac{1-\nu}{r^2}\frac{\partial}{\partial \theta}\left(\frac{\partial^2 Z}{\partial r \partial \theta} - \frac{1}{r}\frac{\partial Z}{\partial \theta}\right) = 0 \tag{4.20}$$

Remembering equation 4.8 the previous boundary condition can be written

$$\frac{\mathrm{d}^2 R}{\mathrm{d}r^2} + \nu\left(\frac{1}{r}\frac{\mathrm{d}R}{\mathrm{d}r} - \frac{n^2}{r^2}R\right) = 0 \tag{4.21}$$

$$\frac{\mathrm{d}^3 R}{\mathrm{d}r^3} + \frac{1}{r}\frac{\mathrm{d}^2 R}{\mathrm{d}r^2} + [(\nu-2)n^2 - 1]\frac{1}{r^2}\frac{\mathrm{d}R}{\mathrm{d}r} + (3-\nu)n^2\frac{R}{r^3} = 0 \tag{4.22}$$

The frequency equation is determined by substituting equation 4.8, with R as given by equation 4.16 and Θ given by equation 4.12, in the boundary conditions. An homogeneous system of four equations with four unknown quantities is obtained. The unknown quantities are the four constants of the solution of equation 4.16, C_n, D_n, E_n and F_n. The simple zero solution must be rejected. The solutions can be found by posing the determinant of the matrix of the coefficients of the system equal to zero. The coefficients of the circumferential solution Θ, A_n and B_n can be found later from initial conditions.

The homogeneous system can be written

$$\begin{bmatrix} b_{11} & b_{12} & b_{13} & b_{14} \\ b_{21} & b_{22} & b_{23} & b_{24} \\ b_{31} & b_{32} & b_{33} & b_{34} \\ b_{41} & b_{42} & b_{43} & b_{44} \end{bmatrix} \begin{Bmatrix} C_n \\ D_n \\ E_n \\ F_n \end{Bmatrix} = \begin{Bmatrix} 0 \\ 0 \\ 0 \\ 0 \end{Bmatrix} \tag{4.23}$$

where

$$b_{11} = J_n(\lambda b) \tag{4.24}$$
$$b_{12} = I_n(\lambda b) \tag{4.25}$$
$$b_{13} = Y_n(\lambda b) \tag{4.26}$$
$$b_{14} = K_n(\lambda b) \tag{4.27}$$
$$b_{21} = \frac{n}{\lambda b} J_n(\lambda b) - J_{n+1}(\lambda b) \tag{4.28}$$
$$b_{22} = \frac{n}{\lambda b} I_n(\lambda b) + I_{n+1}(\lambda b) \tag{4.29}$$
$$b_{23} = \frac{n}{\lambda b} Y_n(\lambda b) - Y_{n+1}(\lambda b) \tag{4.30}$$
$$b_{24} = \frac{n}{\lambda b} K_n(\lambda b) - K_{n+1}(\lambda b) \tag{4.31}$$
$$b_{31} = +\frac{\nu^*}{\lambda a} J_{n+1}(\lambda a) + \left[-1 + (\nu^*) \frac{n^2 - n}{\lambda^2 a^2} \right] J_n(\lambda a) \tag{4.32}$$
$$b_{32} = -\frac{\nu^*}{\lambda a} I_{n+1}(\lambda a) + \left[+1 + (\nu^*) \frac{n^2 - n}{\lambda^2 a^2} \right] I_n(\lambda a) \tag{4.33}$$
$$b_{33} = +\frac{\nu^*}{\lambda a} Y_{n+1}(\lambda a) + \left[-1 + (\nu^*) \frac{n^2 - n}{\lambda^2 a^2} \right] Y_n(\lambda a) \tag{4.34}$$
$$b_{34} = +\frac{\nu^*}{\lambda a} K_{n+1}(\lambda a) + \left[+1 + (\nu^*) \frac{n^2 - n}{\lambda^2 a^2} \right] K_n(\lambda a) \tag{4.35}$$
$$b_{41} = \left[-\frac{n}{\lambda a} - \frac{\nu^* n^2 (n-1)}{\lambda^3 a^3} \right] J_n(\lambda a) + \left[+1 + \frac{\nu^* n^2}{\lambda^2 a^2} \right] J_{n+1}(\lambda a) \tag{4.36}$$
$$b_{42} = \left[+\frac{n}{\lambda a} - \frac{\nu^* n^2 (n-1)}{\lambda^3 a^3} \right] I_n(\lambda a) + \left[+1 - \frac{\nu^* n^2}{\lambda^2 a^2} \right] I_{n+1}(\lambda a) \tag{4.37}$$
$$b_{43} = \left[-\frac{n}{\lambda a} - \frac{\nu^* n^2 (n-1)}{\lambda^3 a^3} \right] Y_n(\lambda a) + \left[+1 + \frac{\nu^* n^2}{\lambda^2 a^2} \right] Y_{n+1}(\lambda a) \tag{4.38}$$
$$b_{44} = \left[+\frac{n}{\lambda a} - \frac{\nu^* n^2 (n-1)}{\lambda^3 a^3} \right] K_n(\lambda a) + \left[-1 + \frac{\nu^* n^2}{\lambda^2 a^2} \right] K_{n+1}(\lambda a) \tag{4.39}$$

and

$$\nu^* = 1 - \nu \tag{4.40}$$

Posing the determinant of the matrix of coefficient, $[b_{ij}]$, equal to zero an equation in the unknown quantity λ is obtained. Such equation has infinite solutions. For a given $n = 0, 1, 2, \ldots$ that represents the number of nodal diameters (see equation 4.12), infinite solutions of the equation can be found. Each solution can be numbered by the subscript $m = 0, 1, 2, \ldots$ that represents the number of nodal circumferences.

A MATLAB® program has been written in order to find the solution λ_{nm} of the problem and then the natural frequencies of the disk from equation 4.6. The subscripts n and m are then added to modes and natural frequencies

$$\omega_{nm} = \sqrt{\frac{\lambda_{nm}^4 D}{\rho h}} \tag{4.41}$$

In order to find the mode shapes, the value of λ_{nm} must be substituted in equation 4.23. Only three equations are independent, so setting $C_n = 1$ the solution of the three coefficients can be found:

$$\begin{Bmatrix} D_n \\ E_n \\ F_n \end{Bmatrix} = \begin{bmatrix} b_{22} & b_{23} & b_{24} \\ b_{32} & b_{33} & b_{34} \\ b_{42} & b_{43} & b_{44} \end{bmatrix}^{-1} \begin{Bmatrix} -b_{21} \\ -b_{31} \\ -b_{41} \end{Bmatrix} \tag{4.42}$$

The coefficient can be mass-normalized in order to make them suitable for modal superposition. The orthogonality of modes can be expressed by [92]

$$\int_{\mathcal{V}} \rho Z_{nm} Z_{n'm'} \, \mathrm{d}V = \rho_{nm} \delta_{nm\,n'm'} \tag{4.43}$$

where $\mathcal{V}$ is the volume of the plate, ρ_{nm} the modal mass and $\delta_{nm\,n'm'}$ is the Kronecker function:

$$\delta_{nm\,n'm'} \equiv \begin{cases} 0 & \text{for} \quad (nm) \neq (n'm') \\ 1 & \text{for} \quad (nm) = (n'm') \end{cases} \tag{4.44}$$

The mass normalization is carried out by dividing the the modes by $\sqrt{\rho_{nm}}$. The mass normalized modes, ϕ_{nm}, are given by

$$\phi_{nm} = \frac{Z_{nm}}{\sqrt{\rho_{nm}}} \tag{4.45}$$

Given equation 4.8 the function ρ_{nm} is

$$\rho_{nm} = \rho \int_0^h \mathrm{d}z \int_0^{2\pi} \Theta^2 \, \mathrm{d}\theta \int_b^a R^2 \, \mathrm{d}r \tag{4.46}$$

Setting $C_n = A_n = 1$ and $B_n = 0$ the function ρ_{nm} can be obtained like

$$\rho_{nm} = \rho h \pi \int_b^a [J_n(\lambda r) + D_n I_n(\lambda r) + E_n Y_n(\lambda r) + F_n K_n(\lambda r)] r \, \mathrm{d}r \qquad (4.47)$$

and the mass-normalized sine mode, ${}_s\phi_{nm}$, can be obtained

$${}_s\phi_{nm} = [C'_{nm} J_n(\lambda_{nm} r) + D'_{nm} I_n(\lambda_{nm} r) + E'_{nm} Y_n(\lambda_{nm} r) + \\ + F'_{nm} K_n(\lambda_{nm} r)] \sin(n\theta) \qquad (4.48)$$

where

$$C'_n = \frac{1}{\sqrt{\rho_n}}; \quad D'_n = \frac{D_n}{\sqrt{\rho_n}}; \quad E'_n = \frac{E_n}{\sqrt{\rho_n}}; \quad F'_n = \frac{F_n}{\sqrt{\rho_n}} \qquad (4.49)$$

Setting $C_n = B_n = 1$ and $A_n = 0$ the mass-normalized cosine mode, ${}_c\phi_{nm}$, can be obtained as

$${}_c\phi_{nm} = [C'_{nm} J_n(\lambda_{nm} r) + D'_{nm} I_n(\lambda_{nm} r) + E'_{nm} Y_n(\lambda_{nm} r) + \\ + F'_{nm} K_n(\lambda_{nm} r)] \cos(n\theta) \qquad (4.50)$$

In conclusion, the typical modal solution of the vibrations of a simple disk is a pair of modes, or a double mode, comprising two modes with the same natural frequency, ω_{nm}, which have the same radial profile and the same circumferential mode shape profile ($\cos n\theta$) but with angular orientations which differ by 90° [93]. These circumferential variations of deflection, which represent motion on the disk, create patterns of n nodal diameters lines on its surface, lying symmetrically and antisymmetrically about a diameter at $\theta = \alpha$.

As the two modes of a pair have identical excitation frequencies, then any combination of the stated mode shapes is also a valid mode shape. In practice, this means that the nodal diameters can lie at any angular position. A mode shape is also characterized by m nodal circles. The nodal circles combined with the nodal diameters describe the specific mode in full. Indeed, two modes are characterized by the same natural frequency if $n \neq 0$. When $n = 0$ only one mode exists. Figure 4.2 shows some examples of modal patterns of a vibrating disk.

The axial displacement of a point on the disk, w, can be expressed by [83, 94]

$$w(r, \varphi, t) = \sum_{n,m=0}^{\infty} [a_{nm}(t) \cos(n\varphi) + b_{nm}(t) \sin(n\varphi)] R_{nm}(r) \qquad (4.51)$$

where the subscripts n and m correspond to the number of nodal diameters and nodal circles of the oscillations, respectively, and $a_{nm}(t)$ and $b_{nm}(t)$ are

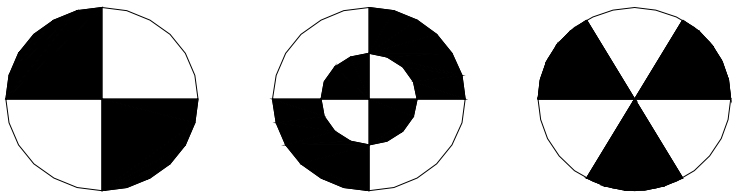

Figure 4.2: Typical axial modes in a disk; n = number of nodal diameters and m = number of nodal circles

the (real) principal co-ordinates. Here $\cos(n\varphi)$ and $\sin(n\varphi)$, and $R_{nm}(r)$ are the eigenfunctions in the circumferential and radial directions, respectively.

The response of a free vibrating annular disk can be seen as the superposition of real modes. Each mode vibrates at its natural frequency. The response of the disk at a natural frequency is given by the superposition of two modes since for each natural frequency, ω_{nm} with $n \neq 0$, there are two coincident modes. Such two modes are usually called 'sine' and 'cosine' modes because are spatially displaced at 90° each other.

Recalling that

$$\sin x = \frac{\mathrm{e}^{\mathrm{i}x} - \mathrm{e}^{-\mathrm{i}x}}{2\mathrm{i}} \tag{4.52}$$

$$\cos x = \frac{\mathrm{e}^{\mathrm{i}x} + \mathrm{e}^{-\mathrm{i}x}}{2} \tag{4.53}$$

equation 4.51 may be also written, in complex form as

$$v(r,\varphi,t) = \frac{1}{2}\sum_{n,m=0}^{\infty}[c_{nm}(t)\mathrm{e}^{-\mathrm{i}n\varphi} + \bar{c}_{nm}(t)\mathrm{e}^{+\mathrm{i}n\varphi}]R_{nm}(r) \tag{4.54}$$

Here the overbar indicates the complex conjugate, i is the imaginary unit and the $c_{nm}(t)$ are referred to as the (complex) wave co-ordinates. Note that $\mathrm{e}^{-\mathrm{i}n\varphi}$ and $\mathrm{e}^{+\mathrm{i}n\varphi}$ also constitute the eigenfunctions in the circumferential direction.

The response of a free vibrating annular disk can be seen as the superposition of complex modes. Each mode is given by a pair of waves propagating in opposite directions around the disk: the forward and backward travelling waves. For each natural frequency, ω_{nm} with $n \neq 0$, there are two modes and one is the complex conjugate of the other.

The two travelling waves have a cosine shape ($\cos n\theta$), a frequency ω_{nm} and they rotate in opposite directions at angular velocity ω_{nm}/n.

Actually, double modes exist only in a perfect or tuned disk where the nodal configurations have an arbitrary position denoted by angle α. When an imperfection exists each mode has a different natural frequency and the angular position of nodes ceases to be arbitrary. Only two nodal positions are then possible for each value of n, the natural frequencies of which deviate by an amount depending on the degree of imperfection. These modes are quite independent of each other, and their nodal position coincide with those of maximum and minimum frequency. Even if all disks have small imperfections only perfect disks were considered in this work.

4.2.3 Forced vibration of a stationary disk

When a single point excitation is applied to a stationary disk, vibration occurs in an ordinary manner as for any other simple structure. The vibration is given by the superposition of the modes which vibrate at the excitation frequency ω_E.

At the same time the motion of each mode may be considered as the superposition of two waves travelling on the disk. One rotates clockwise at angular velocity ω_E/n with the frequency ω_E and the others rotates counter-clockwise at the angular velocity ω_E/n with the frequency ω_E.

4.2.4 Free vibration of a rotating disk

The disk encountered during this work will rotate and so it is appropriate to extend the discussion to include the additional features that apply in this condition. There are essentially two features to describe: first, the effects on the modal properties of the forces which apply under rotating conditions (mainly, those arising from centrifugal and gyroscopic effects); secondly, the implications of the introduction of a second frame of reference which means that vibrations experienced in a rotating disk and observed by a stationary observer appear to occur at different frequencies [93].

The first feature causes the disk to experience and exhibit an increase in effective stiffness so that some natural frequencies rise under rotation. It is found experimentally that the natural frequency w changes with the rotational speed, Ω, with the relation

$$\omega^2 = \omega_0^2 + \beta\Omega^2 \tag{4.55}$$

where ω_0 is the frequency when stationary and β is a constant. Apart from this modification in frequency, the behaviour of rotating disks under free

vibration is similar to that previously described for stationary disks. As the extent of this effect is quite small, except for very high speed, it is not considered in this work.

Moreover, in dealing with rotating disks it is convenient to consider two co-ordinate systems, one fixed to the disk and the other fixed in space. Motions will be stated initially with reference to the former though the latter will be necessary for the interpretation of experimental results recorded by stationary displacement sensors. Equation 4.51 can be transformed into that of the rotating disk subjected to a stationary load by use of the relations between the rotating (body-fixed) co-ordinates (r, θ) and the stationary (inertial) co-ordinates (r, φ)

$$\theta = \varphi - \Omega t \tag{4.56}$$

In the co-ordinate system fixed to the disk the vibration is still given by the superposition of the waves propagating in opposite directions circumferentially in the disk at the frequency $\pm\omega_{nm}$. The frequencies of both travelling waves seen by a stationary observer change as the disk rotational speed increases, the frequency of the forward travelling wave being increased and that of the backward one being decreased. An inertial frame observer views the two travelling waves at the frequencies [84]

$$\omega_{nm}^{(F)} = \omega_{nm} + n\Omega \tag{4.57}$$

$$\omega_{nm}^{(B)} = \omega_{nm} - n\Omega \tag{4.58}$$

where $\omega_{nm}^{(F)}$ and $\omega_{nm}^{(F)}$ are the frequencies of the forward and backward travelling waves respectively. Such frequencies are called "apparent" natural frequencies since they appear as the natural frequencies to an inertial frame observer. The mode (n, m) can be excited to resonance by excitation at either of the inertial frame frequencies $\omega_{nm}^{(F)}$ or $\omega_{nm}^{(B)}$.

4.2.5 Forced vibration of a rotating disk

The steady state response of a rotating disk to a concentrated harmonic force moving in a concentric circular path at a constant velocity is now analyzed. The exciting force f is assumed stationary in space and applied at the radius $(r = r_0)$. Relative to the disk, it will rotate in the θ direction with speed $-\Omega$. The distributed exciting force f of excitation frequency ω_E is then given by

$$f = F\mathrm{e}^{\mathrm{i}\omega_E t}\frac{\delta(r - r_0)}{r}\delta(\theta - \Omega t) \tag{4.59}$$

where it is considered that the angular position of the force at $t = 0$ is $\theta = 0$.

It can be found [83] that the steady state response of the mode (n, m), in the co-ordinates system fixed to the disk, is expressed as

$$w = C_{nm}\left[\frac{\mathrm{e}^{\mathrm{i}n\theta}\mathrm{e}^{\mathrm{i}(\omega_E+n\Omega)t}}{\omega_{nm}^2-(\omega_E+n\Omega)^2}+\frac{\mathrm{e}^{-\mathrm{i}n\theta}\mathrm{e}^{\mathrm{i}(\omega_E-n\Omega)t}}{\omega_{nm}^2-(\omega_E-n\Omega)^2}\right] \tag{4.60}$$

where C_{nm} is a proper constant.

The disk vibration may be again considered as the superposition of two waves travelling on the disk.

With respect to the disk fixed frame, a wave rotates clockwise at angular velocity $\omega_E/n+\Omega$ with the frequency $\omega_E+n\Omega$ and the others rotates counterclockwise at the angular velocity $\omega_E/n-\Omega$ with the frequency $\omega_E-n\Omega$. These are the frequencies at which the modes are vibrating. Thus two pairs of resonant conditions will exist for each mode of vibration:

$$(\omega_E \pm n\Omega)^2 = \omega_{nm}^2 \tag{4.61}$$

With respect to the stationary system, the disk seems to vibrate at the frequency ω_E. But the excitation force that is applied to the disk is characterized by the two frequencies $\omega_E+n\Omega$ and $\omega_E-n\Omega$, that have a different value with respect to the number of nodal diameters of the mode. Then each mode is excited by a different frequency.

Each mode has one resonant frequency, ω_{nm}, which can be excited by the two excitation frequencies $\omega_E \pm n\Omega$. The resonant excitation frequencies are readily obtained

$$\omega_E = \omega_{nm} \pm n\Omega \tag{4.62}$$

The wave travelling clockwise on the disk is at resonance when ω_E equals $\omega_{nm}-n\Omega$ and the wave travelling counterclockwise on the disk is at resonance with ω_E when $\omega_{nm}+n\Omega$.

This relationship can be used to construct the frequency-speed diagram presented in figure 4.3 which shows the apparent vibration frequencies, $\omega_{nm}^{(F)}$ and $\omega_{nm}^{(B)}$, plotted against rotation speed Ω for the mode (n, m) of the rotating disk. An important application of this diagram is to indicate the rotation speed at which the frequency ω_E of a stationary source of vibration excitation will coincide with the apparent natural frequency of the spinning disk.

4.2.6 Lock-in instability

The vibratory behaviour of flexible rotating disks in the presence of friction can be characterized by the onset of unstable vibrations. Papers on analogue problems can be found and among these, the brake squeal is the closest. In

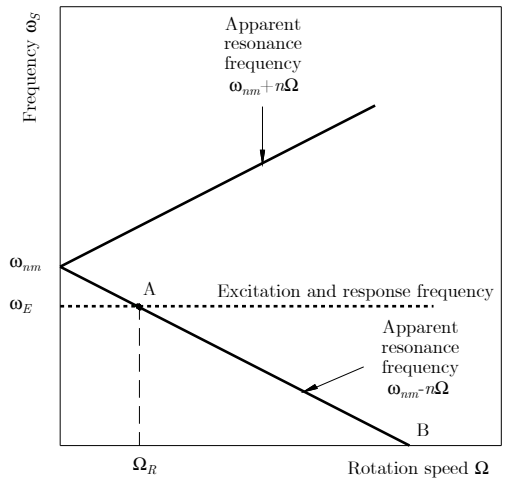

Figure 4.3: Apparent and actual vibration frequencies of a rotating disk observed from a stationary and a rotating frame: — Apparent natural frequencies as detected by a stationary observer; $\cdots$ Excitation frequency; A, critical speed for stationary excitation at frequency ω_E of disk mode; B, critical speed for stationary static force ($\omega_E = 0$) excitation of disk mode

fact such a problem is strictly connected to both the structural dynamics and the friction coefficient at the interface between a disk and a pin.

There are two general causes to brake squeal [86]. One cause is related to self-excited vibration that is induced when the friction material has a negative slope in relation to the relative velocity. The other cause is ascribed to self-excited vibration due to the coupling of two eigenvalues that are present in parts experiencing friction.

One means used to reduce the former type of squeal is to improve the friction characteristic of the friction material. This generally involves reducing the velocity dependence of the friction coefficient of the friction material as much as possible. The latter type of squeal has been reduced by optimizing the vibration characteristics of the brake assembly that cause self-excited vibration. This was accomplished by conducting a complex eigenvalue analysis of a brake assembly model in which the friction coefficient was set to a certain constant value.

For example, Hamabe et al [86] conducted a complex eigenvalue analysis of a drum brake system with a finite element model showing the vibration characteristics that caused the squeal sounds.

Moreover, Tuchinda et al [95] used a pin-on-disc system to simulate how

squeal noise can be generated in vehicle disc brakes. The pin-on-disc system was modelled as a flexible beam in contact with a flexible disc. The two components were coupled together by means of a Coulomb type friction. The response of each component was expressed as a sum of its normal modes which led to a multi degree of freedom model. The model showed that instability can occur when one of the natural frequencies of the pin approaches one of the natural frequencies of the disc. The pin and the disc are said to be "locking-in" to each other.

Lock-in instabilities can arise also during the sharpening of a disk. If two frequencies of disk and grinding wheel are close it is possible to record the onset of lock-in instability because of a self-excitation due to the dynamical coupling of disk and abrasive wheel block.

Modal equations of the disk and the grinding wheel system can be coupled in a single system by means of some hypothesis on the interface contact. For instance the contact between disk and abrasive wheel can be modelled by a Coulomb friction coefficient and it can be assumed that the surfaces of the disk and the wheel remain always in contact. The modes of the coupled structure, which can be calculated by a complex eigenvalue analysis, change with the value of the friction coefficient. Some modes can coincide and cause instability.

Such technique is usually used for a rotating disk with a small rotational speed, and it does not take into account the influence of rotational velocity on the vibrational behaviour of the disk. The only effect of rotation is the creation of frictional forces. Nonetheless, such technique gives useful information to interpret the phenomenon and to design such devices.

The abrasive wheel-disc system used in the study consisted of two components: a flexible disk and a flexible abrasive wheel support, as shown in figure 4.4. The abrasive wheel was modelled as a mass pushed against the disk by a spring, hence it was modelled as a single degree of freedom system. The disc was assumed to be clamped at the inner bore and free at the outer rim. The model assumed that the abrasive wheel can vibrate only in the axial direction, z, whereas the disc can vibrate only in the out-of-plane direction, w. The inclination of the wheel axis is defined by the angle α as shown in figure 4.4.

Assuming that the abrasive wheel is pushing against the disc, the disc applies a normal force P onto the wheel, as shown in figure 4.4. Due to the non-zero relative velocity between wheel and disc, a frictional force is generated in the in-plane direction. In this model, the frictional force is assumed to be of the Coulomb type. Hence, the magnitude of the frictional force is μP where μ is the coefficient of friction and is assumed to be constant.

The disk is excited by forces, f_w, in the out of plane direction, w. The

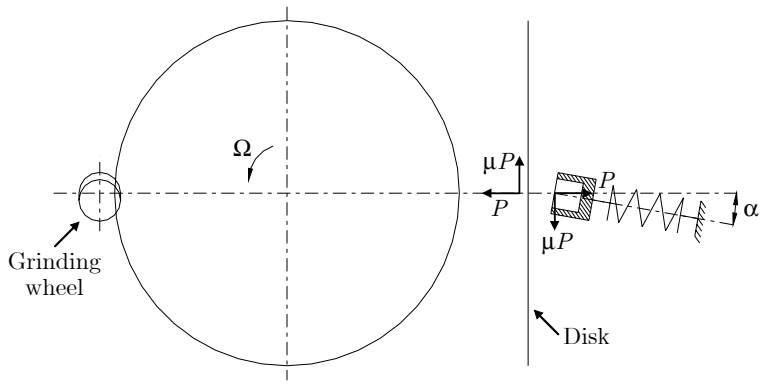

Figure 4.4: Lock-in instability model

force acting on the disk because of the pushing abrasive wheel is

$$f_w = -P \tag{4.63}$$

At the same time the force acting along the axis z on the abrasive wheel system is given by

$$f_z = P(\cos\alpha + \mu \sin\alpha) \tag{4.64}$$

The equation of motion of the abrasive wheel system for a forced axial vibration can be written as

$$m\ddot{z} + kz = f_z \tag{4.65}$$

where m is the abrasive wheel mass and k is the stiffness of the spring pushing the wheel.

The natural frequency of the abrasive wheel disk, ω, is given by

$$\omega = \sqrt{\frac{k}{m}} \tag{4.66}$$

then the equation of motion can be written as

$$\ddot{z} + \omega^2 z = \frac{f_z}{m} \tag{4.67}$$

Assuming small rotational speed, the disc can be assumed to be stationary and that the classical plate equation for the forced vibration in the out-of-plane direction can be applied

$$D\nabla^4 w(r,\theta,t) + \rho h \frac{\partial^2 w(r,\theta,t)}{\partial t^2} = f_w(r,\theta,t) \tag{4.68}$$

where ρ is the density of the disc material, h the thickness, D the bending stiffness, w the out-of-plane displacement and f_w the applied force in the out-of-plane direction. The solution is found by modal superposition and it is assumed to be

$$w(r,\theta,t) = \sum_{n=0}^{\infty}\sum_{m=0}^{\infty} {}_c\phi_{nm}(r,\theta)\,{}_cq_{nm}(t) + \sum_{n=0}^{\infty}\sum_{m=0}^{\infty} {}_s\phi_{nm}(r,\theta)\,{}_sq_{nm}(t) \qquad (4.69)$$

where $q_{nm}(t)$ is the generalized coordinate for the mode which has n nodal diameters and m nodal circles; ϕ_{nm} is the mass-normalized mode shape and its explicit formula is given by equations 4.48 and 4.50. Subscripts c and s denote cosine and sine modes, respectively.

The summation indices in equation 4.69 have different limits according to some authors to take into account that the mode with zero nodal diameters are single. In this work the problem was sorted out by the position

$${}_sq_{0m} = 0 \qquad m = 0, 1, \ldots \qquad (4.70)$$

Substituting equation 4.69 into equation 4.68 the equation of motion can be rewritten as:

$$\begin{aligned} D\sum_{n=0}^{\infty}\sum_{m=0}^{\infty}\left[(\nabla^4\,{}_c\phi_{nm})\,{}_cq_{nm} + (\nabla^4\,{}_s\phi_{nm})\,{}_sq_{nm}\right] + \\ +\rho h\sum_{n=0}^{\infty}\sum_{m=0}^{\infty}\left[{}_c\phi_{nm}\,{}_c\ddot{q}_{nm} + {}_s\phi_{nm}\,{}_s\ddot{q}_{nm}\right] \;=\; f_w \end{aligned} \qquad (4.71)$$

The solution of generalized co-ordinates can be expressed by $q(t) = Q\mathrm{e}^{\mathrm{i}\omega t}$, and in the case of free vibration, $f_w = 0$, the differential equation becomes

$$\nabla^4\phi(r,\theta) = \frac{\rho h}{D}\omega^2\phi(r,\theta) \qquad (4.72)$$

The equation of motion can be simplified to

$$\begin{aligned} \rho h\sum_{n=0}^{\infty}\sum_{m=0}^{\infty}\left[{}_c\phi_{nm}\,{}_c\ddot{q}_{nm} + {}_s\phi_{nm}\,{}_s\ddot{q}_{nm}\right] + \\ +\rho h\sum_{n=0}^{\infty}\sum_{m=0}^{\infty}\left[\omega^2_{nm}\,{}_c\phi_{nm}\,{}_cq_{nm} + \omega^2_{nm}\,{}_s\phi_{nm}\,{}_sq_{nm}\right] \;=\; f_w \end{aligned} \qquad (4.73)$$

To separate the equation of motion into a set of uncoupled linear ordinary differential equations with constant coefficients, the equation was multiplied

by ϕ_{nm}, and integrated from 0 to 2π in θ and from b to a in r. Finally, making use of the orthogonality of the eigenfunctions of the free disc problem, yields:

$$ {}_c\ddot{q}_{nm}(t) + \omega_{nm}\, {}_cq_{nm}(t) = \int_b^a \int_0^{2\pi} f_w(r,\theta,t)\, {}_c\phi_{nm} r \,\mathrm{d}r\mathrm{d}\theta \tag{4.74} $$

$$ {}_s\ddot{q}_{nm}(t) + \omega_{nm}\, {}_sq_{nm}(t) = \int_b^a \int_0^{2\pi} f_w(r,\theta,t)\, {}_s\phi_{nm} r \,\mathrm{d}r\mathrm{d}\theta \tag{4.75} $$

for $n, m = 0, 1, \ldots$

It is assumed that the abrasive wheel remains in contact with the disk at all times and that the displacement amplitudes of the self-induced oscillations are small with respect to the physical dimensions. Considering 4.4, the coupling condition between the wheel and the disc in the out-of-plane direction can be written as:

$$ -w(r_0, \theta_0, t) = z(t)\cos\alpha \tag{4.76} $$

where the co-ordinates (r_0, θ_0) indicate the position of the application of the wheel on the disk system of co-ordinates (r, θ).

The excitation force acting on the disk in the out-of-plane direction can be written in the cylindrical co-ordinates (r, θ) of the disk as

$$ f_w(r,\theta,t) = -\frac{P(t)}{r}\delta(r - r_0)\delta(\theta - \theta_0) \tag{4.77} $$

where δ is the Kronecker function.

Substituting the force equations and the coupling condition all the equations of motion of disk and abrasive wheel system can be assembled with the contact condition in the system:

$$ \begin{cases} {}_c\ddot{q}_{nm}(t) + \omega_{nm}^2\, {}_cq_{nm}(t) = -P\, {}_c\phi_{nm}(r_0,\theta_0) \quad n, m = 0, 1, \ldots \\ {}_s\ddot{q}_{nm}(t) + \omega_{nm}^2\, {}_sq_{nm}(t) = -P\, {}_s\phi_{nm}(r_0,\theta_0) \quad n, m = 0, 1, \ldots \\ \ddot{z} + \omega^2 z = \dfrac{P}{m}(\cos\alpha + \mu\sin\alpha) \\ \displaystyle\sum_{n,m=0}^{\infty} \left[{}_c\phi_{nm}(r_0,\theta_0)\, {}_cq_{nm}(t) + {}_s\phi_{nm}(r_0,\theta_0)\, {}_sq_{nm}(t) \right] + z(t)\cos\alpha = 0 \end{cases} \tag{4.78} $$

From the third equation the value of the force can be obtained

$$ P = a\ddot{z} + a\omega^2 z \tag{4.79} $$

where

$$ a = \frac{m}{\cos\alpha + \mu\sin\alpha} \tag{4.80} $$

Substituting equation 4.79 and differentiating twice the coupling condition in respect to the time, the system becomes

$$\begin{cases} {}_c\ddot{q}_{nm} + a\,{}_c\phi_{nm}(r_0,\theta_0)\ddot{z} + \\ \quad +\omega_{nm}^2\,{}_cq_{nm} + a\,\omega^2\,{}_c\phi_{nm}(r_0,\theta_0) = 0 \qquad n,m = 0,1,\dots \\ {}_s\ddot{q}_{nm} + a\,{}_s\phi_{nm}(r_0,\theta_0)\ddot{z} + \\ \quad +\omega_{nm}^2\,{}_sq_{nm} + a\,\omega^2\,{}_s\phi_{nm}(r_0,\theta_0) = 0 \qquad n,m = 0,1,\dots \\ \displaystyle\sum_{n=0}^{\infty}\sum_{m=0}^{\infty}\left[{}_c\phi_{nm}(r_0,\theta_0)\,{}_c\ddot{q}_{nm} + {}_s\phi_{nm}(r_0,\theta_0)\,{}_s\ddot{q}_{nm}\right] + \ddot{z}\cos\alpha = 0 \end{cases} \tag{4.81}$$

The equation of motion of the combined system reduces to:

$$[M]\underline{\ddot{x}} + [K]\underline{x} = \underline{0} \tag{4.82}$$

where

$$\underline{x} = \{{}_cq_{nm},\ {}_sq_{nm},\ z\}^{\mathrm{T}} \tag{4.83}$$

is the co-ordinates vector.

For example considering only the modes with $n,m = 0,1$ and remembering that ${}_sq_{0m} = 0\ \forall\ m$, the co-ordinates vector is

$$\underline{x} = \{{}_cq_{00},\ {}_cq_{10},\ {}_sq_{10},\ {}_cq_{01},\ {}_cq_{11},\ {}_sq_{11},\ z\}^{\mathrm{T}} \tag{4.84}$$

while the mass matrix is

$$[M] = \begin{bmatrix} 1 & 0 & 0 & 0 & 0 & 0 & a\,{}_c\tilde{\phi}_{00} \\ 0 & 1 & 0 & 0 & 0 & 0 & a\,{}_c\tilde{\phi}_{10} \\ 0 & 0 & 1 & 0 & 0 & 0 & a\,{}_s\tilde{\phi}_{10} \\ 0 & 0 & 0 & 1 & 0 & 0 & a\,{}_c\tilde{\phi}_{01} \\ 0 & 0 & 0 & 0 & 1 & 0 & a\,{}_c\tilde{\phi}_{11} \\ 0 & 0 & 0 & 0 & 0 & 1 & a\,{}_s\tilde{\phi}_{11} \\ {}_c\tilde{\phi}_{00} & {}_c\tilde{\phi}_{10} & {}_s\tilde{\phi}_{10} & {}_c\tilde{\phi}_{01} & {}_c\tilde{\phi}_{11} & {}_s\tilde{\phi}_{11} & \cos\alpha \end{bmatrix} \tag{4.85}$$

and the stiffness matrix

$$[K] = \begin{bmatrix} \omega_{00}^2 & 0 & 0 & 0 & 0 & 0 & a\,\omega^2\,{}_c\tilde{\phi}_{00} \\ 0 & \omega_{10}^2 & 0 & 0 & 0 & 0 & a\,\omega^2\,{}_c\tilde{\phi}_{10} \\ 0 & 0 & \omega_{10}^2 & 0 & 0 & 0 & a\,\omega^2\,{}_s\tilde{\phi}_{10} \\ 0 & 0 & 0 & \omega_{01}^2 & 0 & 0 & a\,\omega^2\,{}_c\tilde{\phi}_{01} \\ 0 & 0 & 0 & 0 & \omega_{01}^2 & 0 & a\,\omega^2\,{}_c\tilde{\phi}_{11} \\ 0 & 0 & 0 & 0 & 0 & \omega_{11}^2 & a\,\omega^2\,{}_s\tilde{\phi}_{11} \\ 0 & 0 & 0 & 0 & 0 & 0 & 0 \end{bmatrix} \tag{4.86}$$

where

$$ {}_i\tilde{\phi}_{jk} =_i \phi_{jk}(r_0, \theta_0) \qquad i = c, s \quad j, k = 0, 1 \tag{4.87} $$

In order to find complex eigenvalues the equation must be re-written in the state space form [92]:

$$ \left\{ \begin{array}{c} \underline{\dot{x}} \\ \underline{\ddot{x}} \end{array} \right\} = \left[\begin{array}{cc} 0 & I \\ -M^{-1}K & 0 \end{array} \right] \left\{ \begin{array}{c} \underline{x} \\ \underline{\dot{x}} \end{array} \right\} + \left\{ \begin{array}{c} 0 \\ M^{-1}P \end{array} \right\} \tag{4.88} $$

and the characteristic equation is then given by

$$ \det \left(\left[\begin{array}{cc} 0 & I \\ -M^{-1}K & 0 \end{array} \right] - \lambda \left[\begin{array}{cc} 1 & 0 \\ 0 & 1 \end{array} \right] \right) = 0 \tag{4.89} $$

For each modal coordinate two complex eigenvalues are obtained, that usually are complex conjugate. They are the poles of the state space system. The absolute value of each eigenvalue gives the natural frequency of the corresponding mode. Instability can be studied by considering the real part of the eigenvalues. A positive real part describes an instability situation.

The method was applied in some MATLAB® programs written by the author. Figure 4.5 shows an example of lock-in where the mode of the abrasive wheel gets coupled with the disk mode (1,0) for a friction coefficient, μ, of about 0.1. The analysis was carried out on a steel disk of thickness $h = 1$ mm, outer radius $a = 190$ mm and inner radius $b = 45$ mm. The grinding wheel mass and spring stiffness were set respectively to $m = 1.3$ kg and $k = 75000$ N/m.

4.3 Starting practical problem

The problem of the onset of self excited vibration during the sharpening process is a common and crucial problem in paper manufacturing machine. In fact rotating disks are used, as knives, to cut sheets and rolls of paper. Self excited vibration can arise when the disk edge is sharpened. Such vibration worsens the sharpening process and the disk edge is spoilt. The phenomenon is very complicated and not yet well explained.

There was the opportunity to investigate such field when a roll cutting paper machine by a company from Lucca presented such a problem. An experimental investigation on this paper roll cutting machine was carried out on-situ in order to highlight the problems concerning the sharpening of the disk blade. As only few experiments could be carried out not many hypotheses could be validated. However, such experimental investigation was

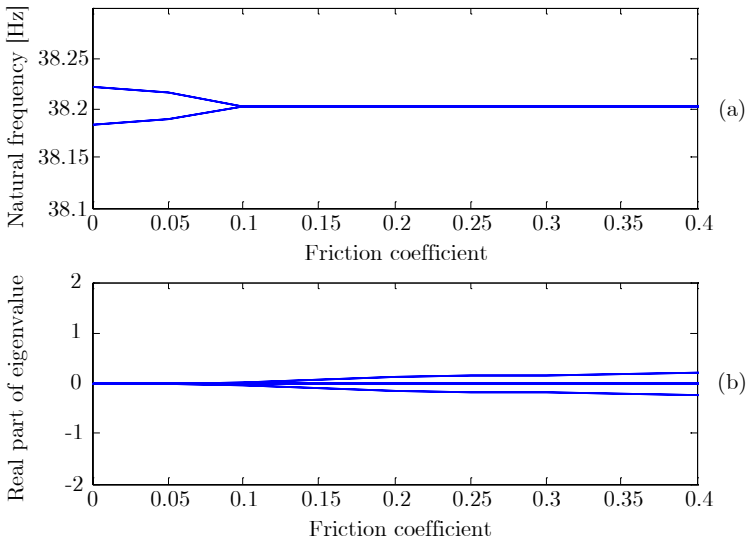

Figure 4.5: Lock-in example: the first mode of the abrasive block gets coupled with the mode (1,0) of the disk; (a) natural frequency and (b) real part of the eigenvalue

the starting point of the more accurate investigation of the process described in this chapter.

The commercial paper cutting machine that was examined is shown in figure 4.6. The steel disk blade initial diameter is about 600 mm and the tapered thickness varies from 4.8 mm to 1.5 mm. The sharpening is achieved by means of two idle, opposed grinding wheels with a 100 mm diameter pressed down on the blade edge by means of two springs. The abrasive wheels are tilted in order to follow the tapered shape of the disk and in order to sharpen the edge. The abrasive wheel are pulled away from the disk by pneumatic actuators. The sharpening process is about 0.5 sec long and is periodically repeated. As during the sharpening process the abrasive wheel are put in rotation by the disk contact, their rotating velocity is grossly given by the ratio of disk and wheel radius.

Investigations over a machine in not-working and working conditions were carried out. In the former case the disk blade was excited by an impact hammer or by the grinding wheels suddenly pressing it. In the latter case the working conditions have been simulated. The sampling acquisition rate was fixed at 5000 Hz in order to obtain reliable results up to the maximum frequency of the range of interest, 500 Hz. In the analysis of the recorded signals,

Figure 4.6: Photo of the paper cutting machine

spectrograms have been used to find the onset time of particular phenomena while power spectral densities (corresponding to different time intervals) have been plotted to show the principal harmonic components. Moreover the disk blade was rotated manually in order to find possible misalignments and thickness irregularities by means of a displacement transducer.

4.3.1 Impact tests

Firstly impact tests using the impulse force hammer were carried out on the stopped machine in order to find natural frequencies with contacting and not-contacting grinding wheels. PSD graphs showed two predominant peaks (about 180 and 270 Hz) when the disk edge was constrained by the grinding wheels and three peaks (105, 180 and 270 Hz) when the disk was free. Secondly the impact tests by pressing the grinding wheels were carried out in order to be closer to the real working conditions. In figure 4.8 a spectrogram shows the instants of the grinding wheels pressing (1.2 s) and moving off (4.5 s). In figure 4.9 signal spectra of an accelerometer fixed to

the disk blade in two different phases are presented. During the pressing the predominant peaks were 106, 156, 180 and 275 Hz whereas during the moving off there was a general attenuation and the greater peak was at 260 Hz. The peaks recorded during the pressing phase are the natural frequencies of the global system. The contact between the disk and the grinding wheel is a not clear non-linearity which makes it difficult to study the problem. The peaks recorded during the moving off are guessed to be the natural frequencies of the disk since it was freely vibrating with no excitation or constraints. Such modes can be easily calculated and are at the basis of all the instability searching process. From such experiments no information about the mode shape was obtained.

4.3.2 Modal analysis

A numerical modal analysis of the disk was carried out. The disk was meshed with `shell63` elements using ANSYS® software. The nodes on the inner collar were fully constrained and a reduced analysis to the displacement perpendicular to the disk surface and to the rotations of the surface was carried out. The material properties of common steel were used (Young's modulus E=210 GPa and density ρ=7800 kg/m^3).

The disk used in the paper cutting machine during the experimental investigation had an outer radius of 301 mm and it was clamped at a radius of 925 mm. The thickness of the disk decreased from 4.8 mm to 1.53 mm linearly from the 114 mm radius and the outer one. Figure 4.7 shows the section of the disk. The results of the modal analysis are shown in table 4.1 where the frequencies are given in Hz. In the table, apart from the natural frequencies, also the "apparent" natural frequencies are given for a rotational speed of 22.2 Hz, that is the operating speed of the paper cutting machine disk. The calculated frequencies can be roughly correlated to the experimental peaks of figure 4.9(b). The natural frequencies (2,0), (3,0) and (5,0) can be easily located. The mode (4,0) should have a natural frequency of 225 Hz but in the figure the closer peak is at 260 Hz.

The natural frequency of the supporting blocks of the grinding wheels were also examined. A solid model of the supports with the grinding wheels were made and meshed in ANSYS® . The 10 nodes tetrahedral solid element `solid92` were used. The Block-Lanczos solution method was employed. The material constants of the aluminium were used (Young's modulus E=70 GPa and density ρ=2700 kg/m^3). The lower natural frequencies are 562.15, 1245.4 and 1624.2 Hz. Figure 4.10 shows the mode shapes of such support. The first natural frequency is close to the natural frequency (7,0) of the disk while the second frequency is close to the natural frequency (12,0) of the disk. The

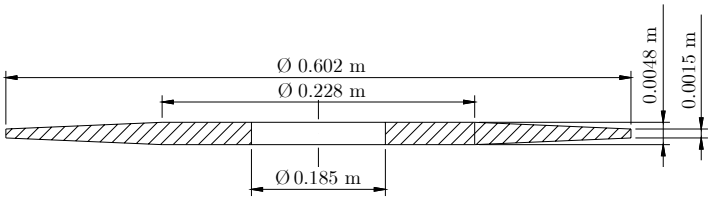

Figure 4.7: Section of the cutting paper machine disc

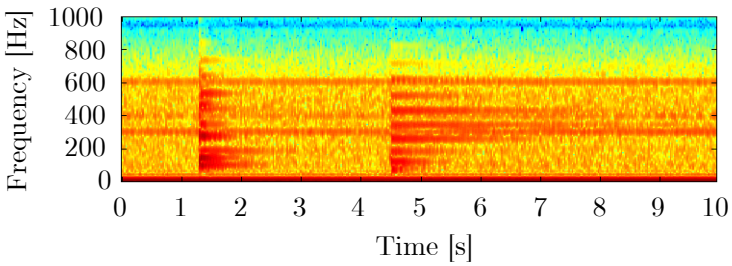

Figure 4.8: Impact test spectrogram, grinding wheels pressing on blade and off

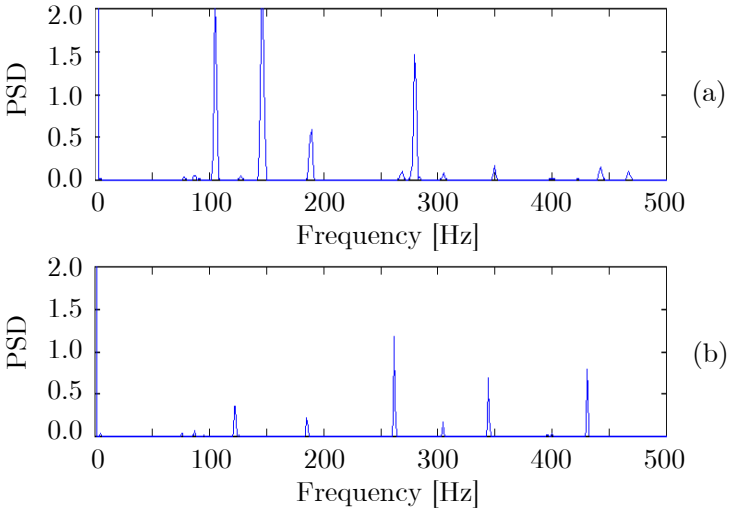

Figure 4.9: PSD of an impact test, grinding wheels pressing on blade (a) and off (b)

Nodal diameters	Nodal circles	Natural frequencies [Hz]	Apparent natural frequencies [Hz]	
n	m	f_n	$f_n - nf_\Omega$	$f_n + nf_\Omega$
0	0	106.42	106.42	106.42
1	0	106.69	84.49	128.89
2	0	117.46	73.06	161.86
3	0	156.64	90.04	223.24
4	0	225.13	136.33	313.93
5	0	313.62	202.62	424.62
6	0	416.60	283.4	549.8
7	0	532.46	377.06	687.86
8	0	661.16	483.56	838.76
9	0	803.03	603.23	1002.83
10	0	958.34	736.34	1180.34
0	1	523.12	523.12	523.12
1	1	536.81	514.61	559.01
2	1	581.80	537.4	626.2
3	1	665.91	599.31	732.51
4	1	793.04	704.24	881.84
5	1	958.41	847.41	1069.41

Table 4.1: Natural frequency of the tapered disk of the cutting paper machine

third frequency is outside of the working range.

4.3.3 Sharpening tests

Then sharpening tests in working conditions were carried out. The disk blade rotational speed was set to 22.2 Hz and a very short sharpening (about 0.5 s) was performed. Instead of accelerometers, non-contact displacement transducers were preferred because less sensitive to environmental disturbance. In figure 4.11 spectra corresponding to different phases show that a 200 Hz peak appears during sharpening. The 22 and 44 Hz peaks, related to the disk blade rotational frequency, are always present.

Consecutive sharpening experiences were carried out in order to measure the grinding wheel angular velocity. The trigger signal, recorded during such tests, showed that the angular velocity quickly reaches a constant value of 100 Hz. Such value is equal to about five times the disk blade angular velocity. This velocity was reached after a short transient (2-3 sharpening phases) but then kept almost constant. Figure 4.12 reports the results of intermittent

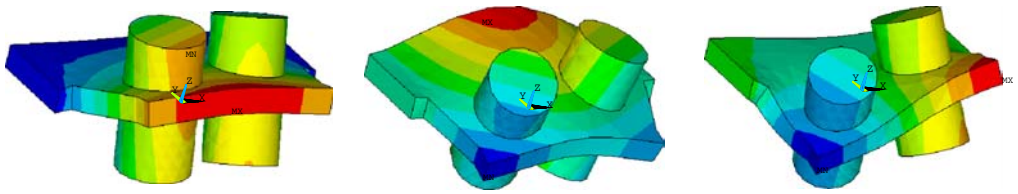

(a) (b) (c)

Figure 4.10: Mode shapes of the grinding wheels support block of the paper cutting machine: first mode $f_n = 562.15$ Hz (a); second mode $f_n = 1245.4$ Hz (b); third mode $f_n = 1624.2$ Hz (c).

sharpening experiments. The graphs on the left refer to sharpening periods whereas those on the right refer to periods in which the grinding wheels are not in contact. During the sharpening a 200 Hz peak is noticed even if its amplitude diminishes in the following phases whereas a 100 Hz peak increases. Moving the grinding wheels away from the disk such peaks vanish. Smaller peaks at 22, 44, 66 and 88 Hz, related to the disk blade rotational frequency, and a 180 Hz peak during the no sharpening period can also be noticed. Increasing the pre-load of the two grinding wheels the 200 Hz peak increases. On the contrary increasing the pre-load of only one grinding wheel the 200 Hz peak decreases. Lastly intermittent sharpening experiences at a higher temperature (the disk blade shaft was at about 65°C) were carried out. In this case the 180 and 200 Hz peaks disappeared.

A 200 Hz vibration during the sharpening process was noticed. The amplitude of such vibrations diminishes increasing the grinding wheel angular velocity and the disk hub temperature, and is influenced by the grinding wheel pre-load. The following disk blade edge examination showed a nine lobe waviness, that increased in time until the disk blade was spoilt.

4.3.4 Comments on the results

The interpretation of the vibration onset during the sharpening process is clearly a difficult task. The phenomenon is difficult to explain because of the huge number of involved parameters. However some considerations can be drawn.

The influence of velocity can be related to the variation of friction conditions. The temperature increase concerns the disk inner zone, nearby the bearings, and can produce a tight fit at the disk inner edge. Consequently there is stiffening and an increase of the natural resonant frequencies. Lastly

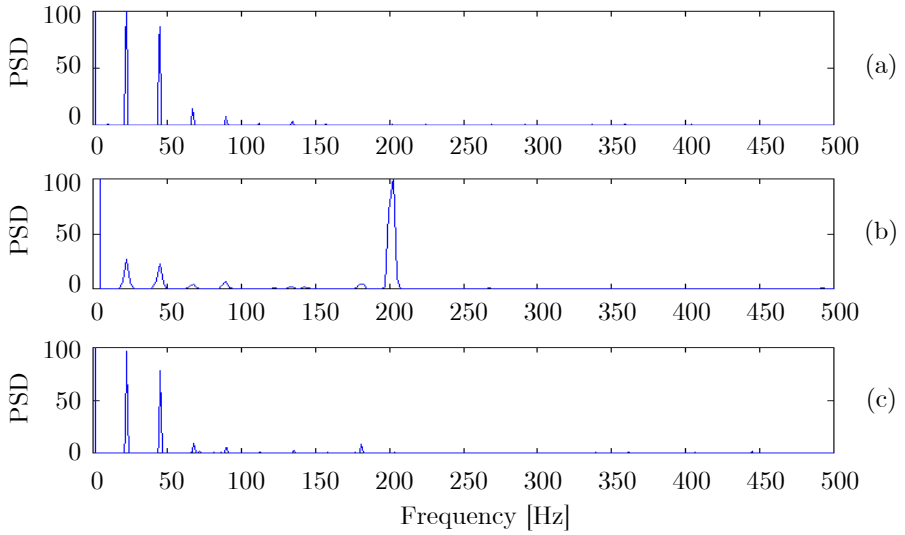

Figure 4.11: PSD of a short sharpening test: (a) before, (b) during and (c) after sharpening

the pre-load of the grinding wheel springs can increase the impact force and so transient oscillations get larger.

The 200 Hz vibration, detected by a ground based observer can be explained referring to a disk-based observer. Such vibration might be related to a natural vibration with five nodal diameters, at about 313 Hz. In fact, 313 Hz-5f_Ω=202 Hz, very close to the 200 Hz peak.

Moreover the 200 Hz response frequency is about nine times the disk blade rotational frequency and so also the observed nine lobe thickness irregularities could be explained. The fact that the phenomenon is dependent on the wheel-disk sliding velocity and suggests that friction conditions and stick-slip could be the source of the detrimental vibrations. Moreover lock-in instabilities can arise.

4.4 Design of the test rig

4.4.1 Description of the test rig

The tests carried out on the commercial paper cutting machine were just few because of company requirements. Such tests were sufficient to record the problem and depict the troublesome resonance but they were not sufficient

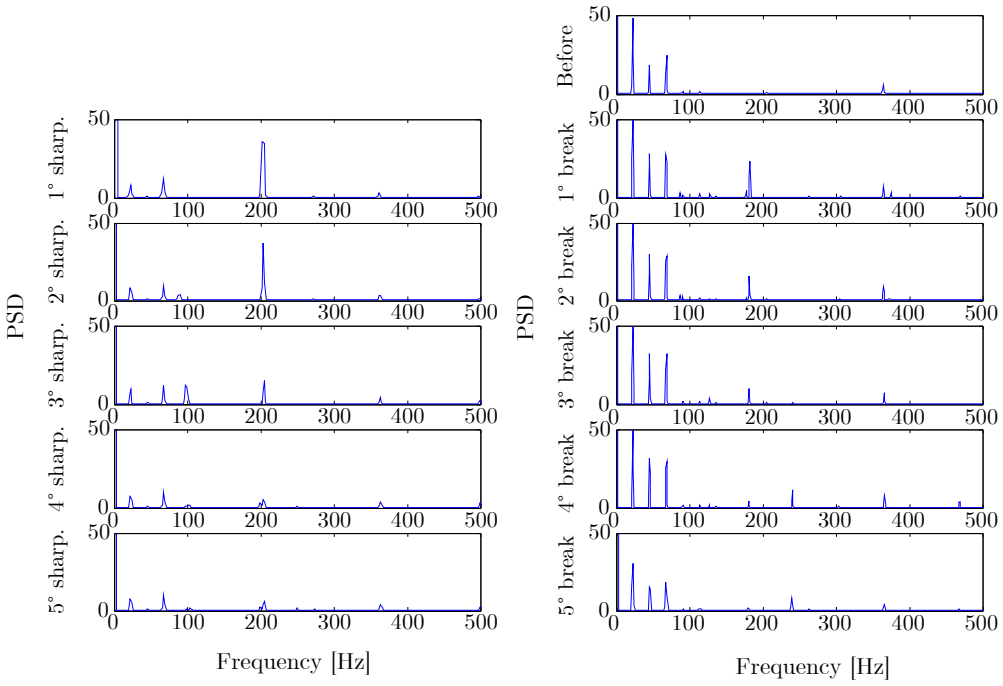

Figure 4.12: PSD of a repeated sharpening test

to discover the reasons of the onset of the self excited vibrations and find out the problem in a precise way. So a test rig, which reproduces the sharpening process and which permits to vary the parameters of the process, has been designed. The aim was to quantify the influence on the onset of self excited vibrations of the sharpening parameters, like for example the pre-load on the spring pushing the grinding wheel or the duration of the sharpening or the angular velocity. The test rig was built up (see figure 4.13) and a campaign of experimental tests was carried out.

Moreover, such test rig can allow the numerical model of the sharpening of the disk to be tuned with respect to the real system or at least, to understand the degree of reliability of the numerical results. The compatibility between experimental and numerical results could give some advantages. In fact a very complex phenomenon could be simply simulated. As the experimental tests necessary for the commercialization of the sharpening machines would be reduced, the design process of the sharpening machines could require less time and money.

The test rig was designed to reproduce to scale the commercial paper cutting machine in its main characteristics. The sharpening process in the

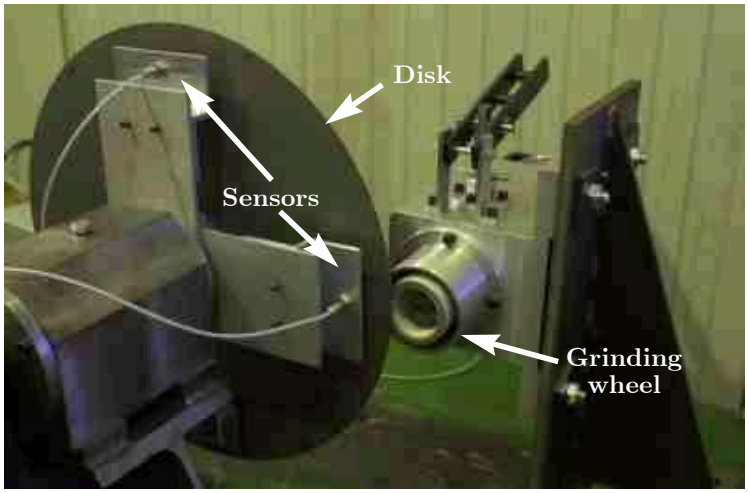

Figure 4.13: Photo of the test rig

machine is achieved by means of the translation of the grinding wheel, that is pushed on the disk by a pre-loaded spring. The translating system can be modelled as a single degree of freedom mass-spring system. The translating system of the grinding wheel block was designed with the same natural frequency of the commercial machine (117 rad/s = 18.6 Hz). In the same way the disk that must be sharpened was designed in order to have the coincidence of the first two natural frequencies with the real disk, that is 130 Hz and 139.72 Hz. The geometry of the test disk was the simplest in order to simplify its production. A steel flat disk with a constant thickness of 3 mm was chosen. Another disk, 1 mm thick, was also tested. The outer diameter was 380 mm and the inner hole was 40 mm. The disk was fastened to a rotating shaft by an annular clamp with the outer radius of 45 mm. The sharpening was achieved by only one cylindrical grinding wheel with the outer diameter of 50 mm (see figure 4.14). Figure 4.15 shows the assembly drawing of the test rig.

The test rig must put the flexible disk in rotation and gather, during the sharpening process, the displacements normal to the disk surface of three points. The points of acquisition must be placed with a variable angle α between them. Simultaneously, the translational displacement of the grinding wheel shaft along its axis, and the rotational speeds of the disk and of the grinding wheel must be measured. Moreover, the test rig should allow all the variables that can affect the sharpening process to be changed in order to underline the influence of each parameter.

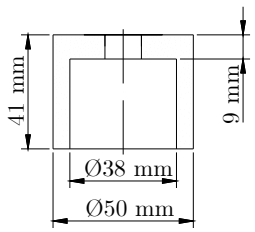

Figure 4.14: Section of the grinding wheel of the test rig (dimensions are in mm)

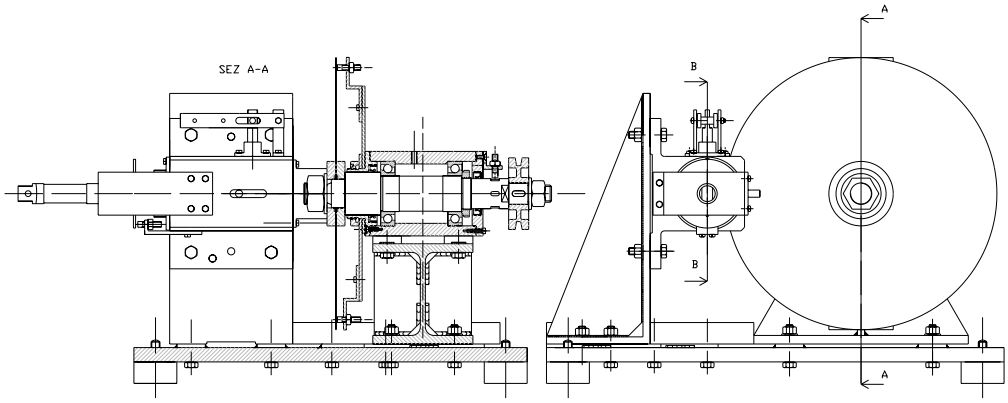

Figure 4.15: Assembly drawing of the test rig

With the designed test rig different kinds of test can be carried out. Impact test can be carried out in order to identify the natural frequencies of the disk-translating grinding wheel system. The load acting on the disk edge can be continuously varied from almost zero to 200 N. The sharpening duration can be changed, varying the time at which the grinding wheel is kept in touch with the disk: short and long, continuous and intermittent sharpening can be performed. The natural frequency of the translating grinding block can be modified by the change of the spring pushing the grinding wheel shaft. The grinding wheel is usually free to spin around its axis. In order to see the effect of the relative sliding velocity between the disk and the abrasive wheel on the self excited vibration onset, the rotation of the grinding wheel can be blocked. Moreover, the geometry of the sharpening contact can be changed. In the basic configuration the rotational axes of the disk and of the grinding wheel are parallel. The rotational axis of the grinding wheel can be tilted by

2° on a plane tangent to the disk edge (see figure 4.4). Thus the contact area can be changed from an annular surface to a point. The latter configuration is closer to the real sharpening configuration since it is the inclination of the grinding wheel shaft that produces the sharp edge on the disk. Finally, the contact friction coefficient can be varied by the adduction in the contact area of a "lubricant" fluid, like for instance water.

The test rig is formed by two main parts as shown in figure 4.16. The former has the function to bear the disk shaft that is connected to a motor which supplies the rotational energy. The latter is the block that bears the grinding wheel shaft and that permits the translation of the wheel against the disk. The two blocks are bolted on a steel plate and they are referred to each other by means of a calibrated square.

Figure 4.16 shows also the main difference between the commercial process and the experimental set up. In the commercial configuration the grinding wheel is tilted in order to follow the tapered shape of the disk blade and create the proper sharp edge. In the test rig configuration the contact is between two parallel surfaces and it is more similar to that of a surface grinder. Anyways the rotating shaft of the grinding wheel can be tilted of 2° that is the slope of the sharp edge in the commercial blade disk (see figure 4.18). Such rotation was obtained by the use of guide pins.

The rotational motion of the disk is transmitted to the disk by means of an asynchronous three-phase motor. The motor has been plugged to inverter "Silcovert V" by Ansaldo. The inverter was remotely controlled by a PC through the RS485 serial interface with the communication protocol ANSI-x3.28-2.5-A4. Thus the rotational speed of the disk can be varied from the PC continuously up to 1500 rpm, that is the velocity at which the commercial machines usually perform the sharpening process. Therefore the influence of the rotational speed of the disk on the sharpening process can be easily investigated.

The disk was fitted on the rotating shaft by means of a steel clamping disk in order to control the constraint conditions of the disk. In fact clamping disks with different diameters can be used in order to change the radius of the inner constraint on the disk. Thus the natural frequencies of the disk can be changed further. A high stiffness shaft was designed so as not to affect the vibrational behaviour of the flexible disk. The rotational motion was transmitted to the shaft by a belt drive. The pulley can be seen in figure 4.16. The belt drive was chosen since the shaft vibrations must be reduced as much as possible in order to preserve the displacement measurements.

The bearing block of the rotating shaft was endowed with sensors properly placed in order to gather the rotational speed and the out-plane displacements of the flexible disk during the sharpening process. The Proximitor®

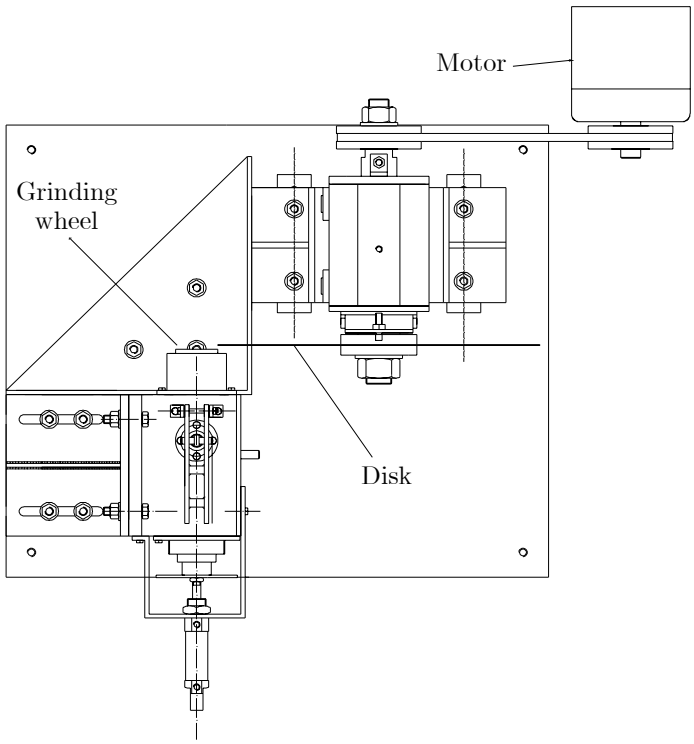

Figure 4.16: Top drawing of the test rig

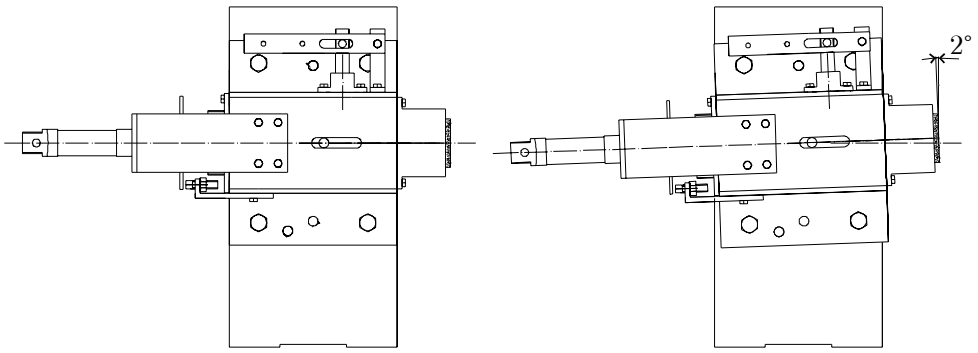

Figure 4.17: Rotation of the grinding wheel: abrasive wheel perpendicular to the disk surface (a); Abrasive wheel tilted of 2° on a plane tangent to the disk edge (b)

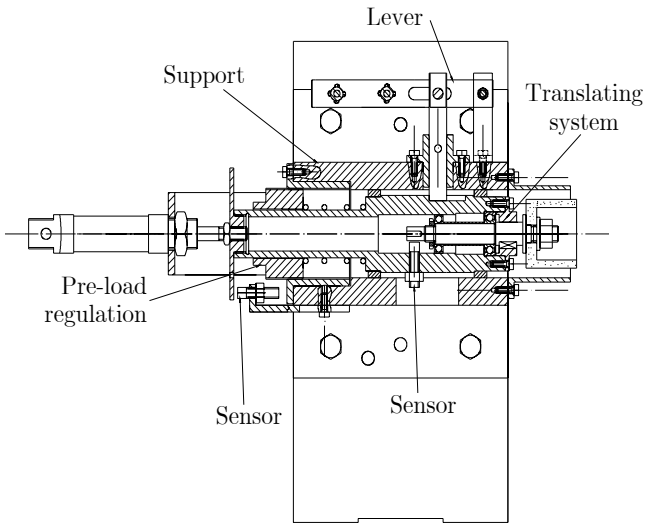

Figure 4.18: Section of the grinding wheel block

sensors were used as displacement non-contacting transducers. The rotational velocity of the shaft can be inferred by the elaboration of the triggered signal of the sensor placed on a section of the shaft with four equidistant grooves. The sensors which measure the out-plane displacements of the flexible disk, were placed on plate supports fitted to the bearing block. Each plate support can be placed at any angle of the disk wherever the others are. Moreover, the radius at which the displacement is gathered can be varied since the sensors can be moved radially inside their housings.

The support block of the grinding wheel is composed by three parts. The first part is a square block that bears the sharpening device and the second part is the support of the translating system. The translating part is the third part that carries the grinding wheel. The latter is formed by a grinding wheel, the shaft on which the grinding wheel is fitted and a translating sleeve that supports the rotating shaft. Figure 4.18 shows the section of the grinding wheel block.

The grinding wheel shaft is fitted inside the translating sleeve by means of two radial rolling bearings so that it can freely translate and rotate at the same time. The translating system is pushed against the disk by a preloaded spring. The rotating disk drags the grinding wheel because of the sliding friction. The sliding friction was estimated to have a value of about 0.4. The translating system has a 1.3 kg mass and the pushing spring has a 16.6 N/mm stiffness coefficient. The natural translating frequency was

set to be about 113 rad/s (17.98 Hz) that is the natural frequency of the commercial paper cutting machine. The translating sleeve was fitted inside a hole in the support by means of teflon rings so as to reduce friction during translation. The rotational displacement of the sleeve is avoided by means of a pin that runs inside a axial groove of the support.

The vibration and the rotational velocity of the grinding wheel shaft can be measured. A sensor measures the displacement of an external disk while an other measures the trigger of a four grooves section. The two sensors are shown in figure 4.18.

The contact force is one of the main parameters affecting the onset of the vibrational phenomenon. A thread sleeve was designed to change the preload of the spring in order to change the force pushing the grinding wheel on the disk.

The translation of the grinding wheel is driven unlocking the translating sleeve either manually by a lever or automatically by a pneumatic actuator. The pneumatic actuator breaks off the contact between the grinding wheel and the disk when it is activated. The pneumatic actuator is driven by a solenoid valve whose solenoid is driven through the PC. Thus pressurized air can be sent through the actuator at established intervals so as to test the disk excitation caused by short or long, continuous or intermittent sharpening.

Moreover, the rotation of the abrasive wheel shaft can be avoided by the insertion of a tongue in a groove on the shaft. Such test permits to analyze the influence of the sliding velocity between the abrasive wheel and steel disk on the self-excited vibrations phenomenon.

An abrasive cylindrical wheel was used in the test. However, more grinding wheels, with different geometries or different hardnesses, can be used in order to investigate even more deeoly the influence of the friction coefficient on the vibration induced by the sharpening process.

4.4.2 Fem modal analysis

A numerical analysis was carried out by means of the commercial software ANSYS® . Such fem software was used also to analyze the natural frequency and mode shape of the grinding wheels support of the test rig. The results of the same analysis carried out on the commercial paper cutting machine are reported in section 4.3.

The disk of the test rig was meshed with `shell63` elements. The nodes on the inner collar were fully constrained in order to model the clamps of the disks. A reduced analysis of the out-of-plane displacements of the disk was carried out. The material properties of common steel were used (Young's modulus E=210 GPa and density ρ=7800 kg/m^3). The disk used in the test

n	m	f_n	n	m	f_n
0	0	118.06	0	1	743.83
1	0	112.71	1	1	787.42
2	0	144.07	2	1	928.04
3	0	266.10	3	1	1180.30
4	0	457.61	4	1	1540.70
5	0	703.61	5	1	1987.30
6	0	1001.20	6	1	2498.90
7	0	1351.20	0	2	2152.90
8	0	1755.30	1	2	2204.70
9	0	2215.50	2	2	2367.50
10	0	2734.40	3	2	2657.40

Table 4.2: Natural frequency of the test rig disk from fem analysis

rig had a constant 3 mm thickness, an outer diameter of 380 mm and it was clamped at a 90 mm diameter.

Table 4.2 shows the natural frequencies of the constant thickness disk while table 4.1 shows the results for the tapered thickness disk of the paper cutting machine. The frequencies (1,0) of the two disks are very close. The thickness of the disk was chosen in fact to have a modal similarity between the paper cutting machine and the test rig.

The natural frequencies and the mass normalized mode shapes were also calculated by means of the procedure described in section 4.2.2. Table 4.3 shows the results. A good agreement can be found between the numerical value (table 4.2) and the theoretical value (table 4.3).

The natural frequencies of the supporting block of the grinding wheel were also examined. A solid model of the support were made and meshed in ANSYS® . The `solid92` solid element were used. They are 10 nodes tetrahedral elements. The Block-Lanczos solution method was employed.

Steel properties were used as material constants, i.e. Young's modulus E=210 GPa and density ρ=7800 kg/m^3. The grinding wheel was not modelled, but the hole of its housing was filled up in order to take into account its influence on the natural frequencies of the support. The hole was filled with a material with a density ρ=3614.5 kg/m^3 so that it had the same weight of the grinding block (2 kg). The base of the support was fully constrained.

The lower frequencies, calculated with the Block-Lanczos method, resulted 134.87 Hz, 258.28 Hz, 542.96 Hz and 859.41 Hz. The related mode shapes are shown in figure 4.19. The first mode was a torsion of the support, the second one was a flexural mode and the third one was a flexural-torsional

n	m	f_n	C_n	D_n	E_n	F_n
0	0	117.36	1.06	-2.52×10^{-1}	-1.18	-1.36
1	0	111.90	1.10	3.20×10^{-1}	1.36	1.00
2	0	143.55	2.24	3.73×10^{-1}	3.77×10^{-1}	2.64×10^{-1}
3	0	265.34	2.80	2.45×10^{-1}	6.71×10^{-2}	4.81×10^{-2}
4	0	454.77	3.26	1.39×10^{-1}	1.10×10^{-2}	8.14×10^{-3}
5	0	695.83	3.70	7.79×10^{-2}	1.66×10^{-3}	1.27×10^{-3}
6	0	983.96	4.11	4.39×10^{-2}	2.34×10^{-4}	1.86×10^{-4}
7	0	1317.81	4.50	2.49×10^{-2}	3.16×10^{-5}	2.59×10^{-5}
0	1	739.80	3.04	1.24×10^{-2}	-6.69×10^{-1}	-6.23
1	1	784.50	5.52×10^{-2}	1.13×10^{-2}	-3.13	-4.82
2	1	929.11	2.39	-8.06×10^{-3}	2.10	2.43
3	1	1188.62	3.16	-4.48×10^{-3}	8.64×10^{-1}	9.27×10^{-1}
4	1	1558.84	3.42	-2.10×10^{-3}	2.76×10^{-1}	2.95×10^{-1}
5	1	2018.66	3.65	-9.17×10^{-4}	7.38×10^{-2}	8.07×10^{-2}

Table 4.3: Natural frequency and mode shape of the test rig disk from theoretical analysis

	Mode 1	Mode 2	Mode 3	Mode 4
Displacement U_x	0.21558	0.17842	-0.15101	0.11908
Displacement U_y	0.21518	0.00019	0.09275	0.00020
Displacement U_z	-0.00066	-0.12304	0.11506	0.18623

Table 4.4: Modal matrix of the test rig support of the grinding wheel

mode. The fourth mode is a torsion of the support around the grinding wheel axis. The first mode is close to the natural frequency (2,0) of the disk and the second mode has a natural frequency close to the (3,0) natural frequency of the disk. The analysis ignored the natural frequency of the grinding wheel (f_n=18 Hz). As such frequencies were calculated ignoring the natural frequency of the grinding wheel and making big approximations, they are valid only for qualitative purposes.

In order to carry out a lock-in instability analysis that took into account also these natural frequencies, the mode shape matrix of the grinding wheel support was computed with respect to the fem node on the axis of the grinding wheel since this is the joint point with the spring/mass subsystem of the lock-in instability model. Table 4.4 shows such modal matrix.

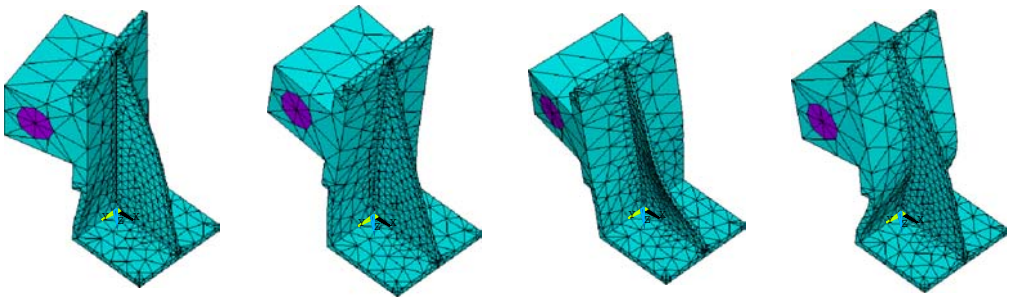

(a) (b) (c) (d)

Figure 4.19: Mode shapes of the grinding wheels support block of the test rig: first mode $f_n = 134.87$ Hz (a); second mode $f_n = 258.28$ Hz (b); third mode $f_n = 542.96$ Hz (c); fourth mode $f_n = 859.41$ Hz (d).

4.5 Fem transient dynamic simulations

4.5.1 Model definition

Before doing the experimental analysis, a numerical analysis of the process was carried out by means of the explicit fem software LS-DYNA® . The aim of such analysis was to see if it was possible to simulate the sharpening process just defining few parameters, like the friction curve between the disk and the grinding wheel, in order to see their effect on the sharpening process. The aim was to have a model that tuned with the experimental results could be a predictive tool in the design of sharpening machines. However the simulation of such problems involves some drawbacks. First of all the simulation time is very large. In order to simulate a short sharpening process of 1.2 s the software takes about 16 hours. An other problem concerns the comparison of numerical and experimental results. In fact, the experimental signals, gathered by no-contact displacement sensors, are the displacements of a circle of the disk referred to the fixed frame. On the contrary, during the simulations the displacements of the disc nodes can be collected only referring to the rotating system. However, such a problem can be simply sorted out by keeping in mind the relationship between the displacement in a fixed or rotating frame, as stated in section 4.2

The sharpening process is a quick process that occurs in a very short time. So a transient analysis is doubtlessly necessary. So the process has been simulated by means of the explicit fem code LS-DYNA® . Explicit analysis is quite suitable for dynamic simulations such as impact and crash even if it

Nodal diameters n	Nodal circle m	Natural frequency f_n
0	0	39.35
1	0	37.57
2	0	48.02
3	0	88.70
4	0	152.54
5	0	234.54
6	0	333.74

Table 4.5: Natural frequency of the 1 mm thickness disk clamped at the inner circle and free at the outer radius

can become prohibitively expensive for long duration or static analyses. The term explicit refers to time integration algorithms. In the explicit approach, internal and external forces are summed at each node point, and nodal acceleration is computed by dividing by the nodal mass. The solution is obtained by integrating acceleration in time. The maximum time step size is limited by the Courant condition, producing an algorithm which typically requires many relatively inexpensive time steps.

The model was built up according to the geometrical characteristics of the test rig. Then a disk with the outer diameter of 380 mm and with the inner diameter of 90 mm was modelled. The disk thickness was set to 1 mm. In order to have all the tools to interpret the results of the simulations the natural frequencies of the disk 1 mm thick are given up to 300 Hz: table 4.5 reports the natural frequencies calculated with the fem code ANSYS® .

Shell Hughes-Liu elements with four integration points have been utilized in the fem model. Such elements have been chosen especially because they have not hourglass energy problems. A model of a perfectly elastic material with steel properties has been used to represent the disk blade behaviour. A little damping has been added to the system in order to avoid too high oscillations. The disk was meshed with 10 radial elements and 32 circumferential elements. The grinding wheel was meshed with 2 radial elements and 20 circumferential elements.

In the test rig the rotating flexible disk is connected to the shaft by means of a very stiff tight fit. So the circular disk model was free at the outer radius and clamped at the inner radius by a central core, assumed to be rigid. The rigid core was constrained to just rotate around its axis at given angular velocities. The simulations were mainly carried out forcing the rigid core to

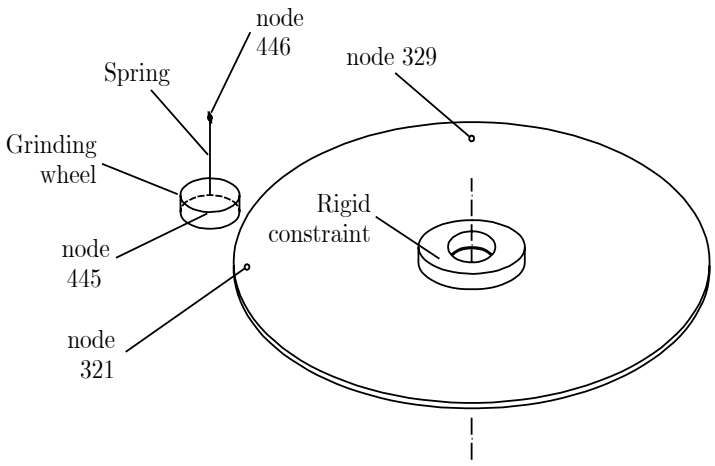

Figure 4.20: Disk blade model with one grinding wheel

rotate with a speed of 157 rad/s (25 Hz) which is the operating velocity of the test rig. The model of figure 4.20, with one wheel pushing perpendicular to the disk surface, has been considered. The grinding wheel, assumed idle, with a 50 mm diameter, a 1.3 kg mass and a 32.4 kgmm^2 inertial momentum, was modelled as a rigid body. The grinding wheel had a 50 mm diameter and it touched the disk up to the 185 mm diameter. The depth of the contact arch was 5 mm. The idle grinding wheel was pushed against the disk by a spring placed in the wheel centre. Such a spring had a 16.6 N/mm stiffness. The initial gap between the disk and grinding wheel surfaces was set to 2 mm.

The rotational speed of the rigid core of the disk was applied as a sinusoidal ramp in order to avoid the onset of huge inertial force. Figure 4.21(a) shows the rotational velocity of the rigid core as a function of time. It is shown that after 0.05 s the rigid core reached the steady state value and that the simulation took 5 s to complete.

In order to push the grinding wheel against the disk surface the node 446, shown in figure 4.20, was moved along the wheel axis. As the gap between the abrasive wheel and the disk is 2 mm, a greater displacement had to be applied in order to generate a contact force. The displacement, shown in figure 4.21(b), was applied with a sinusoidal curve similar to the rotational speed curve. The steady state value was again reached after 0.05 s. This value was kept very small in order to simulate the impact of the grinding wheel on the steel surface.

The contact parameter definition is the principal problem concerning the

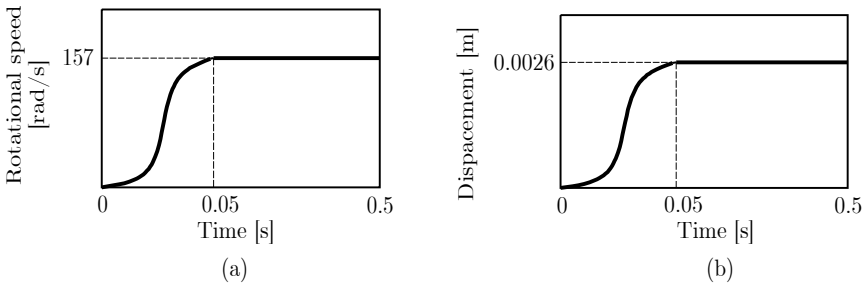

Figure 4.21: Displacements imposed to the fem model: disk rotational speed (a) and spring displacement (b)

sharpening process simulation because it is the interface friction that couples longitudinal and transversal degrees of freedom and makes the system potentially unstable. Moreover it is difficult to find an experimental curve of abrasive on steel friction coefficient versus sliding velocity. However, since the cutting and repulsing forces during the grinding process have about the same size when the cutting ratio is small [96], the static friction coefficient was assumed equal to 1. The sliding friction coefficient was assumed equal to 0.4, lightly greater than for steel on steel. Moreover the friction curve was assumed to have an exponential shape:

$$\mu = FD + (FS - FD)\mathrm{e}^{-DC|v_{rel}|} \tag{4.90}$$

where FS is the static friction coefficient, FD is the dynamic friction coefficient, DC is the exponential decay coefficient and v_{rel} is the relative velocity of the surfaces in contact. For DC, values of 100 and 10 were considered in order to simulate different contact behaviours ranging from a smooth to an irregular friction curve (see figure 4.22).

When the grinding wheel touched the rotating disk oscillations began. The oscillation of the node 445, shown in figure 4.20, were recorded as the oscillation of the grinding wheel. Moreover the displacements perpendicular to the disk surface of nodes 321 and 329 were gathered in order to have the displacements of two disk nodes placed at 90° each other. This permitted to collect displacements data corresponding to nodal and anti-nodal diameters. As stated before, the displacements of the disk nodes were referred to a rotating co-ordinate system fixed to the disk. Moreover, the rotational velocity of the grinding wheel, produced by the sliding contact force, was measured. All the data were collected with a 1 kHz frequency while the time step of the

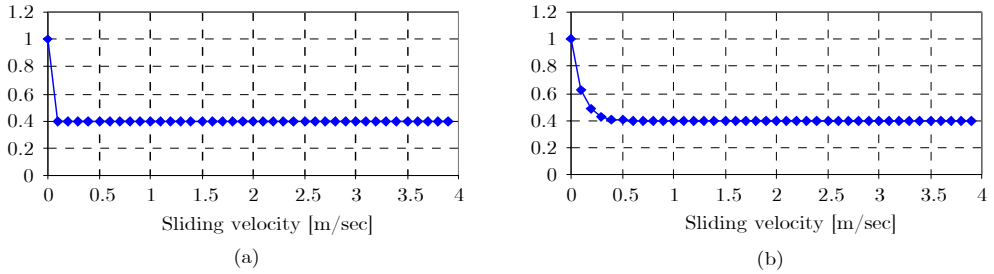

Figure 4.22: Friction coefficient curve: DC=100 (a) and DC=10 (b)

explicit fem solver was 1×10^{-6} s.

Even if all the data were investigated, the analysis described in the next section is focused on the out-of-plane displacement of the disk and on the axial oscillation of the grinding wheel. Nodes 329 and 445 of figure 4.20 were taken as reference to the disk and grinding wheel displacements respectively. The Power Spectral Density (PSD) of the gathered displacements was performed in order to analyze the energy of the signals in the frequency domain. In the next section the results of some of the several simulation carried out to find the influence of some parameters are shown.

4.5.2 Impact and sharpening simulations

First, in order to identify natural frequencies, an impact simulation of one grinding wheel against the non-rotating disk blade was carried out. It can be assumed that the sudden approach of the grinding wheel produces an excitation which is mainly noise. So when the disk angular velocity is set to zero the corresponding PSD peaks show just the natural frequencies of the system. In figure 4.23 the PSD of displacements related to a disk blade peripheral node and to a grinding wheel node are reported as representative of the dynamic behaviour of the two components. The disk blade signal spectrum, shown in figure 4.23(a), exhibits 40 Hz and 140 Hz pronounced peaks and some smaller peaks (about 60 Hz, 80 Hz and 120 Hz). Such frequencies correspond to the natural frequencies of the global disk-grinding wheel system. The grinding wheel signal spectrum, shown in figure 4.23(b), exhibits only a pronounced 18 Hz peak, that is the natural frequency of the grinding wheel system. So it can be deduced that the grinding wheel acts as a filter for higher order harmonics.

Several simulations were carried out to highlight the influence of some

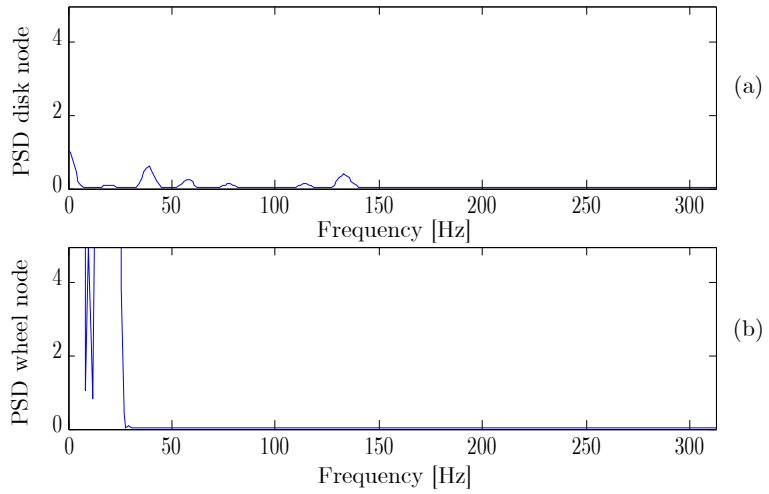

Figure 4.23: PSD of impact simulation for non-rotating disk blade: corresponding to a peripheral node of the disc blade (a) and to a node of the grinding wheel (b)

parameters on the onset of self-excited vibrations during the sharpening process. Thus, a basic test was chosen and the following tests were carried out changing the value of one parameter at a time. This permits to compare tests and see the influence of each parameter.

The basic test was carried out with a disk rotating at a 25 Hz frequency and driving node 446 of the grinding wheel spring with a 2.6 mm displacement. In this way the contact force was about 10 N. The simulation final time was 0.5 s. The parameters of the friction curve of equation 4.90 were defined as follows: static friction coefficient $FS = 1$, dynamic friction coefficient $FD = 0.4$, exponential decay coefficient $DC = 100$.

Figure 4.24 shows the PSD of displacements related to a disk blade peripheral node and to a grinding wheel node. Figure 4.24(a) exhibits a big peak between 40 and 50 Hz. Inside this range there are the disk natural frequencies of the (0,0), (1,0) and (2,0) modes. Figure 4.24(b) exhibits a pronounced peak of the PSD of the abrasive wheel displacement at about 20 Hz. It seems that the natural frequency of the abrasive wheel which is about 20 Hz excites the disk. In fact the oscillations of the grinding wheel are referred to the fixed frame while the disk displacements are referred to the rotating frame. In the rotating frame, a 20 Hz harmonic force, rotating with a negative velocity of 25 Hz, excites the (1,0) disk mode at a 45 Hz frequency, the (2,0) mode at a 70 Hz frequency and the (4,0) mode at a 120 Hz

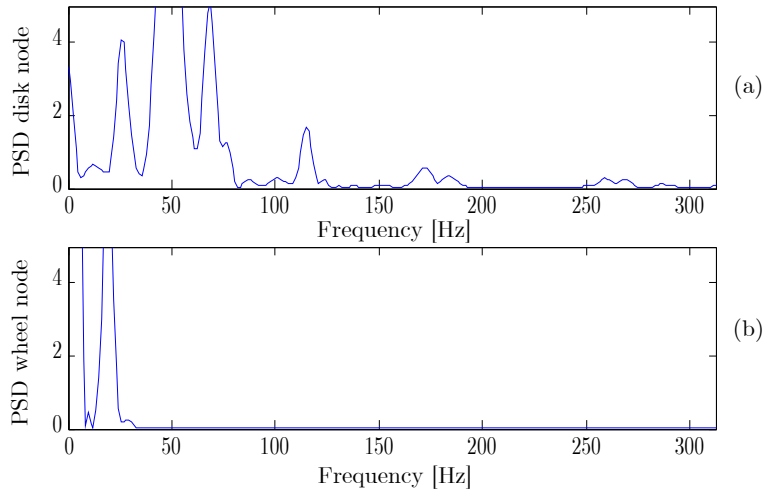

Figure 4.24: Basic simulation of the sharpening process: displacement PSD corresponding to a peripheral node of the disc blade (a) and to a node of the grinding wheel (b)

frequency. This explains the origins of the peaks at 20, 45 and 120 Hz on figure 4.24(a). The peak at 45 Hz is the highest because the mode excited by that excitation frequency is very close to its natural frequency.

The rotating velocity of the grinding wheel was also recorded. The value of the rotational speed of the grinding wheel grew up during the simulation up to a value of 372.54 rad/s, reached after 0.5 s i.e. at the end of the simulation. The velocity ratio was grossly equal to the ratio between disk and wheel radii as expected.

After the basic test a simulation with a reduced force pushing the abrasive wheel against the disk was carried out. In order to halve the pushing force, the displacement imposed to the node 446 of the abrasive system spring was reduced from 2.6 mm to 2.3 mm. In this way the force was roughly reduced from 10 N to 5 N. Figure 4.25 shows that all the peaks were at the same positions but with a much lower amplitude. Only the 120 Hz peak disappeared. It is obvious that reducing the value of the pushing force also the energy involved in the excitation is reduced. Also the sliding force is reduced and the grinding wheel rotational speed reached about 250 rad/s at the end of the simulation.

A test increasing the stiffness of the spring in the abrasive wheel system was carried out. The stiffness was changed from 16.6 N/mm to 33.2 N/mm. In order to keep the pushing force similar to the basic test the displacement

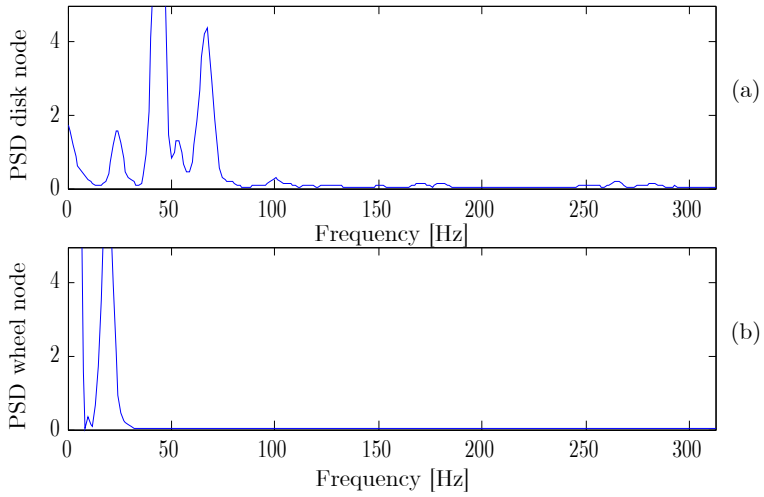

Figure 4.25: Simulation of the sharpening process with reduced load: displacement PSD corresponding to a peripheral node of the disc blade (a) and to a node of the grinding wheel (b)

of node 446, at the end of the spring, was reduced from 2.6 mm to 2.3 mm. The natural frequency of the spring-abrasive wheel system resulted changed from 18 Hz to 25.4 Hz. Figure 4.26 shows the PSD of displacements related to a disk blade peripheral node and to a grinding wheel node. In general terms, the amplitude of the peaks was reduced because the increased stiffness restricts the amplitude of the oscillations of both disk and abrasive wheel. Moreover, the peak are shifted a little toward higher frequencies. As already noted for the basic test the natural vibration of the abrasive wheel can excite some modes of the disk. In the rotating frame, a 25 Hz harmonic force, rotating with a negative velocity of 25 Hz, excites the disk (0,0) mode at a 25 Hz frequency, the (1,0) mode at a 50 Hz frequency and the (2,0) mode at a 75 Hz frequency. This explains the presence of the first three peaks of figure 4.26(a). Again the peak of the (2,0) mode is the highest because excited by a frequency very close to its natural frequency. The rotational speed of the grinding wheel did not show any significant variation.

A test with a reduced spring stiffness of 8.3 N/mm was then performed. Consequently, the natural frequency of the grinding wheel system was changed from 18 Hz to 12.7 Hz. The displacement imposed to the spring node was increased in order to maintain the value of the pushing force. Figure 4.27 shows the PSD of the displacement data gathered during the test. The PSD peaks of the disk displacement were shifted towards lower frequencies.

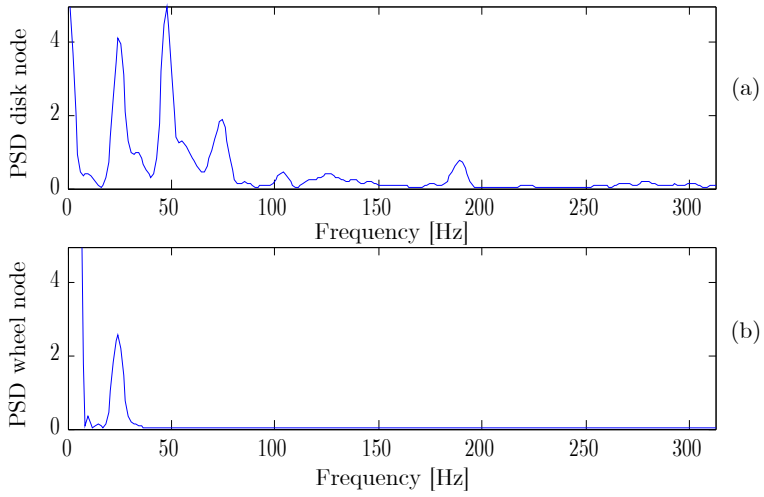

Figure 4.26: Simulation of the sharpening process increasing the spring stiffness: displacement PSD corresponding to a peripheral node of the disc blade (a) and to a node of the grinding wheel (b)

As the excitation frequency seemed again to be the natural frequency of the grinding wheel system, the (0,0) mode was excited with a 12.7 Hz frequency, the (1,0) mode with a 37.7 Hz frequency and the (2,0) mode with a 62.7 Hz frequency. However the peaks at about 25 Hz and 50 Hz are not explained. They seemed to be excited by 1X and 2X harmonics of the rotational speed. The rotational speed of the grinding wheel did not show big difference in comparison with the basic test.

A test with an incremented dynamic friction coefficient was carried out. Such coefficient was increased from $FD = 0.4$ to $FD = 0.6$. Figure 4.28 shows the PSD of disk and grinding wheel node displacements. A comparison between figure 4.24 and figure 4.28 showed that the features of the PSD of the two test were almost the same. However, some little differences could be singled out. In the test carried out with an increased dynamic friction coefficient the peaks at about 20, 43 and 68 Hz were a little bigger while the 120 Hz peak was reduced. On the other hand, the rotational speed of the grinding wheel showed a considerable modification. The maximum value of the rotational speed, reached at the end of the simulation, passed from 372.54 rad/s to 554.83 rad/s. This is reasonable because the rotational speed of the grinding wheel depends directly on the sliding force of the contact. Thus, the amplitude of the peaks did not seem to depend on the relative velocity between the disk and the grinding wheel. Such behaviour

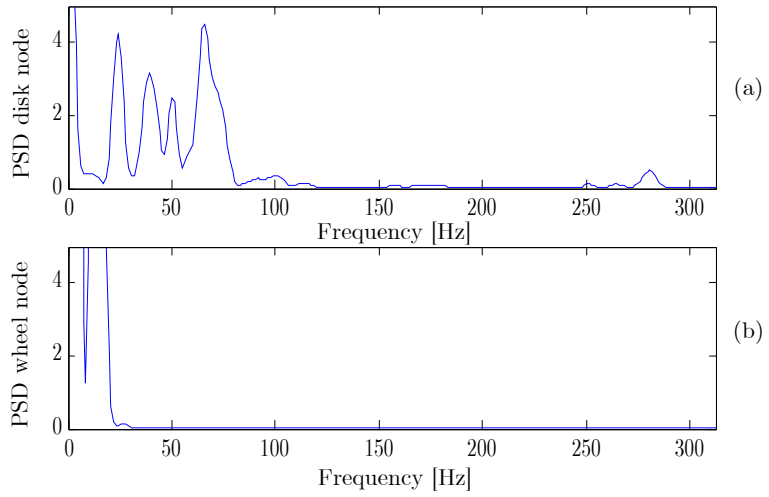

Figure 4.27: Simulation of the sharpening process decreasing the spring stiffness: displacement PSD corresponding to a peripheral node of the disc blade (a) and to a node of the grinding wheel (b)

was not confirmed by the experimental tests and this is one of the reasons the simulation was not considered reliable.

Moreover, a test with a reduced rotational speed of the disk of 100 rad/s (15.9 Hz) was carried out. Figure 4.29 shows the results of this test. The excitation frequency seemed again to be the axial natural frequency of the grinding wheel. The modes of the disk were then excited with different frequencies: the (0,0) mode was still excited by a 18 Hz frequency while the (1,0) mode was excited by a 34 Hz frequency and the (2,0) mode by a 50 Hz frequency. Such excitation frequencies are very close to the natural frequencies of the (1,0) and (2,0) modes, which are 37.57 an 48.02 Hz respectively. So while the peak at about 45 Hz in the basic test was due to the (1,0) mode, in this test it was due to the (2,0) mode. No excitation above 120 Hz appeared in the PSD of the disk node displacement. Moreover, in this case the global excitation appeared to be less. In fact, the reduction of the rotational speed corresponds to the reduction of the energy of the system. The rotational speed of the grinding wheel reached about 260 rad/s at the end of the simulation. Again, the velocity ratio was equal to the ratio of the disk and wheel radii.

The influence of the friction curve was then tested. The decay coefficient of the friction curve (see equation 4.90) was changed from $DC = 100$ to $DC = 10$. The results of the simulations, shown in figure 4.30, do not reveal

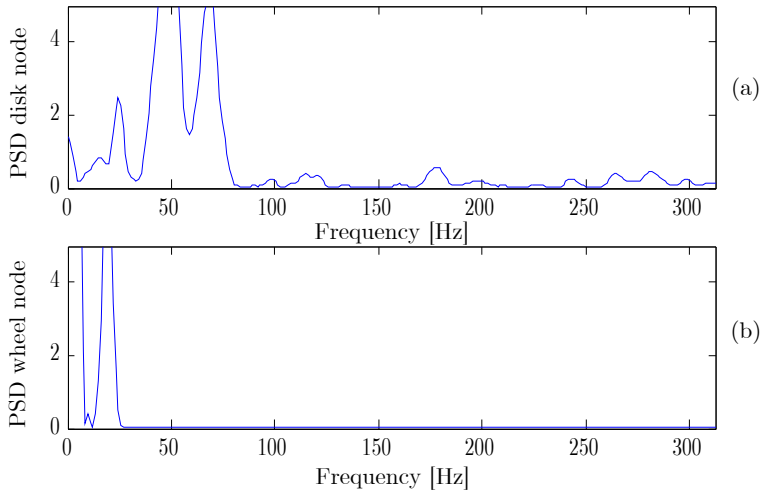

Figure 4.28: Simulation of the sharpening process increasing the dynamic friction coefficient: displacement PSD corresponding to a peripheral node of the disc blade (a) and to a node of the grinding wheel (b)

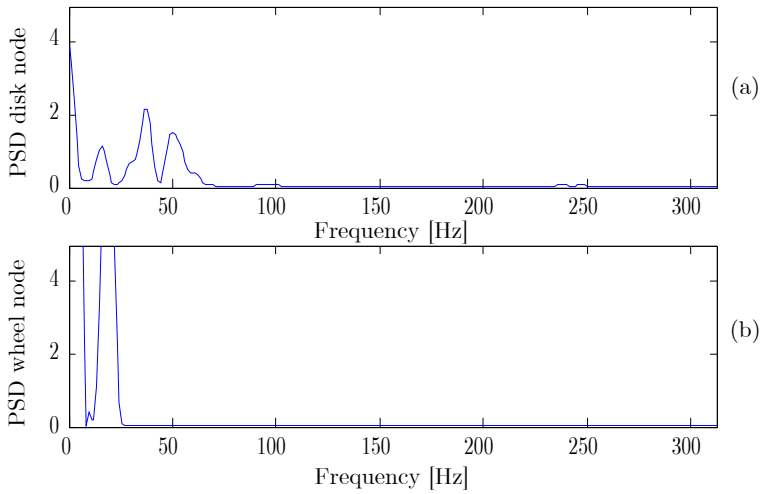

Figure 4.29: Simulation of the sharpening process reducing the disk rotational speed:displacement PSD corresponding to a peripheral node of the disc blade (a) and to a node of the grinding wheel (b)

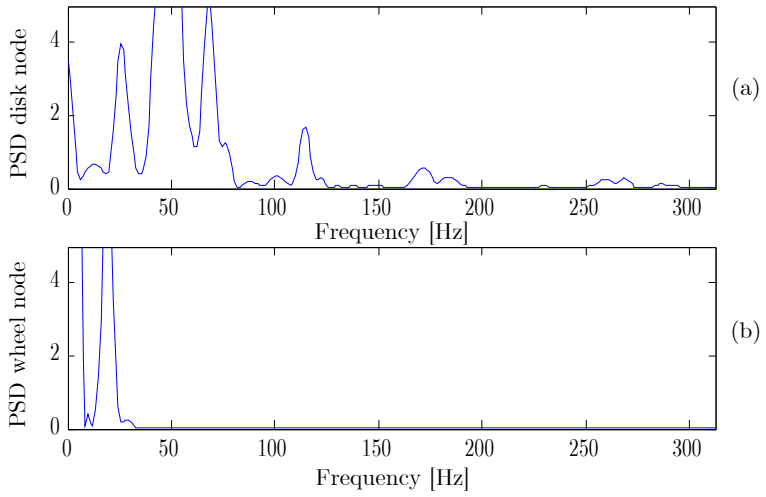

Figure 4.30: Simulation of the sharpening process changing the friction curve: displacement PSD corresponding to a peripheral node of the disc blade (a) and to a node of the grinding wheel (b)

any significant difference. As such result was unexpected, further analysis were carried out. The grinding wheel angular speed was checked in the two cases observing that it took different values so as to reach the same friction force in the sliding contact.

The discussed analysis did not show which parameters most influence the onset of vibrations during the sharpening process. The only conclusion that could be drawn is that high amplitude vibrations arose when the axial natural frequency of the grinding wheel system coincided with the "apparent" natural frequencies of the disk. This conclusion is very similar to the lock-in instability conclusions.

Finally, in order to complete the analysis a Campbell diagram of the responses of the disk was drawn. Several test simulations, with the parameters of the basic simulation, were carried out to build the waterfall plots shown in figure 4.31. The angular velocity range from 0 to 1500 rpm was investigated. In the presented plot the peaks related to 1X and 2X harmonics are the most evident. The highest peaks are in the range from 30 Hz to 60 Hz, where the natural frequencies of the (0,0), (1,0) and (2,0) modes lie.

In the investigation on the influence of stick-slip on the disk vibrations a torsional spring was also added to the axis of the disk model. From some preliminary trials it could be inferred that decay coefficient dependence is more evident when the torsional spring stiffness is smaller. Moreover when

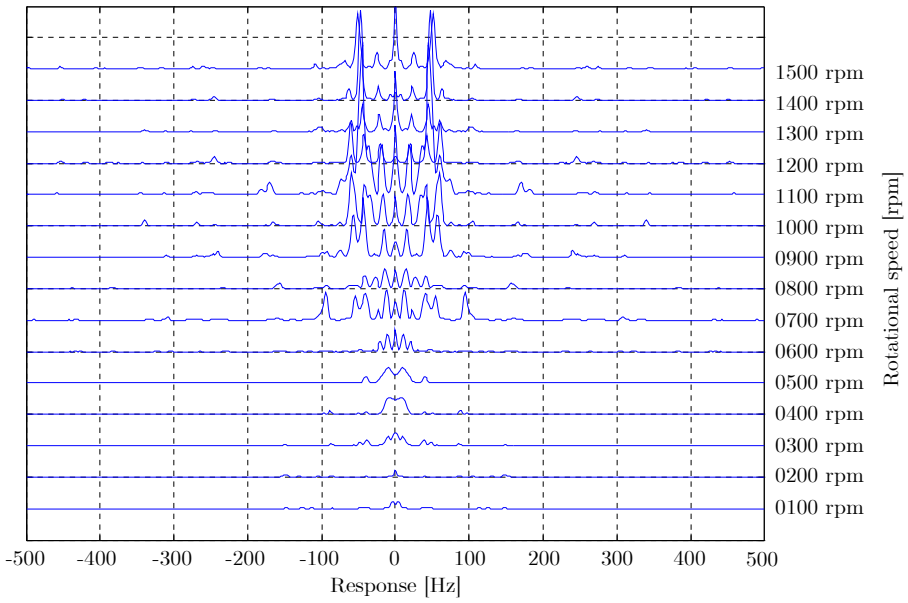

Figure 4.31: Waterfall diagram obtained by simulation data

the peaks of the grinding wheel signal are higher, those of the disc signal are lower as if the former acted as a dynamic damper for the latter.

Comparing the plots with different friction decay coefficients a clear trend is not found. Some conclusions can be drawn, some of which are obvious:

- A reduction of the contact force causes a reduction of the peak amplitudes.
- An increase of the spring stiffness causes a reduction of the peak amplitudes and a shift of the excitation frequency towards higher frequencies.
- A reduction of the rotational disk velocity causes a reduction of the peak amplitudes and the disappearance of peaks above 120 Hz.
- The variation of the dynamic friction coefficient or of the friction curve decay coefficient does not causes any variation in the response of the model.

Therefore, the fem model resulted inappropriate especially in the representation of the contact law. The reasons why the results were not satisfactory can be found in the mesh, which could be not accurate enough, or in the friction curve, which could differ from the real one. On the other hand an

improving of the mesh causes a huge increase in the calculation time which makes the use of the fem model again inconvenient.

An experimental campaign was then planned in order to clarify the influence of the parameters involved in the sharpening process. Moreover, the experimental test could be used to tune the fem model with the real system.

4.6 Experimental investigation

The designed test rig permitted to perform several tests. A short description of the tests carried out is given hereafter.

Planarity test The disk were cut from a sheet steel of the proper thickness and shaped on a lathe at the designed diameter. As the manufacturing process could cause undesired deformations of the disk surface, the planarity of the testing disks was checked before the execution of the experiments. The planarity test was carried out rotating the disk by hand and checking the displacement recorded by the Proximitor® probes.

Basic sharpening test In order to evaluate the effect of each parameter on the onset of self-excited vibrations during the sharpening process was necessary to choose a basic sharpening test. Each test was obtained changing only one parameter at a time and the results where compared with the basic test result.

This test was carried out with a contact force of about 50 N and a spring elastic constant of 16.6 N/mm. The grinding wheel was idle and its axis was parallel the disk axis. The contact area was kept dry. The sharpening process was intermittent, namely a 1 s sharpening was followed by a 1 s break and again by a 1 s sharpening. The first sharpening was done when the rotational velocity of the disk reached a steady state value. The three sensors, that measured the disk displacements, were placed with a relative phase angle $\alpha = \pi/2$. Two more signals were gathered: one measured the axial vibration of the grinding wheel and the other the rotational speed of the disk. A waterfall plot was obtained repeating the test at different rotational speeds of the disk: the speed was increased from 100 rpm (1.6 Hz) up to 1500 rpm (25 Hz) by 100 rpm steps. The complex integral Fourier transform of the disk displacement signals was calculated from each test.

Pre-load change The contact force developed during the sharpening process can be varied by the change of the pre-load of the spring that

pushes the grinding wheel against the disk. Thus, a test with a reduced force of 25 N was carried out. A change in the contact force causes also a change in the sliding force that is related to the former by the friction coefficient.

Change of the sharpening time The translation of the grinding wheel was driven by a pneumatic actuator that permitted to change the sharpening time. Three tests were planned: an intermittent test (two 1 second sharpening times interrupted by a 1 s break); a short time test (a 1 s sharpening time); and a long time test (a 5 s sharpening time).

Friction change The contact surface between the abrasive wheel and the disk was sprinkled by a water stream in order to reduce the friction coefficient. A reduction of the friction coefficient caused also a reduction of the sliding velocity between the grinding wheel and the disk. Moreover, the water stream could change the friction curve in an unpredictable manner.

Non-rotating abrasive wheel test The grinding wheel idle rotation can be avoided. The tests carried out with this configuration showed the influence of the sliding velocity between the disk and the grinding wheel on the vibrations amplitude.

Tilted abrasive wheel test The axis of the grinding wheel can be tilted of 2°, as already stated. Thus, the contact geometry can be varied from a surface to a single point.

Change of the sensors position The tests were carried out also with a phase angle between the sensors on the disk $\alpha = \pi/4$ in order to investigate more disk modes.

Change of the disk thickness Some tests were carried out also with a 1 mm thickness disk. Such a disk showed to be too compliant and, in order to keep the vibration amplitudes small a very low pre-load was applied to the pushing spring and the maximum rotation speed was limited to 1100 rpm.

The results of the test were analyzed to investigate the modal behaviour of the grinding wheel-disk system during sharpening and the self-excited vibration onset. Before the analysis of the sharpening the modal characteristics of the disk and of the grinding wheel support were preliminarily found by impact tests.

4.6.1 Signal analysis

In this section a short review of the methods of signal analysis is shown. Such tools were used in processing the experimental results. Two methods are introduced. The first is a method, proposed by Lee [94], to evaluate the frequency response function for rotating structures. The second method was introduced to perform the integral Fourier transform of the signal without loosing information contained in the signal, such as the directivity of the modes and the number of nodal diameters.

Although the presence of backward and forward travelling wave modes in rotating disks has been extensively investigated in the literature, the modal characteristics, such as the directivity of the modes and the number of nodal diameters, have seldom been emphasized because of the inherent limitation in the analysis of conventional frequency response functions. When conventional modal testing techniques are applied to a rotating disk, the estimated frequency response functions lose the directivity information of the forward and backward travelling waves, since the measured excitation forces and responses are treated as real quantities.

Recently, a new complex modal testing theory based on the two-sided directional frequency response functions (dFRFs) has been developed for rotating shafts, the essence of which is to adopt complex notations treating pairs of time histories as complex quantities. Lee and Kim [94] derived the complex modal testing theory for a rotating disk by employing the complex wave co-ordinates.

The testing method requires simultaneous excitations at two stations, separated by an angle α using two independent exciters and simultaneous measurements at the same stations (see figure 4.32). In essence, the method does not differ from the classical two-input/two-output technique. However, the dFRF estimation procedure is different from the conventional one in that it treats two real forces (responses) as a complex-valued force (response).

Firstly, the conventional frequency response functions (FRFs) between real inputs and outputs, such as $H_{11}(\mathrm{i}\omega)$, $H_{12}(\mathrm{i}\omega)$, $H_{21}(\mathrm{i}\omega)$ and $H_{22}(\mathrm{i}\omega)$ are estimated and then the dFRFs between complex input $g = f_1 + \mathrm{i}f_2$ and output $p = w_1 + \mathrm{i}w_2$, are computed using the direct transformation relation

$$2H_{gp}(\mathrm{i}\omega) = H_{11}(\mathrm{i}\omega) + H_{22}(\mathrm{i}\omega) - \mathrm{i}[H_{21}(\mathrm{i}\omega) - H_{12}(\mathrm{i}\omega)] \quad (4.91)$$

$$2H_{\hat{g}p}(\mathrm{i}\omega) = H_{11}(\mathrm{i}\omega) - H_{22}(\mathrm{i}\omega) + \mathrm{i}[H_{21}(\mathrm{i}\omega) + H_{12}(\mathrm{i}\omega)] \quad (4.92)$$

where $H_{gp}(\mathrm{i}\omega)$ and $H_{\hat{g}p}(\mathrm{i}\omega)$ are the normal and reverse dFRFs and, $\hat{g} = f_1 - \mathrm{i}f_2$.

Note here that the method uses conventional, but two-sided, FRFs which are conjugate even functions of ω and that it is sufficient to have one exciter

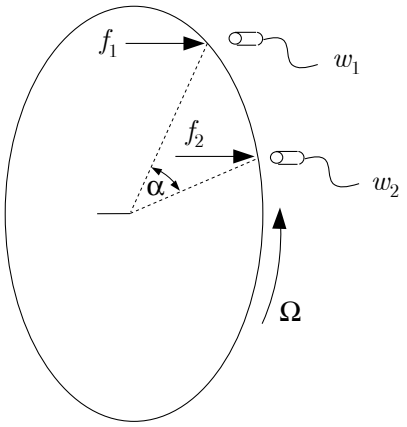

Figure 4.32: A schematic of the experimental modal analysis of a rotating disk

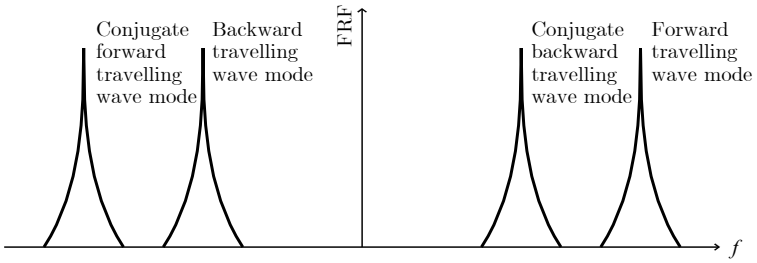

Figure 4.33: Example of real frequency analysis

fixed at a station and three measurements at $\varphi = 0$, $\varphi = -\alpha$ and $\varphi = +\alpha$ as in the experimental test rig.

The two sided FRFs are characterized by four peaks for each mode as shown in figure 4.33. In fact the modes considered as travelling wave are present with their conjugate.

Further analysis suggests that when $sin(n\alpha) = 1$ the effect of the conjugate modal contribution associated with n nodal diameters vanishes in the normal dFRF, $H_{gp}(\mathrm{i}\omega)$, while both the original and conjugate modal contributions associated with n nodal diameters disappears in the reverse dFRF, $H_{\hat{g}p}(\mathrm{i}\omega)$. The normal dFRF shows then only two peaks: the peak at positive frequencies is related to the forward travelling wave mode and its track in the waterfall plot is right tilted; the peak at negative frequencies is related to the backward travelling wave mode and its track is right tilted. In other

Angular distance α between two stations	(n, m) modes of separation	(n, m) conjugate modes of separation
$\pi/2$	(1,•), (5,•), (9,•), ...	(3,•), (7,•), (11,•),...
$\pi/4$	(2,•), (10,•), ...	(6,•), (14,•), ...
$3\pi/2$	(3,•), (7,•), (11,•), ...	(1,•), (5,•), (9,•), ...
$\pi/8$	(4,•), (20,•), ...	(12,•), (28,•), ...
$3\pi/4$	(6,•), (14,•), ...	(2,•), (10,•), ...

Table 4.6: Comparison of the fem and experimental modal testing of the rig support of the abrasive wheel

words, separation of the corresponding forward and backward travelling wave modes is achieved in the normal dFRF when

$$n\alpha = (4k+1)\frac{\pi}{2} \qquad k = 0, 1, 2, \ldots \tag{4.93}$$

Separation of the corresponding conjugate forward and backward travelling wave modes is achieved in the normal dFRF when $sin(n\alpha) = -1$ or

$$n\alpha = (4k+3)\frac{\pi}{2} \qquad k = 0, 1, 2, \ldots \tag{4.94}$$

The track of the conjugate forward and backward travelling wave modes are left tilted. In the reverse dFRF all the corresponding modes are absent.

In practice, the angular positions for sensors and actuators should be determined with consideration of the modes of interest for modal testing and the interference between sensors and actuators. A typical selection of angles associated with the modes of interest is summarized in table 4.6.

For example, with $\alpha = \pi/2$ the forward and backward travelling waves associated with the $(1, \bullet)$, $(5, \bullet)$ and $(9, \bullet)$ modes are simultaneously separated in the normal dFRF. The peaks of the forward travelling wave mode are in the right quadrant and those of the backward travelling wave mode in the left quadrant. At the same time the conjugate forward and backward travelling waves associated with the $(3, \bullet)$ and $(7, \bullet)$ modes are simultaneously separated in the normal dFRF but the peaks of the forward travelling wave modes are in the left quadrant while the peaks of the backward travelling wave modes are in the right quadrant. All the travelling waves associated with the $(1, \bullet)$, $(3, \bullet)$, $(5, \bullet)$, $(7, \bullet)$ and $(9, \bullet)$ modes disappear in the reverse dFRF. Other modes appear, along with conjugate modes, in normal and reverse dFRF. This property can be used to identify the number of nodal diameters from experimentally obtained FRFs. Distinction between the three

modes identified with $\alpha = \pi/2$ may not be a problem, since they normally occupy different frequency bands. However, further test with different values of angle α can be carried out when it is not possible to distinguish all the modes left.

This method was used to analyze the signal obtained with two different angles between the sensors: $\alpha = \pi/2$ and $\alpha = \pi/4$. As the test rig was not equipped with an exciter or with a force sensor, the axial displacement of the grinding wheel was considered as the excitation signal.

The use of the dFRFs makes it possible to have a clear physical insight into the backward and forward modes of rotating disk, by separating the modes in the frequency domain so that modal parameters can be identified. Such method is then very useful in the experimental modal analysis of rotating disk. However, the aim of the experimental investigation was the search of the onset of the self-excited vibrations. For this aim the dFRF technique is not useful, most of all because the displacement of the grinding wheel is used as excitation signal. In fact the normalization performed by the dFRF calculation decreases the amplitude of the peak when the self-excited vibration arises because the grinding wheel is subjected to big amplitude vibrations as well as the disk. Moreover, such normalization can increase the free vibration peaks of the disk since, in such cases, the displacement of the grinding wheel is almost zero.

The integral Fourier transform of a particular combination of the signals was then advised in order to maintain the dFRF advantages, i.e. without losing information about the directivity of the modes and their number of nodal diameters.

The two-sided fourier transform of a signal has four peaks for each mode as for the FRF. The integral Fourier transform of the complex signal $p = w_1 + \mathrm{i}w_2$ permits to distinguish between forward and backward travelling waves of each mode if the displacement signals w_1 and w_2 of two sensors placed at an angular phase α are available. Such analysis permits to distinguish between forward and backward travelling waves of each mode with the same rules of the normal dFRF as stated in equations 4.93 and 4.94, and in table 4.6.

Such assertion can be easily demonstrated. In fact the out-of-plane displacements w_1 and w_2 due to a single mode (i.e. due to two travelling waves) and gathered from two sensors placed at an angular phase α are given by

$$w_1 = \cos(-\Omega t) \tag{4.95}$$

$$w_2 = \cos(n\alpha - \Omega t) \tag{4.96}$$

where Ω is the rotational velocity. The Fourier transform of the signal $p =$

$w_1 + \mathrm{i}w_2$ is given by

$$\begin{aligned}\mathcal{F}_\mathrm{I}\left[\cos(-\Omega t) + \mathrm{i}\cos(n\alpha - \Omega t)\right] = \\ = \sqrt{\frac{\pi}{2}}\{\delta(\omega-\Omega)[1-\sin(n\alpha)] + \delta(\omega+\Omega)[1+\sin(n\alpha)] + \\ +\mathrm{i}\cos(n\alpha)[\delta(\omega-\Omega)+\delta(\omega+\Omega)]\}\end{aligned} \tag{4.97}$$

where δ is the Dirac delta function and $\mathcal{F}_\mathrm{I}$ is the integral Fourier transform defined by

$$\mathcal{F}_\mathrm{I}\left[f(t)\right] = \frac{1}{\sqrt{2\pi}}\int_{-\infty}^{+\infty} f(t)\mathrm{e}^{\mathrm{i}\omega t}\,\mathrm{d}t \tag{4.98}$$

From equation 4.97 the rules stated in equations 4.93 and 4.94 can be easily obtained.

The integral Fourier transform was then used to analyze the sharpening process. In the following section the experimental campaign is described and the results are studied.

4.6.2 Impact modal testing

Since the numerical modal analysis of the support was carried out with big approximations, experimental modal testing was also employed. The modal testing was also applied to check the natural frequencies obtained by the fem analysis.

The impact test method was chosen as modal testing technique. The modal hammer 9724A by Kistler and an accelerometer were used. The force and acceleration signals were gathered by means of the acquisition device PC-M10-16E-4 by National Instruments. In order to drive the equipments and perform the tests proper programs were written using the LabVIEW$^{\mathrm{TM}}$ code. The acquisition was triggered by the force signal of the impact hammer. The experiments were carried out on the disk and on the support of the abrasive wheel. They were fixed on the test rig in order to obtain the natural frequencies with the real boundary conditions.

First, the test was executed on the disk. The sampling frequency was set to 2 kHz, much higher than the highest frequency of interest (300 Hz). The force of the hammer tip and the acceleration of the disk edge were gathered for 6 s. A plastic tip (tip number 9910), which can excite the structure up to 500 Hz, was used. Anti-aliasing filter with a cut-off frequency of 500 Hz was used. The force signal was windowed with a rectangular window and the acceleration signal with an exponential window. From the input (force) and output (acceleration) signals an estimation of the transfer function of the system was obtained. The transfer function estimation (tfe) was calculated

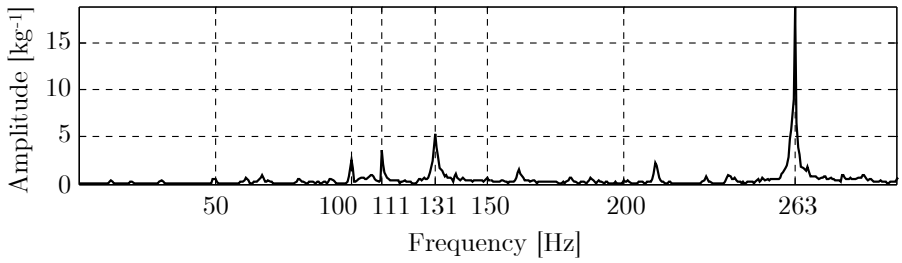

Figure 4.34: Impact test of the disk: transfer function estimation

by the function `tfe` of MATLAB® . Such function finds a transfer function estimate T_{xy} given an input signal vector x and output signal vector y that is the quotient of the cross spectrum of x and y, P_{xy}, and the power spectrum of x, P_{xx}:

$$T_{xy}(f) = \frac{P_{xy}(f)}{P_{xx}(f)} \tag{4.99}$$

where f is the frequency. Such estimate is useful to reduce the negative effects of a noisy output signal [97].

Figure 4.34 shows the transfer function estimate of the disk. The peaks at 100 Hz, 111 Hz and 131 Hz can be correlated to the natural modes (0,0), (1,0) and (2,0) respectively. At 263 Hz there is a very pronounced peak that can be associated to the (3,0) mode. Moreover the coherence function was checked. It was greater than 0.95 in all the range and greater than 0.99 around the natural frequencies.

Table 4.7 compares the natural frequencies estimated by the fem model with those obtained experimentally. The values of the frequencies are very similar. All the natural frequencies obtained from the impact tests are slightly lower than the corresponding ones obtained by numerical investigation. Mode (1,0) shows the bigger difference of about 11%. Such a trend can be explained by the differences between the fem model and the real disk, or better in a lower stiffness of the real system. In fact the fem model was considered perfectly constrained at the inner circle. In the operating condition the disk is clamped with a steel rig, which has not an infinite stiffness even if very high.

Subsequently the abrasive wheel support has been studied. As the natural frequency of the wheel shaft in the axial direction was known (it was designed at 18 Hz), the natural frequencies of the structure in the direction perpendicular to the axis were sought. The support was beaten with the modal hammer near the joint point of the abrasive wheel in the vertical and

Mode	(0,0)	(1,0)	(2,0)	(3,0)
Fem nat. freq. [Hz]	118.06	112.71	144.07	266.10
Exp. nat. freq [Hz]	111	100	131	263
Variation	-6%	-11%	-9%	-1%

Table 4.7: Comparison of the fem and experimental modal testing of the rig disk

horizontal directions. The accelerometer was placed in the diametrically opposite side of the structure. A 10 kHz scan frequency and an acquisition time of 1.5 s were set. The plastic tip 9908 was used since it can excite frequencies up to 800 Hz.

Figure 4.35(a) shows the estimation of the transfer function of the structure in the vertical direction while figure 4.35(b) shows the estimation in the horizontal direction. From the vertical test the peaks 48 Hz, 70 Hz, 86 Hz, 140 Hz, 150 Hz and 250 Hz can be discerned. The transfer function estimate obtained by horizontal excitation has pronounced peaks at the frequencies of 37 Hz, 52 Hz , 74 Hz, 130 Hz and 275 Hz. There are some less pronounced peaks at the frequencies of about 84 Hz, 145 Hz, 200 Hz and 250 Hz. The frequencies are different since the structure is not symmetric.

The coherences of the signals were also checked. They were greater than 0.99 in all the range for both the vertical and horizontal tests. This supports the validity of the results.

Table 4.8 resumes all the modal frequencies of the support of the abrasive wheel shaft obtained by the numerical analysis and by the modal testing. The frequencies calculated by the fem model did not take into account the modal behaviour of the translating sleeve of the abrasive wheel shaft that was modelled by a homogenous cylinder of the same weight. On the contrary, the experimental frequencies contained also the modal frequencies of the translational sleeve. Such a translational block is formed by the abrasive wheel shaft, two rolling bearings supporting the shaft and a sleeve. The shaft is placed on the inner surface of the sleeve while the outer surface slides on two teflon rings in order to make the translation of the abrasive wheel possible. Thus the obtained natural mode took into account the modal behaviour of all these components. The frequencies of the sleeve were recognized as shown in table 4.8. Both the vertical and horizontal impact tests showed modes in the intervals around the frequencies of 50 Hz, 70 Hz and 86 Hz. Such modes must be imputed to the translating sleeve but it is impossible to associate them to a particular component. In the vertical transfer function estimate the second mode of the support at 250 Hz was the most excited. In fact, it

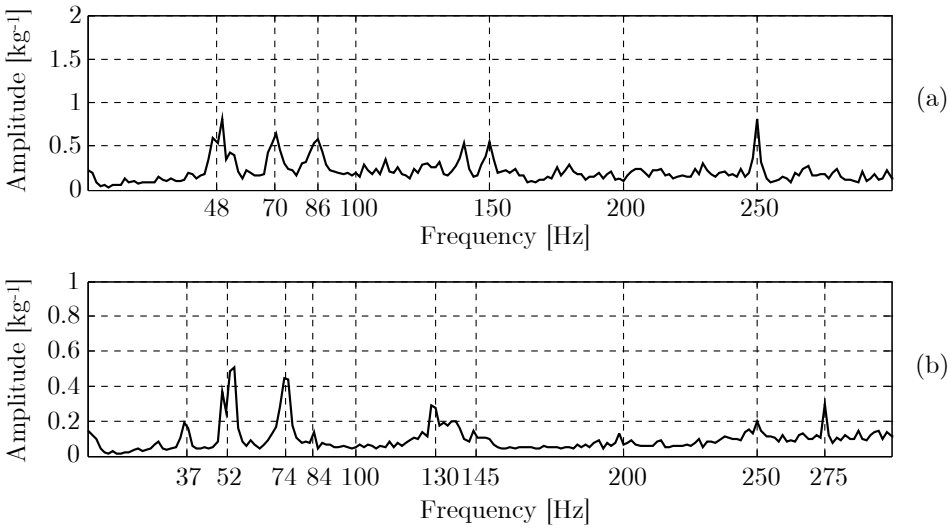

Figure 4.35: Impact test of the grinding wheel support: vertical (a) and horizontal (b) transfer function estimations

Mode		Sleeve	1	2
fem natural frequencies [Hz]		-	134.87	258.28
Experimental natural frequencies [Hz]	Vertical	37; 52; 74; 84	130; 145; 200	275; 250
	Horizontal	48; 70; 86	140; 150	250

Table 4.8: Comparison of the fem and experimental modal testing of the rig support of the abrasive wheel

is the flexural mode of the stem of the support. On the contrary, during the horizontal test the first mode at 130 Hz was the most excited since it is the torsional mode of the stem of the support.

4.6.3 Modal investigation during sharpening

Several tests at many rotational velocities were carried out with different values of the parameters. The aim was to show the influence of the sharpening time, the pushing spring pre-load, the grinding wheel tilting angle and the sliding velocity between disk and wheel. The waterfall plots were obtained by means of the integral Fourier transform of the complex signal obtained from

two displacement sensors placed on the disk. The signals gathered from the sensors were filtered in order to lower the low-frequency noise. A high-pass filter with a cut-off frequency of 40 Hz was utilized. In the figures the tracks of the modes are not always drawn in order to keep the figure readable.

Figure 4.36 shows the Fourier transform of the basic test. In order to give an idea of the dFRF analysis that can be obtained, figure 4.37 shows the normal and reverse dFRF respectively of the basic test.

In figure 4.36 the harmonics due to the disk rotation and a distributed noise are evident. In figure 4.37(a) the forward and backward travelling waves of the (1,0) and (3,0) modes are separated. The (1,0) mode is present only with the original tracks that are tilted towards the right. On the contrary, the (3,0) mode is present only with the conjugate tracks that are tilted towards the left. Mode (2,0) is present with all four tracks. As the reverse dFRF, shown in figure 4.37(b), has no peaks of the (1,0) and (3,0) modes, it is easy to single out the (2,0) mode. Moreover, in figure 4.37(b) the harmonics 2x, 4x and 6x, related to the disk rotation, are signed together with the (0,0) mode.

Figure 4.37(a) and figure 4.36 contain the same information but the peaks of the normal dFRF waterfall plots have the same magnitude in all the frequency range because they are normalized over the input signal. Such characteristic is useful to locate the modes because all the modes have the same importance. However, this characteristic is deceptive to recognize which mode causes the instability. For this reason further analyses where carried out on the integral Fourier transform of the signal.

A test with a reduced pushing force from 50 N to 25 N was carried out. Figure 4.38 shows the waterfall plot of the integral Fourier transform of the displacement signal. A slight reduction in the amplitudes and an increase in the dispersion of the peaks were recorded. The modes tracks could be hardly singled out because a decrease on the pre-load of the spring is equivalent to a decrease in the excitation power.

When the rotation of the grinding wheel was prevented, the waterfall plot shown in figure 4.39 was obtained. The peak tracks of the modes could not be easily located. The general attenuation of the peaks magnitude could be explained by a limitation of the excitation acting on the disk. In fact, as the grinding wheel did not rotate, the excitation was not affected by its geometry imperfections. Moreover, the passage from the rotating-sliding condition to the full sliding condition entails a reduction on the global friction coefficient. Consequently the excitation due to the contact force is reduced.

When the grinding wheel was tilted 2°, in the direction opposite to the disk rotation, the peaks increased considerably in magnitude as shown in figure 4.40. The increased vibrational response during the sharpening process

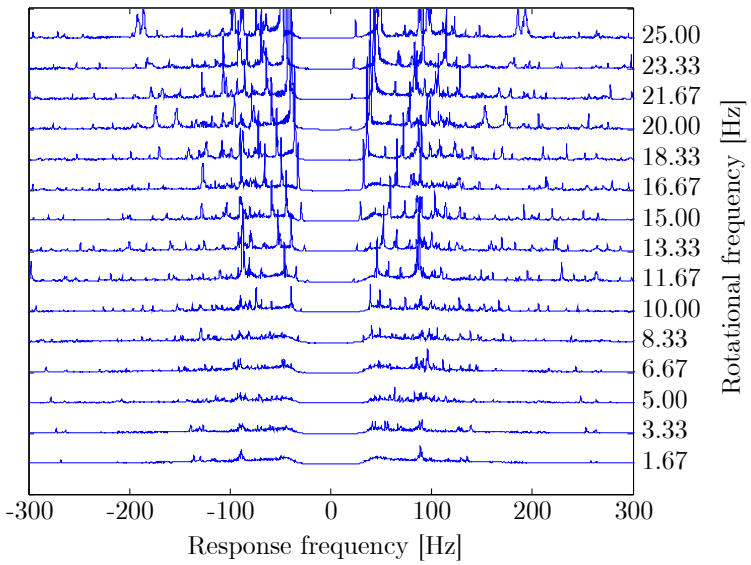

Figure 4.36: Waterfall plot of the basic test

could be explained by the coupling between a natural mode of the disk and a natural mode of the grinding wheel. A deeper analysis of such behaviour is discussed in the next section. Besides, a slight increase of the noise was recorded.

As the friction coefficient is a fundamental factor in the sharpening process, it was changed by sprinkling the disk with water. A reduction of the response, as shown in figure 4.41, could be clearly recognized. The reduction of the friction was useful to reduce vibration but, at the same time, it worsened the sharpening process. In fact the abrasive property of the grinding wheel was reduced and the edge sharpening took a longer time.

The basic test was obtained by an intermittent sharpening process: two 1 s sharpening intervals where separated by a 1 s break. Then two tests, changing the contact time and pushing the abrasive wheel against the disk only once, were carried out. Figure 4.42 shows the former test, where the abrasive wheel was kept in touch with the disk for 5 s. Such a long sharpening time increased the noise of the disk response and made it difficult to single out the natural mode peaks. The second test, shown in figure 4.43, was carried out sharpening the disk for 1 s. On the contrary, the short sharpening time test, caused a reduction of the distributed noise.

All the tests were then repeated with the relative angular position of the Proximitor® sensors changed from $\alpha = \pi/2$ to $\alpha = \pi/4$ and, with a 1 mm

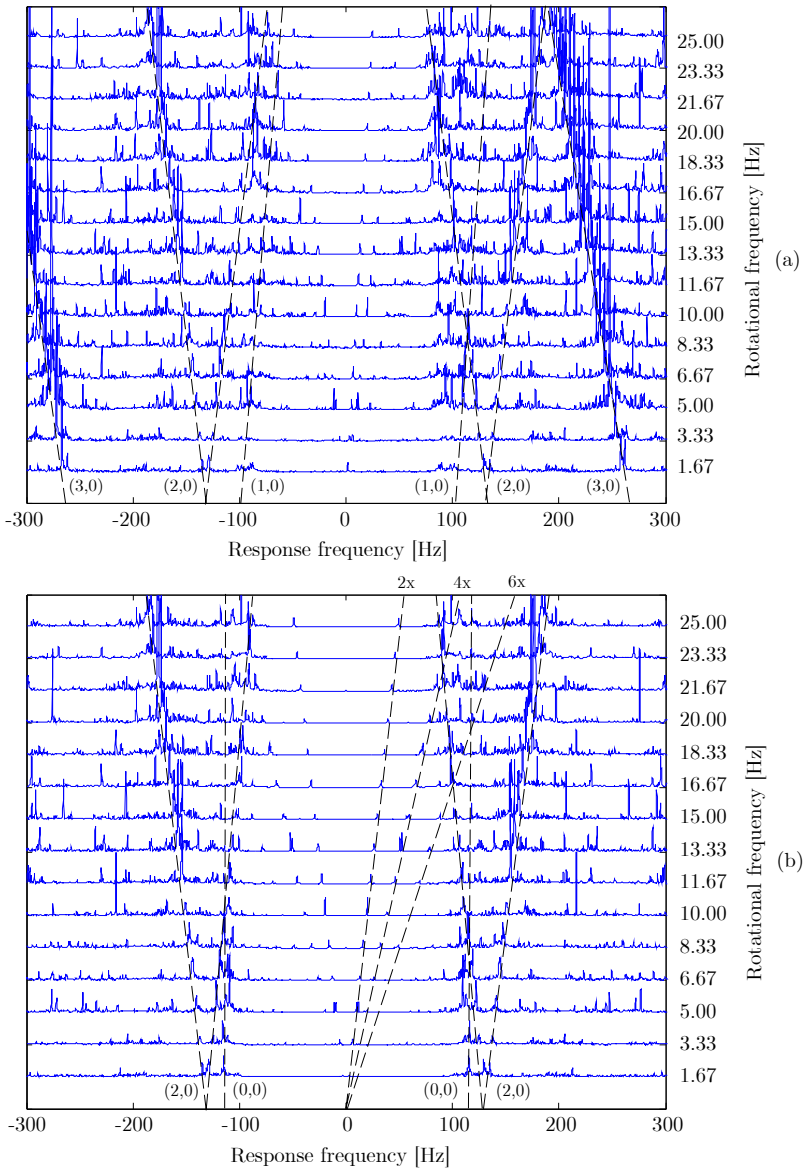

Figure 4.37: Waterfall dFRF plot of the basic test: normal (a) and reverse (b) dFRF

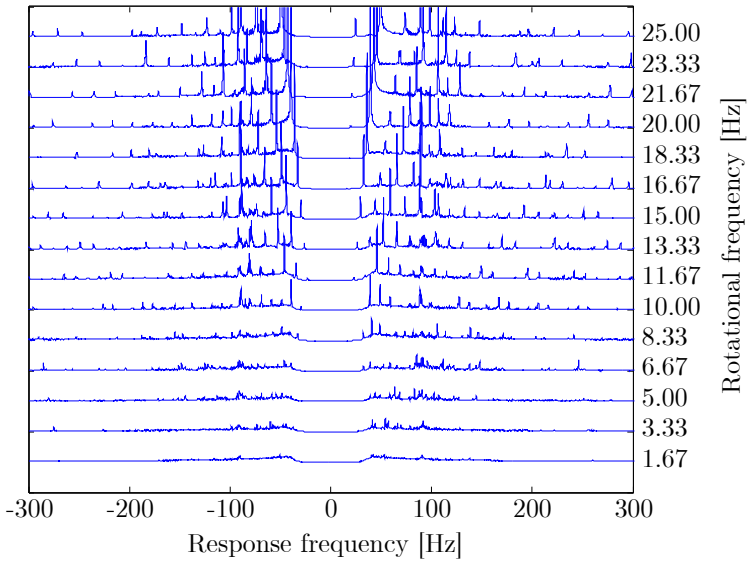

Figure 4.38: Waterfall plot of the test carried out with a reduced pushing force

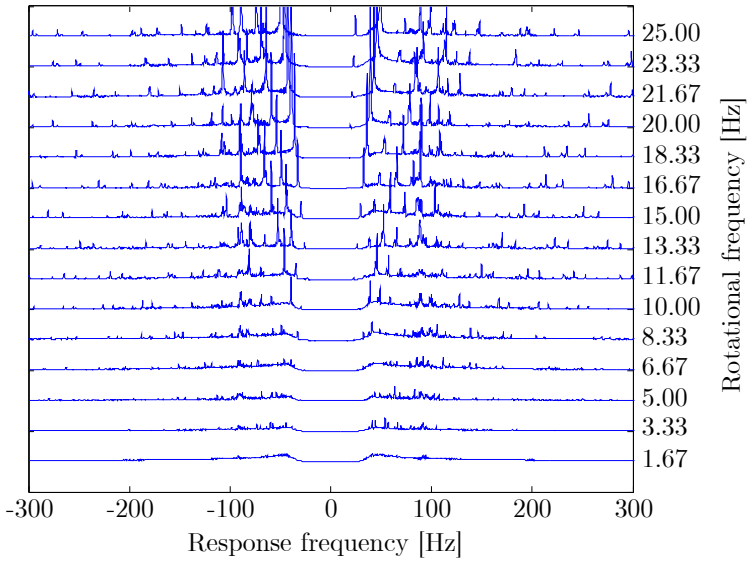

Figure 4.39: Waterfall plot: test carried out obstructing the rotation of the abrasive wheel

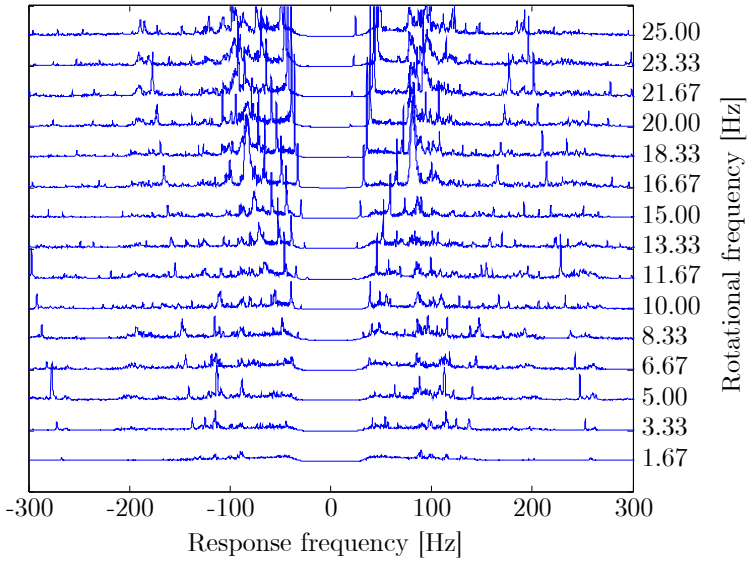

Figure 4.40: Waterfall plot: test carried out tilting the abrasive wheel axis

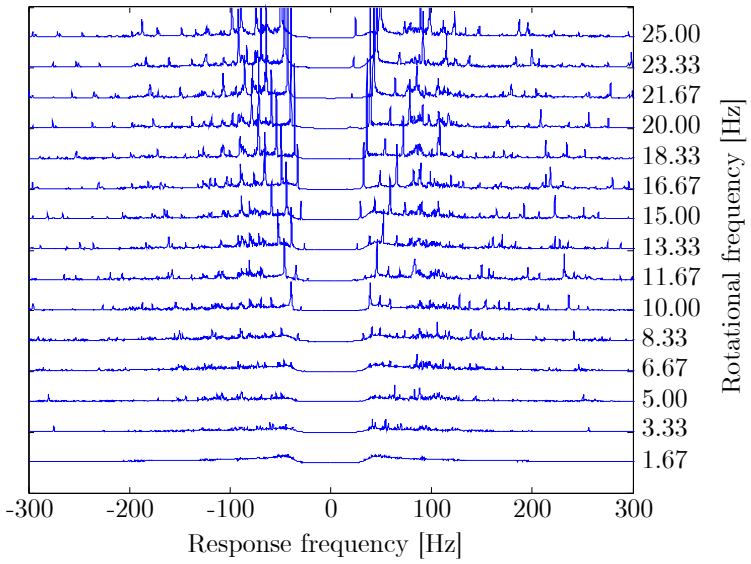

Figure 4.41: Waterfall plot: test carried out reducing the contact friction by water inlet

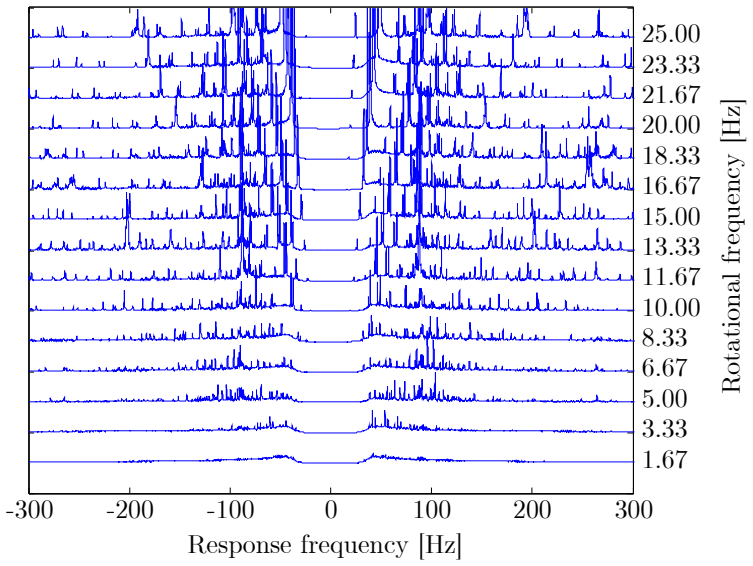

Figure 4.42: Waterfall plot of the long sharpening time test: the disk was sharpened continuously for 5 s

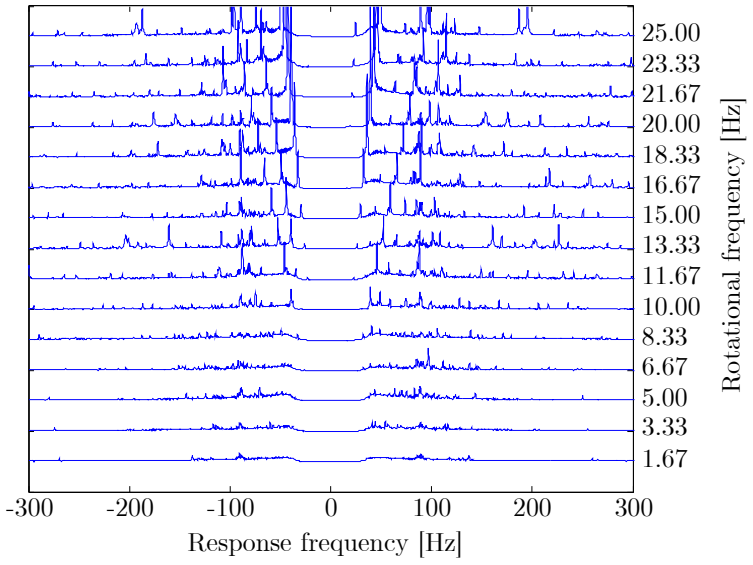

Figure 4.43: Waterfall plot of the short sharpening time test: the disk was sharpened continuously for 1 s

thickness disk instead of the 3 mm thickness disk. As the same trends were observed, such results are not shown. Moreover, the results obtained from the 1 mm thickness disk tests were not reliable because of the uncertainty on the contact between the disk and the grinding wheel. In fact, the pushing force was kept very low in order to avoid an over-strain of the disk.

From the analysis of all the results some trends on the influence of the sharpening parameters on the disk vibrations have been recognized:

- The decreasing of the sharpening time entailed a reduction of the distributed noise and of the peak amplitudes.
- The lowering of the spring pre-load caused, apart from the general lowering of the peak amplitudes, the appearance of more peaks spread on all the frequency range.
- Blocking the rotational displacement of the grinding wheel brought about a reduction of the peaks and the disappearance of some of these.
- The tests carried out sprinkling the disk with water showed a lowering and broadening of the peaks.
- Tilting the abrasive wheel axis caused a big increase in the vibrations amplitude.

The analysis techniques employed during this part of the work, beside the separation of forward and backward travelling wave, allowed the modal analysis of the disk to be performed even during the sharpening process. In the next section the possible lock-in instability phenomenon between disk and wheel modes is investigated.

4.6.4 Analysis of the sharpening process

The data gathered from the experimental campaign were then analyzed in order to understand the origin of the self-excited vibration that arise sometimes during the sharpening process. So the integral Fourier transform was applied only to part of the experimental data. In particular, the interval where the the grinding wheel is sharpening the edge of the disk and the following interval were considered and called for simplicity sharpening and break periods. With the Fourier transform of these partial data the waterfall plot was plotted.

Figure 4.44 shows the waterfall plot obtained from the data of the basic test. Figure 4.44(a) shows the behaviour of the disk during the first sharpening period while figure 4.44(b) concerns the break period. The peaks related

to the harmonics of the rotational speed of the disk are the most pronounced. Such peaks are caused by the geometrical imperfection on the disk planarity, in fact, they were noticed also before the first sharpening.

A peak in figure 4.44(a) denotes the onset of the self-excited vibration. It is a peak at the 90 Hz constant frequency and its track is indicated by a continuous line in the figure. This frequency is very close to the 85 Hz natural frequency of the grinding wheel support obtained from experimental modal testing (see section 4.6.2). Thus, the peak can be correlated to a flexural mode of the grinding wheel support. Such peak increases when it crosses the harmonic 4x and 8x but the largest increase is recorded at the crossing of such constant peak by the backward travelling wave (1,0) mode. In fact the (1,0) mode has a natural frequency of 100 Hz as obtained from experimental modal testing (see section 4.6.2). After the sharpening period the 90 Hz peak correlated to a flexural mode of the grinding wheel support vanishes as shown in figure 4.44(b) and only the free oscillations of the disk at the natural frequencies are recorded.

This situation is then compatible with the onset of lock-in instability due to the coupling between the flexural mode of the grinding wheel mode and the disk (1,0) mode. However, this situation occurs together with the resonance of the 85 Hz mode of the grinding wheel support excited by the imperfections of the disk and it is difficult to distinguish which phenomenon is predominant.

All the tests of the campaign were examined in this way. The test carried out tilting the grinding wheel of 2° in the rotating direction is of particular interest. In fact, in this test the coupling of the mode of the grinding wheel with the modes of the disk is possible even with no friction and more instability situations can be met. The results are shown in figure 4.45. However, apart from a general noise and peak amplitude increase, more lock-in situations were not recorded. The lock-in instability recorded at the 90 Hz frequency can still be seen.

The same analysis were carried out on the results of the test with reduced pushing force, with the blocked grinding wheel and with reduced friction. The obtained waterfall plots were compared again with the results of the basic test. From such analyses few results were drawn:

- When the pushing force was reduced the instability phenomenon with the 90 Hz frequency was not recorded. Moreover the harmonic peaks were shrunk. A general decrease of the vibratory level was also obtained.

- When the grinding wheel was blocked a general lowering of the harmonic peaks was noticed but the 90 Hz natural frequency again leads

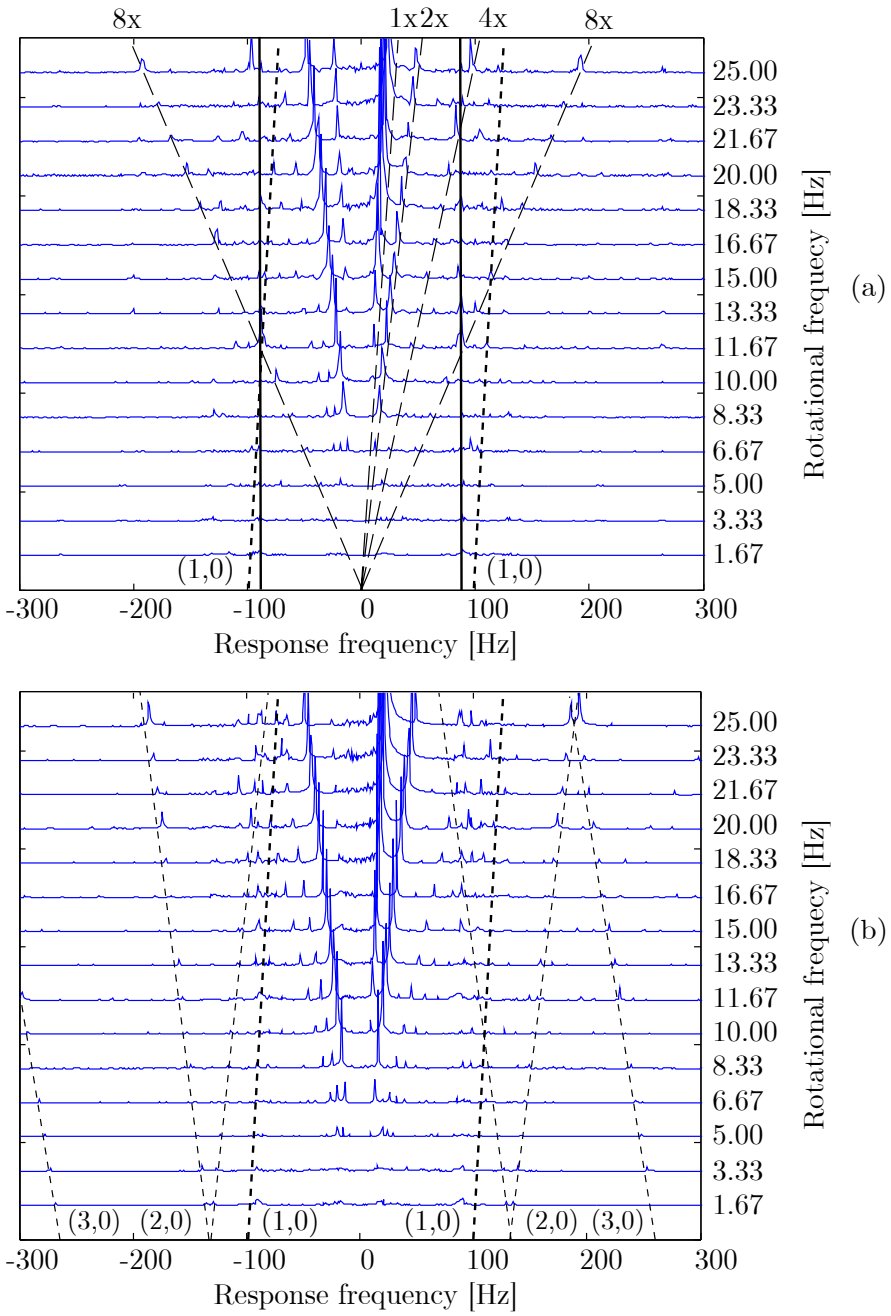

Figure 4.44: Waterfall plot of the sharpening phases of the basic test: during (a) and after (b) the sharpening

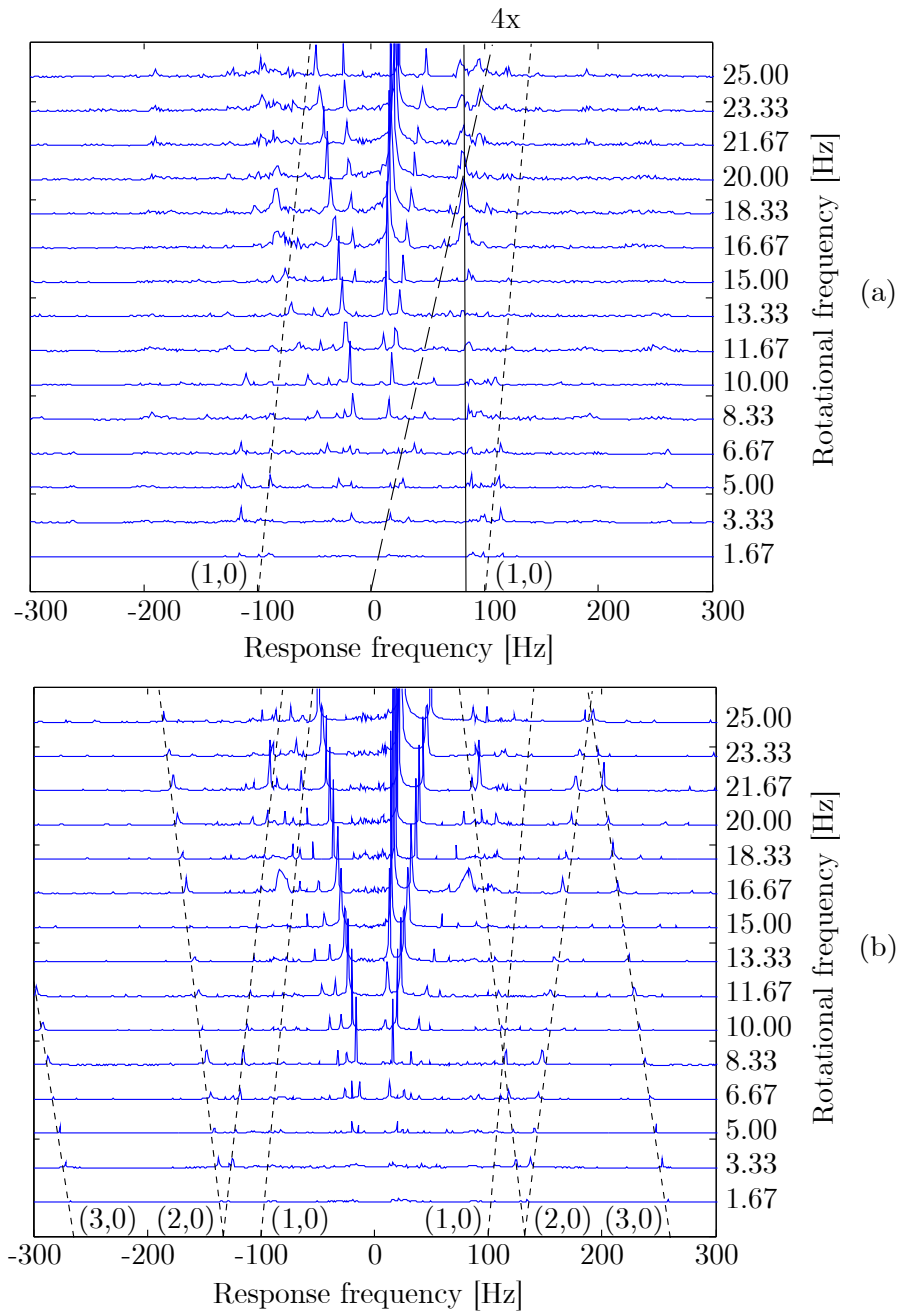

Figure 4.45: Waterfall plot of the sharpening phases of the tilted wheel test: during (a) and after (b) the sharpening

to instability conditions.

- When the contact area was sprinkled with water, there was a general lowering of the harmonic peaks and a complete disappearance of the 90 Hz peaks.

4.7 Conclusions

The disk blade sharpening process of the paper cutting machine was examined both experimentally and numerically.

The results of an experimental investigation carried out on a commercial paper roll cutting machine have been presented and the problems concerning the sharpening of a disk blade have been highlighted. A harmful 200 Hz vibration has been observed. This vibration is a multiple of the blade angular velocity and gave rise to a wavy edge thickness. The commercial machine was analyzed also numerically by fem modal analysis and transient analysis by the explicit fem software LS-DYNA® .

Then the design of a test-rig for the study of the vibratory behaviour of a rotating disc subjected to a sharpening process has been described. The device was conceived with the same dynamic characteristics of the real sharpening process. On the test rig, suitably equipped with sensors, the displacement of two peripheral points of the disk and its rotating speed are measured as well as the grinding disc oscillation and rotating speed. The design of the test rig made it possible to carry out a series of tests varying the process parameters such as the grinding contact force, duration and relative position of the two mating elements, the disc rotating speed, the spring stiffness and the friction law, in order to point out the most important variables for the system vibrations.

A campaign of numerical simulations by means of the finite element code LS-DYNA® was carried out, applying the geometric and material characteristics of the actual test-rig. The results of the investigation have been presented and discussed. The influence of the friction decay coefficient and of idle grinding wheels has been taken into account. Some hypotheses have been proposed to explain the phenomenon, among which the effect of stick-slip. The model adopted in the simulation was suitably simplified and partial results have been obtained. Nevertheless more specific and extensive experimental tests were planned to validate the model in order to obtain more significant results.

In the mean time, an experimental campaign was carried out on the test rig. The use of non conventional analytical tools permitted to characterize

the vibrational behaviour of the rotating disk and to point out the natural modes and the resonance conditions with the variation of the parameters of the sharpening process. The influence of some operating and geometric parameters was sought, as for example the friction interface coefficient, the tilting angle of the grinding wheel axis, the sliding velocity, the sharpening time and the pushing force. A condition of instability was found from the analysis of the sharpening period and two main conclusions can be drawn. Firstly, during the break periods the recorded out-of-plane displacements were given by the harmonics and the free vibrations of the mode while during the sharpening period the peaks at the natural frequencies of the disk disappeared while the harmonic peaks were still present. Secondly, a 90 Hz frequency, related to a flexural natural mode of the grinding wheel support, increased in amplitude when it crossed the (1,0) disk mode, confirming the coupling between the two modes.

Chapter 5

Conclusions and suggestions for further work

The research described in this thesis concerned the main aspects of dynamics of rotating machinery focusing on few specific topics. In particular, the aim was to study and develop some tools to design high-efficiency rotating machinery with low vibratory level. The means to reduce the vibratory level are usually classified in passive, active and semi-active control. However, in order to design the proper action the designer needs to have an accurate knowledge of the mechanical system he works on. Moreover, an on-line identification of mechanical system can be useful to tune the parameters of automatic controllers of active and semi-active devices.

First, the present work focused on the application of the modulating functions, used up to now only for the identification of the characteristics of electric and electronic systems, for the identification of rotor-bearings systems. The method of identification was first tested on simpler mechanical systems. Therefore, a test rig for the identification of simple one and two degrees of freedom mass-spring systems has been set up. Minimizing the difference between the responses of the theoretical model, in the time domain, and of the real system subjected to the same excitation, the system dynamic coefficients were identified with satisfactory approximation. The extension to the identification of more complex systems, such as the hydrodynamic bearings, was straightforward. Numerical and experimental tests showed the good performance of the method and, the errors in the signal reconstruction were about 10%. However, in order to apply properly the method a deep knowledge of the system is necessary since a detailed model has to be set-up beforehand.

Among the devices that can be used to reduce the vibratory level of rotor dynamic systems, the squeeze film damper is one of the most widespread.

However, the behaviour of the squeeze film damper cannot easily be controlled on-line to meet the requirements of the rotor system in all the operating conditions. Then a controllable damper, based on the conventional one, was developed. As in the last decade there has been an increasing attention toward the employment of magnetorheological fluids in the development of smart devices, the attention of the research focused on the design of a controllable squeeze film damper filled up with magnetorheological fluid. In this work the design of a magnetorheological squeeze film damper has been presented and discussed. The damper was fitted on the shaft of Bently Nevada Rotor Kit test rig. Since the damping characteristics could be varied continuously by controlling the magnetic field, it was possible to have the optimum conditions for each regime of rotational speed. Moreover, expecting a commercial application of the device an automatic controller was devised. A Fuzzy logic semi-active control technique was designed by means of heuristic rules written down by the operators. Optimal performance were recorded. For instance, in the simulation of a rotor run-up the amplitude of the rotor orbit could be reduced up to 82% thanks to the controller. The Fuzzy rules of the controller were then optimized using a Genetic algorithm. In the simulation of a rotor run-up the amplitude of the rotor orbit could be reduced only up to 52% thanks to the optimized controller. However, the new controller permitted to reduce the energy supplied to the damper coils of about an order of magnitude. Even if there are unresolved problems such as cavitation or two-dimensional effects, the MR squeeze film damper seems to be applicable to commercial products. Thus, future works could consider some industrial application of the MR squeeze film damper, for example to aero engine rotors. It would be interesting to check the performance of the MR squeeze film damper with rotor systems closer to the real system. For example more stiff rotors and larger unbalance forces could be considered.

Other components commonly found in rotating machinery are flexible rotating disks. The reduction of the flexural vibrations of the disk is more difficult and there are no standard tools to cope with this. The situation is worsened by the complexity of the dynamical behaviour of rotating disk to non-standard excitations not yet well understood. In this work the results of an investigation about the onset of self-excited vibration during the sharpening of a flexible disk have been discussed. The results of an experimental campaign, carried out on a test rig, has been presented. Modal and transient analyses on the fem models of the test rig components were carried out as well as an analysis of lock-in instability on a simplified model to highlight the observed phenomena and support the analysis of the experimental results. Directional frequency response functions have been applied for the experimental signal analysis. The investigation has shown the influence of some

operating and design parameters on the system dynamic behaviour. Moreover, the possibility of lock-in instability onset has been recorded when a modal frequency of the disk was close to a natural frequency of the abrasive wheel block. As the work gave all the basic instruments to understand and to cope with rotating disk vibration, future work could consider the application of passive, active or semi-active devices to such a problem. The application could then be extended to face other problems such as the brake squeal or the vibration arising in the saw disk during the timber cutting.

Appendix A

Publications

1. M.J. Brennan, P. Bonello, E. Rustighi, B.R. Mace and S.J. Elliott, "Designs of variable stiffness element for a tunable vibration absorber", *The 18th International Congress on Acoustics ICA 2004*, April 4 to 9, Kyoto, Japan, 2004.

2. E. Rustighi, M.J. Brennan, B.R. Mace, "*A shape memory alloy adaptive tuned vibration absorber: design and implementation*", submitted to: Smart materials and structures, October 2003.

3. E. Rustighi, M.J. Brennan, B.R. Mace, "*Design of an adaptive vibration absorber using shape memory alloy*", Technical Memorandum 920, University of Southampton, Institute of Sound and Vibration Research, 2003.

4. C. Carmignani, P. Forte, E. Rustighi, "Studio sperimentale su un modello di lama a disco delle vibrazioni indotte dal processo di affilatura", *XXXII Convegno Nazionale dell'Associazione Italiana per l'Analisi delle Sollecitazioni*, Salerno, 3-6 Settembre 2003.

5. C. Carmignani, P. Forte, E. Rustighi, "Controllo vibrazionale semiattivo di un rotore flessibile tramite smorzatore a squeeze-film magnetoreologico", *XXXII Convegno Nazionale dell'Associazione Italiana per l'Analisi delle Sollecitazioni*, Salerno, 3-6 Settembre 2003.

6. F. Frendo, G. Giannoni, E. Rustighi, E. Vitale, "Valutazione dell'integrità strutturale di telai per motorscooter tramite simulazione di prove di caduta", *Virtual prototyping today: industrial impact and future trends, Engin Soft & mode Frontier Conference and users' meeting*, pp. 15-27, Stezzano (BG), 3-4 Ottobre 2002.

7. P. Forte, M. Paternò, E. Rustighi, "A magnetorheological fluid damper for rotor applications", *IFToMM Sixth International Conference on Rotor Dynamics*, Vol. 1, pp. 63-70, University of New South Wales, Sydney, Australia, September 30 - October 3, 2002. Publishing on: International Journal of Rotating Machinery

8. C. Carmignani, P. Forte, E. Rustighi, "Theoretical and experimental investigation on the dynamic behaviour of disc blades during sharpening", *IFToMM Sixth International Conference on Rotor Dynamics*, Vol. 2, pp. 936-943, University of New South Wales, Sydney, Australia, September 30 - October 3, 2002.

9. C. Carmignani, P. Forte, E. Rustighi, "Identificazione dei coefficienti dinamici di sistemi meccanici tramite la tecnica delle funzioni modulanti", *XXXI Convegno Nazionale dell'Associazione Italiana per l'Analisi delle Sollecitazioni*, Parma, 18-21 Settembre 2002.

10. C. Carmignani, P. Forte, E. Rustighi, "Analisi delle vibrazioni nell'affilatura di lame a disco", *XXX Convegno Nazionale dell'Associazione Italiana per l'Analisi delle Sollecitazioni*, Alghero (SS), 12-15 Settembre 2001.

11. C. Carmignani, P. Forte, E. Rustighi, "Active control of rotor vibrations by means of piezoelectric actuators", *Proceedings of DETC'01 ASME 2001 Design Engineering Technical Conferences and Computers and Information in Engineering Conference*, Pittsburgh, Pennsylvania, September 9-12 2001.

12. C. Carmignani, P. Forte, E. Rustighi, "Controllo attivo della dinamica dei rotori mediante attuatori piezoelettrici", *XXIX Convegno Nazionale dell'Associazione Italiana per l'Analisi delle Sollecitazioni*, Lucca, 6-9 Settembre 2000.

Appendix B

Education and training

Courses

- "ANSYS® /LS-Dyna©", Italcae S.p.A., Pisa c/o DIMNP, February 21-23, 2001
- "Analisi modale sperimentale", LMS Italia Formazione Clienti, Novara, April 3-5, 2001
- "Materiali compositi a matrice polimerica", Dipartimento di Ingegneria Chimica, Chimica Industriale e Scienza dei Materiali, Università di Pisa, December 13, 2001
- "Corso sulle curve utilizzate nel CAD", Prof. Guiggiani, DIMNP, Pisa, February 2002
- "Advanced dynamics and control of structures and machines", International Centre for Mechanical Sciences (CISM), Udine, April 15-19, 2002
- "Vibration Control", ISVR, University of Southampton, July 1-5, 2002
- "Advanced course in acoustic, noise and vibration", ISVR, University of Southampton, September 23-27, 2002
- "Introduction to signal processing", ISVR, University of Southampton, October 21-25, 2002
- "Dinamica aleatoria e non lineare", Prof. Carmignani (DIMNP), Pisa, Febbruary 2003
- "Design of Experiment (DoE) e Metodologie statistiche", Dipartimento di Matematica Applicata, Pisa, June 2003

Exams

- "Tribologia", Prof. Meozzi
- "Calcolo delle probabilità", Prof. Flandoli
- "Comportamento meccanico dei materiali", Prof. Beghini
- "IELTS, International English Language Testing System", Academic module, Overall Band Score 7.0

Conferences

- "Active 2002", International symposium on active control of sound and vibration, ISVR, University of Southampton, July 15-17, 2002
- "Marie Curie Fellowships European Scientific Workshop, "Developing a scientific career", Donostia-San Sebastian, November 28-30, 2002
- "VIII International Conference on Recent Advances in Structural Dynamics", University of Southampton, Southampton, United Kingdom, 14-16 July 2003

Didactics

- Helper to the class of "Disegno al calcolatore"
- Supervisor of the thesis: "Progettazione e realizzazione di uno smorzatore a squeeze film con fluido magnetoreologico per il controllo delle vibrazioni di un rotore" by Marco Paternò
- Supervisor of the thesis: "Indagine sperimentale sulle vibrazioni flessionali di dischi rotanti" by Andrea Borzoni
- Supervisor of the thesis: "Identificazione dei coefficienti dinamici di sistemi meccanici tramite la tecnica delle Funzioni Modulanti" by Marcello Venturi
- Supervisor of the thesis: "Controllo vibrazionale semiattivo di un rotore flessibile tramite smorzatore a squeeze-film magnetoreologico" by Cristiano Arfanotti and Gabriele Bicci
- Supervisor of the thesis: "Indagine sperimentale sulle vibrazioni flessionali di lame a disco durante il processo di affilatura" by Alessandro Bechi

Bibliography

[1] A. Musznynka, D.E. Bently, W.D. Franklin, and R.D. Hayashida. Identification of modal parameters of rotating systems using perturbation techniques: part 1 and 2. In *Proc. 12th Biennal ASME Conf. on Mech. Vib. and Noise*, pages 107–118, Montreal, Canada, September 17-21 1989.

[2] F. Everett Reed. *Shock and vibration handbook*, chapter Dynamic vibration absorbers and auxiliary mass dmapers. McGraw Hill, third edition, 1987.

[3] R. Larsonneur, S. Siegwart, and A. Traxler. Active magnetic bearing control strategies for solving vibration problems in industrial rotor systems. *IMechE*, pages 83–90, 1992.

[4] U. Ulbrich and J. Althaus. Actuator design for rotor control. In *Proceedings of the 12*$^{\text{th}}$ *ASME Design Technical Conferences, Mechanical Vibration and Noise*, pages 17–22, Montreal, Quebec, Canada, September 17-21 1989.

[5] I. F. Santos. Design and evaluation of two types of active tilting pad journal bearings. In *IUTAM Symposium: The active control of vibration*, pages 79–87, London, 1994.

[6] J. M. Krodkiewski and L. Sun. Stability control of rotor-bearing system by an active journal bearing. In M. J. Goodwin, editor, *Vibration and Noise*, pages 217–225, Venezia, Italy, April 25-27 1995.

[7] G. G. Lisini and M. Verardi. L'instabilità del processo di rettifica. *Automazione e automatismi*, 6:3–12, 1967.

[8] B. Bartalucci, G.G. Lisini, and P.C. Pinotti. Grinding at variable speed. In S.A. Tobias and F. Koenigsberger, editors, *Advances in Machines Tool Design and Research*, pages 633–652, Geneva, 1971. Pergamon Press.

[9] J.S. Chen and D.B. Bogy. Natural frequencies and stability of a flexible spinning disk-stationary load system with rigid-body tilting. *Transactions of the ASME Journal of Applied Mechanics*, 60:470–477, 1993.

[10] I.Y. Shen and C.P.R. KU. A nonclassical vibration analysis of multiple rotating disk and spindle assembly. *Transactions of the ASME Journal of Applied Mechanics*, 64:165–174, 1997.

[11] S.C. Huang and W.J. Chiou. Modeling and vibration analysis of spinning-disk and moving-head assembly in computer storage system. *Transactions of the ASME Journal of Vibration and Acoustics*, 119:185–191, 1997.

[12] I.Y. Shen. Recent vibration issues in computer hard disk drives. *Journal of Magnetism and Magnetic Materials*, 209:6–9, 2000.

[13] J.E. Mottershead and S.N. Chan. Brake squeal - an analysis of symmetry and flutter instability. In R.A. Ibrahim and A. Soom, editors, *Friction-Induced Vibration, Chatter, Squeal, and Chaos*, volume ASME DE-49, pages 87–97, New York, 1992. Elsevier Science Publishers.

[14] R.A. Ibrahim. Friction-induced vibration, chatter, squeal, and chaos: Part ii - dynamics and modeling. In R.A. Ibrahim and A. Soom, editors, *Friction-Induced Vibration, Chatter, Squeal, and Chaos*, volume ASME DE-49, pages 123–138, New York, 1992. Elsevier Science Publishers.

[15] R. W. Ellis and C. D. Mote Jr. A feedback vibration controller for circular saws. *Transaction of the ASME: Journal of Dynamic Systems, Measurement, and Control*, 101:44–49, 1979.

[16] C. J. Radcliffe and C. D. Mote Jr. Identification and control of rotating disk vibration. *Journal of Dynamic Systems, Measurement, and Control*, 105:39–45, March 1983.

[17] X. G. Wang, F. J. Xi, D. Li, and Z. Qin. Estimation and control of vibrations of circular saws. In *Proceedings of the 1999 IEEE International Conference on Control Applications*, pages 514–520, Kohala Coast-Island, Hawaii, USA, August 22-27 1999.

[18] J. C. Sun, X. G. Wang, and F. J. Xi. Sliding mode active vibration control of circular saws. In *Proceedings of the 2000 IEEE International Conference on Control Applications*, pages 953–958, Anchorage, Alaska, USA, September 25-27 2000.

[19] Lennart Ljung. *System Identification Toolbox User's Guide*. The MathWork, Inc., version 5 edition, 2002.

[20] Lennart Ljung. *System identification: theory for the user*. Prentice Hall, 2nd edition, 1999.

[21] K. Glover. *Concise encyclopedia of Modelling and Simulation*, chapter Identification: Frequency-Domain Methods, pages 161–168. Pergamon Press, 1992.

[22] M. Shinbrot. On the analysis of linear and non linear systems. *Trans. ASME*, 79:547–552, 1957.

[23] A. Balestrino, A. Sani, and L. Sani. Parameter identification of continous systems with multiple input time delay via modulating functions. *IEE Proc. D, Contr. Theory Appl.*, 147:19–27, 2000.

[24] D.W. Parkins. Measured characteristics of a journal bearing oil film. *J. Lub. Technol.*, 103:120–125, 1981.

[25] M. Casini, P. Lacitignola, G.G. Lisini, and P. Toni. Determinazione sperimentale delle caratteristiche dinamiche dei cuscini. *Quaderni Pignone*, 43:31–41, 1987.

[26] S. Hisa, T. Matsuura, and T. Someya. Experiments on the dynamics characteristics of large scale journal bearings. *I. Mech E.*, pages 223–229, 1980.

[27] P.G. Morton. The derivation of bearing characteristics by means of transient excitation applied directly to a rotating shaft. In *IUTAM Symposium*, pages 350–378, Lyngby, Denmark, Aug. 12-16 1974.

[28] R. Nordmann and K. Schollhorn. Identification of stiffness and damping coefficients of journal bearings by means of the impact method. *I. Mech E.*, pages 231–238, 1980.

[29] Y.Y. Zhang, Y.B. Xie, and D.M. Qiu. Identification of linearized oil-film coefficients in a flexible rotor-bearing system, part i: Model and simulation, and part ii: Experiment. *Journal of Sound and Vibration*, 52(3):531–559, 1992.

[30] C. Yasuda, H. Kanki, T. Ozawa, and T. Kawakami. Application of random excitation technique to dynamic characteristics measurement of bearing. In *Int. Conf. on Rotordynamics*, Tokyo, 1986.

[31] J. Frêne, D. Nicolas, B. Deguerce, D. Berthe, and M. Godet. *Hydrodynamic Lubrication, bearing and thrust bearing*, volume 33 of *Tribology Handbook*. Elsevier, 1990.

[32] O. Bonneau and J. Frene. Non-linear behavior of a flexible shaft partly supported by a squeeze film damper. *Wear*, 206:244–250, 1997.

[33] S. Morishita and U. Tamaki. Er fluid applications to vibration control devices and an adaptive neural-net controller. *J. Intelligent Material Systems and Structures*, 4:366–372, 1993.

[34] K.D. Weiss, T.G. Duclos, J.D. Carlson, M.J. Chrzan, and A.J. Margida. High strength magneto- and electro-rheological fluids. *Society of Automotive Engineers Technical Paper Series*, 932451:1–6, 1993.

[35] C. Shakeri, M.N. Noori, and Z. Hou. Smart materials and structures - a review. In *Proceedings of the 1996 4th Materials Engineering Conference*, volume 2 of *Materials for the New Millennium*, pages 863–876, Washington, DC, USA, Nov 10-14 1996. ASCE, ASCE.

[36] J.D. Carlson and K.D. Weiss. A growing attraction to magnetic fluids. *Machine design*, 66(15):61–64, 1994.

[37] J. A. Tichy. Hydrodynamic lubrication theory for the bingham plastic flow model. *Journal of Rheology*, 35(4):477–496, 1991.

[38] J. A. Tichy. Behavior of a squeeze film damper with electrorheological fluid. *STLE Tribology Transactions*, 36(1):127–133, 1993.

[39] A. D. Dimarogonas and A. Kollias. Electorheological fluid-controlled "smart" journal bearings. *STLE Tribology Transactions*, 35(4):611–618, 1992.

[40] S. Y. Jung and S. B. Choi. Analysis of a short squeeze-film damper operating with electrorheological fluids. *STLE Tribology Transactions*, 38(4):857–862, 1995.

[41] S. Morishita and Y.K. An. On dynamic characteristics of er fluid squeeze film damper. *JSME International Journal, Series C*, 39(4):702–707, 1996.

[42] P. G. Nikolakopoulos and C. A. Papadopoulos. Controllable high speed journal bearings, lubricated with electro-rheological fluids. an analytical and experimental approach. *Tribology International*, 31(5):225–234, 1998.

[43] W. I. Kordonsky. Magnetorheological effect as a base of new devices and technologies. *Journal of Magnetism and Magnetic Materials*, 122:395–398, 1993.

[44] M. R. Jolly and J. D. Carlson. Controllable squeeze film damping using magnetorheological fluid. In *5th International Conference on New Actuators*, pages 333–336, Bremen, Germany, 26-28 June 1996.

[45] M. R. Jolly, J. W. Bender, and J. D. Carlson. Properties and applications of commercial magnetorheological fluids. In *Spie 5th Annual Int. Symposium on Smart Structures and Materials*, San Diego, CA, March 15 1998.

[46] R. Bolter and H. Janocha. Design rules for mr fluid actuators in different working modes. *Proceedings of the Society for Optical Engineering*, 3045:148–159, 1997.

[47] C. Zhu, D. A. Robb, and D. J. Ewins. Magnetorheological fluid dampers for rotor vibration control. *AIAA Paper*, 2001-1469:2121–2127, 2001.

[48] F. Marazzi and G. Magonette. Active and semi-active control of structures: a comparison. In *European Meeting on Intelligent Structures*, Ischia, Italy, September 22-28 2001.

[49] Michael D. Symans and Michael C. Constantinou. Semi-active control systems for seismic protection of structures: a state-of-the-art review. *Engineering Structures*, 21:469–487, 1999.

[50] F. Marazzi, G. Magonette, and V. Renda. From active to semi-active control: Theoretical and implementation aspects. In *Third World Conference on Structural Control (3WCSC)*, Como, Italy, April 7-12 2002.

[51] Heinz Ulbrich. Active bearing support for rotating machine elements. *Machine Vibration*, 1:2–12, 1992.

[52] A. B. Palazzolo, S. Jagannathan, A. F. Kascak, G. T. Montague, and L. J. Kiraly. Hybrid active vibration control of rotorbearing system using piezoelectric actuators. *Journal of Vibration and Acoustics, Trans. of ASME*, 115:111–119, 1993.

[53] G. Genta. *Vibration of structures and machines, pratical aspects*. Springer-Verlag, New York, 1993.

[54] R. Holmes. Rotor vibration control using squeeze-film dampers. In *IFTOMM - Fifth International Conference on Rotor Dynamics*, pages 32–51, Darmstadt, University of Technology, Germany, September 7-10 1998.

[55] Lord Materials Division. What is the difference between mr and er fluid? Presentation, May 2002.

[56] J.D. Carlson, D.N. Catanzarite, and K.A. St Clair. Commercial magneto-rheological fluid devices. In W. Bullough, editor, *5th Int. Conf. on ER Fluids, MR Suspensions and Associated Technology*, pages 20–28, Singapore, 1996. World Scientific.

[57] Lord Materials Division. Designing with mr fluids. Engineering Note, December 1999.

[58] J. L. Nikolazsen and M. S. Honue. An electro-viscous damper. In *Proceedings of Workshop on Rotor-dynamic Problems in High-Performance Turbo-Machinery*, volume NASA CP-3215, pages 65–73, Texas, 1988.

[59] J. M. Vanve and D. Yang. Experimental measurements of the actively controlled bearing damper with an electrorheological fluid. Technical Report 99-GT-17, ASME, 1999.

[60] S. Morishita and J. Mitsui. Squeeze film damper as an application of electro-rheological fluid. In *Proceedings 3rd International Conference on Rotor Dynamics*, pages 277–282, Lyon, France, 1990.

[61] C. Zhu, D. A. Robb, and D. J. Ewins. A variable stiffness damping support for passing through the critical speeds of rotors. In *IMAC-XIX*, pages 1264–1269, Hyatt Orlando, Kissimmee, Florida, 2001. Society for Experimental Mechanics, Inc.

[62] Chang sheng Zhu. Dynamics of a rotor supported on magnet-rheological fluid squeeze film damper. *Chinese journal of aeronautics*, 14(1):6–12, February 2001.

[63] C. Zhu, D. A. Robb, and D. J. Ewins. A magneto-rheological fluid squeeze film damper for rotor vibration control. In *IMAC-XX*, pages 516–522, Los Angeles, California, 2002. Society for Experimental Mechanics, Inc.

[64] C. Zhu, D. A. Robb, and D. J. Ewins. Effectiveness of a disk-type magneto-rheologic fluid damper for rotor system vibration control. In *SPIE*, volume 4331, pages 379–385, 2001.

[65] C. Zhu, D. A. Robb, and D. J. Ewins. Dynamics of an over-hung rotor with a disc-type magneto-rheological fluid damper. In E. J. Hahn and R. B. Randall, editors, *IFToMM Sixth International Conference on Rotor Dynamics*, volume 2, pages 607–614, University of New South Wales, Sydney, Australia, September 30 - October 3, 2002 2002.

[66] M. Ahmadian. *Encyclopedia of Vibration*, chapter Active control of vehicle vibration, pages 37–45. Academic Press, 2001.

[67] L. M. Jansen and S. J. Dyke. Semiactive control strategies for mr dampers: Comparative study. *Journal of Engineering Mechanics*, 126(8):795–803, 2000.

[68] Kevin M. Passino and Stephen Yurkovich. *Fuzzy Control*. Addison Wesley Longman, Inc., 1998.

[69] N. Al-Holou, D. Sung Joo, and A. Shaout. The development of fuzzy logic based controller for semi-active suspension system. In *Proceedings of the 37th Midwest Symposium on Circuits and Systems. Part 2 (of 2)*, volume 2, pages 1373–1376, Lafayette, LA, USA, Aug 1994.

[70] Kyle C. Schurter and Paul N. Roschke. Neuro-fuzzy control of structures using magnetorheological damper. In *American Control Conference*, pages 1097–1102, Arlington, VA, June 2001.

[71] C.-S. Ting, T.-H. S. Li, and F.-C. Kung. Design of fuzzy controller for active suspension system. *Mechatronics*, 5(4):365–383, 1995.

[72] *Fuzzy Logic Toolbox User's Guide*. The MathWorks, Inc., 2000.

[73] Franco Busetti. Genetic algorithms overview, 2001.

[74] David Beasley, David R. Bull, and Ralph R. Martin. An overview of genetic algorithms: Part 1, fundamentals. *University Computing*, 15(2):58–69, 1993.

[75] Alen Varšek, Tanja Urbančič, and Bodgan Filipič. Genetic algorithms in controller design and tuning. *IEEE Transactions on Systems, Man and Cybernetics*, 23(5):1330–1339, Sep-Oct 1993.

[76] T. Hashiyama, S. Behrendt, T. Furuhashi, and Y. Uchikawa. Fuzzy controllers for semi-active suspension system generated through genetic algorithms. *Proceedings of the IEEE International Conference on Systems, Man and Cybernetics*, 5:4361–4366, 1995.

[77] A. J. Chipperfield, P. J. Fleming, and C. M. Fonseca. Genetic algorithm tools for control systems engineering. In *Adaptive Computing in Engineering Design and Control*, Plymouth, UK, September 21-22 1994.

[78] Andrew Chipperfield, Peter Fleming, Hartmut Pohlheim, and Carlos Fonseca. *Genetic Algorithm TOOLBOX v1.2 User's Guide*. 1994.

[79] Richard Dorf and Richard Bishop. *Modern Control Systems*. Prentice Hall, 2001.

[80] S. A. Tobias and R. N. Arnold. The influence of dynamical imperfection on the vibration of rotating disks. *Proceedings of Mechanical Engineers*, 171:669–690, 1957.

[81] C.D. Mote Jr. Stability of circular plates subjected to moving loads. *Journal of The Franklin Institute*, 290(4):329–344, 1970.

[82] W.D. Iwan and T.L. Moeller. The stability of a spinning elastic disk with a transverse load system. *Transactions of the ASME Journal of Applied Mechanics*, 4:485–490, 1976.

[83] Y. Honda, H. Matsuhisa, and S. Sato. Modal response of a disk to a moving concentrated harmonic force. *Journal of Sound and Vibration*, 102(4):457–472, 1985.

[84] D. Lee and A. M. Waas. Stability analysis of a rotating multi-layer annular plate with a stationary frictional follower load. *Int. J. Mech. Sci.*, 39(10):1117–1138, 1997.

[85] H. Ouyang, J.E. Mottershead, M.P. Cartmell, and M.I. Friswell. Friction-induced parametric resonance in disks: effect of a negative friction-velocity relationship. *Journal of Sound and Vibration*, 209(2):251–264, 1998.

[86] T. Hamabe, I. Yamazaki, K. Yamada, H. Matsui, S. Nakagawa, and M. Kawamura. Study of a method for reducing drum brake squeal. *Sae Transactions*, 108:523–529, 1999.

[87] H. Mehdigholi. *Forced vibration of rotating disks and interaction with non-rotating structures*. PhD thesis, Imperial College of Science, Technology and Medicine - University of London, London, 1991.

[88] S. M. Vogel and D. W. Skinner. Natural frequencies of transversely vibrating uniform annular plates. *Transaction of the ASME, Journal of Applied Mechanics*, pages 926–931, 1965.

[89] Werner Soedel. *Vibrations of shells and plates*, volume 10 of *Mechanical Engineering*. Marcel Dekker, Inc., New York, 1981.

[90] G. N. Watson. *A treatise on the theory of Bessel functions*. Cambridge University Press, Cambridge, 2nd edition, 1995.

[91] Royal Eugene Collins. *Mathematical methods for physicists and engineers*. Reinhold, New York, 1968.

[92] Costantino Carmignani. *Dinamica Strutturale*. Edizioni ETS, Pisa, 2001.

[93] D. J. Ewins. *Encyclopedia of Vibration*, chapter Disks. Academic Press, 2001.

[94] C. W. Lee and M. E. Kim. Separation and identification of travelling wave modes in rotating disk via directional spectral analysis. *Journal of Sound and Vibration*, 187:851–864, 1995.

[95] A. Tuchinda, N. P. Hoffmann, D. J. Ewins, and W. Keiper. Mode lock-in characteristics and instability study of the pin-on-disc system. In *IMAC-XIX: A Conference on Structural Dynamics*, pages 71–77, Hyatt Orlando Kissimmee, Florida, February 5-8 2001.

[96] G. F. Micheletti. *Tecnologia Meccanica*. UTET, Torino, 1979.

[97] D.J. Ewins. *Modal testing: theory, practice and application*. Research Studies Press Ltd., 2nd edition, 2000.